UNIVERSITY OF CALIFORNIA,
IRVINE

Quasi-One Dimensional Flow Through a Nozzle With a Shock

THESIS

submitted in partial satisfaction of the requirements
for the degree of

MASTER OF SCIENCE

in Mechanical and Aerospace Engineering

by

Isaiah Christian Navarro

Thesis Committee:
Professor William Sirignano
Professor Feng Liu
Professor Dimitri Papamoschou

2019

Dedication

To

Mommer 1
Who has supported me throughout my entire life.

"Retreat, hell! We're not retreating, we're just advancing in a different direction."
-Gen. Oliver Prince Smith, USMC

Contents

List of Figures

List of Tables

Acknowledgments

I would like to thank Professor William Sirignano, my graduate advisor, for all his guidance and counseling during my Masters Studies.

I would also like to thank Professor Feng Liu and Professor Dimitri Papamoschou, the Thesis Committee members, for their support and review.

Abstract of the Thesis

Quasi-One Dimensional Flow Through a Nozzle With a Shock

By

Isaiah Christian Navarro

Masters of Science in Mechanical and Aerospace Engineering

University of California, Irvine, 2019

Professor William Sirignano, Chair

The Soave-Redlich-Kwong cubic equation of state (EoS) was used in real-gas investigations for a mixture of species. An algorithm for a direct solution using a modified version of the Cardanos method is described in order to solve the cubic EoS more efficiently compared to previous methods. Isentropic, choked flow through a convergent-divergent nozzle was investigated using classical mixing rules and compared to flow with the ideal-gas law. Two novel methods were described to solve for the downstream conditions of a normal shock and the results compared to ideal-gas solutions. A computer script was written to solve the cubic EoS. A wide range of stagnation pressure and stagnation temperatures were investigated to analyze the effects on the real-gas solutions. Upon tabulation of results, it was concluded that most solutions with lower stagnation temperatures and higher stagnation pressures are furthest in value to ideal-gas solutions. However, the range of agreement is dependent upon the species present as well as the concentration of those species in a gas.

1 Introduction

The calculation for ideal-gas is well known and requires straightforward equations to solve. However, ideal-gas behavior is significantly different from real-gas behavior. Thus, the need for solving for real-gas properties motivated numerous investigative studies. While there are a number of methods that provides close approximations to real-gas behavior, with the increasing accuracy of the models also comes an increasing difficulty of calculations. In 1948, Redlich and Kwong developed a method to give an accurate approximation dependent on an algebraic relation for a two-parameter equation of state (EoS) [1]. This relation, (listed below), made it possible to solve for the thermal and volumetric properties of compounds, for both single species and mixtures of gases:

$$P = \frac{RT}{v-b} - \frac{a/T^{0.5}}{v(v+b)} \tag{1}$$

Still, Equation (1) was not able to accurately model the dependency on temperature. Thus, attempts were made to find a model that was more temperature dependent and to rectify its inaccuracies. While not an extensive list, the book The Properties of Gases and Liquids by Poling et al., gives a number of variations of the above equation's dependencies on temperature [2]. One of the more popular models to study real-gas was developed by Soave [3]. By replacing the $a/T^{0.5}$ term with $a(T)$, then rewriting Equation (1), the Soave-Redlich-Kwong (SRK) equation becomes:

$$P = \frac{RT}{v-b} - \frac{a(T)}{v(v+b)} \tag{2}$$

The compressibility factor Z is defined as follows for normalized values used in this study:

$$Z = \frac{P}{T\mathscr{R}} \tag{3}$$

In the above equation, $\mathscr{R}$ is a normalized density which will be addressed later in this study. A and B are defined as:

$$A = -\frac{aP}{R_u^2 T^2} \tag{4}$$

$$B = \frac{bP}{R_u T} \tag{5}$$

R_u is the universal gas constant and is not specific to any species of gas. The SRK equation can now be turned into a cubic EoS:

$$Z^3 - Z^2 + (A - B - B^2)Z - AB = 0 \tag{6}$$

The SRK EoS was an improvement compared to the Redlich-Kwong equations, but still had issues with polar compounds, hydrogen mixtures and carbon dioxide. Soave recognized that the future studies can expand upon more temperature dependent parameters such as the specific heat ratio [4].

Since Soave's original paper, multiple studies have improved the accuracy for such compounds by altering the binary interaction coefficient in the mixture rules. (Further explanation of the binary interaction coefficient is provided in Section 2.1). With these improvements, modeling polar molecules has become more accurate and the SRK EoS is no longer associated with a large inability to perform this function.

This study utilizes the classic mixing rules when dealing with gases of multiple species. However, there are several different approaches to modeling the interaction of species. One such method of mixing is the one generally accepted by Huron-Vidal mixing rules [5]. The Huron-Vidal method assumes that at infinite pressures the excess properties of the mixtures have finite limits. An advantage to this method is the exclusion of the binary interaction coefficient. Instead of accounting for multiple species reaction, an interaction parameter is created and can be determined by the type of species involved. Meanwhile, the binary

interaction parameter relies upon experimental data. It was noted in the investigation that the mixing rules fail to model polar compounds with enough fidelity, but this is probably due to the binary interaction coefficients used at that time.

Soave, Gamba and Pellegrini in 2010 investigated the use of the SRK equations but instead of using the classical mixing rules, they used Huron-Vidal mixing rules [4]. In the investigation it outlined how to solve for the interaction parameter seen and using this equation was proposed to solve for the binary interaction parameter in classical mixing rules. The resulting binary interaction parameter was shown to hold for a number of CO_2-aromatic systems. Using the Huron-Vidal mixing rules to solve for binary interaction coefficient would lead to a cumbersome equation. This results because of the temperature-dependent Huron-Vidal equation, the additional temperature-dependent interaction parameter, and the temperature-dependent equation proposed in the paper. Thus, efficiency of computation will be lacking, but binary interaction coefficients of species yet to be found experimentally can be deduced.

Graboski and Daubert demonstrated a few useful tendencies with the interaction between multiple species of gas [6] [7] [8]. This study included vapors and gases, however, it only focuses on gases. Additionally, Graboski and Daubert noticed that it was unnecessary to give k_{ij} a value for interactions between hydrogen and hydrocarbon species. Furthermore, it was also found that interactions between two hydrocarbon species can also be neglected. Meanwhile, temperature dependent interactions were given, mainly for species involved in fracking or industrial energy related endeavors. Graboski and Daubert concluded that more empirical data between species would improve binary interaction coefficient and thus the SRK EoS.

Fewer studies have been done to calculate or estimate the real-gas conditions, downstream of a normal shock, than studies of isentropic flow. All papers have agreed that there is no direct solution and a numerical/iterative method is needed for finding these conditions. These solutions, along with experimental data, have shown that conditions after a normal

shock vary significantly in real-gases compared to calculating ideal-gases. Thus, studies that use real-gas equations for most of the flow, and then utilize ideal-gas relations for normal shocks are not valid solutions such as that proposed by Wilson and Regan [9].

Knowledge of downstream conditions of a shock are not required in order to fully solve for state variables. Kourmonos developed two methods for calculating real-gas effects of a shock using the Redlich-Kwong EoS. The first focused on Mach number and the second on specific volume [10]. The first method utilized is more computationally efficient but requires some knowledge of downstream conditions. The second method requires more effort but does not need downstream information; instead, only critical values are necessary.

Two methods have proven valid in finding these downstream flow properties. The first involves calculating an analytical solution by using the EoS. The second relies on finding two non-linear curves that relate two parameters of downstream condition, (such as temperature and volume) and then finding the point where each curve intersects. The EoS can then be used to find the remaining parameters [11]. Kourememnos-Antonopoulos has shown that use of the Redlich-Kwong equations can be made, concluding that ideal-gas and real-gas behavior differ widely with normal shock. They demonstrated showed that it has decent accuracy for more moderate temperature ranges, but it also demonstrates deviation at high pressures and near critical values. Passman showed similar results by taking a different mathematical approach using Novec 649 as the observed fluid [12].

Sirignano described a third method in order to find downstream conditions. By varying the density ratio, a system of equations can be established to find downstream P_d and T_d [13]. In an earlier paper, Sirignano used an approximate version of the SRK EoS to find results for both isentropic flow and shock flows. The approximation described was valid when both A and B where very small ($A << 1$ and $B << 1$). This specific instance gave rise to the following relation:

$$Z \approx 1 + B - A \tag{7}$$

This approximation was proven to hold for a wide range of values and is compared to this study in Section 4.2.4.

While certain mixtures such as air or CO_2 and H_2O are more relevant to this paper, the original work for developing the Redlich-Kwong equations was for use in fracking. The Redlich-Kwong study was in part for an energy company and their studies were more focused on compounds found in natural gas.

Both Lujan et al. and Passmann's study with different working fluids demonstrated the usefulness of cubic EoS in power cycles, organic ranking cycles, heat transfer and thermal management [14] [12]. An advantage to using the SRK EoS is how it models vapor-liquid mixtures. Modeling certain cycles that use a combination of vapor-liquid and gas phases ordinarily requires more complex planning when creating the program. The original Redlich-Kwong EoS proved that their EoS can be used to model the vapor-liquid properties with relatively decent accuracies. The original Soave model was able to improve upon it further with more accurate computational results when compared to the experimental data found in Sage and Lacey [3] [15]. Even further improvement has been made upon the SRK EoS for investigation into vapor-liquid calculations. For example, Fuller (1976) modified the SRK EoS to give more accurate results than Soave's equation did [16]. Ultimately, Fuller noted that his modified SRK EoS can be implemented to produce Pressure-Volume-Temperature tables.

While the SRK EoS and similar cubic equations are good at modeling real-gas equations, given a limited number of information about the properties of the flow and species, a more precise EoS has been developed and designed for modeling specific compounds. Twu et al. developed a modified version of the Redlich-Kwong EoS that was developed specifically for predicting hydrogen in hydrocarbons for a cubic EoS [17]. It has a similar approach as the SRK EoS in that it utilizes a more general dependency on temperature to replace the $a/T^{0.5}$ with a more general term, $\alpha(T)$. The α term used in Twu et al. is able to make more accurate predictions at lower vapor pressures. Their paper demonstrated that while the

SRK is a very useful tool, a modified Redlich-Kwong EoS specifically designed for a species or mixture would prove to model the gas/ vapor more effectively. However, development of these models does take extensive time and resources, while the resulting increase in accuracy might not be worth the effort expended into the model, or even necessary for the range of temperature and pressure investigated.

For this study, on a wide range of temperatures and pressures, the focus is upon fluid flow through a jet or rocket engine nozzle. Thus, this study does not investigate vapor-liquid mixtures. The previous studies mentioned never investigated temperatures above 1000 K because the accuracy was considered too low with experimental data. On the contrary, higher pressure values have been investigated in some papers, such as Sirignano's investigation [18]. While binary interaction parameters of certain species have yet to be investigated for temperature ranges seen in jet nozzle or rocket engines, it is still important to understand its relationship to an ideal-gas.

This thesis study demonstrates a direct solution using Cardano's method for solving real-gas calculations using a cubic EoS. Compared to previous studies that rely upon utilizing root functions, this will decrease the time of computation. Also, while other investigations were focused on vapor equilibrium calculations, turbomachinery or other systems, this investigation applies the cubic EoS to convergent-divergent nozzles as seen in rocket or jet engines. The normal shock calculations use a method not previously described in literature and are combined with the method for direct solutions.

Since rocket engines experience a large pressure and temperature range, this thesis study investigates the stagnation pressure at 10 bar, 30 bar, 50 bar, 100 bar, 200 bar, and 500 bar. Meanwhile, 500 K, 1000 K, 2000 K, 4000 K are utilized as total values for temperature in isentropic flow. For normal shock calculations, only 500 K and 1000 K are considered, while the pressures remain the same.

1.1 Literature Review

The goal of Redlich-Kwong's study was to derive a two-parameter EoS to make simplistic calculations for real-gas modeling [1]. Note however, this was prior to the first computers becoming readily available to the public. (At the time, they were only available to government agencies, universities or large private companies). The need for a simple algebraic method for modeling real-gas was legitimate. Redlich and Kwong utilized many different calculations, which ultimately led to what is known today as the Redlich-Kwong EoS. The investigators discovered this calculation based on a trial-and-error method.

This equation is a modification of the original Johannes Diderik van der Waals equation which models ideal-gas [19]. This new Redlich and Kwong EoS was met with a wide range of acceptance and is still used a foundation to build other equations. Also, this was not the first time that a set of equations was proposed to model real-gas effects, but it was generally accepted because of its accuracy. These two equations were vital building blocks to understanding the prior research completed, and thus necessary to complete this thesis study.

Unfortunately, as the paper notes, the pair only covered a limited range of temperatures and pressures. These were heavily focused on vapor-equilibrium. Note that this paper was published under the Shell Development Company; thus, much of its focus was on energy-industry-related hydrocarbons.

Sage and Laceys literature piece covers experimental results from studies utilized in various media [15]. It is well cited for comparing the different authors works. Thus, I did not a significant amount of time reviewing it.

Wilson and Regan describe a method for calculating real-gas flow inside a wind tunnel [9]. However, it utilizes ideal-gas laws for different parts of the flow. Wilson and Regan give an example of using the ideal-gas equation for entropy, claiming it holds for certain temperature and pressure regions, but otherwise uses correction factors to improve accuracy

elsewhere. However, it has been established through other pieces that using the ideal-gas law across a shock with real-gas conditions is generally considered to be highly inaccurate. When describing the method used for correcting ideal-gas flow, the authors simply took an experimental table and placed a best fit curve based upon a relation between temperature and the desired correlated value. It even described how the accuracy only depended on the validity of the tables from which they utilized to correct ideal-gas law. The given range was not accurate past smaller Mach numbers. This might be useful for a wind tunnel, (which the paper points out was its primary purpose) for a small set of range of values.

Soave's original paper used a modified version of the Redlich-Kwong equation in vapor pressure calculations [3]. Calculations were done using pure components and compared with the previous Redlich-Kwong equation. The Redlich-Kwong EoS was accepted at the time for being easy to use. At this point in time, computer resources were still scarce; so the need for a model with a small amount of calculations was necessary. Soave changed the dependency on temperature to a form that gave more accurate results for real-gas calculations. Soave continued the research on hydrocarbons, some of which are often seen in the use of energy companies today.

Soave worked as a design engineer for an energy company in Italy. He used the generalized mixing rules in his study, which is essentially the same methodology used in this thesis study. It was unclear how the cubic EoS was solved. Since his paper gave rise to large amounts of information used in this thesis study, it is important to note that a few differences are used in the calculations. First, Soave's study mentioned the use of binary interaction coefficients but since it only investigated pure species, it was never used. Second, the species used in his paper were different. The paper concluded having greater accuracy over the Redlich-Kwong EoS, but is not very accurate when approaching polar molecules.

Fuller's paper begins by stating that he used a modified version of SRK to model saturated liquids with more accuracy than the original SRK [16]. Fuller improved upon Soave's work by adding a more generalized term for temperature with the acentric factor in the

term. Again, the study was used for single species with each compound being modeled over a different temperature range. The highest temperature was 647 K. However, there were a reasonably large range of pressure that mainly focused on covering pressures that would be seen in a pressure-volume-temperature table. Fuller claims that cases with polar molecules have a reasonable accuracy when using this method. While the range of temperature, compressibility, and phase regions are off, it should be demonstrated that there have been multiple papers trying to improve the accuracy of the equations to model real-gas.

The Peng Robinson equation of state is another cubic EoS that relies upon an iterative method for finding real-gas values [20]. The proposed EoS has gain wide acceptance alongside the SRK EoS and is often compared together in later works with each other. It is similar in the respect that it uses a more generalized approach for a temperature dependence as the SRK EoS but adds another term from the original ideal-gas EoS. Peng and Robinson noted that the original van der Waal EoS was broken down into two separate pressure terms, the attractive pressure and the repulsive pressure. These pressures model the interaction between the molecules in a gas with the focus of Redlich-Kwong and the SRK EoS modifying the attractive pressure.

In addition to adding a term in the denominator, the a, b and $\alpha(T)$ equations have modified constants. This leads to a different cubic EoS than the SRK for finding the compressibility. Note that the binary interaction coefficient in Peng and Robinson was not stated anywhere in the paper; thus, it is not clear whether these are the same values used in Soave's investigation into different mixtures of species. Peng and Robinson ultimately state that it has more accuracy in the region seen in pressure-volume-temperature tables. However, it is only able to compare results from pure substances, since in neither paper, binary interaction coefficient values were mentioned. Thus, it might show more favorable results with single species, however, it is not conclusive which method shows better results for mixtures or for higher pressure outside the saturated value ranges.

In addition to this concern, comparison was shown over a small number of species, all

hydrocarbons. It is unclear if the same conclusion can be drawn for a different group of gases, such as oxygen or nitrogen. The paper also does not discuss the accuracy of polar molecules, but later works such as Huron-Vidal, point out the issue with it [5].

Graboski and Daubert state that the American Petroleum Institutes Technical Databook Petroleum Refining adopted a modified Soave method for use in vapor-liquid equilibria calculations [6]. There were three works published in succession and all generally related to each other. The first was focused on demonstrating the use of the SRK equations for mixtures of hydrocarbons. Again, note that the limited amount of information needed for these calculations, along with the simplicity of the procedure, makes it very useful for models. The second publication demonstrates the use of SRK with non-hydrocarbon molecules in mixtures [7]. The third work in this series investigated the reaction of hydrogen with other gases [8].

In one paper, a list of experimentally tested binary interaction coefficients is tested for a number of nonhydrocarbon- hydrocarbon interactions. It was concluded in this work that binary interaction coefficients greatly improve the accuracy of the SRK equations. The third publication focused instead on the use of hydrogen and its interaction with other species. The reason for keeping the discussion of hydrogen separate was because contrary to the range of pressure and temperature for other species interaction, hydrogen exhibits super critical values at much lower temperatures and pressures. Thus, most of useful modeling (at least for the use in energy companies) will be done in the super-critical region.

In the final conclusion of the paper, Graboski and Daubert stated that hydrocarbon-hydrocarbon and hydrogen-hydrocarbon interactions do not require a binary interaction coefficient for decent accuracy. When non-hydrocarbons appeared in the mixture, it became necessary. This makes the SRK equations useful when modeling different hydrocarbon that have yet to be fully tested, only needing a small amount of information to calculate. Since this study only focused on the subcritical, it is not apparent if binary interaction values are needed for supercritical hydrocarbon relations or whether these values are valid for

supercritical use. Later works demonstrated that k_{ij} has a temperature dependence to allow SRK to more accurately model.

The main purpose of Huron and Vidals work was to introduce another method for calculating the mixture of species [5]. The general approach, (which is also used in this thesis study,) is to use the classical mixing rules and is described in Section 2. This approach uses a different interaction coefficient similar to a binary interaction coefficient, but does not need experimental data to calculate and can then be used to solve for the binary reaction coefficient if needed. Coined the Huron-Vidal mixing rules, it is not as explored as the classical mixing rules, but still proves to be a useful tool and alternative method for mixing species. Later works still tend to use the classical mixing rules, whether it be for better comparison to previously accepted works or simply because it was utilized first.

Saad's Compressible Fluid Flow is a widely accepted textbook on compressible flow that is used often in university courses [21]. A large part of the book discusses compressible flow and normal shock related to this study. It does have a limited amount of information on computational fluid dynamics, but it does provide several examples of calculations for nozzle design using various computer techniques. While the discussion is related to ideal-gas equations, Saad goes through the derivations for these equations which serves reference material for deriving some of the real-gas equations in this study.

Twu et al. noted that both the Soave-Redlich-Kwong and Peng-Robinson EoS have less accuracy at values far above supercritical [17]. While this seems not to contradict previous works, Twu et al.'s definition of far above super-critical values differs from other works. The temperatures and pressures investigated, using their proposed modified Redlich-Kwong EoS, are still in the range of vapor-equilibrium calculations. The stated goal of the paper was to investigate hydrogen-hydrocarbon interactions and like previous works before, follow Soave's approach of modifying the dependency on temperature.

Twu et al.'s conclusion is a modified Reldlich-Kwong EoS that is tailored for a set of species so that there is no need to include any binary interaction parameters. Referring

back to the previously mentioned works by Graboski and Daubert, their paper concluded that it was already not necessary to use binary interaction parameters for use with the SRK EoS because of its already strong accuracy for the range of temperatures and pressures [6]. Twu et al. was sponsored by Simulation Science Inc., a software simulation company for processing petroleum, oil and other chemicals. It is unclear the level of increased accuracy needed for this paper or whether the resources were worth the added accuracy or not.

Another question arises, why the binary interaction coefficient was simply not added to the mixing rules for increased fidelity of the already proven SRK equation. There might be an undisclosed need for the level of accuracy greater than what is reached, but the amount of resources to obtain such an equation for a specific set of species might not be worth it for general research.

Poling et al. has a large collection of different topics pertaining to fluids [2]. Since it was cited often as a reference in papers of varying topics, I sought it as a reference. It does contain a number of cubic EoS for real-gas, including SRK, Redlich-Kwong and Peng-Robinson. In addition to containing the general idea for each equation, it also defines other useful properties specifically for each cubic EoS, such as entropy or enthalpy.

John Anderson's Modern Compressible Flow: With Historical Perspectives is a standard textbook used at universities for teaching compressible flow [22]. Anderson's book is very similar to Saad's work, but approaches some topics uniquely and in a different order of discussion. While both Anderson's and Saad's books roughly cover the same areas, one derived equation or approach might be more convenient to use for a given application. Note that for both Saad and Anderson's works, each give little to no mention of compressibility factors or calculations of real-gas.

After Soave's original paper, he continued his work, but used the Huron-Vidal mixing rules instead of the classical mixing rules [4] [5]. The paper was largely focused on deriving interaction parameters from vapor-liquid-equilibrium data. However, a relation was derived between interaction parameters and binary interaction parameters so that the binary inter-

action parameters can be solved for. There has not been as many investigations into using the Huron-Vidal mixing rules as there have been for the classical mixing rules. Even if the Huron-Vidal mixing rules are not used as frequently, their use to derive classical mixing rules binary interaction parameter without experimental data is valuable.

2 Isentropic One Dimensional, Compressible Flow For A Real-Gas

The concept for this method is that given the P and T values the Cubic EoS, Equation 6 can be solved directly using only initial conditions where P_0, T_0, and u_0 (initial velocity) are required. The flow is assumed to be initially at rest, but for practical applications u_0 will not be zero. If the velocity is not initially zero, both the static and stagnation temperature and pressure must be known for that velocity. Solving for the velocity will not be used until Section 2.3.

For ease of comparison, a non-dimensional form is used such that the relations are:

$$P = \frac{P_d}{P_0} \tag{8}$$

$$T = \frac{T_d}{T_0} \tag{9}$$

Note that the subscript d signifies a variable with a dimensional value, while a variable without a subscript d signifies a non-dimensional variable.

Recalling the only variables in the Cubic EoS are A, B, and Z, Equations 4 and 5, Z can be solved using Cardano's method for a depressed cubic equation. However, both Equations 4 and 5 need to be modified slightly to account for a mixture of species, as well as, to normalize the values:

$$A = \frac{aP_d}{(R_u T_d)^2} = \frac{\hat{a}P}{T^2} \tag{10}$$

$$B = \frac{bP_d}{R_u T_d} = \frac{\hat{b}P}{T} \tag{11}$$

Referring back to Equation 2, Soave defines a more general relation between $a(T)$ and temperature. Equation 12 is the classical mixing rules being applied to a while Equation 13

is the definition of a for a single species of gas. Note, these are still in the dimensional form. Essentially, a is changed to $\hat{a}$ and b to $\hat{b}$, where the circumflex denotes a normalized value. To avoid confusion the equations are stated below in normalized form and the dimensionalized form:

$$a = \sum_{i=1}^{N} \sum_{j=i}^{N} \sqrt{a_i a_j}(1 - k_{ij}) X_i X_j \tag{12}$$

$$a_i = 0.42748 \frac{(R_u T_{ci,d})^2}{P_{ci,d}} \left[1 + S_i \left(1 - \sqrt{\frac{T_d}{T_{ci,d}}} \right) \right]^2 \tag{13}$$

N denotes the number of species. For the case of a single species, where N=1, a_i is equal to a. Both i and j correspond to a specific species within the index of species being calculated. This implies, if there are two species in a gas mixture, i and j will denote whichever species is being calculated at that given time. For example, given the case of air, there are oxygen and nitrogen present in the index. Utilizing the equation for a, there should be four terms added together. The first term is when O_2 corresponds to both i and j. Second, when i corresponds to O_2 and j to N_2. Third, when i denotes N_2 and j O_2. Finally, the fourth for when both i and j correspond to N_2. Now the $\hat{a}$ value can be found by solving the equation below:

$$\hat{a} = \frac{a P_0}{(R_u T_0)^2} = \sum_{i=1}^{N} \sum_{j=1}^{N} \sqrt{\hat{a}_i \hat{a}_j}(1 - k_{ij}) X_i X_j \tag{14}$$

where $\hat{a}_i$ is for the species i, and k_{ij} is the binary reaction coefficient that will be explained further in Section 2.1.

$$\hat{a}_i = \frac{a P_d}{(R_u T_d)^2} = 0.42748 \frac{T_{ci}^2}{P_{ci}} [1 + S_i (1 - \sqrt{\frac{T}{T_{ci}}})]^2 \tag{15}$$

T_{ci} is the critical temperature of species i and is normalized by T_0 so that:

$$T_{ci} = \frac{T_{ci,d}}{T_0} \tag{16}$$

P_{ci} is also normalized in a similar manner:

$$P_{ci} = \frac{P_{ci,d}}{P_0} \tag{17}$$

$$S_i = 0.48508 + 1.5517\omega_i - 0.15613\omega_i^2 \tag{18}$$

Note w_i is the acentric factor and can be found in many textbooks. Soave defines b as follows [3]

$$b_i = 0.08664\frac{R_u T_{ci}}{P_{ci}} \tag{19}$$

$$b = \sum_{i=1}^{N} X_i b_i \tag{20}$$

Further, in the non-dimensional form:

$$\hat{b_i} = \frac{b_i P_0}{R_u T_0} = 0.08664\frac{T_{ci}}{P_{ci}} \tag{21}$$

$$\hat{b} = \frac{bP_0}{R_u T_0} = \sum_{i=1}^{N} X_i \hat{b_i} \tag{22}$$

At this point it is convenient to calculate $\frac{dA}{dT}$ and $\frac{d^2A}{dT^2}$ which will be required later:

$$A' = \frac{dA}{dT} = T\frac{d\hat{a}}{dT} = \sum_{i=1}^{N}\sum_{j}^{N} \frac{1-k_{ij}}{2} X_i X_j T\left[\sqrt{\frac{\hat{a}_i}{\hat{a}_j}}\frac{d\hat{a}_j}{dT} + \sqrt{\frac{\hat{a}_j}{\hat{a}_i}}\frac{d\hat{a}_i}{dT}\right] \tag{23}$$

$$A'' = \frac{d^2A}{dT^2} = T^2\frac{d^2\hat{a}}{dT^2} =$$
$$\sum_{i=1}^{N}\sum_{j=1}^{N}\frac{1-k_{ij}}{2}T^2X_iX_j\left[\sqrt{\frac{\hat{a}_i}{\hat{a}_j}}\frac{d^2\hat{a}_j}{dT^2} + \frac{1}{\hat{a}_i\hat{a}_j}\frac{d\hat{a}_i}{dT}\frac{d\hat{a}_j}{dT} - \frac{1}{2}\frac{\hat{a}_i^{0.5}}{\hat{a}_j^{1.5}}\frac{d\hat{a}_j^2}{dT^2} + \sqrt{\frac{\hat{a}_j}{\hat{a}_i}}\frac{d^2\hat{a}_j}{dT^2} - \frac{1}{2}\frac{\hat{a}_j^{0.5}}{\hat{a}_i^{1.5}}\frac{d^2\hat{a}_i}{dT^2}\right] \tag{24}$$

With $\frac{d\hat{a}_i}{dT}$ and $\frac{d^2\hat{a}_i}{dT^2}$ defined by:

$$\frac{d\hat{a}_i}{dT} = 0.42748\frac{T_{ci}^{1.5}}{P_{ci}T^{0.5}}S_i\left[1 + S_i(1 - \sqrt{\frac{T}{T_{ci}}})\right] \tag{25}$$

$$\frac{d^2\hat{a}_i}{dT^2} = -\frac{0.21374}{P_{ci}}\left(\frac{T_{ci}}{T}\right)^{1.5}S_i(1 + S_i) \tag{26}$$

2.1 Interaction Coefficient k_{ij}

The binary interaction coefficient relates the interaction of two species from each species enthalpy and entropy. Each pair of species has a unique coefficient that is ordinarily temperature dependent and its range varies depending on the type of molecular bonds of the species.

The initial Soave paper stated that polar molecules, such as H_2O, were not able to be accurately accounted for; however, it has been determined since that a more appropriate value of k_{ij} negates this limitation [3]. For use in a computational environment, k_{ij} can be written as a matrix where each i,j element corresponds to a specific interaction:

	O_2	N_2
O_2	0	-.003
N_2	-.003	0

Note, the interaction between two different molecules of the same species equals zero. Thus, when i=j, $(1 - k_{ij})$ becomes 1 and then the X_iX_j terms become X_i^2. Studies have been done to calculate the value of k_{ij} for various hydrocarbon and non-hydrocarbon species,

but most of these specific species are not typically seen in the exhaust gas of a convergent-divergent nozzle. Since much of the initial research was done by energy companies, the researched species correspond to interactions found in fracking and boilers [6]. Regarding the interaction of O_2 and N_2, for use in this study Peng-Robinson was used with $k_{ij} = -0.00978$, (from Stoll et. al.). [23] A more useful list of k_ij values are found in Appendix B.

2.2 Cardano's Method and Other Necessary Steps

It should be noted here that when solving for the exact value of Z in the cubic EoS, a numerical solution is used, meaning a computational program runs a subroutine to find the correct fitting zero of a cubic EoS. This was true for the other papers that have been mentioned. On the other hand, this study utilizes Cardano's method to find the solutions of a cubic equation explicitly.

Now that A and B can be calculated, the coefficients of the Cubic EoS can be found and Z solved for. For the exact solution, a variation of Cardano's method must be used to solve for a polynomial equation of degree 3. For convenience sake, each leading coefficient will be assigned a new variable to reduce the number of variables required in Cardano's method:

$$N_1 = -1; N_2 = A - B - B^2; N_3 = -AB \tag{27}$$

Now, the cubic equation becomes:

$$Z^3 - N_1 Z^2 + N_2 Z - N_3 = 0 \tag{28}$$

From here a reduced cubic equation is necessary. Thus, substituting $Z = r - \frac{N_1}{3}$ the cubic equation will become:

$$r^3 + q_1 r + q_2 = 0 \tag{29}$$

where q_1 and q_2 are as follows:

$$q_1 = N_2 - \frac{N_1^2}{3} \tag{30}$$

$$q_2 = N_3 + \frac{2N_1^3 - 9N_1N_2}{27} \tag{31}$$

The goal here is to find a solution for the depressed cubic equation (Equation 29). In order to do so, two new variables u and v, where $r = u + v$:

$$u^3 + v^3 + (u + v)(3uv + q_1) + q_2 = 0 \tag{32}$$

In order for the above equation to be satisfied, the following relation is defined:

$$3uv + q_1 = 0 \tag{33}$$

This allows another relation to occur:

$$u^3 + v^3 + q_2 = 0 \tag{34}$$

With Equation 33 and 34, both u and v can be solved for. Next utilizing algebra, u and v become:

$$u^3 = \frac{-q_2}{2} + v\frac{q_2^2}{4} + \frac{q_1^3}{27} \tag{35}$$

$$v^3 = \frac{-q_2}{2} - v\frac{q_2^2}{4} + \frac{q_1^3}{27} \tag{36}$$

By substituting the above equations into each other and solving for u now yields:

$$u = \sqrt[3]{\frac{q_2}{2} + \sqrt[2]{\frac{q_2^2}{4} + \frac{q_1^3}{27}}} \tag{37}$$

Note that a few different computational errors might occur at this point. First, solving the square root term might yield an imaginary number that is very close to zero. For this

study, any occurrences have been on a small magnitude of 10^{-5} or less. Second, certain programs have difficulty calculating cubic roots that have values near 1, thus other methods are necessary. In the case of the program Matrix Laboratory, the nthroot command fixed this issue of giving erroneous answers near the number 1. Details on the use of this built in function can be found here: (https://www.mathworks.com/help/matlab/ref/nthroot.html)

Since u has been solved for, v is found by rearranging Equation 33 and substituting Equation 37 into it. Next, the first and most important root of the cubic EoS can be solved for:

$$Z_1 = v - u - \frac{N_1}{3} \tag{38}$$

The other two roots can be found by stating a new variable w as the cubic root of 1. These other two roots are never the correct solution to the Cubic EoS. Either the other two roots are imaginary or not closer to 1 than Z_1. If only the roots can be given, the correct root would be the number closest to 1 that is positive. While most Z values are greater than 1, in low temperature and low pressure environments, Z can dip below 1, but never below zero.

For reference, the other two roots are found using ω_1 (the cubic root of 1) and the following equations:

$$\omega_1 = -\frac{1}{2} + (\sqrt{\frac{3}{2}})i \tag{39}$$

$$Z_2 = v\omega_1^2 - u\omega_1 - \frac{N_1}{3} \tag{40}$$

$$Z_3 = v\omega_1 - u\omega_1^2 - \frac{N_1}{3} \tag{41}$$

These method can be written as a subroutine in a code and be called upon with a relatively small amount of clutter. In addition this modified Cardano's method is applicable to all cubic EoS. The only difference would be the leading coefficients of Z terms.

2.3 Solving for Density, Temperature, Velocity and Sound Speed

Now that Z has been solved for the exact solution, the EoS can be used to solve for $\mathscr{R}$ giving the three most valuable variables $(P, T, \mathscr{R})$. While $\mathscr{R}$ represents the density term and is called the normalized density in this study, it should be noted that $\mathscr{R}$ is not equal to $\frac{\rho}{\rho_0}$, rather $\mathscr{R}$ is defined as:

$$\mathscr{R} = \frac{\rho R T_0}{P_0} \tag{42}$$

This study changes the deviation in pressure (dP) and relates the change in pressure to the change in the rest of the calculated properties. If a relation between T and P can be found, then a new value of A, B and thus Z can be solved for by the previous mentioned equations. Sirignano derived in his investigation a relation between dT and dP based on variables of the flow [13]:

$$\frac{dT}{T} = \beta \frac{d\rho}{\rho} + \frac{1}{c_v + k} ds \tag{43}$$

$$\frac{dP}{P} = (f + g\beta) \frac{d\rho}{\rho} + \frac{1}{c_v + k} ds \tag{44}$$

In the case of isentropic flow the change in entropy, ds, will become zero so the entire second term will cancel out in both Equations 43 and 44.

$$\frac{d\rho}{\rho} = \frac{1}{f + g\beta} \frac{dP}{P} \tag{45}$$

By substituting Equation 43 into Equation 45 a relation between the change in pressure, dP, and the change in temperature, dT, can be found:

$$\frac{dT}{dP} = \frac{\beta T}{P(f + g\beta)} \tag{46}$$

The terms f, g and β in Equation 46 are defined as [13]:

$$f = \frac{2Z^3 - Z^2 + AB}{Z^3 - B^2 Z} \tag{47}$$

$$g = \frac{1}{Z - B} - \frac{A'}{Z(Z + B)} \tag{48}$$

$$\beta = \frac{(\gamma - 1)Zg}{1 + \frac{k}{c_v}} \tag{49}$$

$$\frac{k}{c_v} = (\gamma - 1)\frac{A''}{B} ln\left(\frac{Z + B}{Z}\right) \tag{50}$$

For consideration of velocity, an initial velocity can be defined as u_0. The algorithm developed was specifically developed to accommodate the possibility of u_0=0, even though in practical application this should not occur. When dealing with nozzle flow, when velocity is zero at the beginning of a nozzle, where the area ratio is at infinity, the fluid will still have some initial velocity and finite area, even if the final velocity at the end of the nozzle is a few order of magnitudes larger. Like the rest of the variables, velocity is normalized, but this time by $\sqrt{RT_0}$ so that R is the specific gas constant of a species. This means that the final solution to the calculations will depend on the specific properties of the gas:

$$U = \frac{u_d}{\sqrt{RT_0}} \tag{51}$$

Unfortunately this means that U would be solved for a given specific pressure and temperature, where the dimensional velocity is also known. This gradient equation is required to solve for velocity through the flow:

$$\frac{dU^2}{dP} = -\frac{2}{\mathscr{R}} \tag{52}$$

While it is possible to find the gradient $\frac{dU}{dP}$, it is inversely proportional to U, thus near very small or large values the derivative gives either very small or large $\frac{dU}{dP}$ values. This also means that there must always be an initial velocity in the beginning of the flow. This may not prove to be a hindrance in practical applications, but used in theoretical studies will prove to be problematic. However, it is needed later for solving for area, thus so it is listed below:

$$\frac{dU}{dP} = -\frac{2}{\mathscr{R}U} \tag{53}$$

The same term is applied to normalize the initial value of the sound speed, so that the normalization is:

$$C = \frac{c_d}{\sqrt{RT_0}} \tag{54}$$

A partial derivative could be derived for the change of the normalized sound speed with respect to pressure, but at very small changes in the values of C it is not that convenient to use. The gradient equation closely resembles that of $\frac{dU}{dP}$. Also, with a small change in P there are larger changes in C. Thus, the following equation was derived and used to find the sound speed, (for inviscid fluids):

$$C = \sqrt{TZ\big(f + g\beta\big)} \tag{55}$$

Equation 55 is derived from the general definition of sound speed:

$$C^2 = \left(\frac{\partial P}{\partial \rho}\right)\bigg|_{Entropy} \tag{56}$$

Equation 45 can be rearranged and then substituted into Equation 56 to yield Equation 55.

2.4 Application to Nozzle Flow

This section is for the application of a Quasi-One-Dimensional Flow as seen in a basic nozzle calculation. The basic mapping of P, T, C, U is required, which is found utilizing the prior steps taken to calculate these parameters. Once this is complete, the variables of state for the throat of the nozzle must be found. This can be done by finding where Mach number, M, is 1 or where C and U are equal. However, since a computational method is used, there will not be a point where C exactly equals U, so an interpolation is necessary.

When the interpolation of the properties are found, the flow can be distinguished between the convergent portion of a nozzle and the divergent portion. This is important in calculation of the area. While the exact area cannot be found based on properties at an exact location in a nozzle, a gradient equation can be found for the area ratio, α, or the area of the location in the nozzle to that of the throat. Using the throat as a new starting point, the isentropic calculation can be re-done in either the direction of the convergent part of the nozzle (increasing P) or the divergent part of the nozzle (decreasing P). The relation between change in α to that of P is derived from continuity and is defined as:

$$\frac{d\alpha}{dP} = -\alpha[\frac{1}{P(f + g\beta)} - \frac{1}{\mathscr{R}U^2}] \tag{57}$$

Starting with a form of the continuity equation a derivative with respect to pressure is taken and divided by $\rho_d u_d \alpha$. Equation 58 is the form of the continuity equation used and Equation 59 is the normalized version. Both can be used to derive Equation 57, but it easier to follow in the normalized form. Equation 60 is formed after derivation with respect to dP and division of $\mathscr{R}U\alpha$.

$$\rho_d u_d \alpha = constant \tag{58}$$

$$\mathscr{R}U\alpha = constant \tag{59}$$

$$\frac{1}{\mathscr{R}}\frac{d\mathscr{R}}{dP}+\frac{1}{U}\frac{dU}{dP}+\frac{1}{\alpha}\frac{d\alpha}{dP}=0 \tag{60}$$

Now isolate $\frac{d\alpha}{dP}$:

$$\frac{d\alpha}{dP}=-\alpha[\frac{1}{\mathscr{R}}\frac{d\mathscr{R}}{dP}+\frac{1}{U}\frac{dU}{dP}] \tag{61}$$

Referring back to Equation 45, the term $\frac{d\mathscr{R}}{dP}$ is already known and can be substituted into the Equation 61 after it has been normalized. In addition, the second term is already known from Equation 53 and can be immediately substituted into Equation 61. With both the described substitutions and some simplification the derivation of Equation 57 will be complete.

Through the diverging part of the nozzle, the pressure will continue to drop but will dramatically drop when nearing the exit of the nozzle where α is much larger. This dramatic pressure drop requires a small step size of dP in order to accurately calculate the expansion of the nozzle. A non-uniform mesh-grid might be appropriate here for efficient calculations. If the shape of the nozzle is already known and a correlation of axial distance is required, this relationship can be found with a change in P and the α. A function of axial distance could be substituted in for α and Equation 57 rearranged so that a change P can be found for a change in distance across the nozzle:

$$dP=\frac{d\alpha}{-\alpha}\left[\frac{1}{P(f+g\beta)}-\frac{1}{\mathscr{R}U^2}\right]^{-1} \tag{62}$$

2.5 Critical Value For a_i

A sudden jump in $\frac{a_i}{a_j}$ values causes the calculations to have a variation in the curve's trends for all variables versus pressure. For coarse meshes, the effects of this will be undetectable for properties such as normalized temperature or velocity. Fine meshes can be used to isolate the jump to a small number of points on the grid. Techniques can be used to

"smooth" out this region, if necessary. This issue should not appear in rocket engine nozzles because of the higher temperature range, but it should appear in jet engine nozzles due to the lower temperature range. These critical values have been found to be related to where the temperature crosses the S_i values.

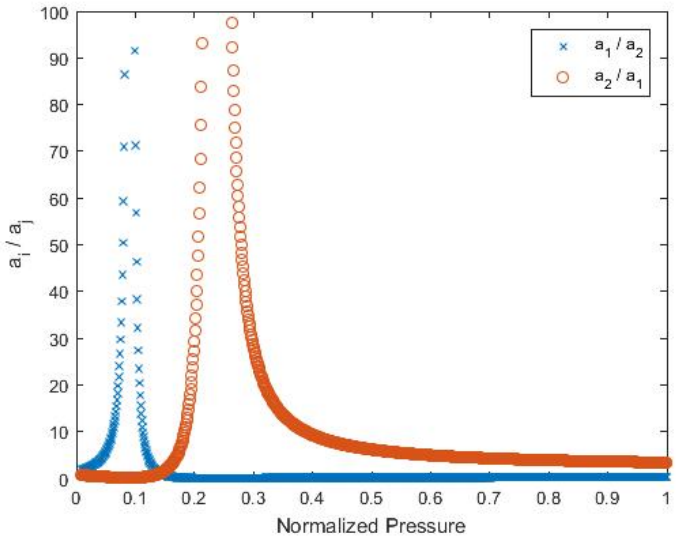

Figure 1: $\frac{a_i}{a_j}$ jump example

At a certain temperature for each species a, as defined in Equation 15, it will come to zero and for a short time be close to zero. During these range of values the ratio $\frac{a_i}{a_j}$ will become extremely large. Referring back to Equation 15, the only part that is able to make the entire equation a zero value is the squared term:

$$[1 + S_i(1 - \sqrt{\frac{T}{T_{ci}}})]^2 \tag{63}$$

Solving for S_i will lead to the following:

$$S_i = \frac{-1}{1 - \sqrt{\frac{T}{T_{ci}}}} \tag{64}$$

When S_i reaches the value described in Equation 64, the ratio $\frac{a_i}{a_j}$, will become very large

because a_j will either become zero or pass very close to it.

2.6 Real versus Ideal-Gas One Dimensional Comparison

Using the isentropic flow equations for ideal-gases, the flow is independent of initial temperature. Rather the Mach number, M, dictates the ratios $\frac{P_0}{P}$ and $\frac{T_0}{T}$. From $\frac{P_0}{P}$ and $\frac{T_0}{T}$, P and T can be found respectively. However, changing P_0 and T_0 will not affect $\frac{P_0}{P}$ and $\frac{T_0}{T}$. The different species of the gas will change γ, thus slightly taking into account the specific properties.

Meanwhile, utilizing the SKR method, changing P_0 and T_0 will affect the value of $\frac{P_0}{P}$ and $\frac{T_0}{T}$, at a given Mach number. The effects of a species individual characteristics are taken into account due to most of the equations and variables stated in Section 2, and are dependent on specific heat capacities, γ, T_{ci}, P_{ci}, MW and ω_i. This will provide a more accurate representation of the flow for various temperature and pressure ranges.

The following are the ideal-gas, isentropic relations that are commonly found in books discussing compressible flow. Taken from Anderson [21] [22]:

$$\frac{T_0}{T} = 1 + \frac{\gamma - 1}{2} M^2 \tag{65}$$

$$\frac{P_0}{P} = (1 + \frac{\gamma - 1}{2} M^2)^{\frac{\gamma}{\gamma - 1}} \tag{66}$$

$$\frac{\rho_0}{\rho} = (1 + \frac{\gamma - 1}{2} M^2)^{\frac{1}{\gamma - 1}} \tag{67}$$

$$\alpha^2 = \frac{1}{M^2} \Big[\frac{2}{\gamma + 1} (1 + \frac{\gamma - 1}{2} M^2) \Big]^{\frac{\gamma + 1}{\gamma - 1}} \tag{68}$$

As seen in the Equations 65 to 68, the ideal-gas ratios are only affected by a single property of the flow field, M, and γ, a property of the composition.

3 Normal Shock Calculation

For an ideal-gas, solutions generally contain ratios across the shock and are easily found. We require upstream values for pressure and temperature, and Mach number (or velocity). From the conservation equations, downstream pressure, temperature, and Mach number (or velocity) can easily be found in terms of ratios for both static and stagnation conditions. However, for the case of a real-gas, the static and stagnation values need to be solved separately. In addition, simple relations for pressure ratios and temperature ratios are not found and thus, a numerical or iterative approach is necessary.

Analysis of static values begins with the fundamental equations of fluid dynamics: Continuity (Equation 69), Momentum (Equation 70) and Energy (Equation 71). Until this point, the calculations have been done using normalized values, but for the equations used to find downstream conditions of a normal shock, dimensional values must be used. Note, these equations are already in their constant area form and are greatly simplified from their original form:

$$\rho_1 u_1 = \rho_2 u_2 \tag{69}$$

$$\rho_1 u_1^2 + P_1 = \rho_2 u_2^2 + P_2 \tag{70}$$

$$h_1 + \frac{u_1^2}{2} = h_2 + \frac{u_2^2}{2} \tag{71}$$

In the energy equation, h is the specific enthalpy, with the total enthalpy being held constant. Following, is the equation for direct calculation of the static enthalpy (Equation 72) as well as the equation for total enthalpy (Equation 73) [2]:

$$h = h_{ideal} + \frac{1}{MW}\left[R_u T(Z-1) + \frac{T\frac{da}{dT} - a}{b} ln\frac{Z+B}{Z}\right] \tag{72}$$

$$h_{ideal} = C_p T$$

$$H = h + \frac{u^2}{2} \tag{73}$$

Equation 73 is essentially the same as 71, but instead of a conservation equation it calculates the constant value. This is used later in the Normal Shock calculations to converge to a solution. Note that the terms $\frac{da}{dT}$, b, and a are not from the normalized terms, (B is the same for both normalized and dimensional values). C_p is the specific heat capacity of the gas and for this investigation is held constant, not varying with temperature or pressure. In addition, when investigating multiple species, the mixing rules need to be properly accounted for. The specific heat capacity is defined as:

$$C_p = \frac{\gamma R}{\gamma - 1} \tag{74}$$

In this study there are two algorithms that are identified. The first algorithm does not require knowledge of the upstream velocity, u_1. The second relies upon complete knowledge of the upstream conditions including: P_1, T_1, h_1, u_1, and ρ_1. This is more convenient for calculating downstream conditions of a shock inside a nozzle.

3.1 Method 1 of Normal shock

Even with manipulations and substituting Equations 69, 70, 71, 72 and the Cubic EoS, there is still is no equation that will be able to directly solve for any single downstream variable. Thus, choosing a ratio across the shock for a variable over a range was necessary. Choosing a ratio for Z would not give any useful information. An enthalpy ratio, again would not reveal very useful information. Previous studies have used a density ratio that worked well, especially considering the relationship between a density ratio and the velocity

ratio, which are just reciprocals of each other. However, the density ratio saturates to a constant and will not go past that ratio no matter how strong the shock. Thus, knowledge of the saturated density ratio is needed beforehand when indexing the range of density to be calculated. This makes it more challenging to calculate shock conditions at high pressure or temperature ratios because the iteration between density ratio values will be consistently smaller.

The remaining options are to choose between a pressure ratio ($p_r = \frac{p_2}{p_1}$) or temperature ratio ($T_r = \frac{T_2}{T_1}$). When dealing with a mixture of species the dependencies on temperature become very cumbersome and are prone to errors in the calculation. Thus, if one were to choose a pressure ratio, a number of temperature-dependent equations would first still be required to be solved in order to figure out the correct density ratio. For dealing with multiple species it was more convenient to choose a temperature ratio then use it to solve for a,b, and $\frac{da}{dT}$.

Up to this point, the only downstream condition of a shock that is known is T_2. Even with this knowledge, the rest of the variables can not be directly solve for. Another variable must be chosen, this time as a "guess" in order to find the correct value corresponding to T_2. Choosing a pressure ratio as this guess will allow use of the cubic EoS to solve for a Z_2 and thus ρ_2. However, a guess where $p_2 = p_1$ will result in multiple undefined equations later. In order to avoid this, an initial guess for p_2 should be slightly above p_1. A guess where $p_r = 1 + (1)^{-9}$ would suffice. With knowledge of T_2,p_2,ρ_2, and Z_2, then h_2 can be solved for using Equation 72.

Manipulating and substituting Equation 69 into Equation 70 results in a relationship between p_2,p_1,ρ_1, and u_1:

$$u_1^2 = \left(\frac{p_1}{\rho_1}\right)\frac{1 - \frac{p_2}{p_1}}{\frac{\rho_1}{\rho_2} - 1} \tag{75}$$

With the velocity u_1 and the density ratio $\frac{\rho_2}{\rho_1}$ known, the velocity ratio can be found easily and consequently u_2 is determined.

With T_2 known and P_2, u_2, ρ_2 and h_2 found, the total enthalpy downstream and upstream can be found utilizing Equation 73. Note that besides the chosen T_r ($\frac{T_2}{T_1}$) value, the rest of the calculations are found based of a guess of p_2 and thus still need to be verified that it satisfies all conservation equations. Thus the total enthalpy of both upstream and downstream will be compared to make certain that they are equal to each other. At this point a tolerance must be chosen to decide whether the solution is "good enough." For most of the range of temperatures, a tolerance investigated of 10^{-5} is used to produce smooth curves when graphing the final values.

When comparing H_1 and H_2, if the tolerance is acceptable, the values that were calculated for p_2, u_2, ρ_2, and h_2 correctly correspond to the chosen T_2. If the error is larger than the designated tolerance, then p_r must be adjusted depending on whether H_1 or H_2 is bigger. When H_2 is bigger than H_1, that means the guessed shock is not strong enough and p_r (and in turn p_2) must be increased. When H_2 is lower than H_1, then the proposed value p_r must be decreased, (a weaker shock). From here the calculations for the following T_r values can be found, using the previously described method.

3.2 Method 2 of Normal Shock

The second method for calculating normal shock relies upon knowing the value for upstream velocity u_1. With this additional knowledge, the exact position inside a nozzle can be taken into account versus having a random P_1 and T_1 with no way to determine the correct downstream conditions. Basically u_1 gives precise information that can be used to determine exact downstream conditions, rather than having a large amount of possible conditions.

Initially it might be tempting to consider using the knowledge of u_1 to quicken the calculations. While it is possible to get some of the state variables more easily, such as the density ratio or velocity ratio, it is more cumbersome to find the exact solution that satisfies all downstream conditions, not just possible solutions. While the downstream Mach number

decreases as the upstream velocity increases, the velocity downstream does not monotonically increase or decrease. Thus, when numerically solving for the normal shock solution it is not certain if the strength of the shock needs to increase or decrease for the next guess.

Starting the calculations of the normal shock solution by guessing the velocity ratio would work based upon previous studies that demonstrated success of using the density ratio and Equation 69. However, this will run into the same issue as choosing the density ratio to start out with, because both the density ratio and velocity ratio eventually converge to a set value at infinite Mach number. This is the same issue as choosing the density ratio in the beginning as described in Section 3.1.

Thus, the solution that was used in this thesis study evidently resembles Method 1 of solving for normal shock, but with a slight difference. Method 1 solved for a long list of solutions to normal shock, each with a different upstream flow velocity and Mach number. The solution of Method 2 needs to result in a single solution, thus for the first iteration of the normal shock solution, only one set of downstream conditions is solved for.

As previously a Tr will be chosen, but this time as a guess. The rest of the downstream conditions will be found the same as Method 1 and a correlating pseudo upstream velocity found. The velocity that was found using the guessed Tr is compared to the actual upstream velocity. If the actual upstream velocity is greater than the guessed velocity, then the guessed Tr needs to be decreased. If the actual upstream velocity is lower than the guessed velocity, then the guessed Tr needs to be increased. The actual Tr can be solved for and thus the downstream conditions using the difference in actual velocity and guessed velocity as an error analysis. For this thesis study, a 0.001 $\frac{m}{s}$ error between the actual upstream velocity and velocity based on a guessed Tr is considered acceptable.

4 Results

4.1 Computational Cost

One reason for this thesis study is to identify a method of increasing the computational efficiency of solving for real-gas calculations. The typical method for solving a cubic equation is using the built in roots function of the computer language being utilized to write the script. The cost of computation using the root function will dramatically increase over a large amount of points found. Thus, it was necessary to investigate the actual cost of the roots function versus the described Cardano's Method. Note that MatLab was used for the script and other languages or packages are going to have varying degrees of computational efficiency.

In addition, Sirignano described an approximate solution to the EoS that sacrifices accuracy for an extreme increase in computational efficiency [18]. In order to measure the impact of these calculations on computer cost, the cubic EoS was solved over a large range of pressure and temperature for fifty times. The reason for repeating the same calculation over is for the computer's re-allocation of memory, central processing unit (CPU), pausing background tasks, etc., when focused on a specific task versus a quick one second run of script. Each time a point was calculated, the time needed was stored and at the end of the fifty runs, the results were averaged. The comparison of the time of computation results as expected and is tabulated below. Cardano's Method was over twice as efficient as using the roots function. On the other hand the approximate solution only took on average 3.27% of the time of Cardanos Method.

	Root Function	Approximate Solution
Computational Cost	2.0454	0.0327

Table 1: Since each computer will give different times for computations it was necessary to normalize the computational time by the time it took for Cardano's Method to be completed.

The cost of computation between the real-gas calculations and ideal-gas calculations was done in the same manner with repeating all of the calculations relatively. While it may seem trivial, if the ideal-gas calculations provide a "good enough" solution for a particular application, it may be more beneficial to run a large amount of code using the ideal-gas calculations instead of real-gas. The only discrepancy was a line of code used to create the matrix of the normalized pressure, or in the case of the ideal-gas, the pressure ratio. On average it took the same PC $3 * 10^{-6}$ seconds to create the matrix. However, this small discrepancy is not inconsequential considering that the cost of computation for ideal-gas is 0.28% to that of the script developed in this thesis study for real-gas.

4.2 Isentropic Flow

Real-gas calculations of Air were compared to ideal-gas using the multi-species SRK equations. For these calculations, the specific heat ratio γ is 1.4 and is constant. For a more accurate model that might expand upon this work, temperature-dependent specific heat capacities should be included. The composition of air, 20% 0_2 and 80% N_2. This way $X_{O_2} = 0.2$ and $X_{N_2} = 0.8$. The constants used that are specific to each species of gas are listed in Appendix B. The general arrangement for most of the investigated flow properties is to first display the graphs where P_0 is held constant and examine the variation of T_0 over a wide range. Then, after demonstrating how T_0 affects the flow, T_0 is held constant while P_0 varies over a wide range. For most of the flow the species and mixtures investigated are well inside the super-critical range. However, some calculations are done in the gaseous region of a phase diagram. No calculations were done near pressure or temperature values that would result in a phase change.

All species of gases exhibited the same trend as air but with different levels of agreement with the ideal-gas law. Generally, the model derived in this thesis study showed the most agreement to ideal-gas equations when the P_0 is at a lower value and T_0 is higher in nature. The range of T_0 investigated was 500 K to 4000 K, while the P_0 range was from 10 bar to

500 bar. When discussing the differences between real-gas solutions and ideal-gas solutions, it should be noted that in the case of isentropic flow, there is no difference in the trends of the properties. When pressure changes, the real-gas still increases or decreases how ideal-gas would in turn. However, the actual values of the solutions do differ from each other. When proceeding through Section 4.2, when "divergence" or "difference" is discussed comparing the real-gas and ideal-gas, it is referring to the difference in values of the solution. For example, at a given P, the U for real and ideal-gas would still be decreasing or increasing in the same direction, but $U_{real} \neq U_{ideal}$ at that specific P.

The k_{ij} value for air was taken from Peng-Robinson so that k_{ij} for the interaction between O_2 and N_2 is -.00978. Stoll-Vrabec-Hasse propose other values for this k_{ij}, and the difference in real-gas calculations between different k_{ij} values is very small [23]. This is likely because the binary interaction coefficient is so small between diatomic species.

Other species and mixtures were investigated in addition to air and their results are shown in the Appendix D. This thesis study was mainly concerned with modeling air using the SRK EoS because air has a wide use in other investigations and its ease of study for future experimental studies in control laboratory environments, such as a wind tunnel.

Originally, when the graphs were compiled there was a noticeable jump in compressibility, Z, at certain P values for the highest pressure, $P_0 = 500$ bar, and lowest temperature, $T_0 = 500$ K. Upon considerable review of the code, the jump was thought to have been related to a limitation of the software used. MatLab has trouble calculating Equation 37 as already mentioned in Section 2.2, but has further trouble calculating a few of the terms in the same equation at the temperature and pressure values mentioned above. Thus, instead of using Cardano's method for the described temperature and pressure values, the roots function that is built into MatLab was used. Using the roots function for this particular pressure and temperature range removed the region where the Z jumped.

4.2.1 Temperature Results

The first set of figures, from Figure 2 to Figure 7, hold P_0 for each graph then vary T_0. The second set of figures, from Figure 8 to Figure 11, does the opposite, holding T_0 constant and varying P_0 for each curve in the graph. There are no significant deviations in the T versus P curves for any of the initial temperature or initial pressure ranges. In fact, the difference in the curves is not distinguishable until Figure 6, where the curve corresponding to T_0= 500K and P_0 = 200 bar, slightly jets out from the rest of the curves. This continues to be noticeable for all curves corresponding to P_0 = 200 bar, for a T_0 = 500 K. The highest temperature investigated, T_0 = 4000 K, all had close agreement with the ideal-gas law.

The calculation of the real-gas equations relies upon the gradient equation for temperature, Equation 46; thus, a summation error might arise for values if a small enough pressure change is not chosen.

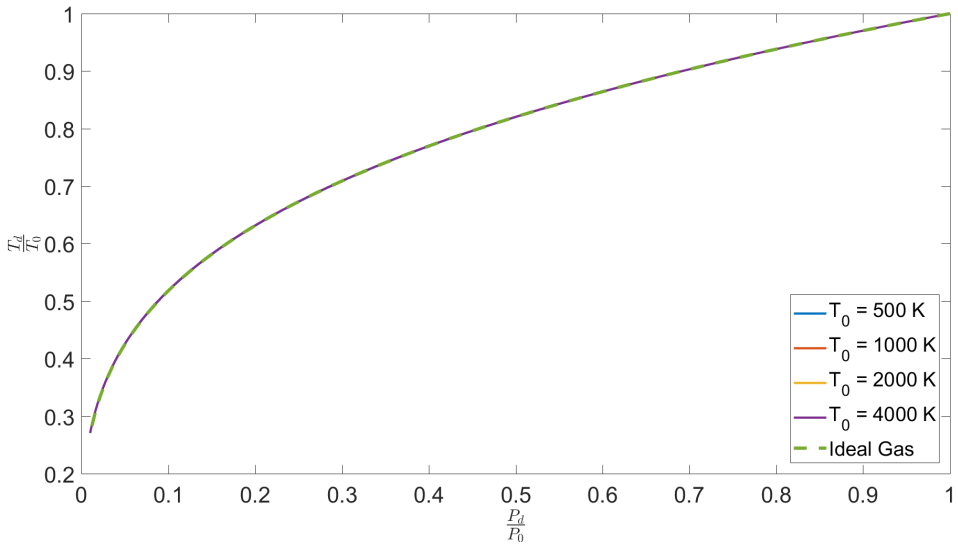

Figure 2: Comparison $\frac{T_d}{T_0}$ versus $\frac{P_d}{P_0}$ for Air with fixed P_0 = 10 bar, for T_0 = 500 K, 1000 K, 2000 K, 4000 K

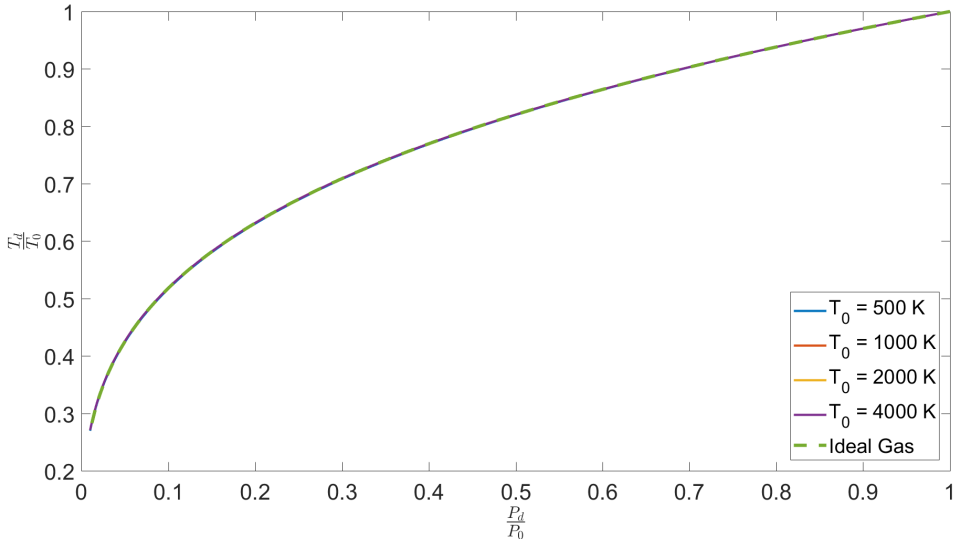

Figure 3: Comparison $\frac{T_d}{T_0}$ versus $\frac{P_d}{P_0}$ for Air with fixed $P_0 = 30$ bar, for $T_0 = 500$ K, 1000 K, 2000 K, 4000 K

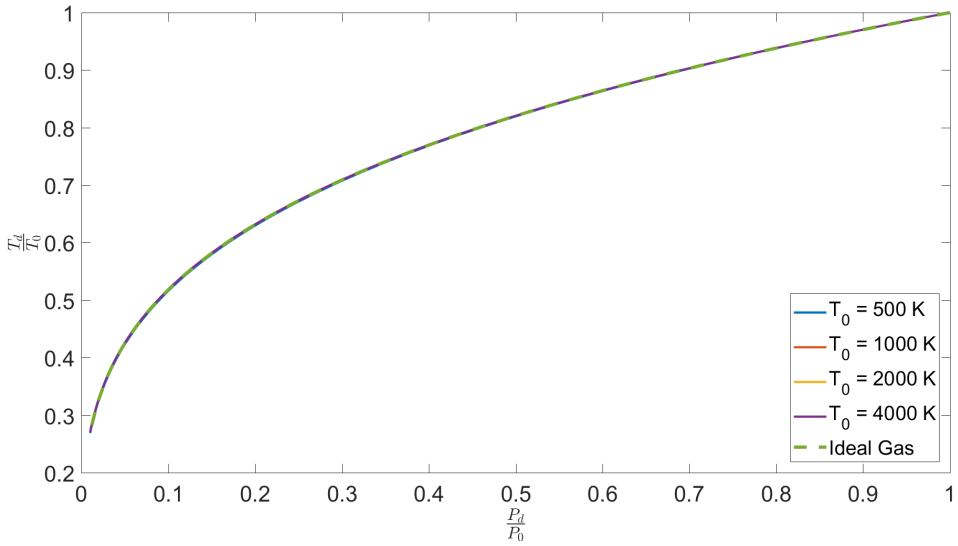

Figure 4: Comparison $\frac{T_d}{T_0}$ versus $\frac{P_d}{P_0}$ for Air with fixed $P_0 = 50$ bar, for $T_0 = 500$ K, 1000 K, 2000 K, 4000 K

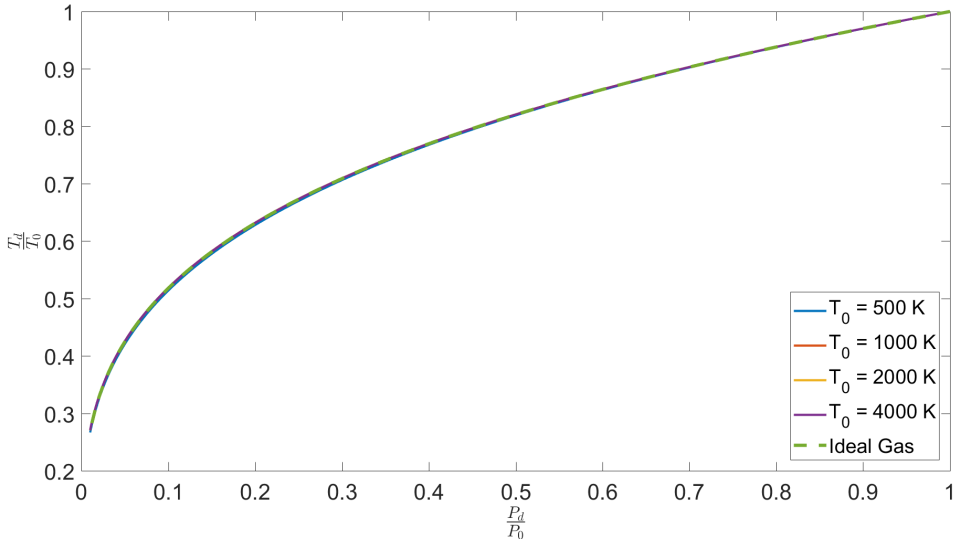

Figure 5: Comparison $\frac{T_d}{T_0}$ versus $\frac{P_d}{P_0}$ for Air with fixed $P_0 = 100$ bar, for $T_0 = 500$ K, 1000 K, 2000 K, 4000 K

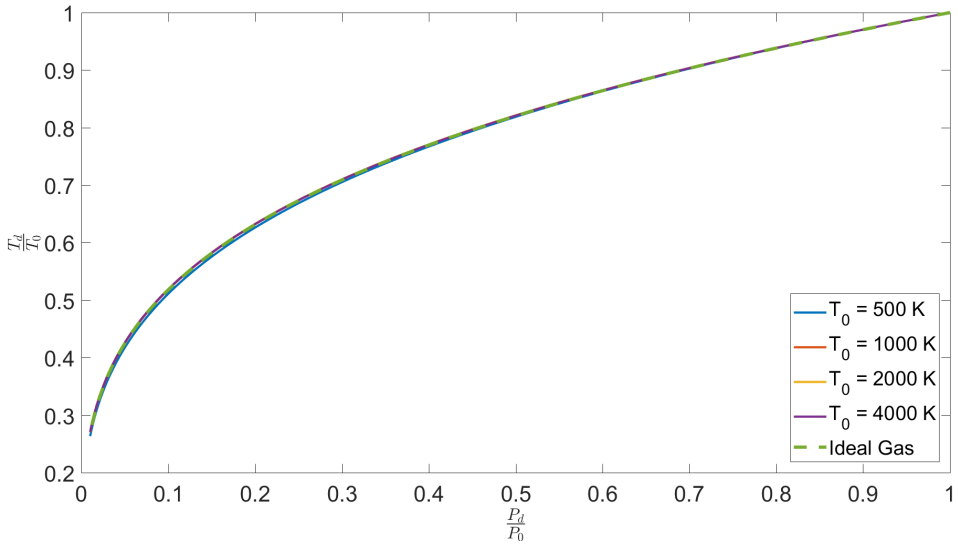

Figure 6: Comparison $\frac{T_d}{T_0}$ versus $\frac{P_d}{P_0}$ for Air with fixed $P_0 = 200$ bar, for $T_0 = 500$ K, 1000 K, 2000 K, 4000 K

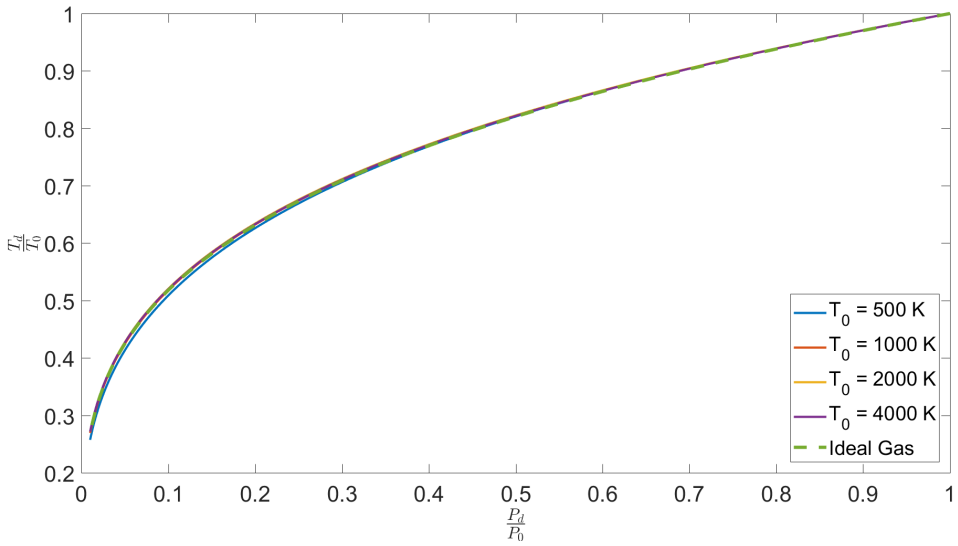

Figure 7: Comparison $\frac{T_d}{T_0}$ versus $\frac{P_d}{P_0}$ for Air with fixed $P_0 = 500$ bar, for $T_0 = 500$ K, 1000 K, 2000 K, 4000 K

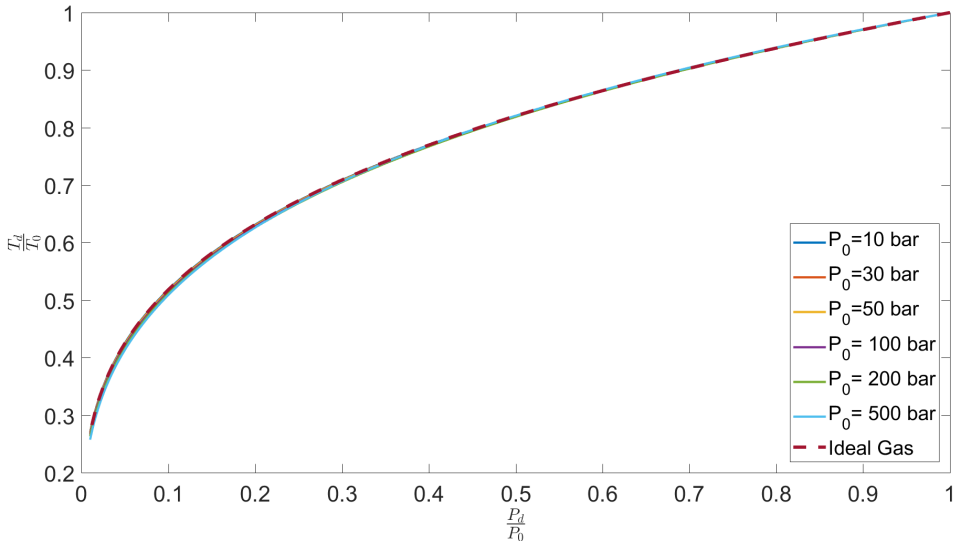

Figure 8: Comparison $\frac{T_d}{T_0}$ versus $\frac{P_d}{P_0}$ for Air with fixed $T_0 = 500$ K, for $P_0 = 10$ bar, 30 bar, 50 bar, 100 bar, 200 bar, 500 bar

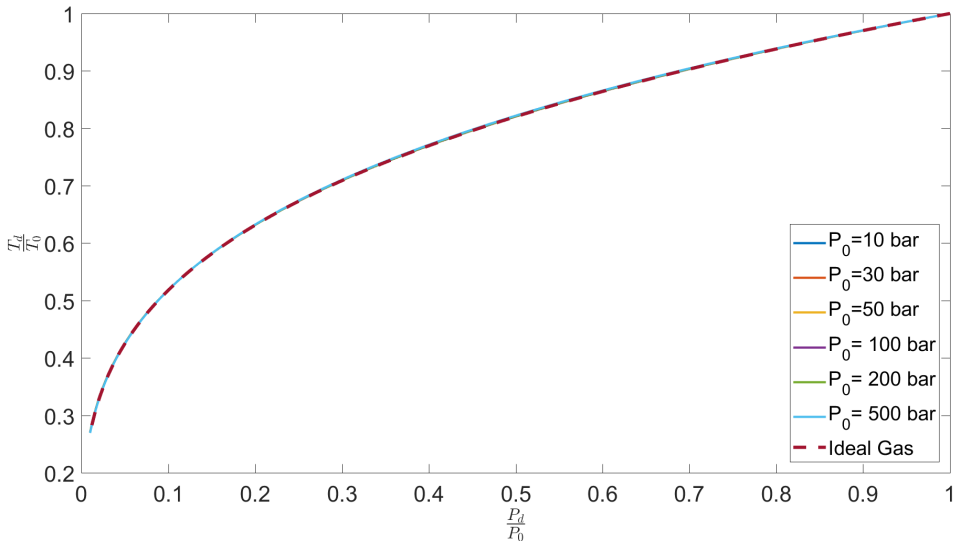

Figure 9: Comparison $\frac{T_d}{T_0}$ versus $\frac{P_d}{P_0}$ for Air with fixed $T_0 = 1000$ K, for $P_0 = 10$ bar, 30 bar, 50 bar, 100 bar, 200 bar, 500 bar

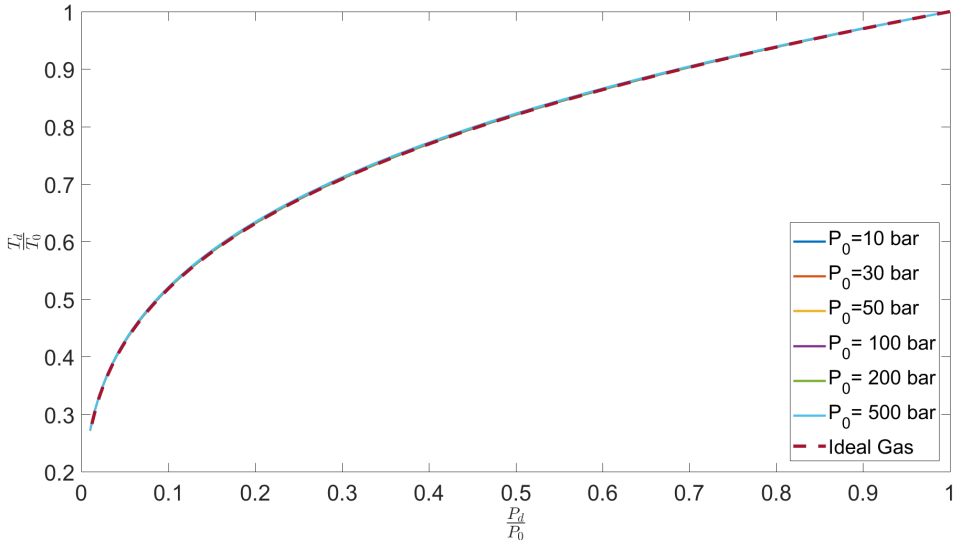

Figure 10: Comparison $\frac{T_d}{T_0}$ versus $\frac{P_d}{P_0}$ for Air with fixed $T_0 = 2000$ K, for $P_0 = 10$ bar, 30 bar, 50 bar, 100 bar, 200 bar, 500 bar

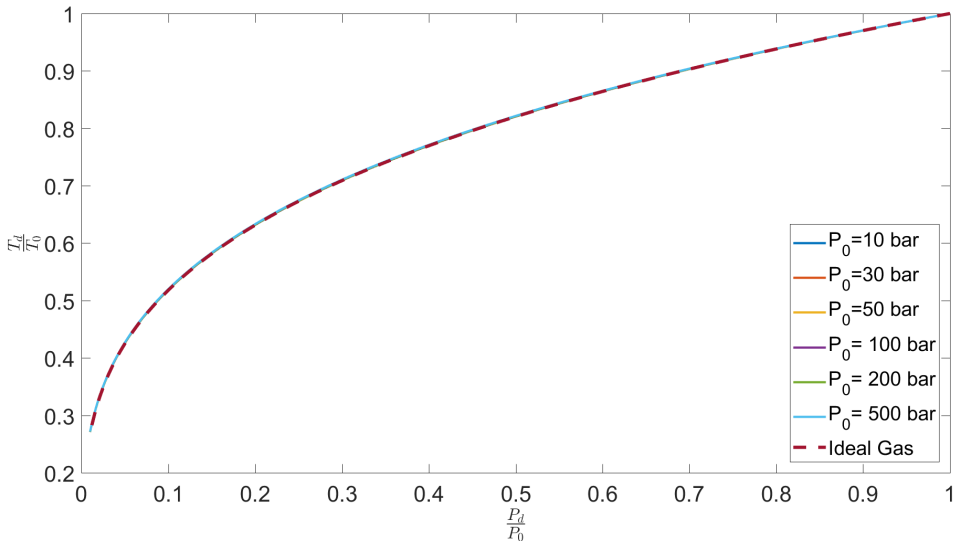

Figure 11: Comparison $\frac{T_d}{T_0}$ versus $\frac{P_d}{P_0}$ for Air with fixed $T_0 = 4000$ K, for $P_0 = 10$ bar, 30 bar, 50 bar, 100 bar, 200 bar, 500 bar

4.2.2 Density Results

The first set of figures, Figure 12 to Figure 17, each have a constant P_0, while T_0 varies. Figures 18 to Figure 21 are the opposite where T_0 is constant and P_0 is varied. Density definitely had the largest variation of the flow between pressure, density and temperature. The first thing to note is that unlike P and T, the normalized density $\mathscr{R}$ is not defined by $\frac{\rho}{\rho_0}$ but rather by Equation 42. In reviewing this equation it is evident that $\mathscr{R}$ is not just dependent on ρ_d, but T_0, and P_0 as well. This means that for ideal-gas. $\mathscr{R}$ will start out as 1 and decrease as density and pressure decrease. Figure 12 shows $\mathscr{R}$ starting out as close to 1, but there is not much distinguishing between each T_0.

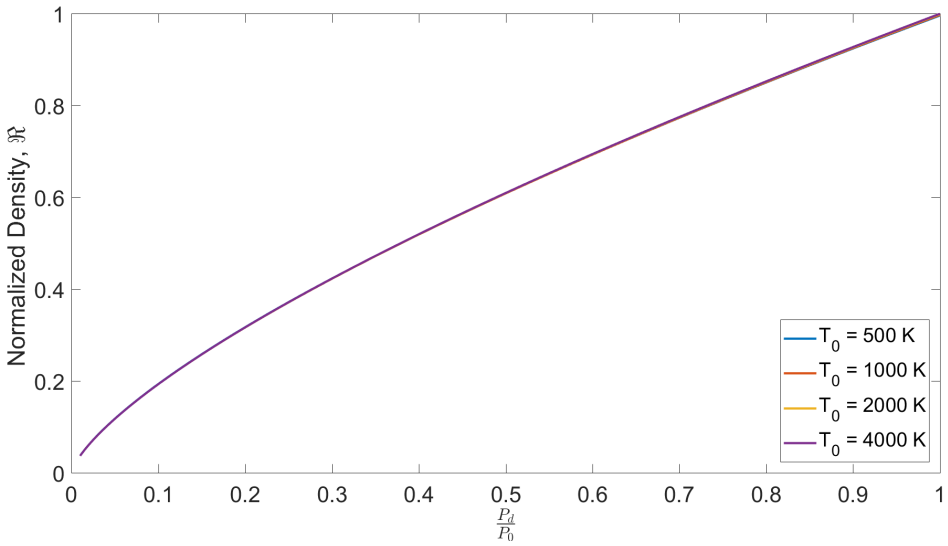

Figure 12: Comparison $\mathscr{R} = \frac{\rho RT}{P}$ versus $\frac{P_d}{P_0}$ for Air with fixed $P_0 = 10$ bar, for $T_0 = 500$ K, 1000 K, 2000 K, 4000 K

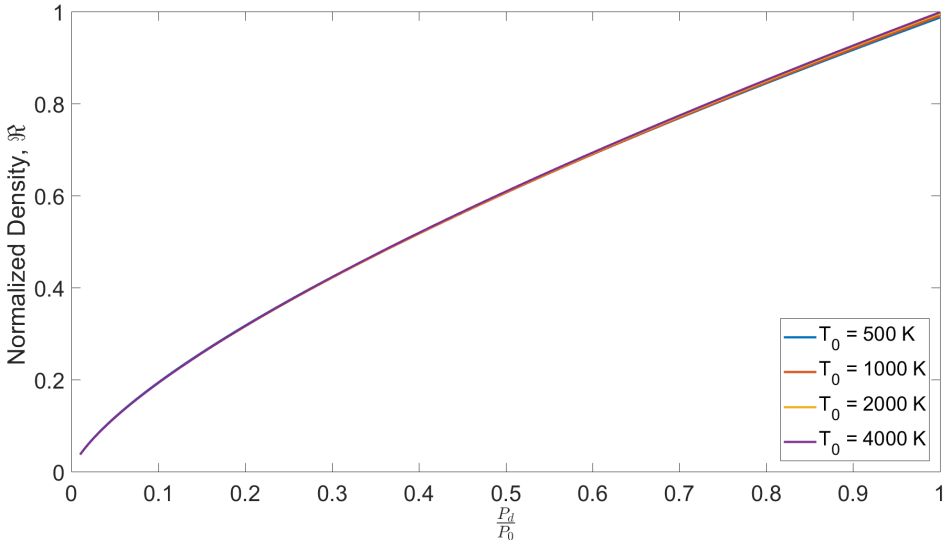

Figure 13: Comparison $\mathscr{R} = \frac{\rho RT}{P}$ versus $\frac{P_d}{P_0}$ for Air with fixed $P_0 = 30$ bar, for $T_0 = 500$ K, 1000 K, 2000 K, 4000 K

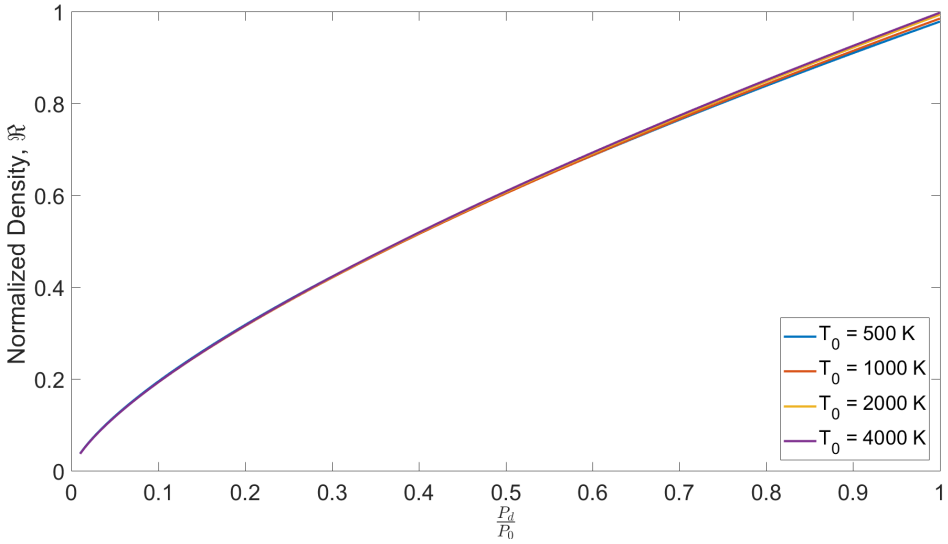

Figure 14: Comparison $\mathscr{R} = \frac{\rho RT}{P}$ versus $\frac{P_d}{P_0}$ for Air with fixed $P_0 = 50$ bar, for $T_0 = 500$ K, 1000 K, 2000 K, 4000 K

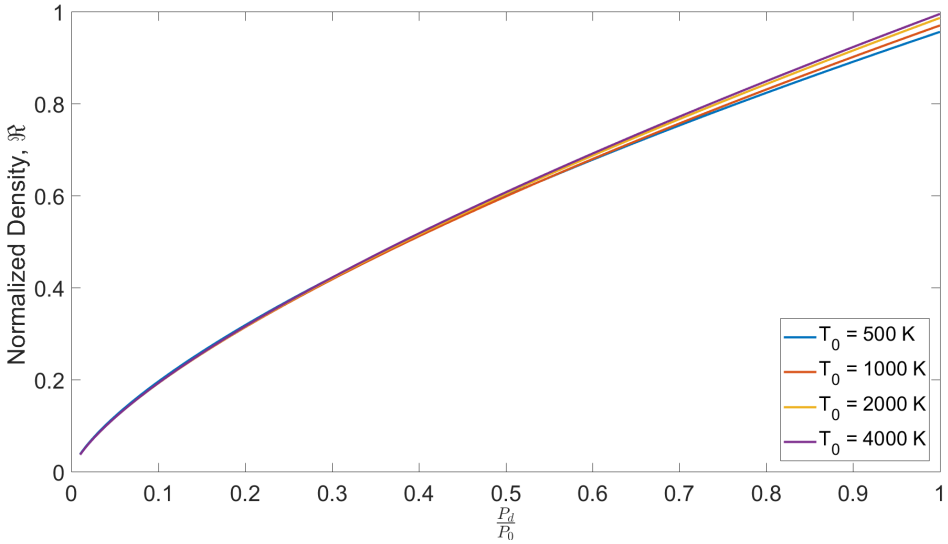

Figure 15: Comparison $\mathscr{R} = \frac{\rho RT}{P}$ versus $\frac{P_d}{P_0}$ for Air with fixed $P_0 = 100$ bar, for $T_0 = 500$ K, 1000 K, 2000 K, 4000 K

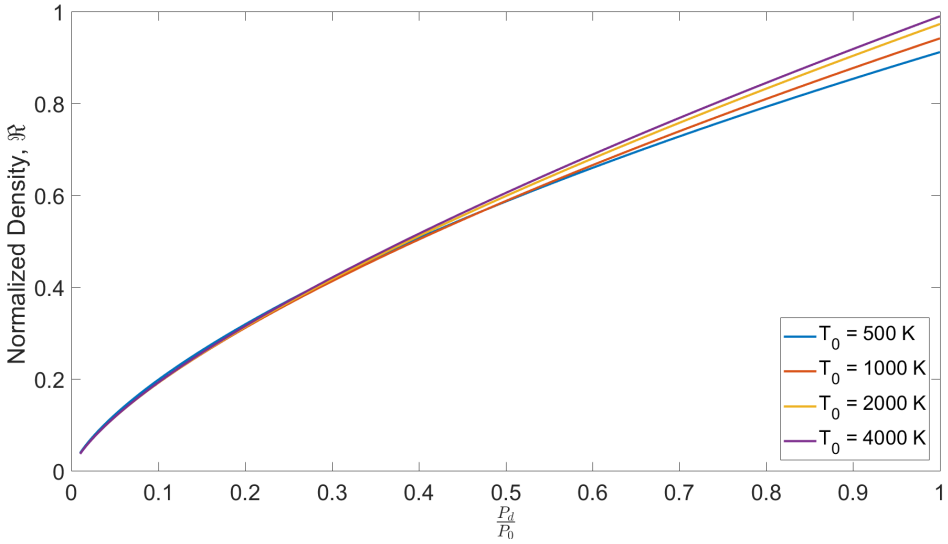

Figure 16: Comparison $\mathscr{R} = \frac{\rho RT}{P}$ versus $\frac{P_d}{P_0}$ for Air with fixed $P_0 = 200$ bar, for $T_0 = 500$ K, 1000 K, 2000 K, 4000 K

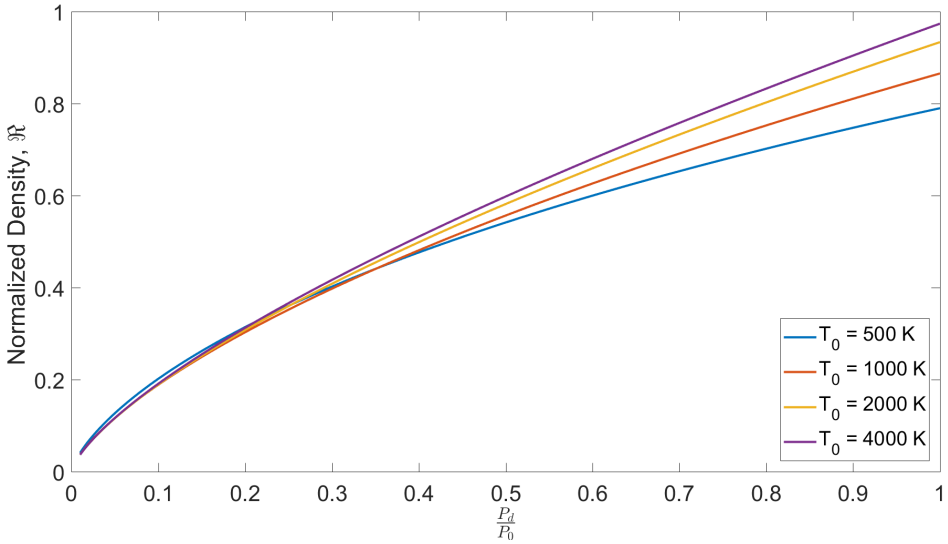

Figure 17: Comparison $\mathscr{R} = \frac{\rho RT}{P}$ versus $\frac{P_d}{P_0}$ for Air with fixed $P_0 = 500$ bar, for $T_0 = 500$ K, 1000 K, 2000 K, 4000 K

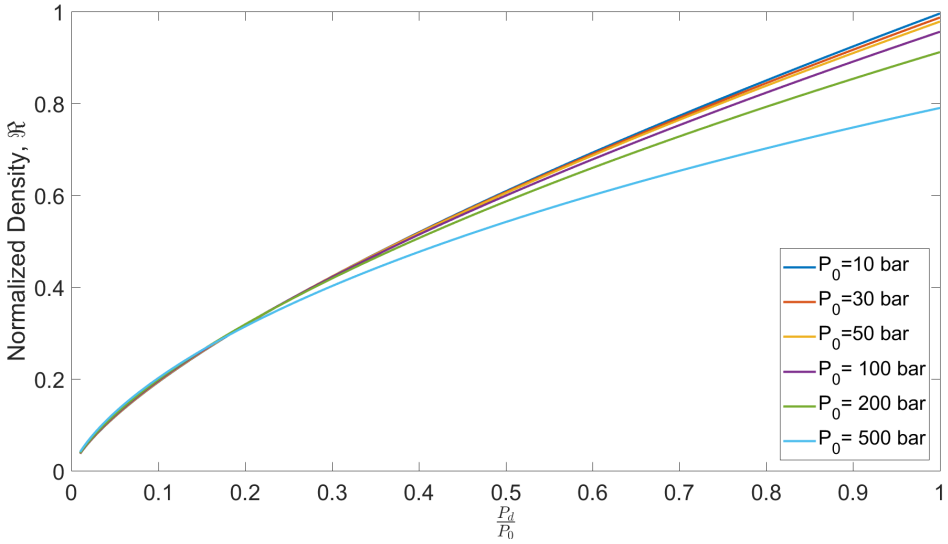

Figure 18: Comparison $\mathscr{R} = \frac{\rho RT}{P}$ versus $\frac{P_d}{P_0}$ for Air with fixed $T_0 = 500$ K, for $P_0 = 10$ bar, 30 bar, 50 bar, 100 bar, 200 bar, 500 bar

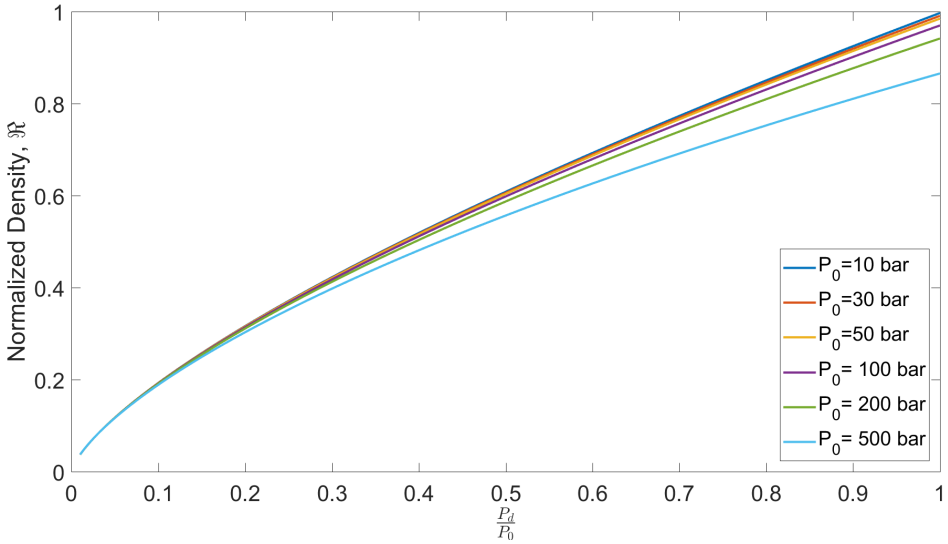

Figure 19: Comparison $\mathscr{R} = \frac{\rho RT}{P}$ versus $\frac{P_d}{P_0}$ for Air with fixed $T_0 = 1000$ K, for $P_0 = 10$ bar, 30 bar, 50 bar, 100 bar, 200 bar, 500 bar

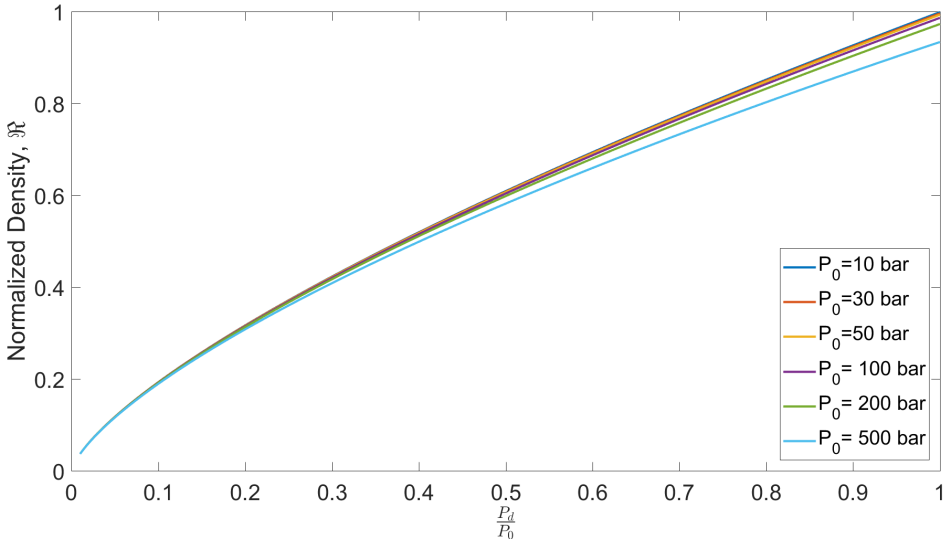

Figure 20: Comparison $\mathscr{R} = \frac{\rho RT}{P}$ versus $\frac{P_d}{P_0}$ for Air with fixed $T_0 = 2000$ K, for $P_0 = 10$ bar, 30 bar, 50 bar, 100 bar, 200 bar, 500 bar

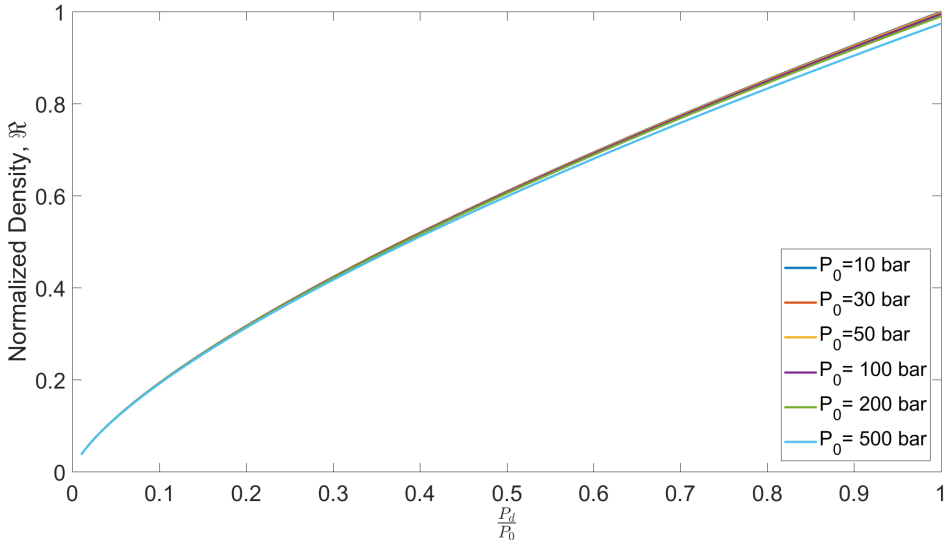

Figure 21: Comparison $\mathscr{R} = \frac{\rho RT}{P}$ versus $\frac{P_d}{P_0}$ for Air with fixed $T_0 = 4000$ K, for $P_0 = 10$ bar, 30 bar, 50 bar, 100 bar, 200 bar, 500 bar

The remaining figures, Figure 22 to Figure 25, are modeling the $\frac{\rho}{\rho_0}$ with a constant T_0 and varying P_0. Figure 22 showed the largest deviation from ideal-gas calculations across all

the P_0 values. On the other hand, Figure 25, corresponding to a T_0 of 4000 K demonstrated the closest relation to ideal. The graph itself is indistinguishable between ideal-gas calculations and real-gas. Across all the remaining Figures in this section, any curve on a graph correlated to a P_0 of 500 bar is indistinguishable between that curve and ideal-gas calculations. These graphs follow the general trend of ideal-gas calculations being more accurate at higher P_0 and T_0 values.

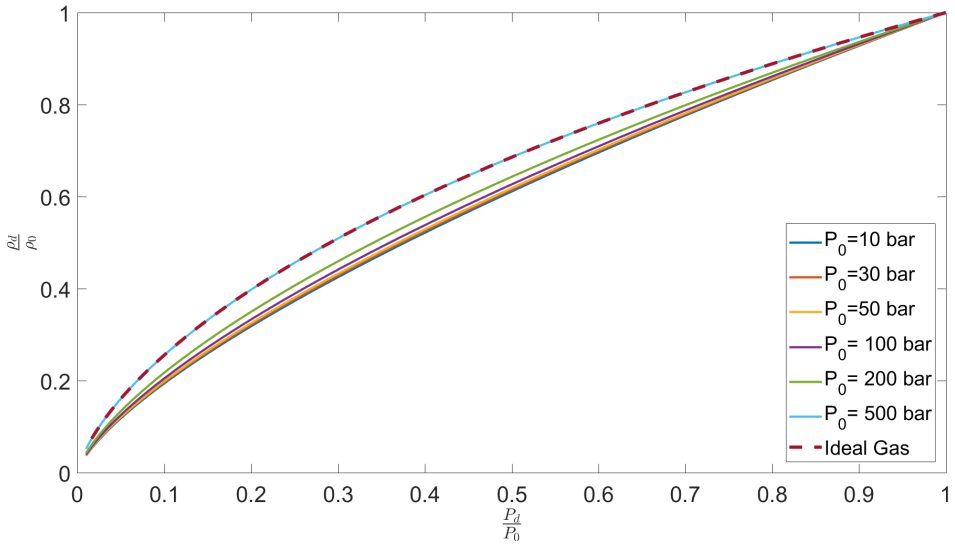

Figure 22: Comparison $\frac{\rho_d}{\rho_0}$ versus $\frac{P_d}{P_0}$ for Air with fixed $T_0 = 500$ K, for $P_0 = 10$ bar, 30 bar, 50 bar, 100 bar, 200 bar, 500 bar

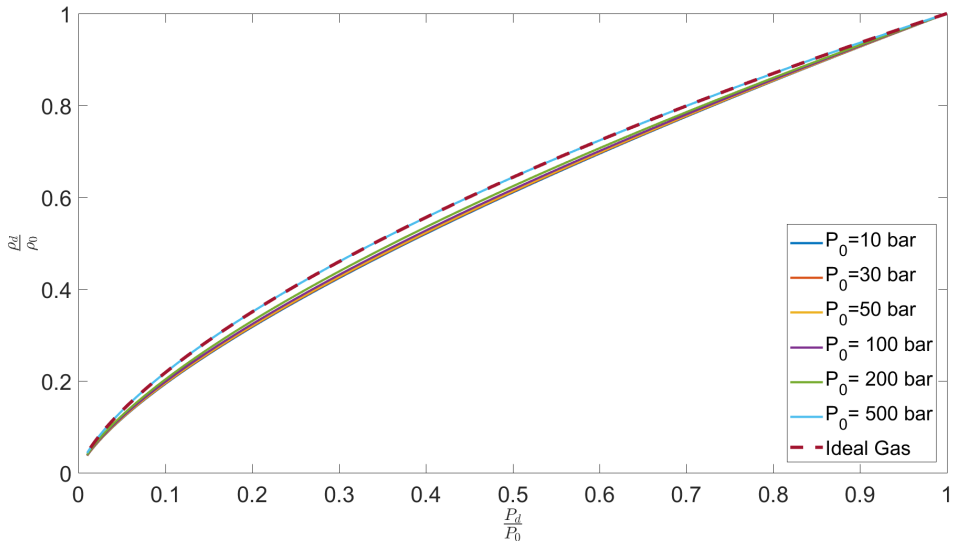

Figure 23: Comparison $\frac{\rho_d}{\rho_0}$ versus $\frac{P_d}{P_0}$ for Air with fixed $T_0 = 1000$ K, for $P_0 = 10$ bar, 30 bar, 50 bar, 100 bar, 200 bar, 500 bar

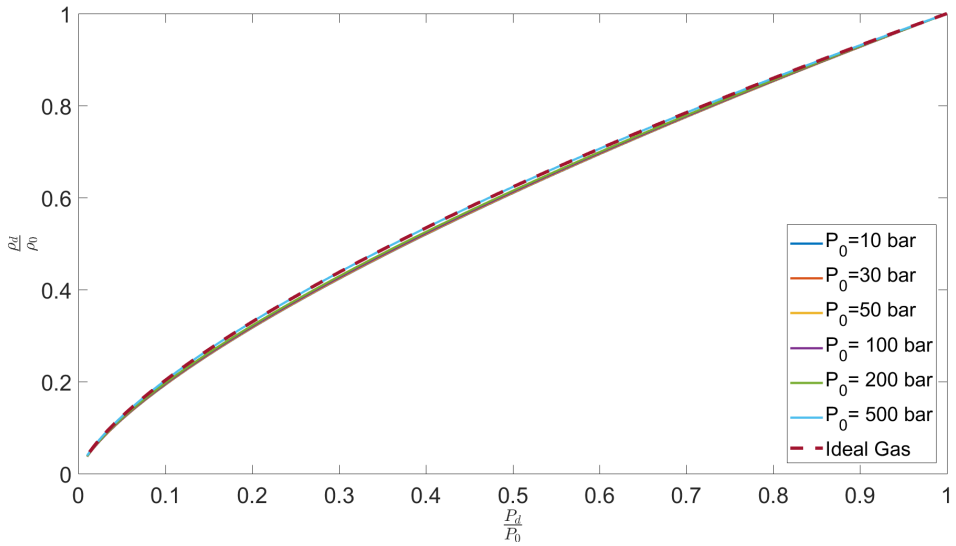

Figure 24: Comparison $\frac{\rho_d}{\rho_0}$ versus $\frac{P_d}{P_0}$ for Air with fixed $T_0 = 2000$ K, for $P_0 = 10$ bar, 30 bar, 50 bar, 100 bar, 200 bar, 500 bar

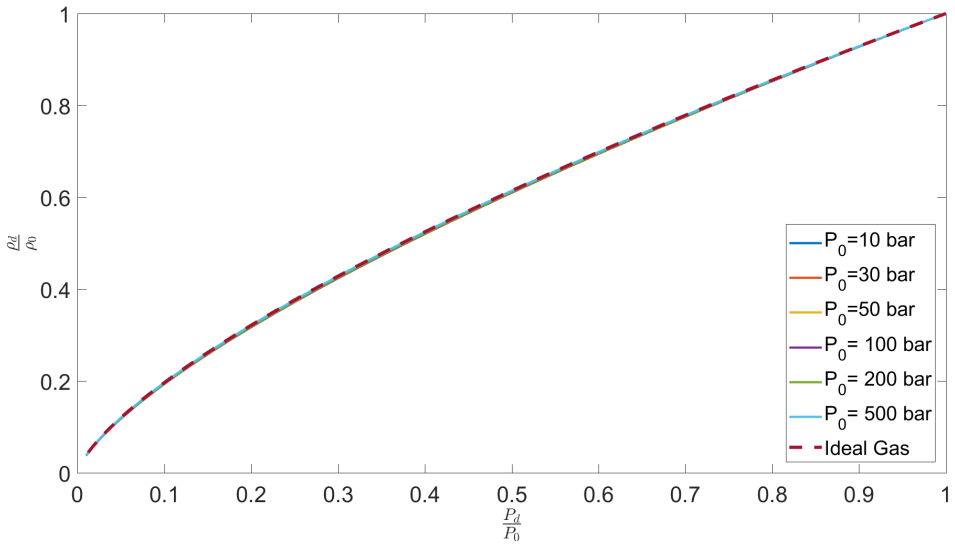

Figure 25: Comparison $\frac{\rho_d}{\rho_0}$ versus $\frac{P_d}{P_0}$ for Air with fixed $T_0 = 4000$ K, for $P_0 = 10$ bar, 30 bar, 50 bar, 100 bar, 200 bar, 500 bar

4.2.3 Area Ratio Results

As demonstrated by the graphs of this section, the change in α has a very small change until the P is either approaching 0 or 1. Next, the area ratio dramatically increases or decreases. For each case of initial stagnation pressure and stagnation temperature, the throat conditions were determined by finding where Mach is equal to 1. Then, the flow was expanded subsonically and supersonically. Like previous properties, lower P_0 and higher T_0 of real-gas solutions are more in agreement with ideal-gas values. The real-gas solutions were so close to ideal-gas values for low P_0 that for the sake of clarity the graphs corresponding to $P_0 = 30$ bar and 50 bar were omitted. As Figure 26 demonstrates, the difference in values is indistinguishable. It is not until $P_0 = 100$ bar that there is a divergent in values on the graphs that is discernible by simply viewing the graph.

The method for α calculations is described in Section 2.4. For the sake of clarity of reading the graphs, each Figure represents either the subsonic, convergent portion of a nozzle or the supersonic, divergent portion of a nozzle.

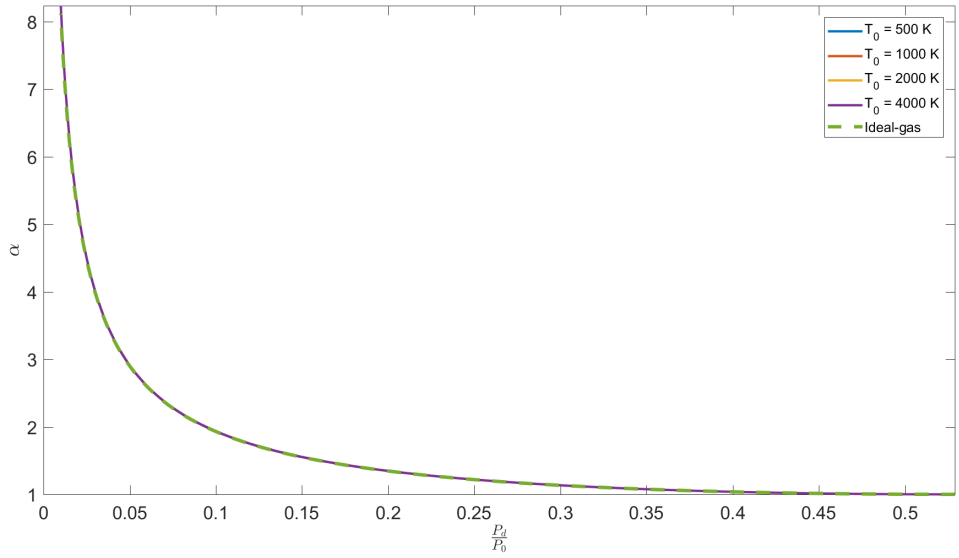

Figure 26: Comparison α versus $\frac{P_d}{P_0}$ for Air at $P_0 = 10$ bar. This figure graphs the supersonic expansion of a nozzle, where $T_0 = 500$ K, 1000 K, 2000 K, 4000 K.

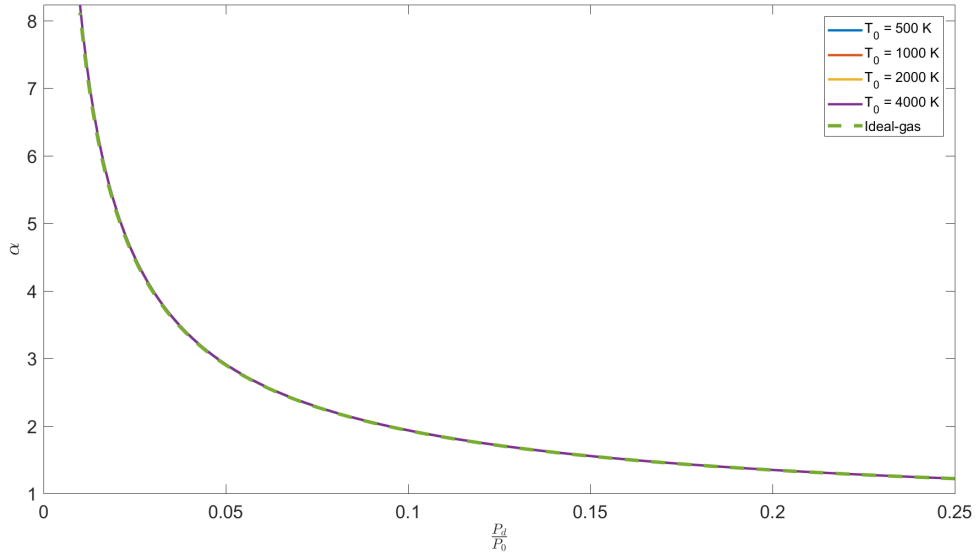

Figure 27: Comparison α versus $\frac{P_d}{P_0}$ for Air at $P_0 = 10$ bar. This figure graphs the supersonic expansion of a nozzle, where $T_0 = 500$ K, 1000 K, 2000 K, 4000 K. This figure is zoomed in for clarity.

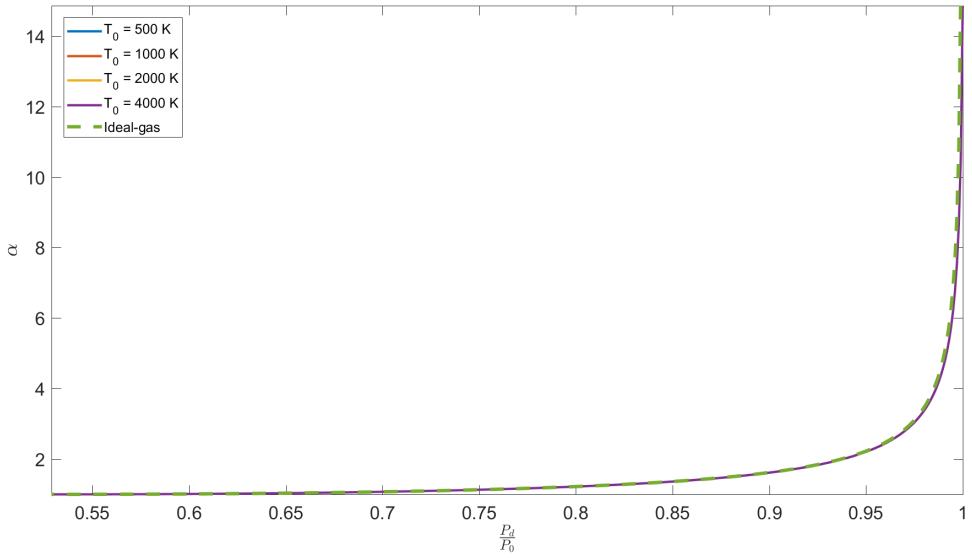

Figure 28: Comparison α versus $\frac{P_d}{P_0}$ for Air at $P_0 = 10$ bar. This figure graphs the subsonic expansion of a nozzle, where $T_0 = 500$ K, 1000 K, 2000 K, 4000 K.

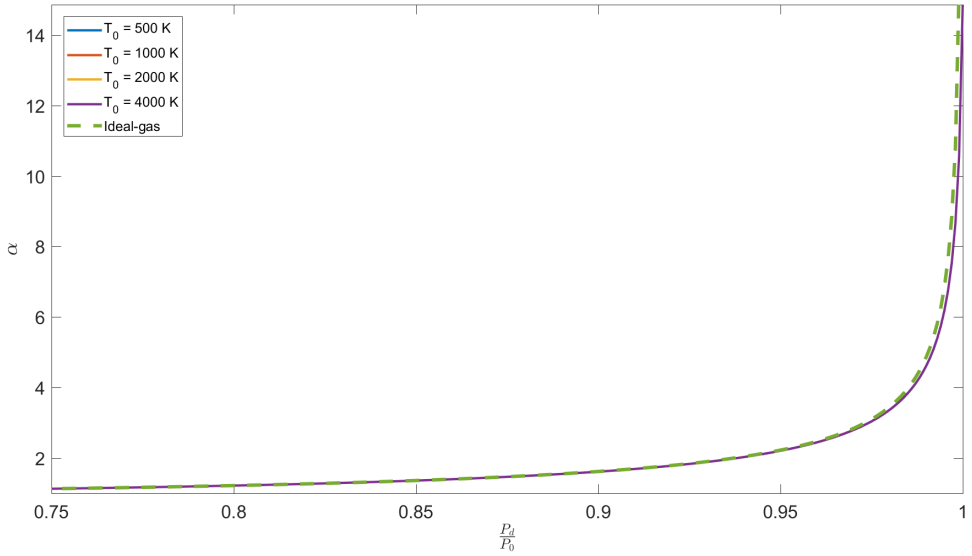

Figure 29: Comparison α versus $\frac{P_d}{P_0}$ for Air at $P_0 = 10$ bar. This figure graphs the subsonic expansion of a nozzle, where $T_0 = 500$ K, 1000 K, 2000 K, 4000 K. This figure is zoomed in for clarity.

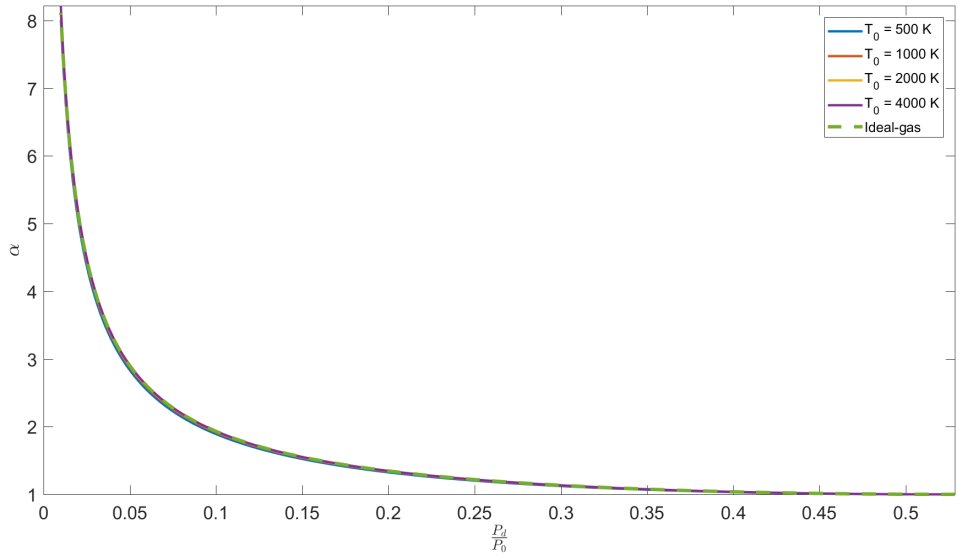

Figure 30: Comparison α versus $\frac{P_d}{P_0}$ for Air at $P_0 = 100$ bar. This figure graphs the supersonic expansion of a nozzle, where $T_0 = 500$ K, 1000 K, 2000 K, 4000 K.

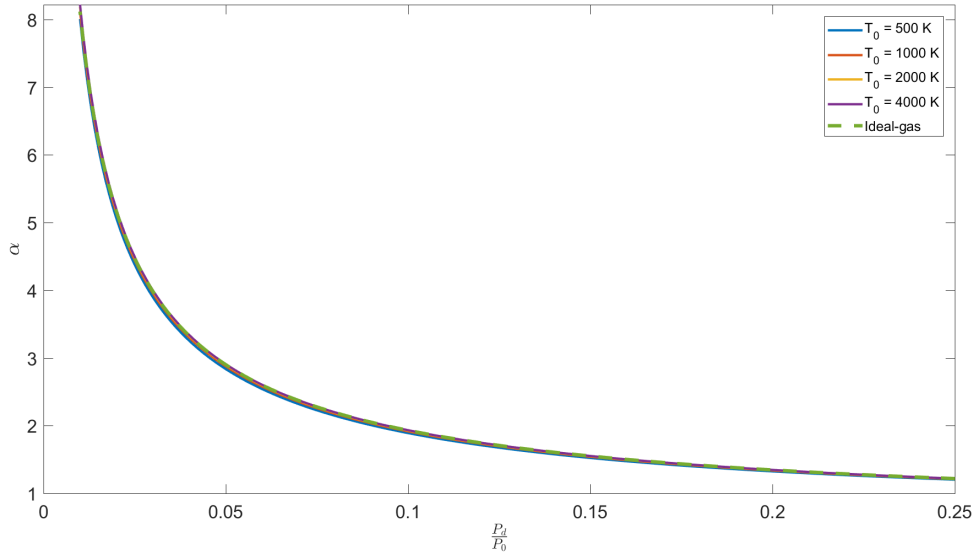

Figure 31: Comparison α versus $\frac{P_d}{P_0}$ for Air at $P_0 = 100$ bar. This figure graphs the supersonic expansion of a nozzle, where $T_0 = 500$ K, 1000 K, 2000 K, 4000 K. This figure is zoomed in for clarity.

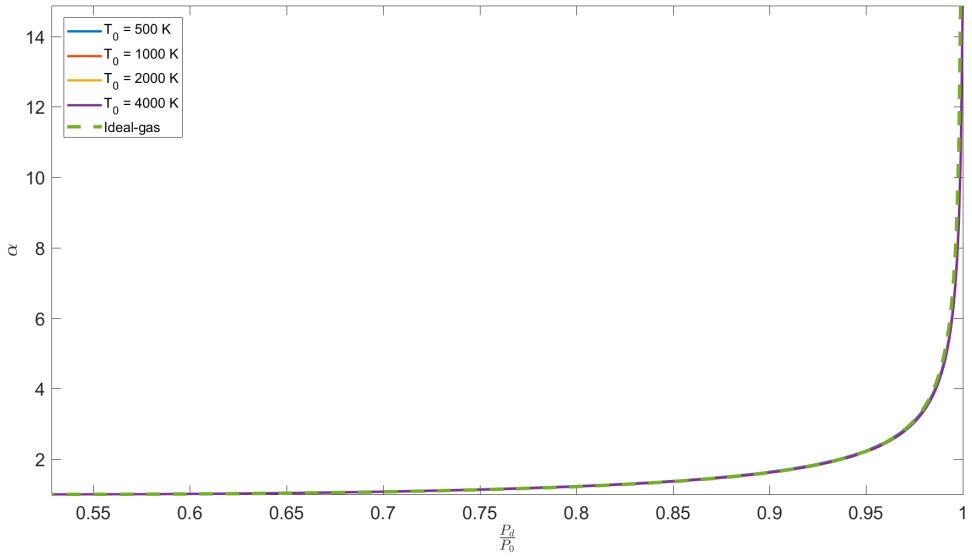

Figure 32: Comparison α versus $\frac{P_d}{P_0}$ for Air at $P_0 = 100$ bar. This figure graphs the subsonic expansion of a nozzle, where $T_0 = 500$ K, 1000 K, 2000 K, 4000 K.

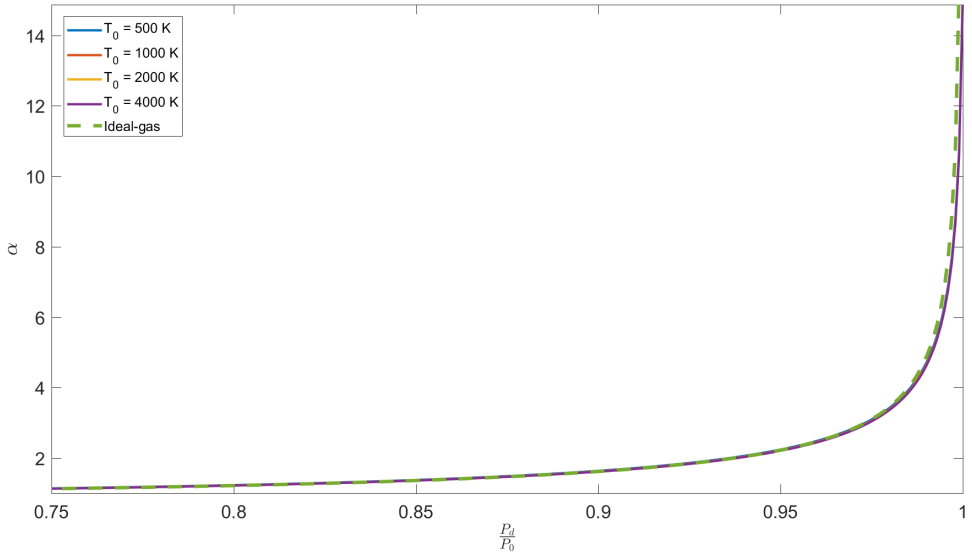

Figure 33: Comparison α versus $\frac{P_d}{P_0}$ for Air at $P_0 = 100$ bar. This figure graphs the subsonic expansion of a nozzle, where $T_0 = 500$ K, 1000 K, 2000 K, 4000 K. This figure is zoomed in for clarity.

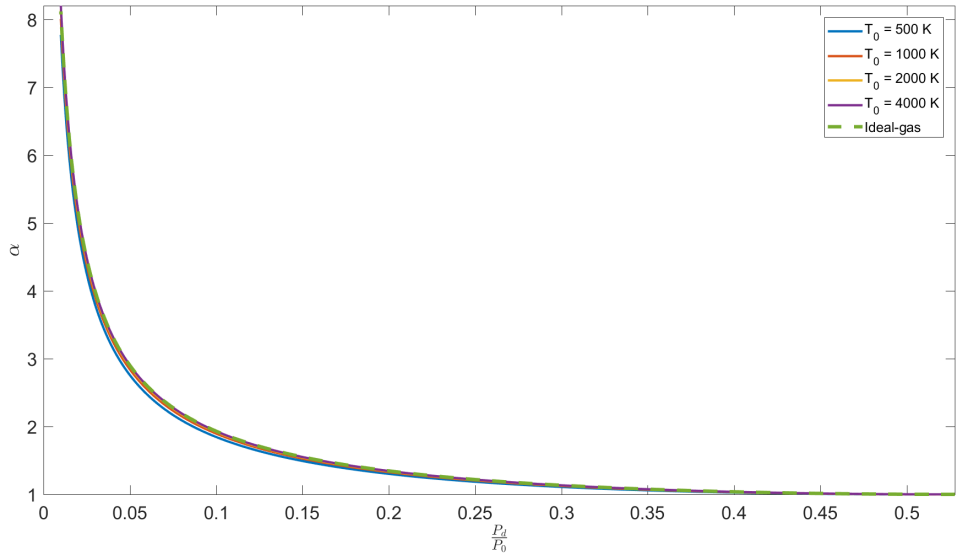

Figure 34: Comparison α versus $\frac{P_d}{P_0}$ for Air at $P_0 = 200$ bar. This figure graphs the supersonic expansion of a nozzle, where $T_0 = 500$ K, 1000 K, 2000 K, 4000 K.

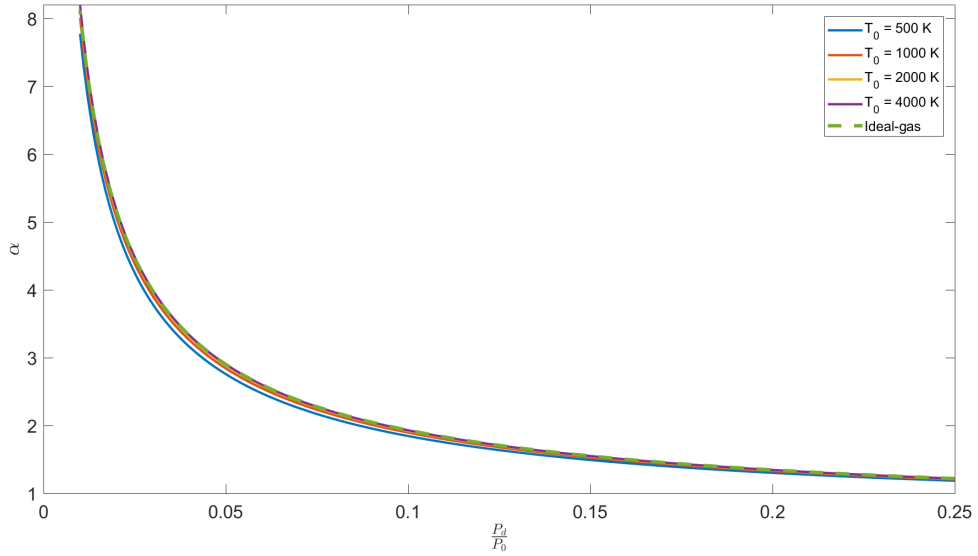

Figure 35: Comparison α versus $\frac{P_d}{P_0}$ for Air at $P_0 = 200$ bar. This figure graphs the supersonic expansion of a nozzle, where $T_0 = 500$ K, 1000 K, 2000 K, 4000 K. This figure is zoomed in for clarity.

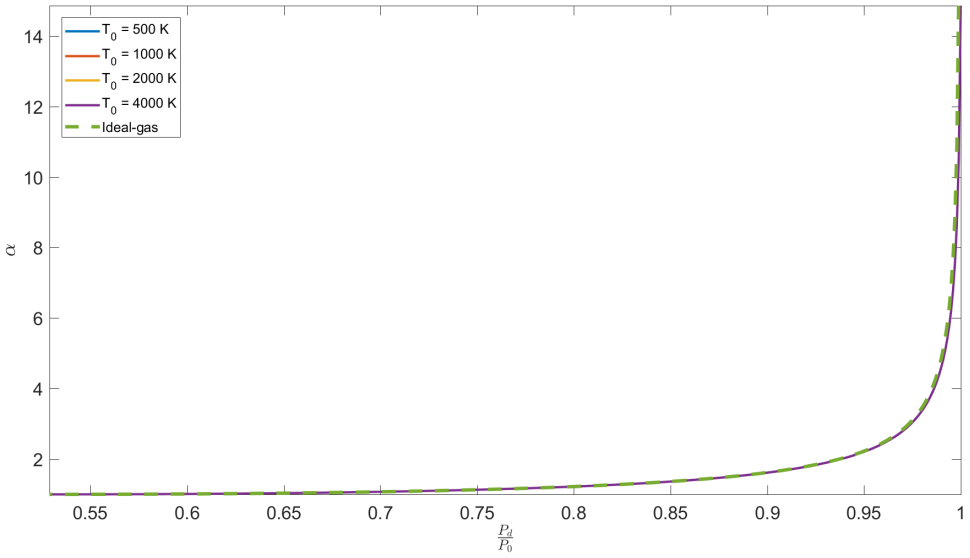

Figure 36: Comparison α versus $\frac{P_d}{P_0}$ for Air at $P_0 = 200$ bar. This figure graphs the subsonic expansion of a nozzle, where $T_0 = 500$ K, 1000 K, 2000 K, 4000 K.

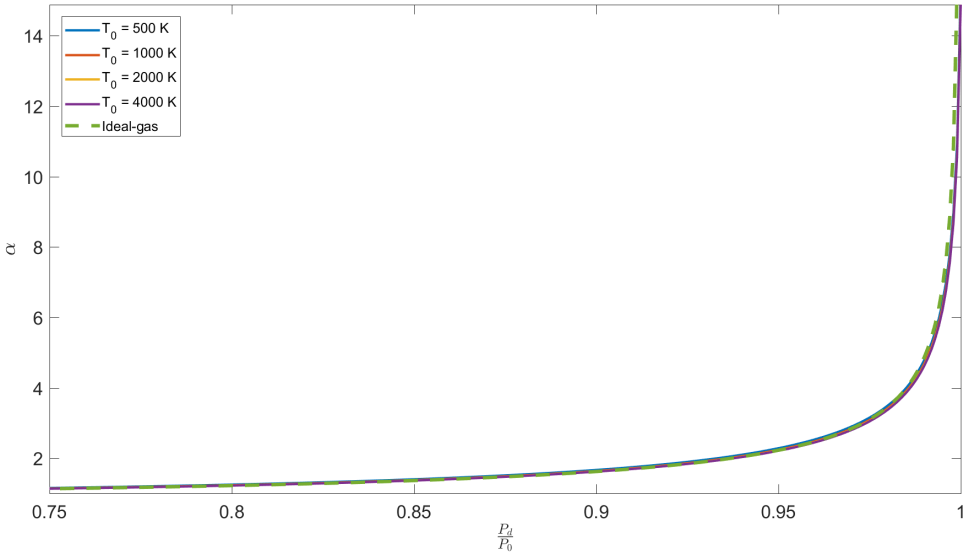

Figure 37: Comparison α versus $\frac{P_d}{P_0}$ for Air at $P_0 = 200$ bar. This figure graphs the subsonic expansion of a nozzle, where $T_0 = 500$ K, 1000 K, 2000 K, 4000 K. This figure is zoomed in for clarity.

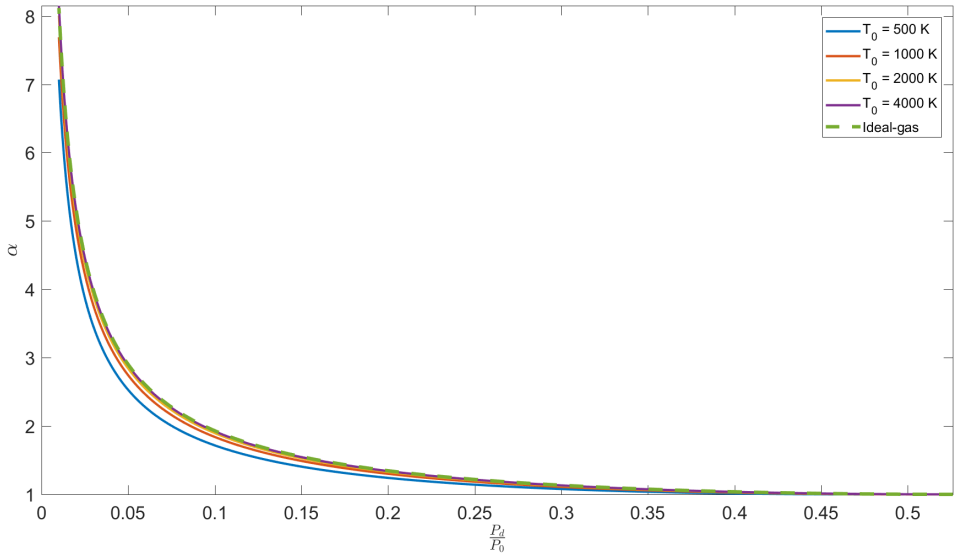

Figure 38: Comparison α versus $\frac{P_d}{P_0}$ for Air at $P_0 = 500$ bar. This figure graphs the supersonic expansion of a nozzle, where $T_0 = 500$ K, 1000 K, 2000 K, 4000 K.

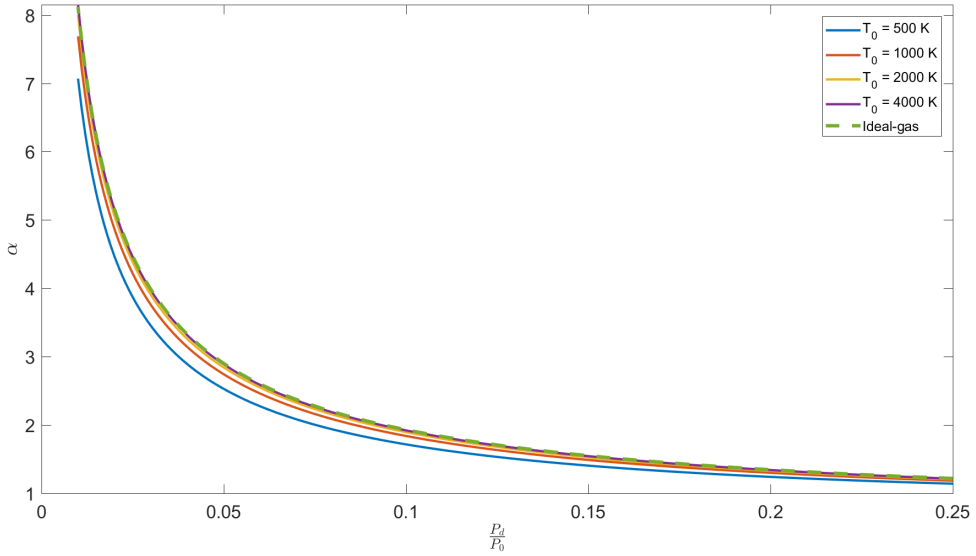

Figure 39: Comparison α versus $\frac{P_d}{P_0}$ for Air at $P_0 = 500$ bar. This figure graphs the supersonic expansion of a nozzle, where $T_0 = 500$ K, 1000 K, 2000 K, 4000 K. This figure is zoomed in for clarity.

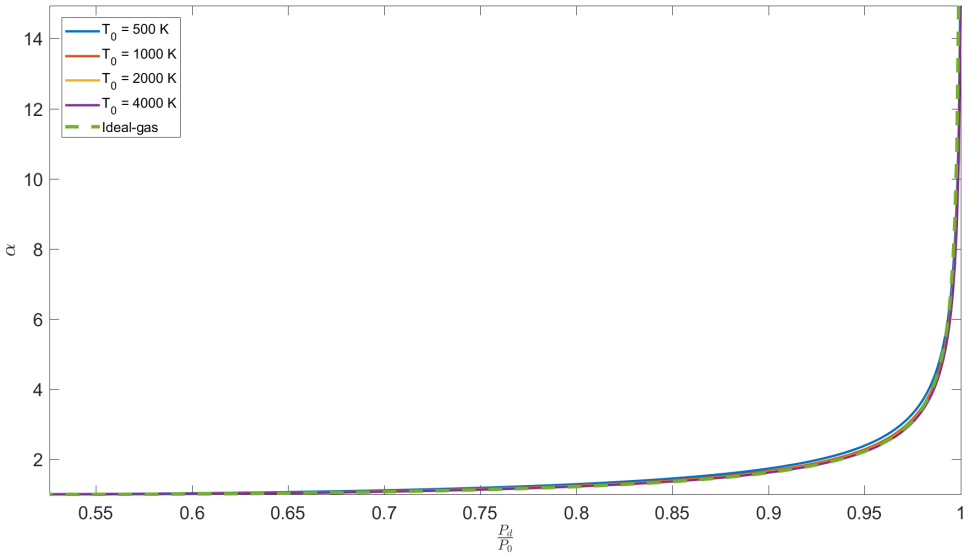

Figure 40: Comparison α versus $\frac{P_d}{P_0}$ for Air at $P_0 = 500$ bar. This figure graphs the subsonic expansion of a nozzle, where $T_0 = 500$ K, 1000 K, 2000 K, 4000 K.

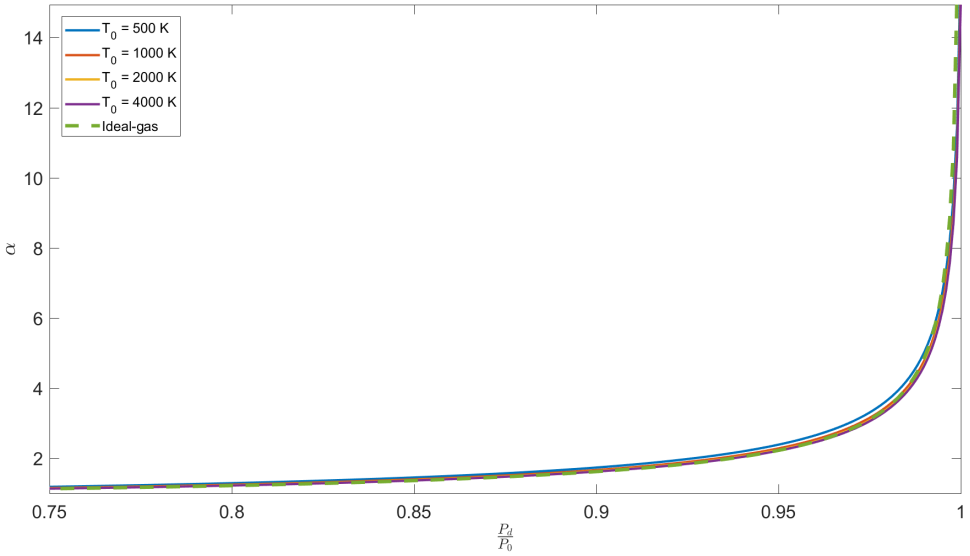

Figure 41: Comparison α versus $\frac{P_d}{P_0}$ for Air at $P_0 = 500$ bar. This figure graphs the subsonic expansion of a nozzle, where $T_0 = 500$ K, 1000 K, 2000 K, 4000 K. This figure is zoomed in for clarity.

4.2.4 Compressibility Factor Z, Results

The following graphs show similar curves corresponding to the same T_0 as P_0 is increased. However, upon a closer look at the vertical axis, it shows that the Z value does change. When $P_0 = 10$ bar, Z ranges from near 1 to 1.0045. When $P_0 = 30$ bar, Z ranges from around 1 to 1.014. Now, making a large jump to $P_0 = 500$ bar, Z ranges from ~ 1 to ~ 1.3. While a difference between 1.0045 and 1.3 may seem small on the Z plots, it does give rise to a very significant change to density for higher P and P_0 values for a wide T_0 range. The graphs in this section plot the relationship between P and Z.

The graphs that hold P_0 and vary T_0 also include the comparison to previously discussed approximate solution for compressibility factor. This includes Figure 42 to 47 and Equation 7, that were discussed in the literature review as an approximation that could be used in place of another method for solving the cubic EoS. However, this approximation sacrifices accuracy for lower computational cost. Across the range of pressures and temperatures calculated the maximum error associated with the approximate solution to the exact solution is 3.89%.

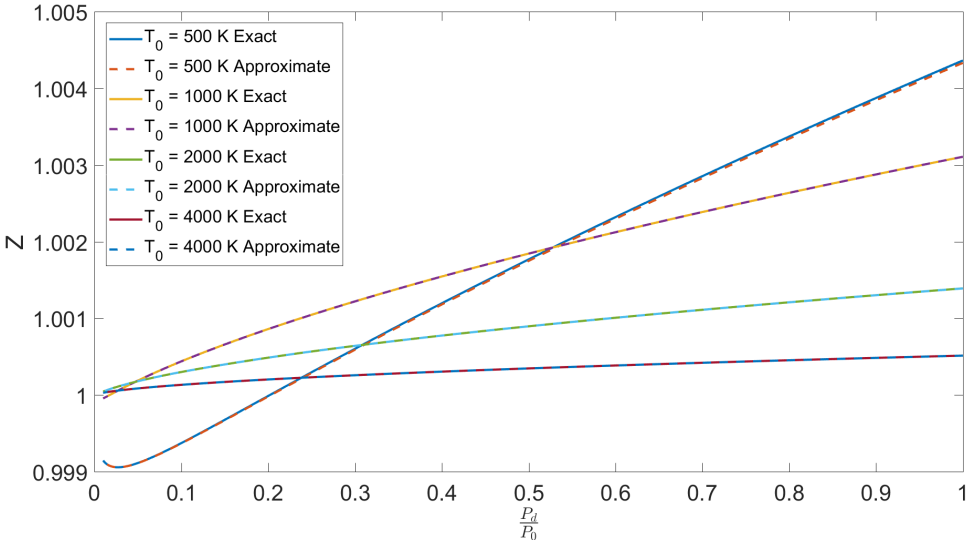

Figure 42: Comparison Z versus $\frac{P_d}{P_0}$ for Air with fixed $P_0 = 10$ bar, while varying T_0 where T_0= 500 K, 1000 K, 2000 K, 4000 K. The solid lines indicates Cardano's method was used to sovle for Z. The dashed lines indicated the approximate solution proposed by Sirignano [18]

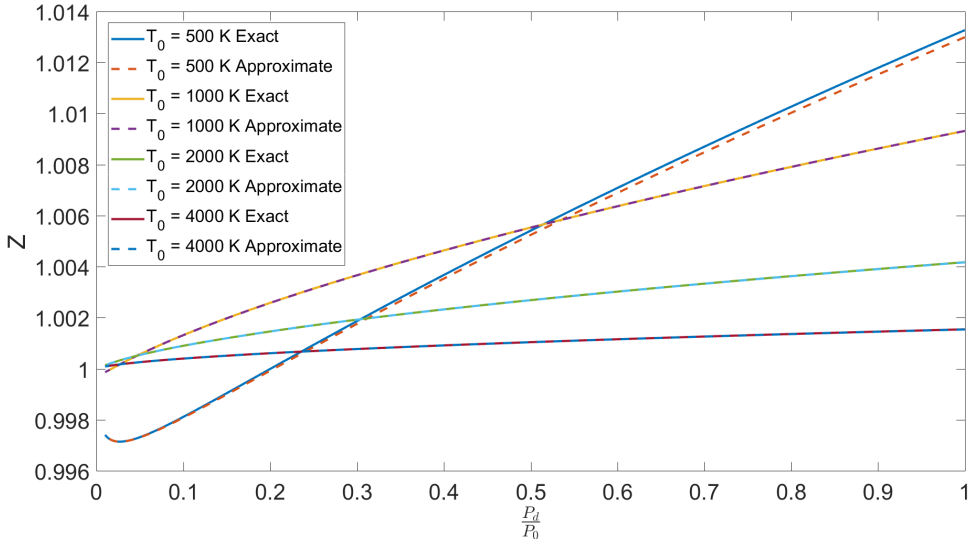

Figure 43: Comparison Z versus $\frac{P_d}{P_0}$ for Air with fixed $P_0 = 30$ bar, while varying T_0 where T_0= 500 K, 1000 K, 2000 K, 4000 K. The solid lines indicates Cardano's method was used to sovle for Z. The dashed lines indicated the approximate solution proposed by Sirignano [18]

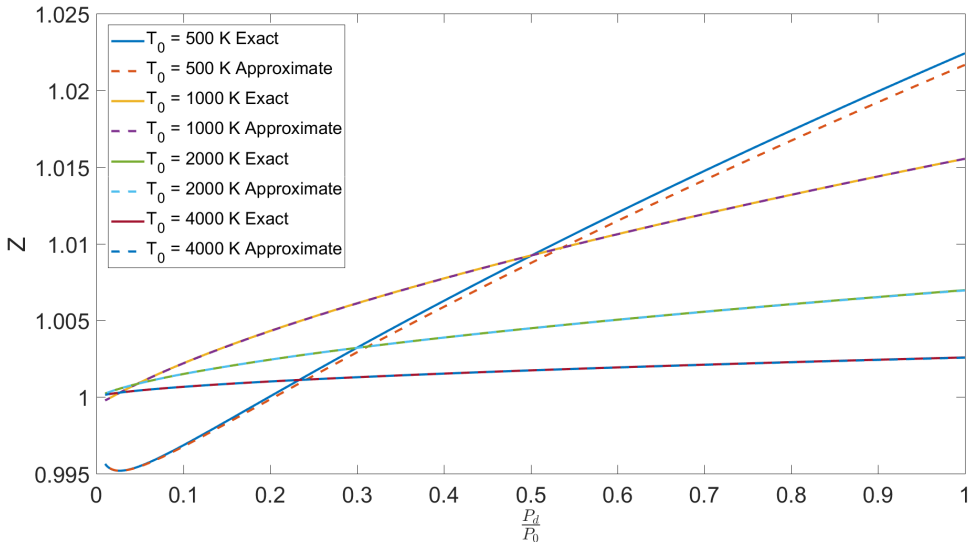

Figure 44: Comparison Z versus $\frac{P_d}{P_0}$ for Air with fixed $P_0 = 50$ bar, while varying T_0 where T_0= 500 K, 1000 K, 2000 K, 4000 K. The solid lines indicates Cardano's method was used to sovle for Z. The dashed lines indicated the approximate solution proposed by Sirignano [18]

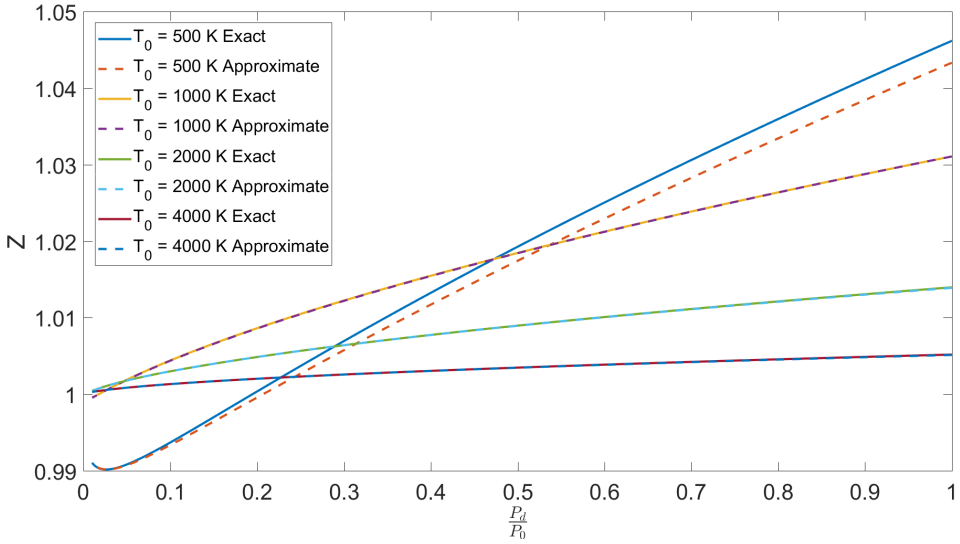

Figure 45: Comparison Z versus $\frac{P_d}{P_0}$ for Air with fixed $P_0 = 100$ bar, while varying T_0 where T_0= 500 K, 1000 K, 2000 K, 4000 K. The solid lines indicates Cardano's method was used to sovle for Z. The dashed lines indicated the approximate solution proposed by Sirignano [18]

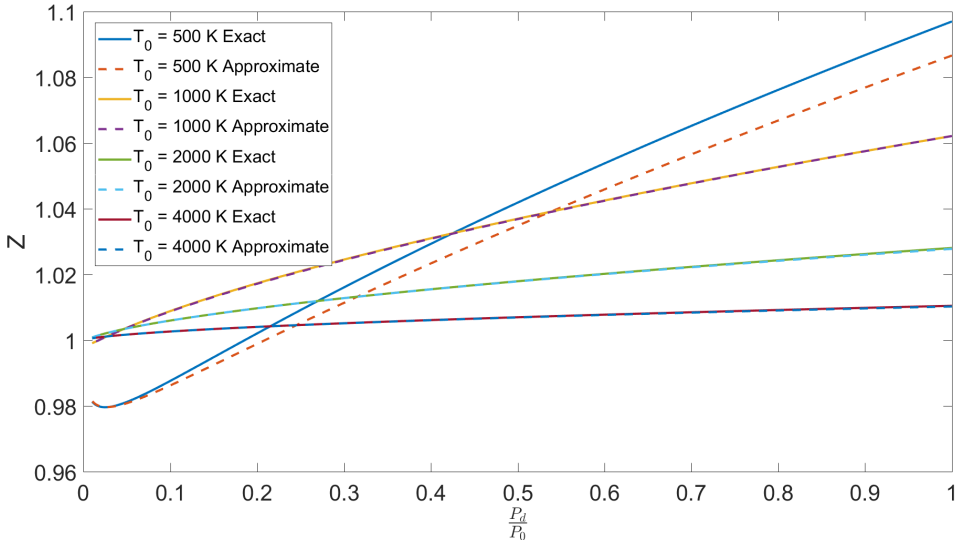

Figure 46: Comparison Z versus $\frac{P_d}{P_0}$ for Air with fixed $P_0 = 200$ bar, while varying T_0 where T_0= 500 K, 1000 K, 2000 K, 4000 K. The solid lines indicates Cardano's method was used to sovle for Z. The dashed lines indicated the approximate solution proposed by Sirignano [18]

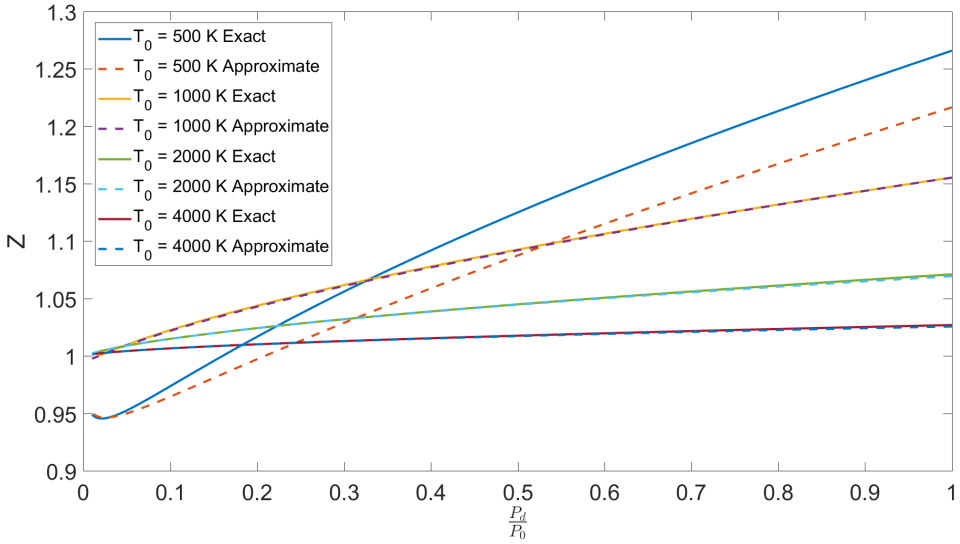

Figure 47: Comparison Z versus $\frac{P_d}{P_0}$ for Air with fixed $P_0 = 500$ bar, while varying T_0 where T_0= 500 K, 1000 K, 2000 K, 4000 K. The solid lines indicates Cardano's method was used to sovle for Z. The dashed lines indicated the approximate solution proposed by Sirignano [18]

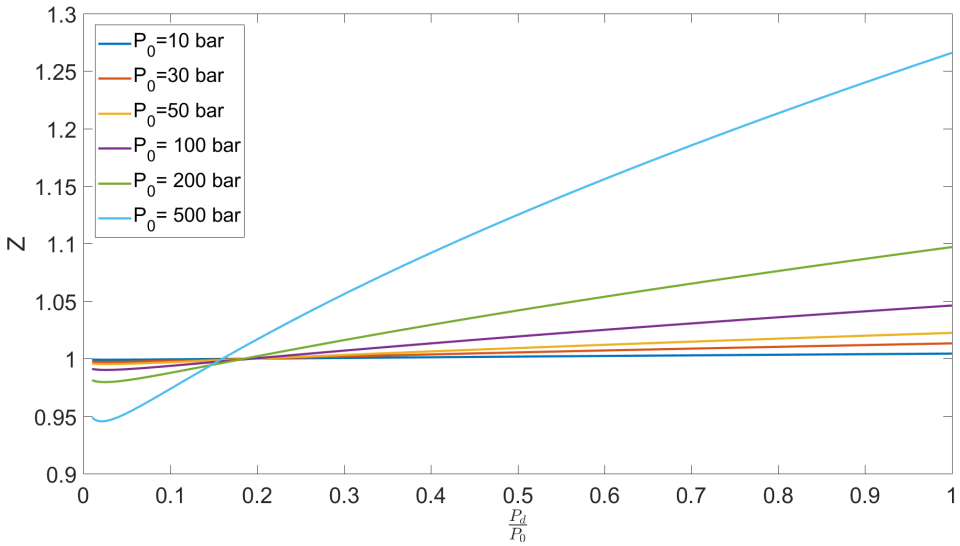

Figure 48: Air, 500 K

Figure 49: Comparison Z versus $\frac{P_d}{P_0}$ for Air with fixed $= T_0 = 500$ K, while varying P_0 where P_0= 10 bar, 30 bar, 50 bar, 100 bar, 200 bar, 500 bar.

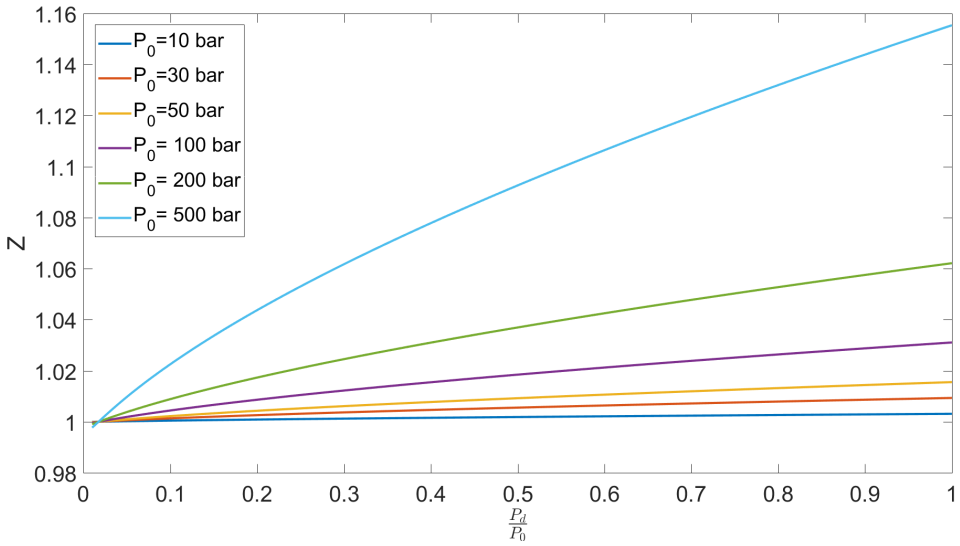

Figure 50: Comparison Z versus $\frac{P_d}{P_0}$ for Air with fixed $= T_0 = 1000$ K, while varying P_0 where P_0= 10 bar, 30 bar, 50 bar, 100 bar, 200 bar, 500 bar.

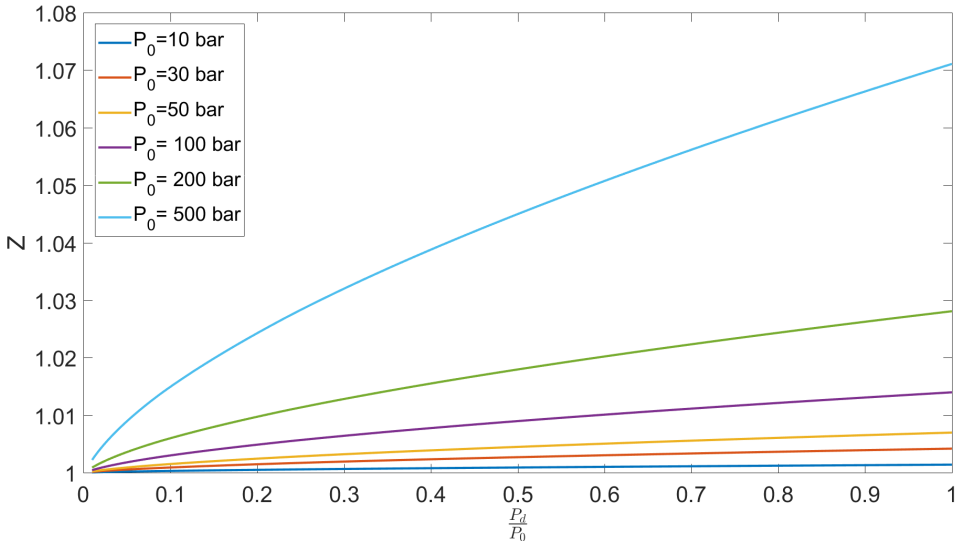

Figure 51: Comparison Z versus $\frac{P_d}{P_0}$ for Air with fixed $= T_0 = 2000$ K, while varying P_0 where P_0= 10 bar, 30 bar, 50 bar, 100 bar, 200 bar, 500 bar.

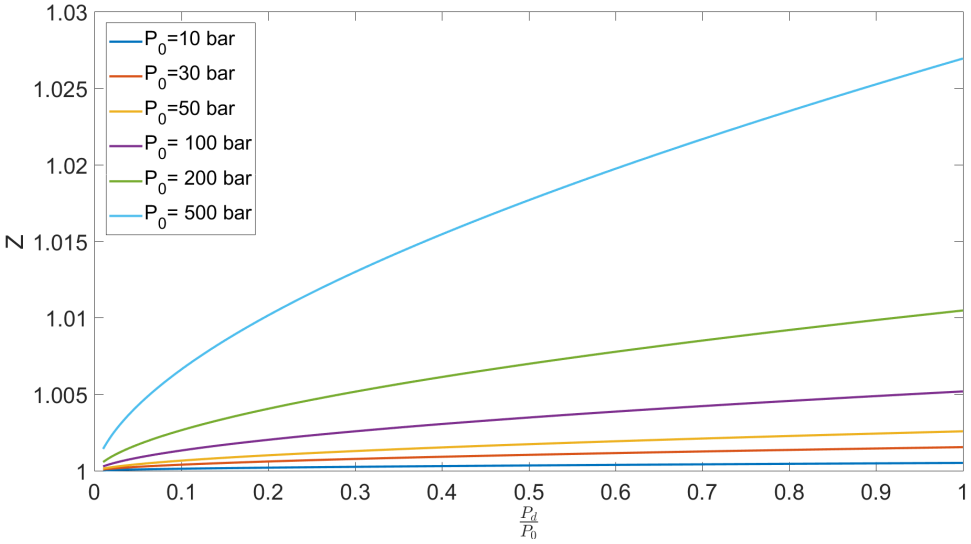

Figure 52: Comparison Z versus $\frac{P_d}{P_0}$ for Air with fixed $= T_0 = 4000$ K, while varying P_0 where P_0= 10 bar, 30 bar, 50 bar, 100 bar, 200 bar, 500 bar.

4.2.5 A Results

The calculations of A across the range of investigation has many different trends of curve, mainly depending on the stagnation temperature. The effects of a very low temperature change the trend so much that it over-shadows the other curves. The effect can be seen not only in the graphs plotted, but also, in Equation 4. Therefore, the graphs of A are re-plotted at the end of this section without the curves corresponding to 500 K. The curves of the 500 K all increase at the beginning of the graph until a certain low normalized pressure value. At this point, the plot gradually decreases. The 1000 K curves show a similar trend, but after the peak it decreases rapidly with increasing normalized pressure. For the 2000 K curve there is a distinct difference from the lower temperature graphs and no longer is concave down. The 2000 K curve is concave up with a small decrease while increasing the normalized pressure reaches a minimum and then dramatically increases in value. The final stagnation temperatusre, 4000 K almost looks like a linear line except for the very beginning

of the plot.

Varying the stagnation pressure does not change the shape of the curve, but it does change the magnitude of the values. As the pressure increases, so does the values corresponding to A. Without looking at the graphs, this trend based on pressure can be seen by Equation 4.

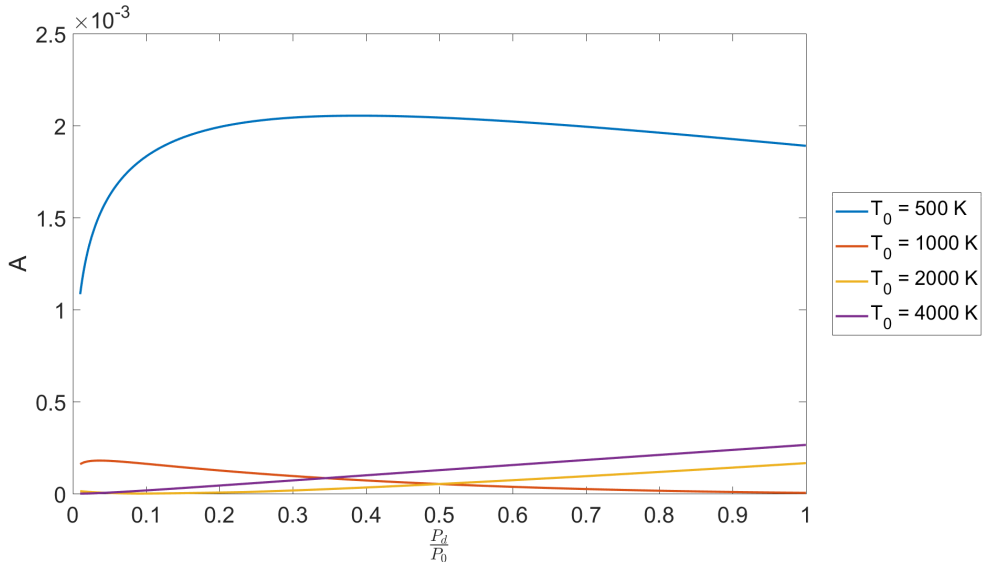

Figure 53: Comparison A versus $\frac{P_d}{P_0}$ for Air with fixed $P_0 = 10$ bar, while varying T_0, where $T_0 = 500$ K, 1000 K , 2000 K , 4000 K.

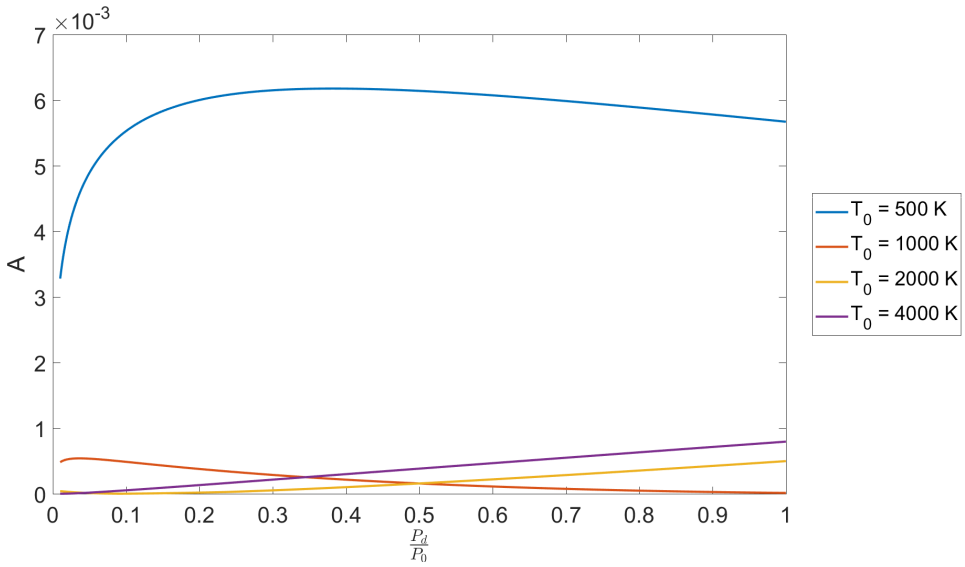

Figure 54: Comparison A versus $\frac{P_d}{P_0}$ for Air with fixed $P_0 = 30$ bar, while varying T_0, where $T_0 = 500$ K, 1000 K , 2000 K , 4000 K.

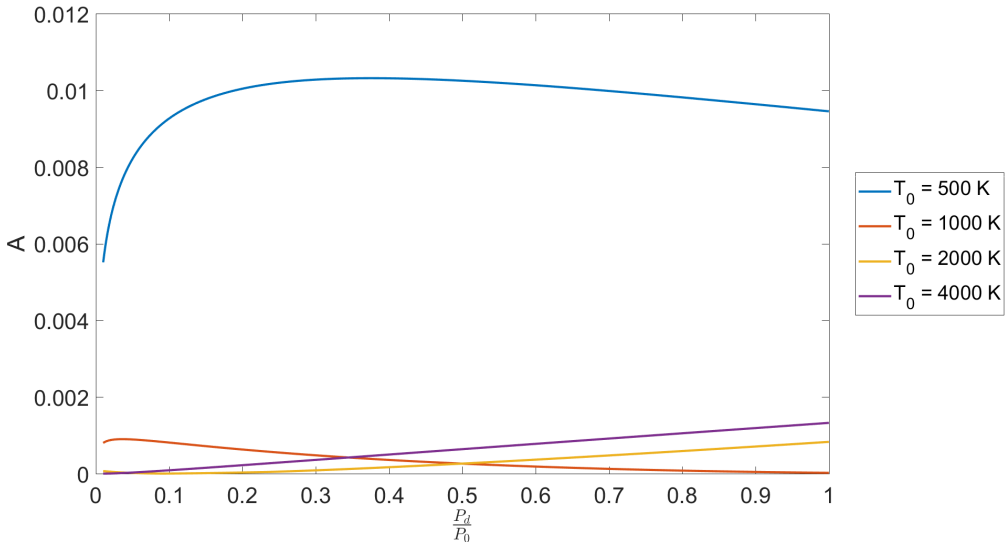

Figure 55: Comparison A versus $\frac{P_d}{P_0}$ for Air with fixed $P_0 = 50$ bar, while varying T_0, where $T_0 = 500$ K, 1000 K , 2000 K , 4000 K.

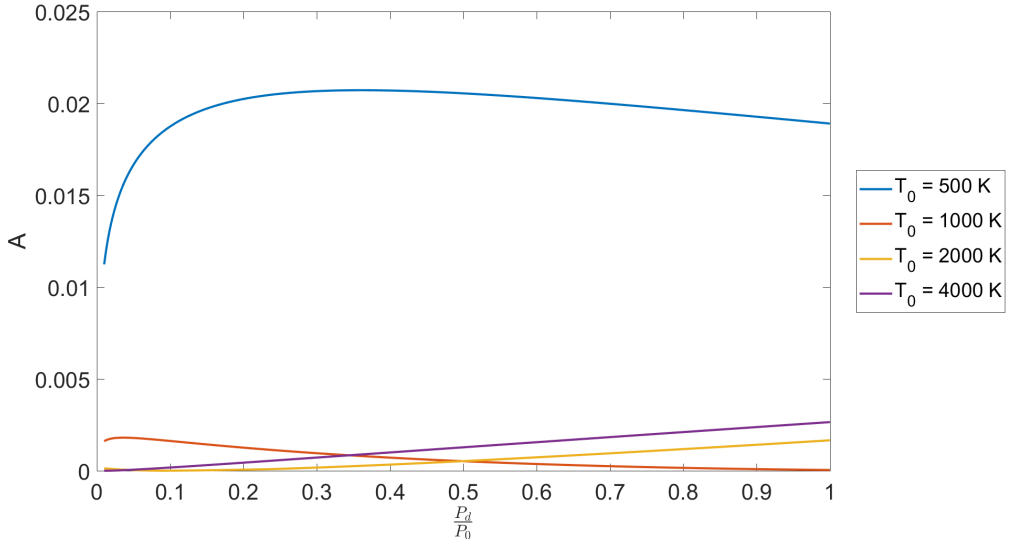

Figure 56: Comparison A versus $\frac{P_d}{P_0}$ for Air with fixed $P_0 = 100$ bar, while varying T_0, where $T_0 = 500$ K, 1000 K , 2000 K , 4000 K.

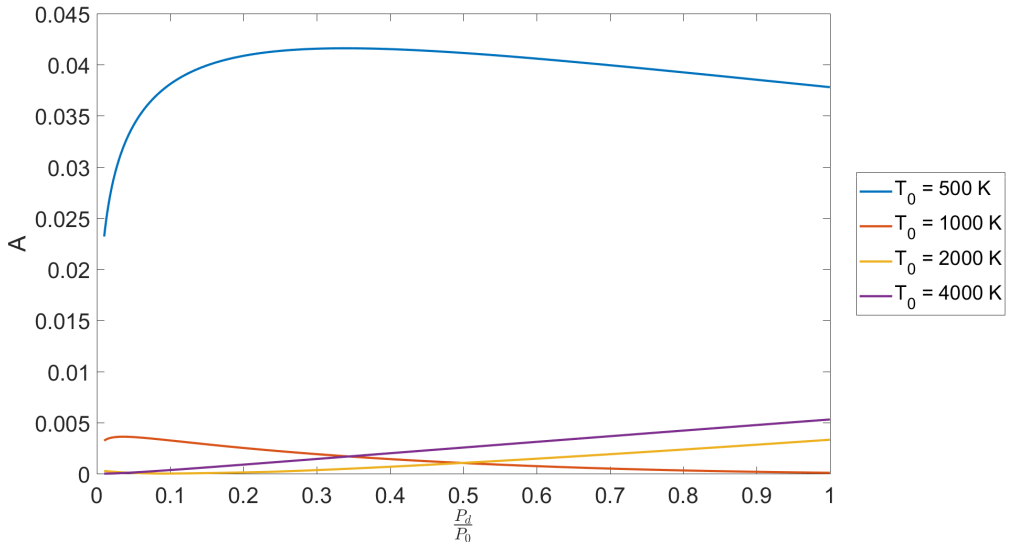

Figure 57: Comparison A versus $\frac{P_d}{P_0}$ for Air with fixed $P_0 = 200$ bar, while varying T_0, where $T_0 = 500$ K, 1000 K , 2000 K , 4000 K.

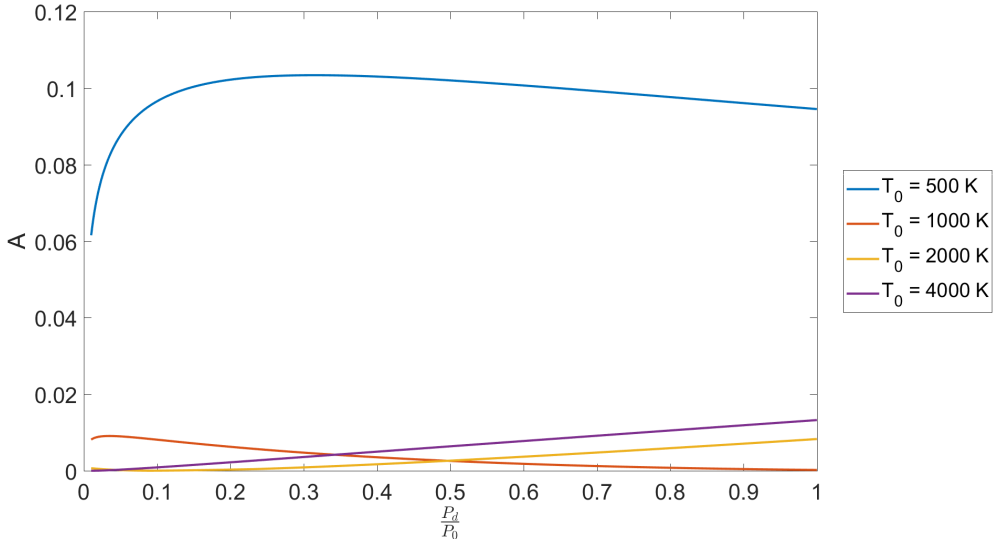

Figure 58: Comparison A versus $\frac{P_d}{P_0}$ for Air with fixed $P_0 = 500$ bar, while varying T_0, where $T_0 = 500$ K, 1000 K , 2000 K , 4000 K.

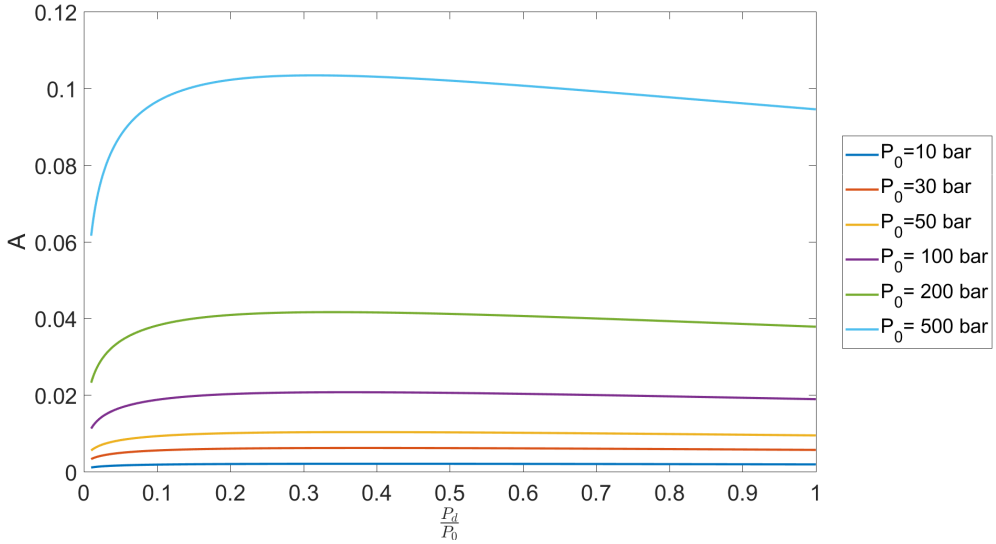

Figure 59: Comparison A versus $\frac{P_d}{P_0}$ for Air with fixed $T_0 = 500$ K, while varying P_0, where $P_0 = 10$ bar, 30 bar, 50 bar, 100 bar, 200 bar, 500 bar.

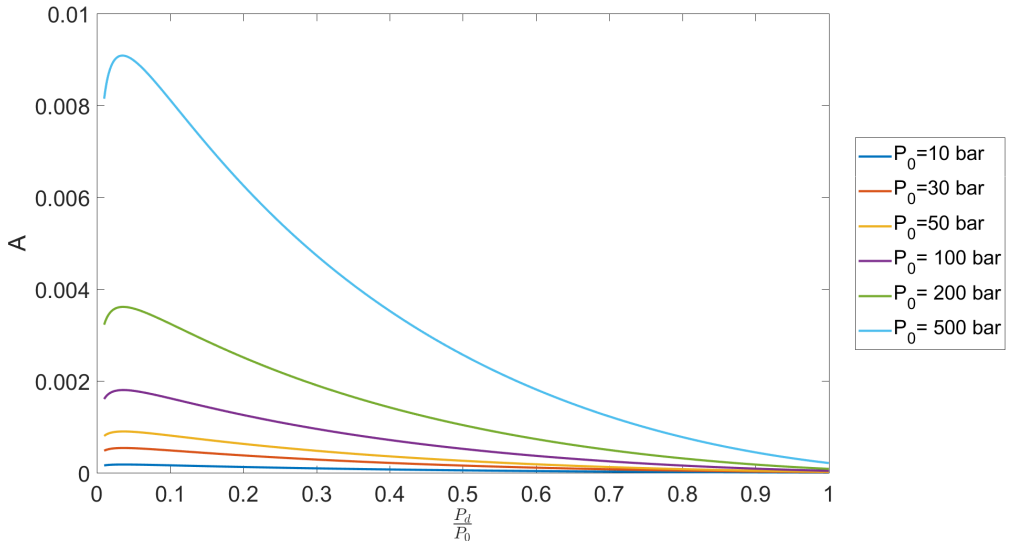

Figure 60: Comparison A versus $\frac{P_d}{P_0}$ for Air with fixed $T_0 = 500$ K, while varying P_0, where $P_0 = 10$ bar, 30 bar, 50 bar, 100 bar, 200 bar, 500 bar.

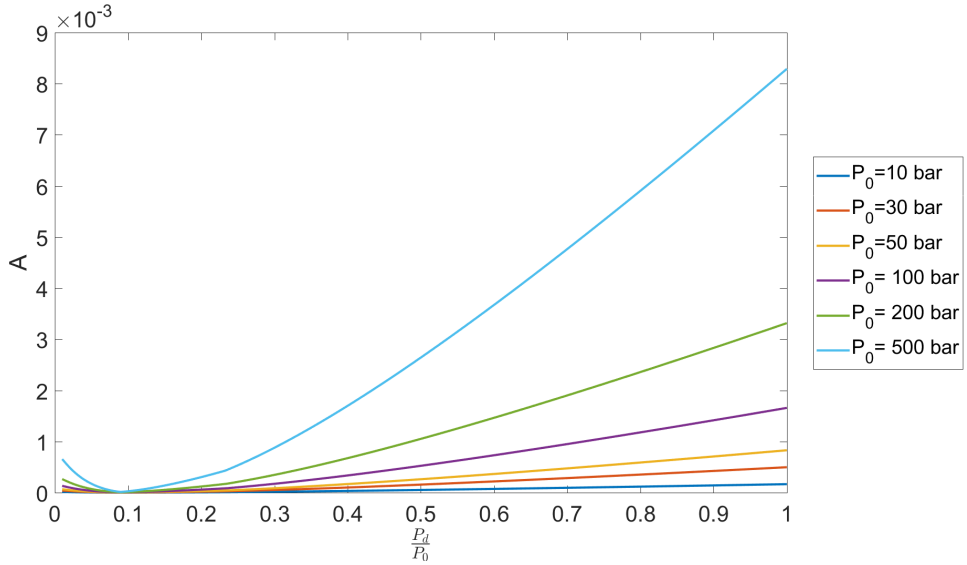

Figure 61: Comparison A versus $\frac{P_d}{P_0}$ for Air with fixed $T_0 = 2000$ K, while varying P_0, where $P_0 = 10$ bar, 30 bar, 50 bar, 100 bar, 200 bar, 500 bar.

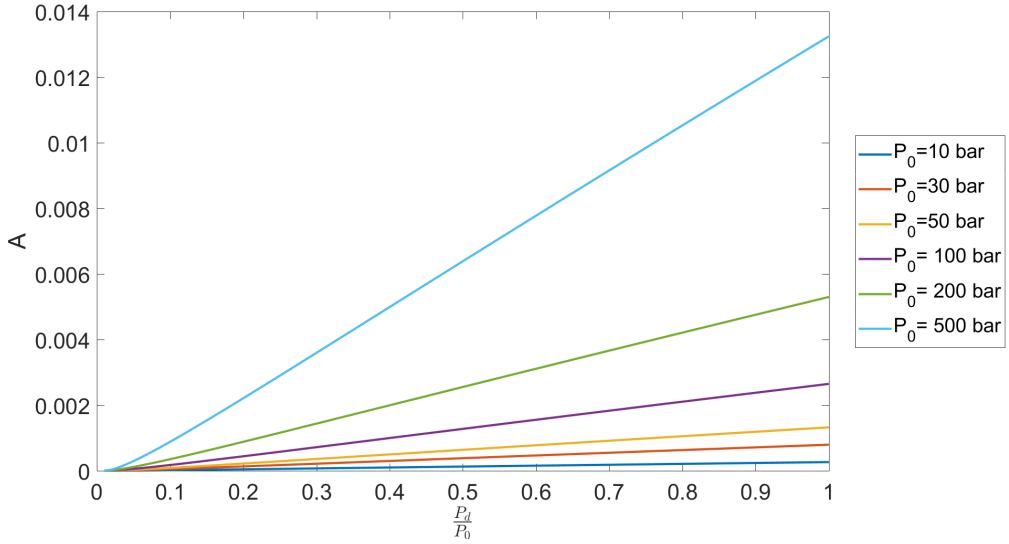

Figure 62: Comparison A versus $\frac{P_d}{P_0}$ for Air with fixed $T_0 = 4000$ K, while varying P_0, where $P_0 = 10$ bar, 30 bar, 50 bar, 100 bar, 200 bar, 500 bar.

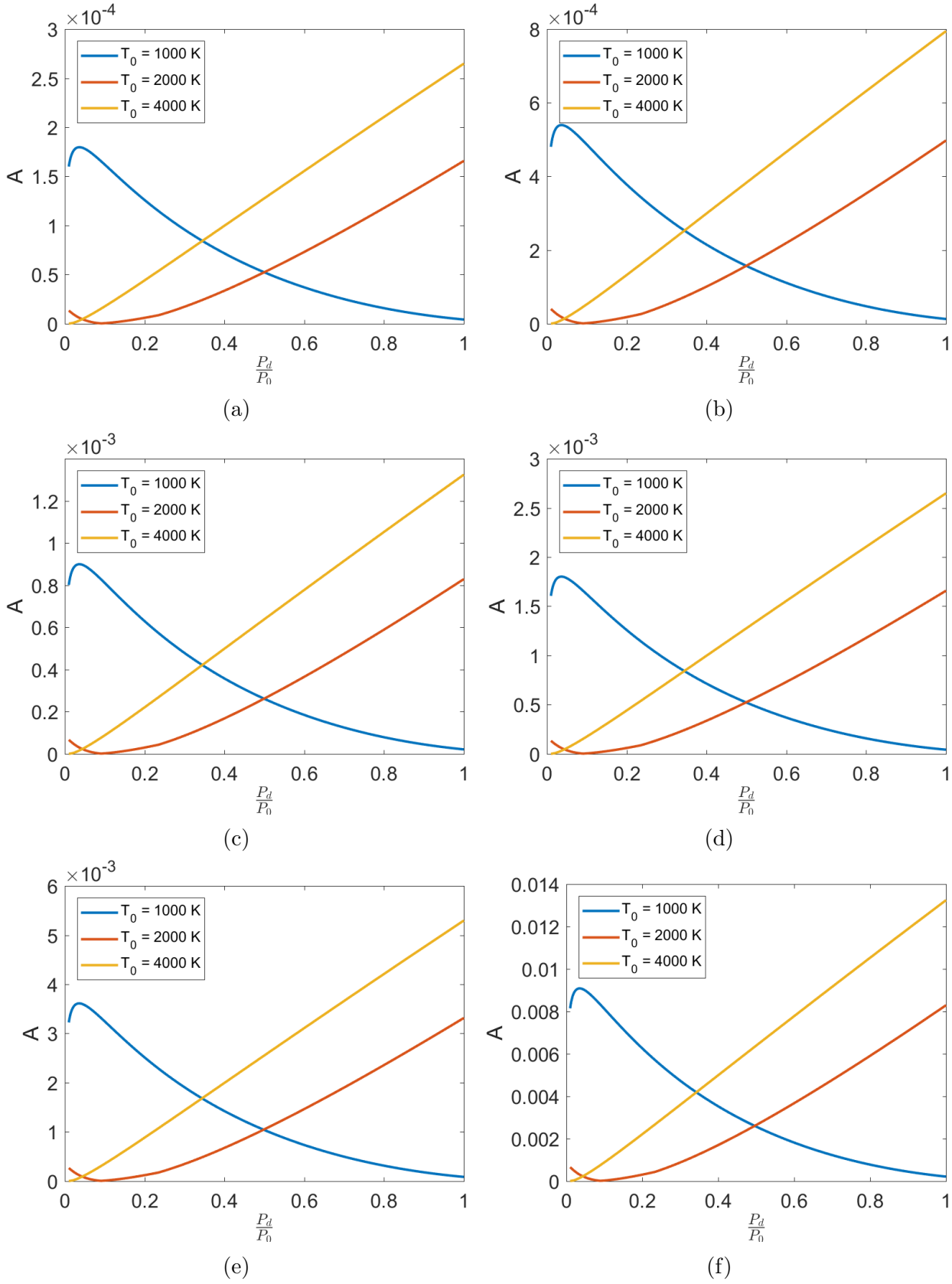

Figure 63: Plots of A Using Air. Vertical Axis is A like previous graphs but without 500 K so this demonstrates relationship more clearly. a)10 bar; b)30 bar; c) 50 bar; d) 100 bar; e) 200 bar; f) 500 bar

4.2.6 B Results

The results of B are pretty simplistic compared to that of A in that the plots follow a constant trend that is easily seen by the definition in Equation 5. As the normalized value of pressure increases, so does the value of B. Increasing the stagnation temperature decreases the value of B as well as decreases the rate at which B increases when normalized pressure increases. The effects of increasing stagnation pressure have a more dramatic effect on B where there is an order of two difference on the scales of the graph. While the first set of graphs, Figures 64 to 67, are for constant T_0 values, the order of mangitude used to plot B is the same. However Figures 68 to 73 have a difference. These have to hold different values to describe the changes in B across the range of normalized pressure.

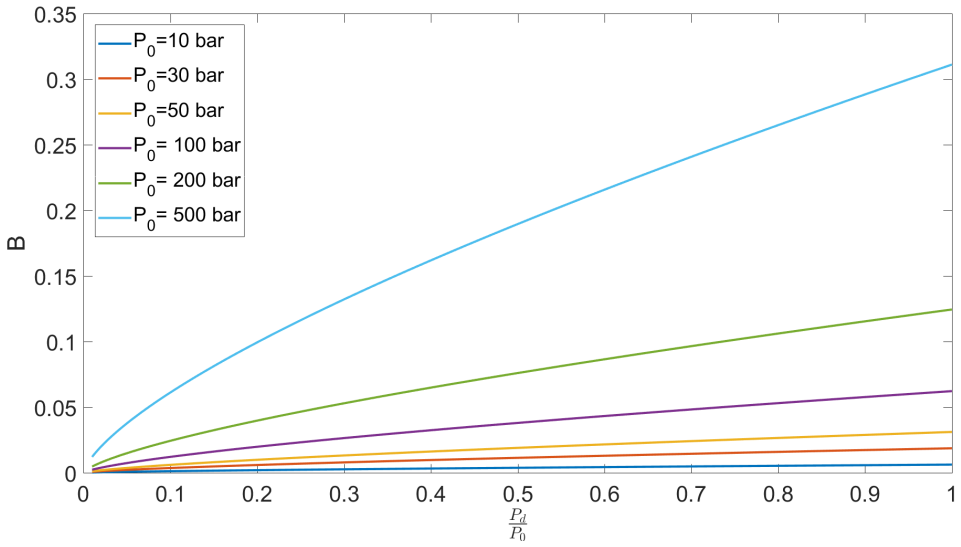

Figure 64: Comparison A versus $\frac{P_d}{P_0}$ for Air with fixed $T_0 = 500$ K, while varying P_0, where $P_0 = 10$ bar, 30 bar, 50 bar, 100 bar, 200 bar, 500 bar.

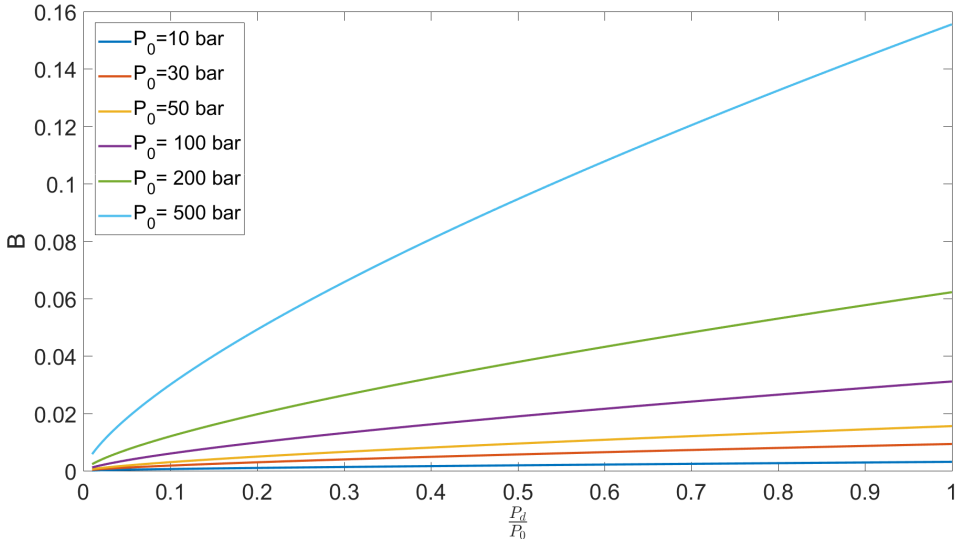

Figure 65: Comparison A versus $\frac{P_d}{P_0}$ for Air with fixed $T_0 = 10\text{s}00$ K, while varying P_0, where $P_0 = 10$ bar, 30 bar, 50 bar, 100 bar, 200 bar, 500 bar.

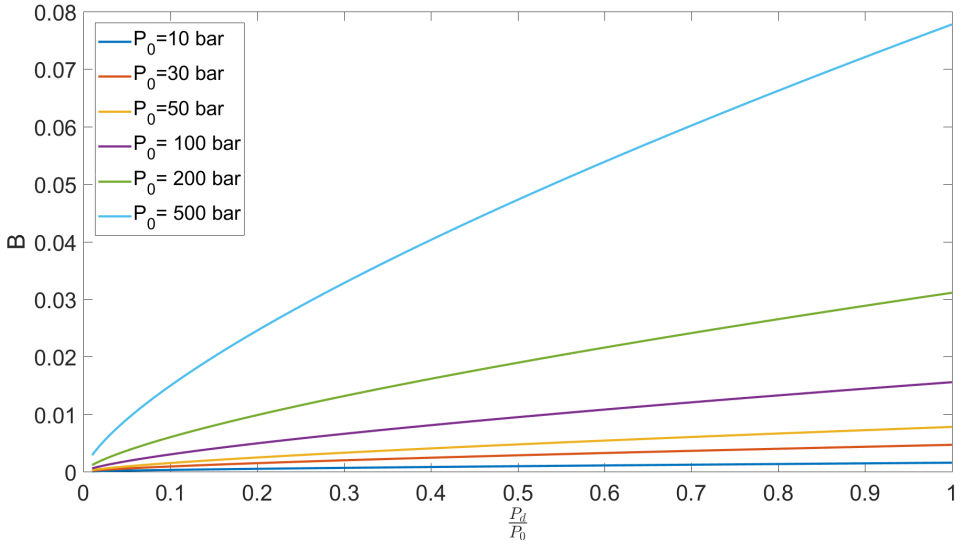

Figure 66: Comparison A versus $\frac{P_d}{P_0}$ for Air with fixed $T_0 = 2000$ K, while varying P_0, where $P_0 = 10$ bar, 30 bar, 50 bar, 100 bar, 200 bar, 500 bar.

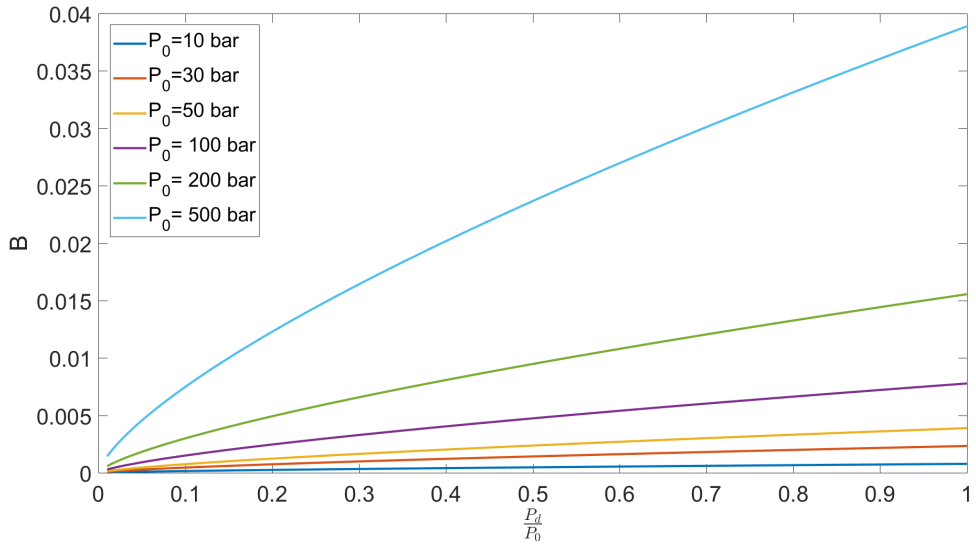

Figure 67: Comparison A versus $\frac{P_d}{P_0}$ for Air with fixed $T_0 = 500$ K, while varying P_0, where $P_0 = 10$ bar, 30 bar, 50 bar, 100 bar, 200 bar, 500 bar.

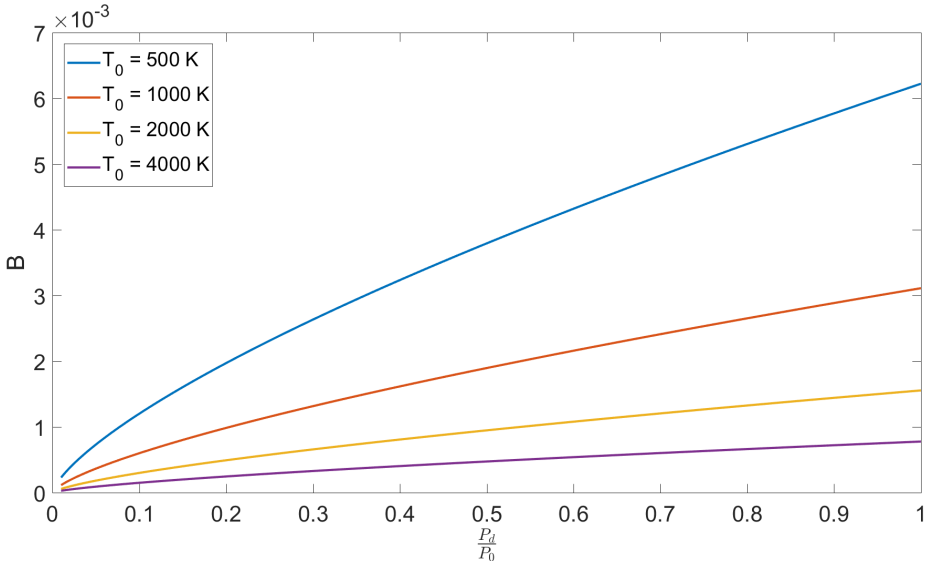

Figure 68: Comparison A versus $\frac{P_d}{P_0}$ for Air with fixed $P_0 = 10$ bar, while varying T_0, where $T_0 = 500$ K, 1000 K , 2000 K , 4000 K.

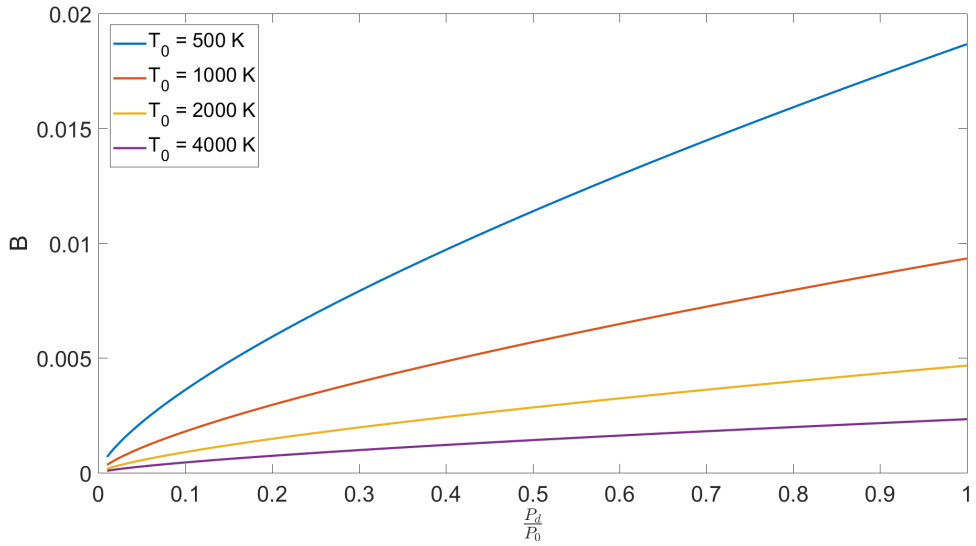

Figure 69: Comparison A versus $\frac{P_d}{P_0}$ for Air with fixed $P_0 = 30$ bar, while varying T_0, where $T_0 = 500$ K, 1000 K , 2000 K , 4000 K.

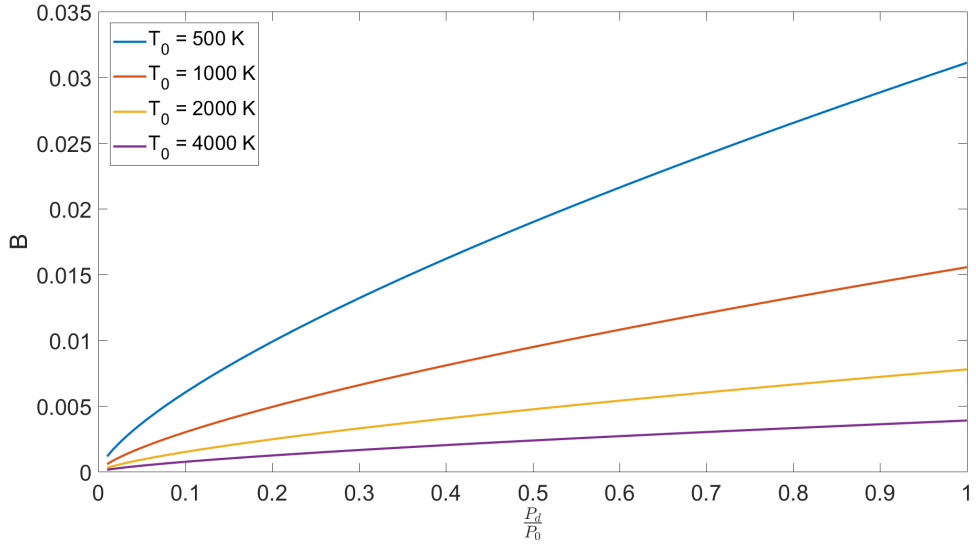

Figure 70: Comparison A versus $\frac{P_d}{P_0}$ for Air with fixed $P_0 = 50$ bar, while varying T_0, where $T_0 = 500$ K, 1000 K , 2000 K , 4000 K.

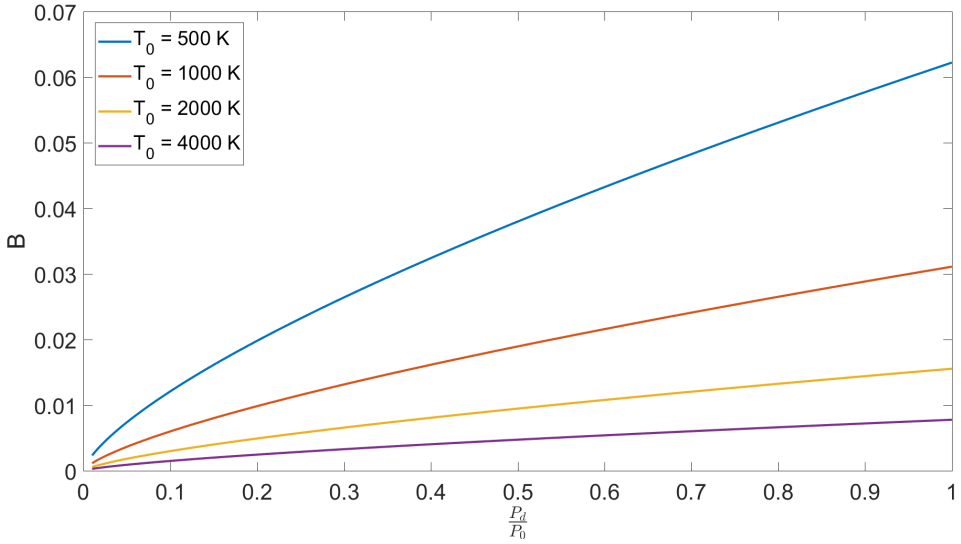

Figure 71: Comparison A versus $\frac{P_d}{P_0}$ for Air with fixed $P_0 = 100$ bar, while varying T_0, where $T_0 = 500$ K, 1000 K , 2000 K , 4000 K.

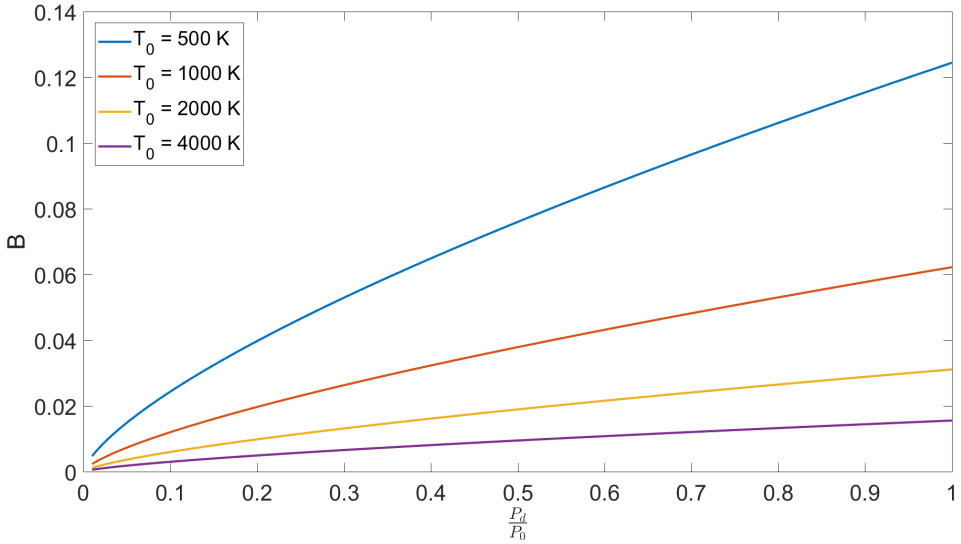

Figure 72: Comparison A versus $\frac{P_d}{P_0}$ for Air with fixed $P_0 = 200$ bar, while varying T_0, where $T_0 = 500$ K, 1000 K , 2000 K , 4000 K.

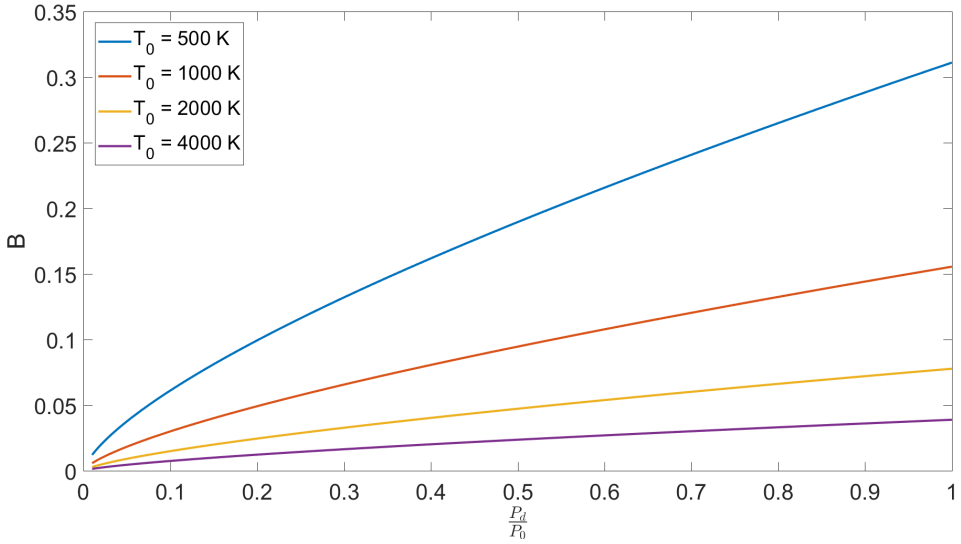

Figure 73: Comparison A versus $\frac{P_d}{P_0}$ for Air with fixed $P_0 = 500$ bar, while varying T_0, where $T_0 = 500$ K, 1000 K , 2000 K , 4000 K.

4.2.7 Sound Speed Results

Changing stagnation temperature and pressure had a different effect on the real-gas solutions than the other properties investigated. All the normalized sound speed graphs demonstrated almost congruent solutions at the low normalized pressure values. The only graph that does not show this trend is Figure 79 where the plots cross each other. When the normalized pressure increases, the curves corresponding to different pressures and temperatures diverge. The largest variation of the normalized sound speed plots is in Figure 80, corresponding to the lowest stagnation temperature while varying stagnation pressure. On the same Figure, the plot corresponding to the lowest temperature and highest pressure is the highest normalized sound speed value.

Referring to Equation 76, the sound speed for ideal-gas should not be impacted by static or stagnation pressure at a given temperature. However, the normalized pressure ratio still effects the sound speed, just not static pressure or stagnation pressure by itself.

However, based on the graphs in this section, this does not seem to be the case for real-

gas with maximum deviation of 24.05% to that of ideal-gas. The definition of the speed of sound for ideal-gas is as follows:

$$c = \sqrt{\gamma T \bar{R}} \tag{76}$$

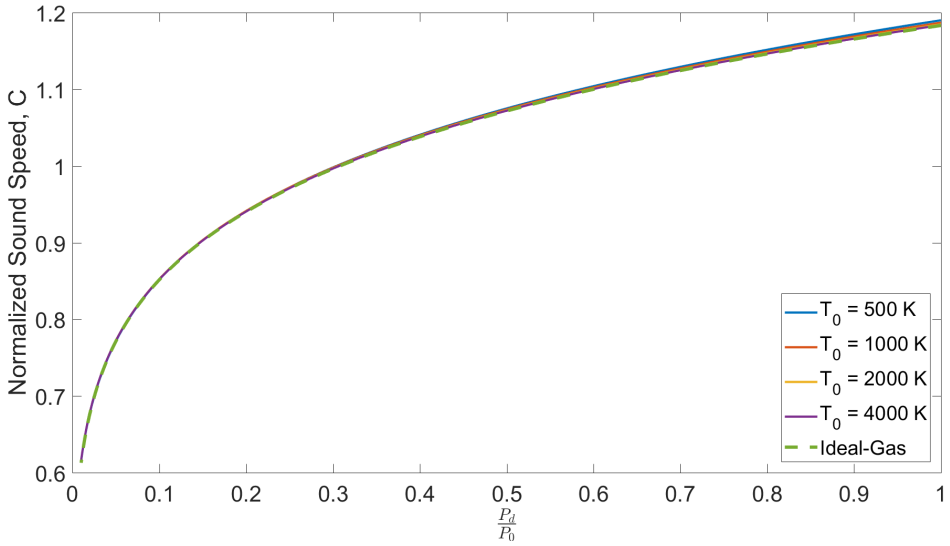

Figure 74: Comparison $C = \sqrt{TZ(f + g\beta)}$ versus $\frac{P_d}{P_0}$ for Air with fixed $P_0 = 10$ bar, while varying T_0, where $T_0 = 500$ K, 1000 k, 2000 K, 4000 K.

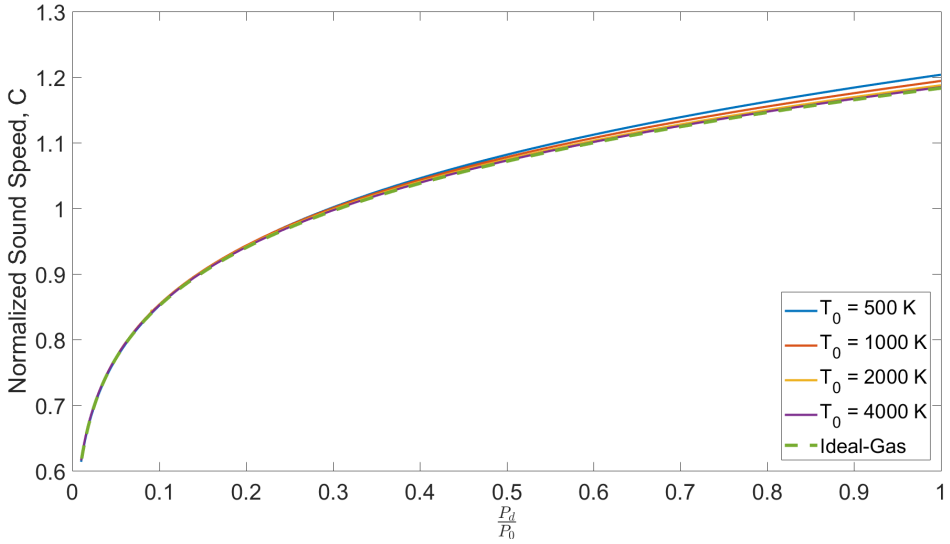

Figure 75: Comparison $C = \sqrt{TZ(f + g\beta)}$ versus $\frac{P_d}{P_0}$ for Air with fixed $P_0 = 10$ bar, while varying T_0, where $T_0 = 500$ K, 1000 k, 2000 K, 4000 K.

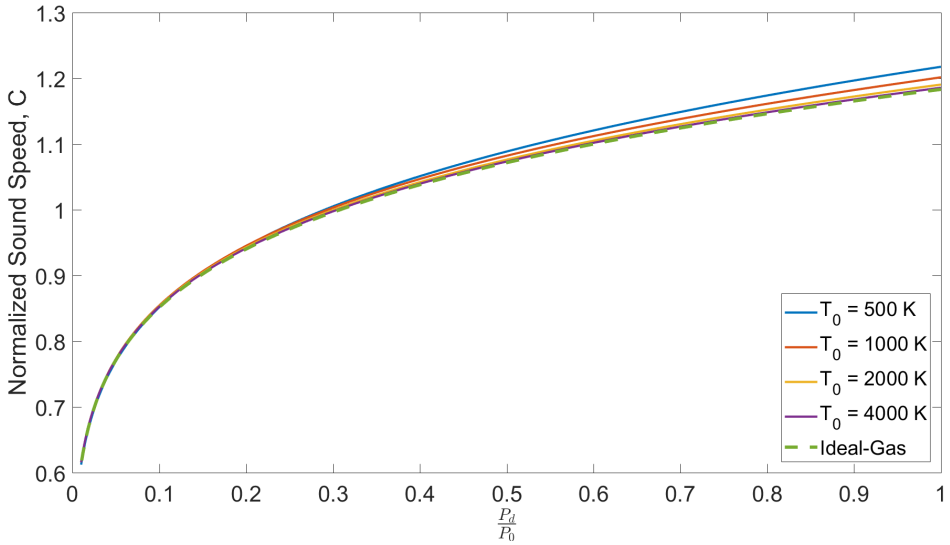

Figure 76: Comparison $C = \sqrt{TZ(f + g\beta)}$ versus $\frac{P_d}{P_0}$ for Air with fixed $P_0 = 50$ bar, while varying T_0, where $T_0 = 500$ K, 1000 k, 2000 K, 4000 K.

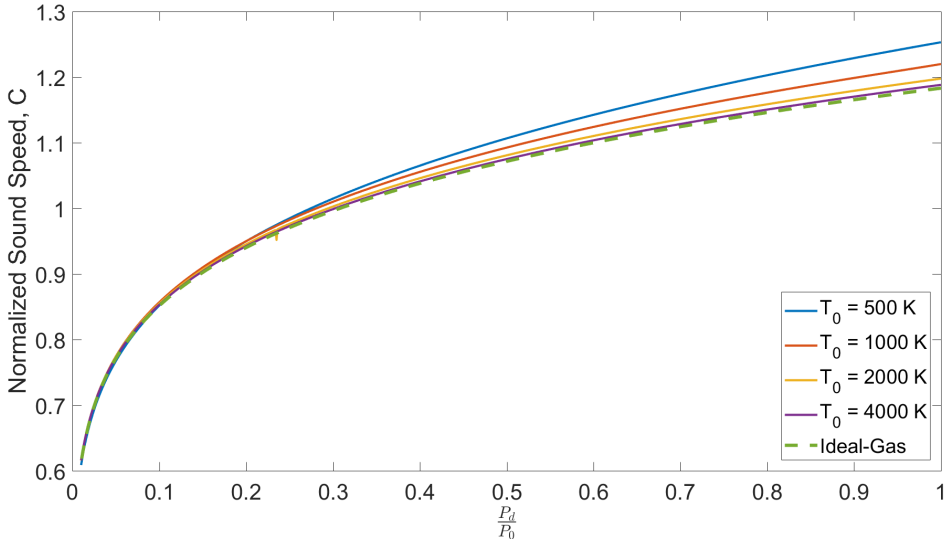

Figure 77: Comparison $C = \sqrt{TZ(f + g\beta)}$ versus $\frac{P_d}{P_0}$ for Air with fixed $P_0 = 100$ bar, while varying T_0, where $T_0 = 500$ K, 1000 k, 2000 K, 4000 K.

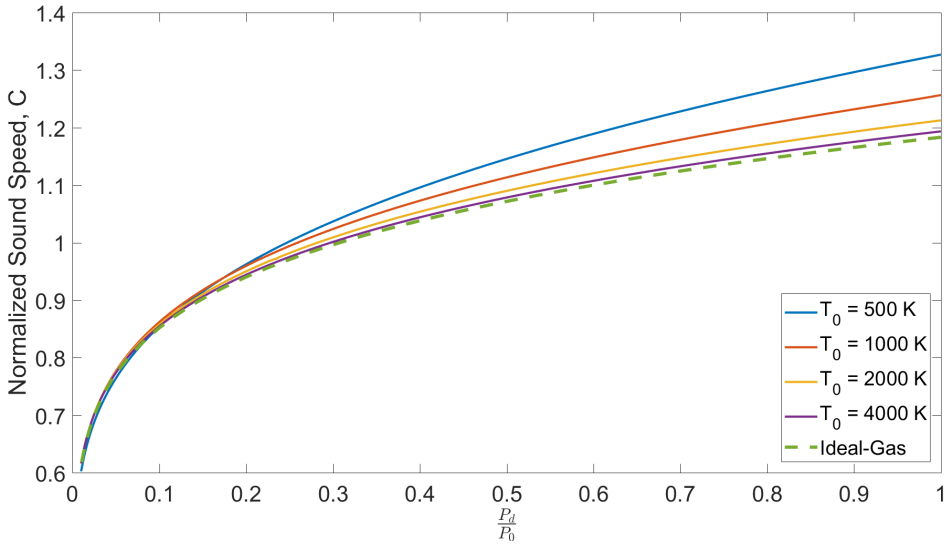

Figure 78: Comparison $C = \sqrt{TZ(f + g\beta)}$ versus $\frac{P_d}{P_0}$ for Air with fixed $P_0 = 200$ bar, while varying T_0, where $T_0 = 500$ K, 1000 k, 2000 K, 4000 K.

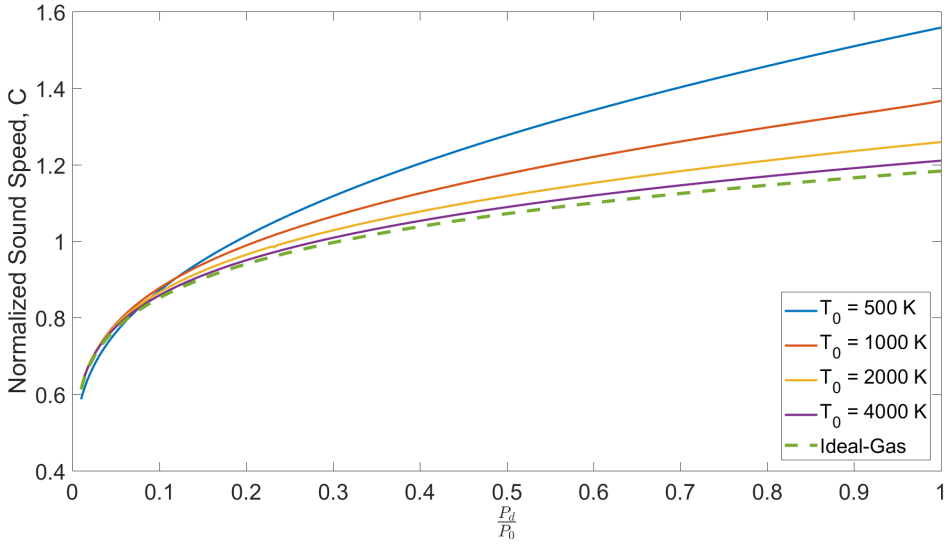

Figure 79: Comparison $C = \sqrt{TZ(f + g\beta)}$ versus $\frac{P_d}{P_0}$ for Air with fixed $P_0 = 500$ bar, while varying T_0, where $T_0 = 500$ K, 1000 k, 2000 K, 4000 K.

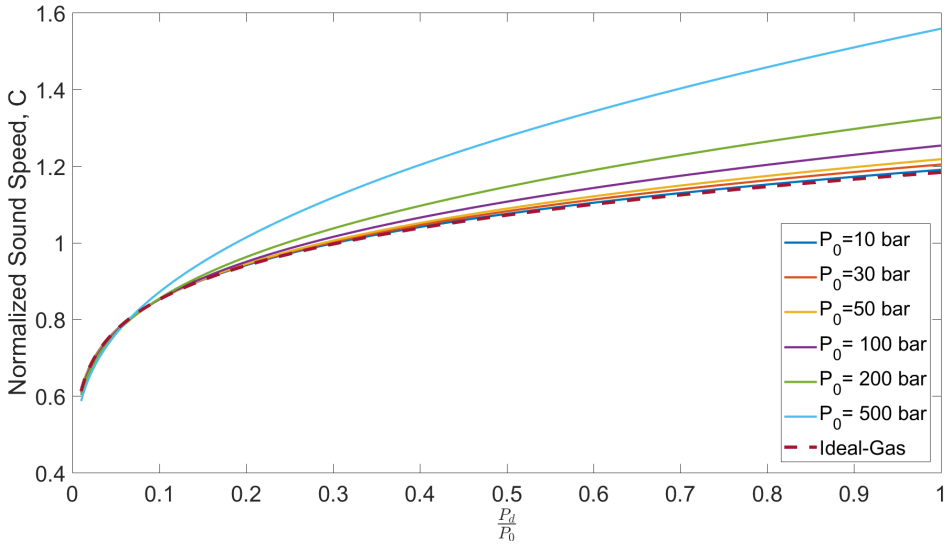

Figure 80: Comparison $C = \sqrt{TZ(f + g\beta)}$ versus $\frac{P_d}{P_0}$ for Air with fixed $T_0 = 500$ K, while varying P_0, where $P_0 = 10$ bar, 30 bar, 50 bar, 100 bar, 200 bar, 500 bar.

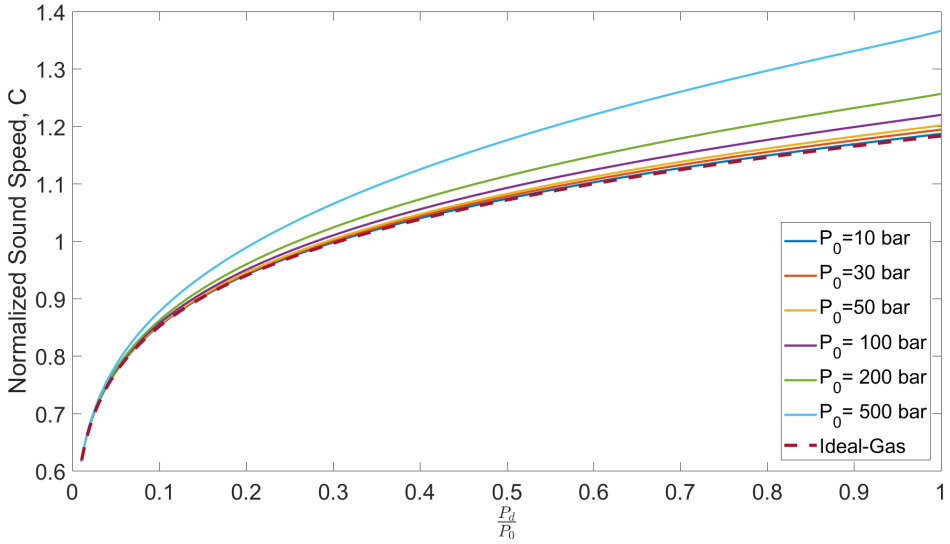

Figure 81: Comparison $C = \sqrt{TZ(f + g\beta)}$ versus $\frac{P_d}{P_0}$ for Air with fixed $T_0 = 1000$ K, while varying P_0, where $P_0 = 10$ bar, 30 bar, 50 bar, 100 bar, 200 bar, 500 bar.

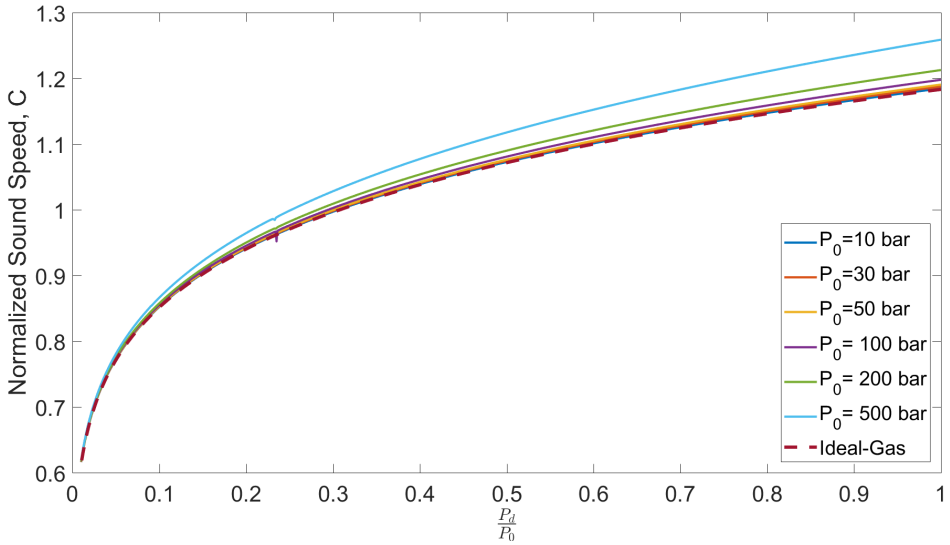

Figure 82: Comparison $C = \sqrt{TZ(f + g\beta)}$ versus $\frac{P_d}{P_0}$ for Air with fixed $T_0 = 2000$ K, while varying P_0, where $P_0 = 10$ bar, 30 bar, 50 bar, 100 bar, 200 bar, 500 bar.

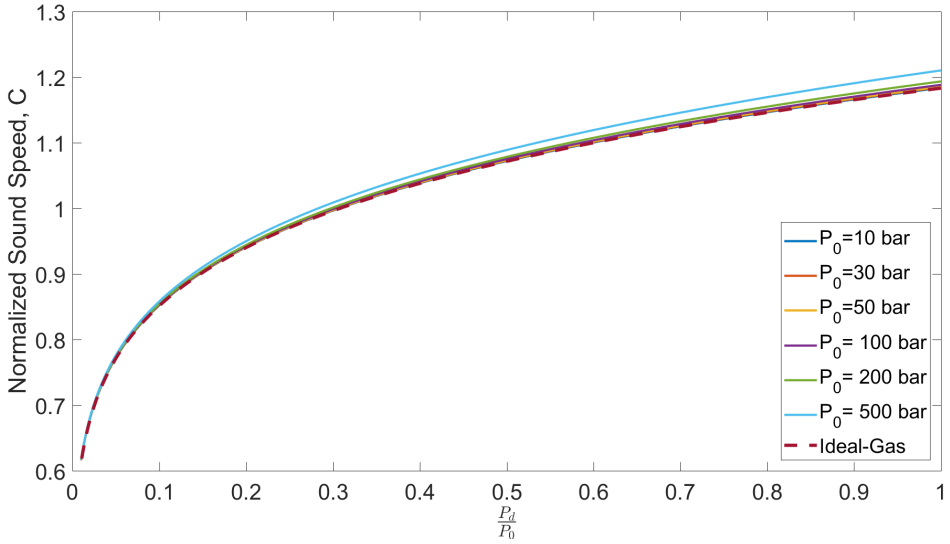

Figure 83: Comparison $C = \sqrt{TZ(f + g\beta)}$ versus $\frac{P_d}{P_0}$ for Air with fixed $T_0 = 4000$ K, while varying P_0, where $P_0 = 10$ bar, 30 bar, 50 bar, 100 bar, 200 bar, 500 bar.

4.2.8 Velocity Results

The normalized velocity shows little change when varying temperature in low pressure regions. However, when the P_0 reaches around 200 bar there is a noticeable difference between the varying temperature curves. The graph corresponding to 500 bar, Figure 89, displays a distinct difference between each temperature curve. The effects of temperature are definitely less dramatic than that of pressure. In Figures 90 to 93, these have all the curves grouped closely together, except for the curves corresponding to the 500 bar.

Across all the ranges of stagnation pressure and temperature investigated, the maximum deviation of the real-gas solutions from ideal-gas was not a useful metric to compare. Since the beginning of the calculation starts with P as one and U at zero, the error between ideal-gas and real-gas become highly dependent on equations that are sensitive to small numbers. When dealing with small values, a small change leads to a large change in difference between ideal-gas values and real-gas. Meaning, while the the velocities are of similar order, the values of the numbers being used in the equations to solve for both causes a large fluctuation

of errors. Thus, it is more appropriate in this case to state that the highest deviation in ideal-gas value to that of real-gas solutions corresponded to the lowest stagnation temperature, T = 500 K, and the highest stagnation pressure, P = 500 bar. At this particular instance the average difference in value between ideal-gas and real-gas is 8.41% across the entire curve (P=1 to P = 0). While this does not give the largest error for normalized velocity, it does give an idea of how much of an offset in values the real-gas is to the ideal-gas values.

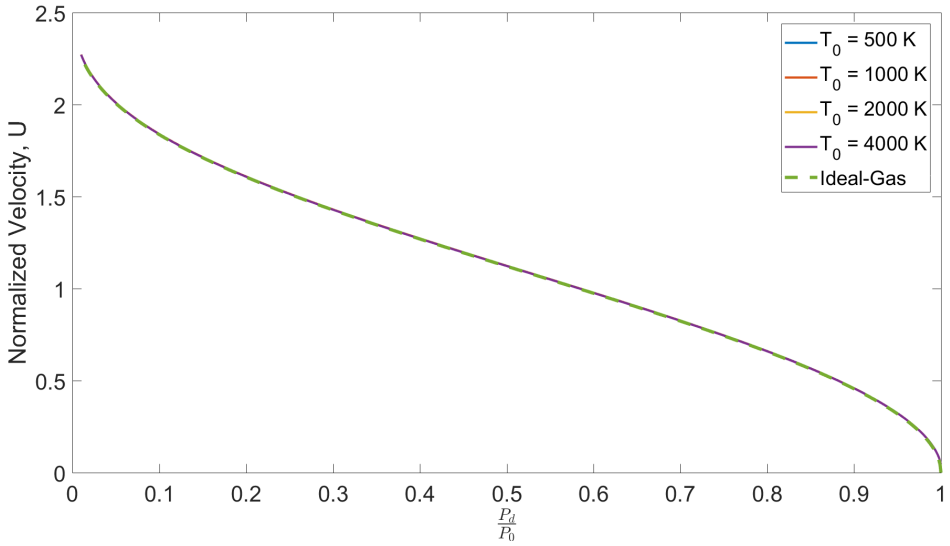

Figure 84: Comparison $U = \frac{u}{\sqrt{RT_0}}$ versus $\frac{P_d}{P_0}$ for Air with fixed P_0 = 10 bar, while varying T_0, where T_0 = 500 K, 1000 K, 2000 K, 4000 K.

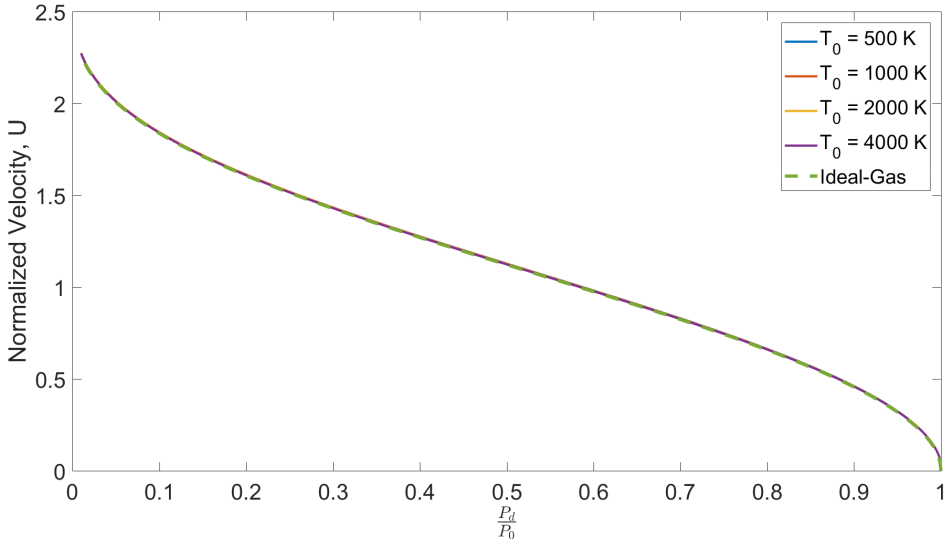

Figure 85: Comparison $U = \frac{u}{\sqrt{RT_0}}$ versus $\frac{P_d}{P_0}$ for Air with fixed $P_0 = 30$ bar, while varying T_0, where $T_0 = 500$ K, 1000 K, 2000 K, 4000 K.

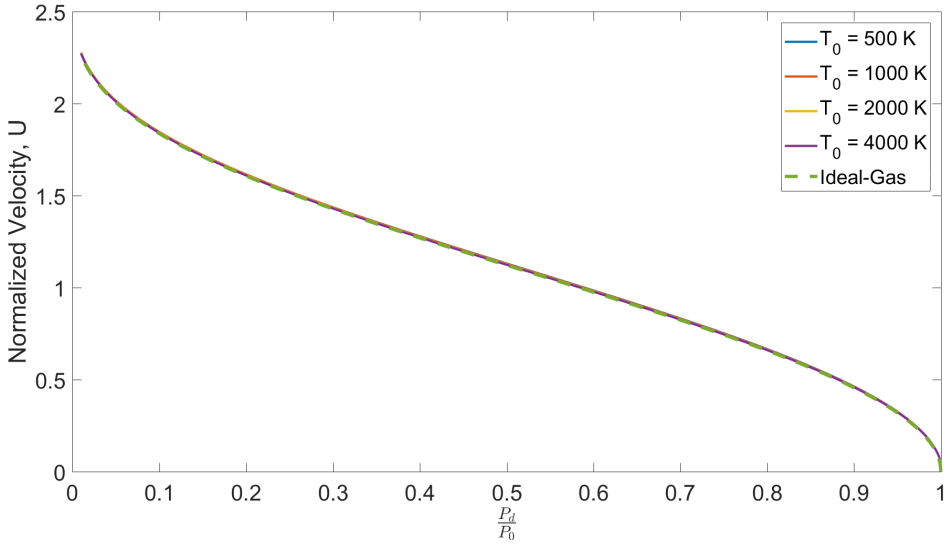

Figure 86: Comparison $U = \frac{u}{\sqrt{RT_0}}$ versus $\frac{P_d}{P_0}$ for Air with fixed $P_0 = 50$ bar, while varying T_0, where $T_0 = 500$ K, 1000 K, 2000 K, 4000 K.

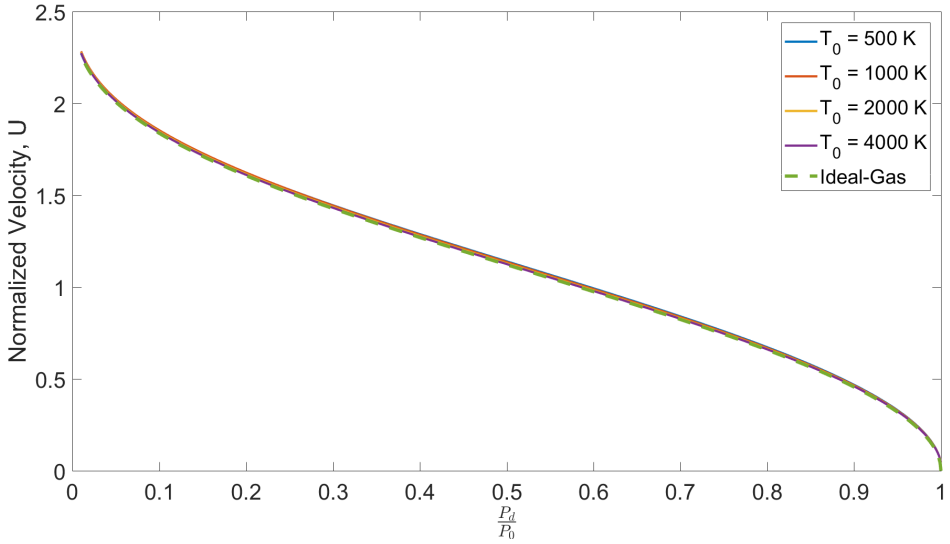

Figure 87: Comparison $U = \frac{u}{\sqrt{RT_0}}$ versus $\frac{P_d}{P_0}$ for Air with fixed $P_0 = 100$ bar, while varying T_0, where $T_0 = 500$ K, 1000 K, 2000 K, 4000 K.

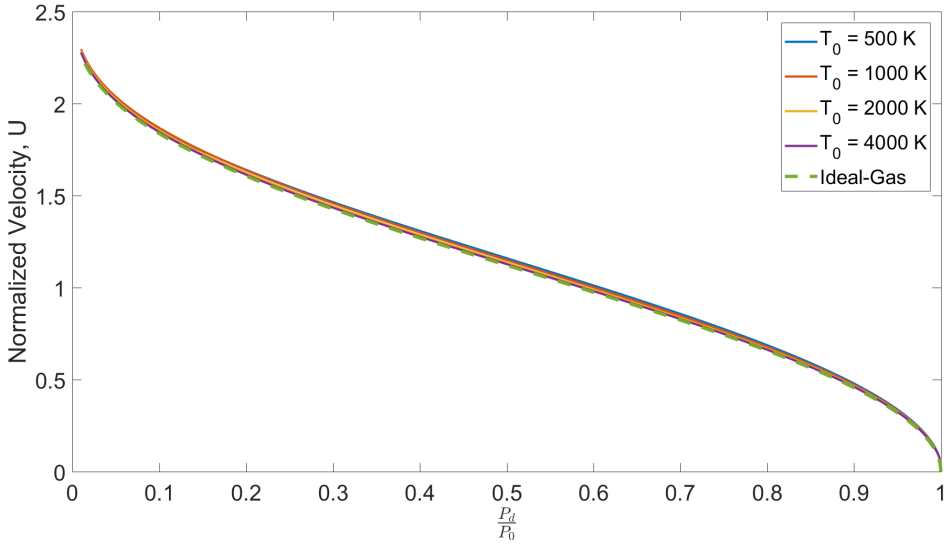

Figure 88: Comparison $U = \frac{u}{\sqrt{RT_0}}$ versus $\frac{P_d}{P_0}$ for Air with fixed $P_0 = 200$ bar, while varying T_0, where $T_0 = 500$ K, 1000 K, 2000 K, 4000 K.

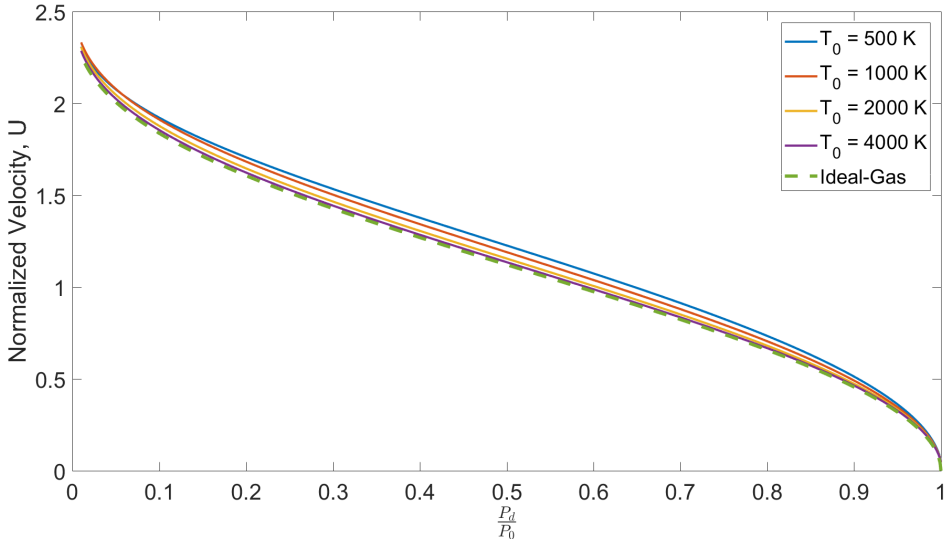

Figure 89: Comparison $U = \frac{u}{\sqrt{RT_0}}$ versus $\frac{P_d}{P_0}$ for Air with fixed $P_0 = 500$ bar, while varying T_0, where $T_0 = 500$ K, 1000 K, 2000 K, 4000 K.

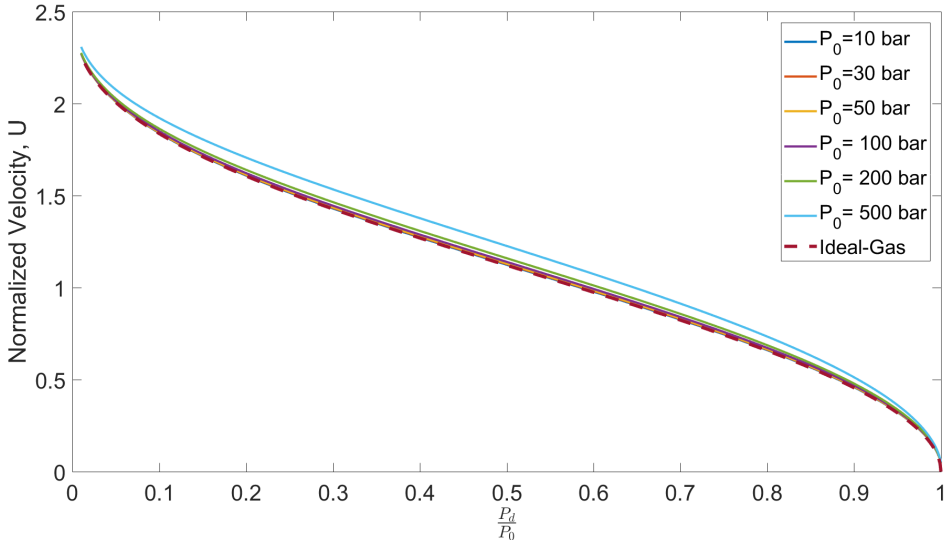

Figure 90: Comparison $U = \frac{u}{\sqrt{RT_0}}$ versus $\frac{P_d}{P_0}$ for Air with fixed $T_0 = 500$ K, while varying P_0, where $P_0 = 10$ bar, 30 bar, 50 bar, 100 bar, 200 bar, 500 bar.

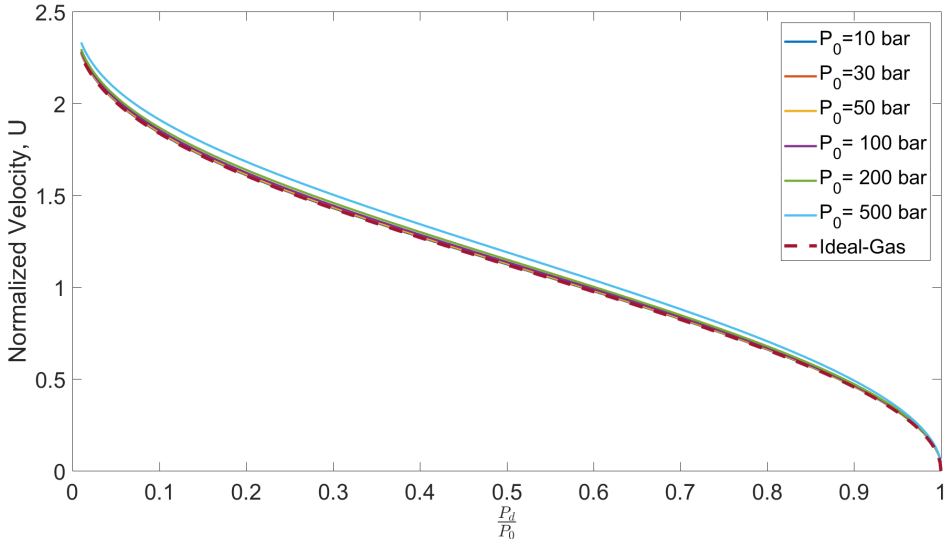

Figure 91: Comparison $U = \frac{u}{\sqrt{RT_0}}$ versus $\frac{P_d}{P_0}$ for Air with fixed $T_0 = 1000$ K, while varying P_0, where $P_0 = 10$ bar, 30 bar, 50 bar, 100 bar, 200 bar, 500 bar.

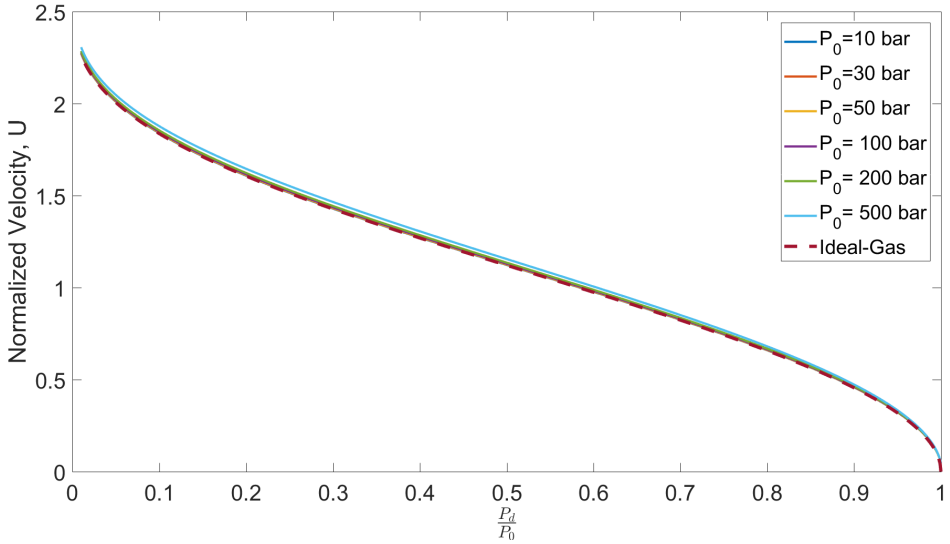

Figure 92: Comparison $U = \frac{u}{\sqrt{RT_0}}$ versus $\frac{P_d}{P_0}$ for Air with fixed $T_0 = 2000$ K, while varying P_0, where $P_0 = 10$ bar, 30 bar, 50 bar, 100 bar, 200 bar, 500 bar.

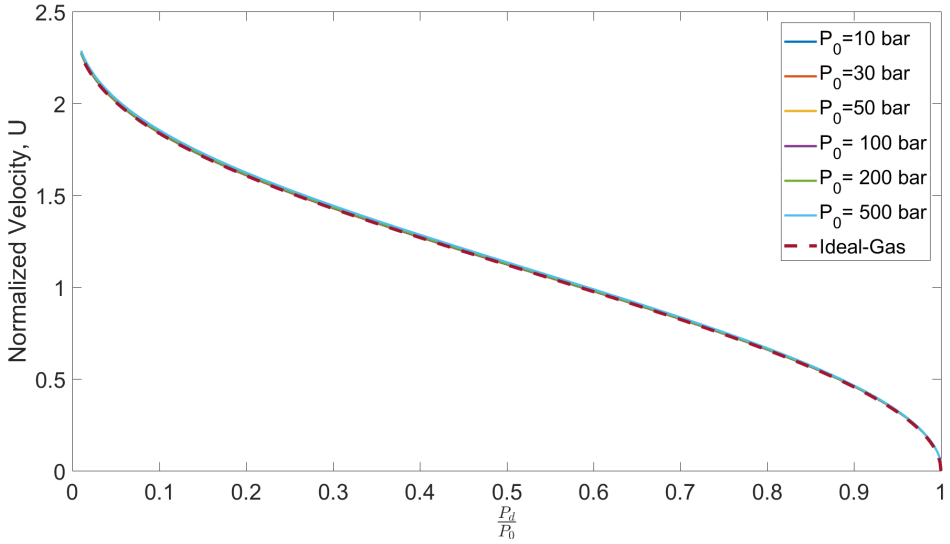

Figure 93: Comparison $U = \frac{u}{\sqrt{RT_0}}$ versus $\frac{P_d}{P_0}$ for Air with fixed $T_0 = 4000$ K, while varying P_0, where $P_0 = 10$ bar, 30 bar, 50 bar, 100 bar, 200 bar, 500 bar.

4.2.9 Mach Number Results

The Mach number shows small variation when changing stagnation temperature, T_0 for a wide pressure range. While normalized velocity changes vary little over both large P_0 and T_0 ranges, the sound speed has a noticeable difference in value at lower T_0 and higher P_0. A slight variation of Mach number occurs at 500 bar when T_0 is 500 K. However, the rest of the T_0 range shows little difference to ideal-gas values.

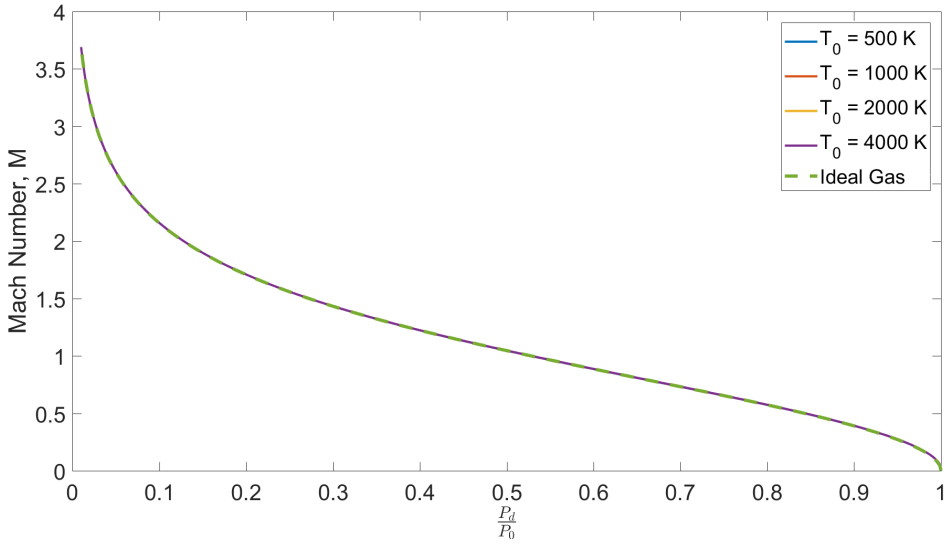

Figure 94: Comparison M versus $\frac{P_d}{P_0}$ for Air with fixed $P_0 = 10$ bar, while varying T_0, where $T_0 = 500$ K, 1000 K, 2000 K, 4000 K.

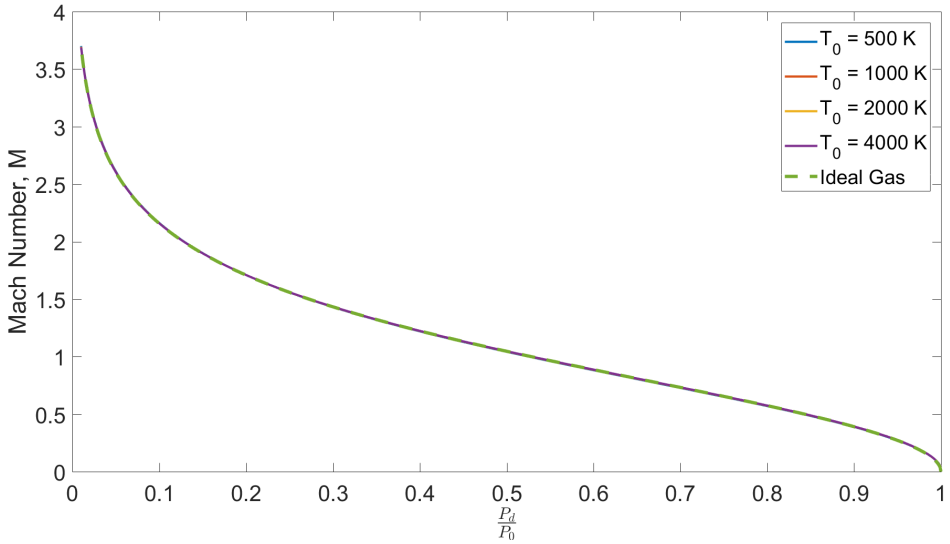

Figure 95: Comparison M versus $\frac{P_d}{P_0}$ for Air with fixed $P_0 = 30$ bar, while varying T_0, where $T_0 = 500$ K, 1000 K, 2000 K, 4000 K.

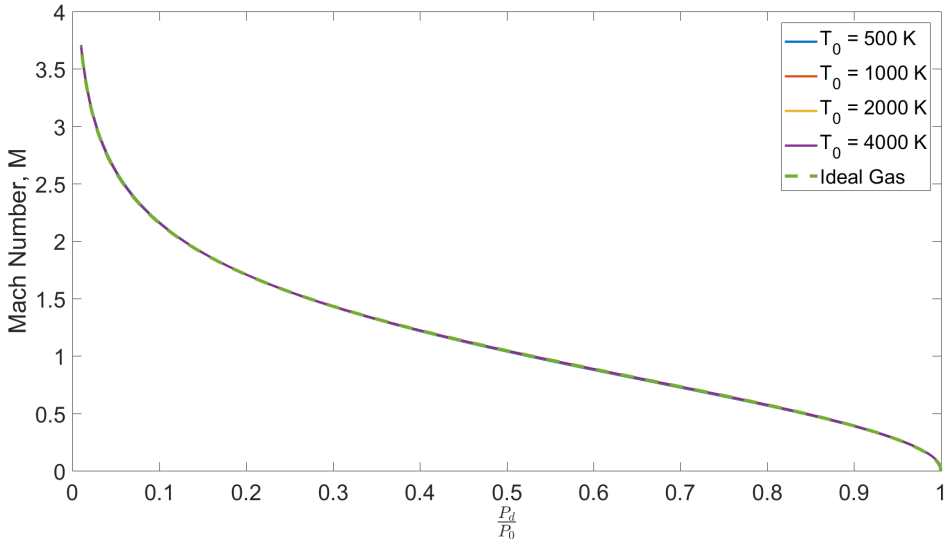

Figure 96: Comparison M versus $\frac{P_d}{P_0}$ for Air with fixed $P_0 = 50$ bar, while varying T_0, where $T_0 = 500$ K, 1000 K, 2000 K, 4000 K.

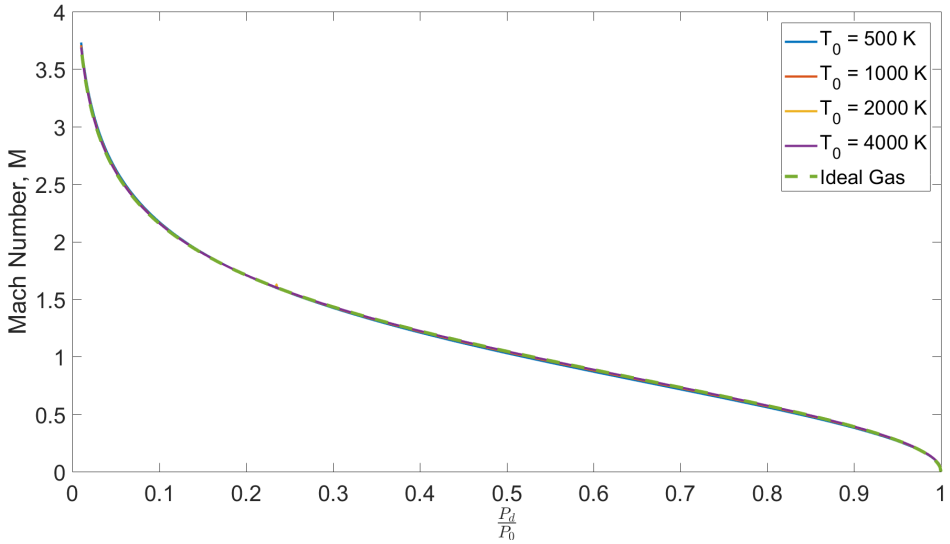

Figure 97: Comparison M versus $\frac{P_d}{P_0}$ for Air with fixed $P_0 = 100$ bar, while varying T_0, where $T_0 = 500$ K, 1000 K, 2000 K, 4000 K.

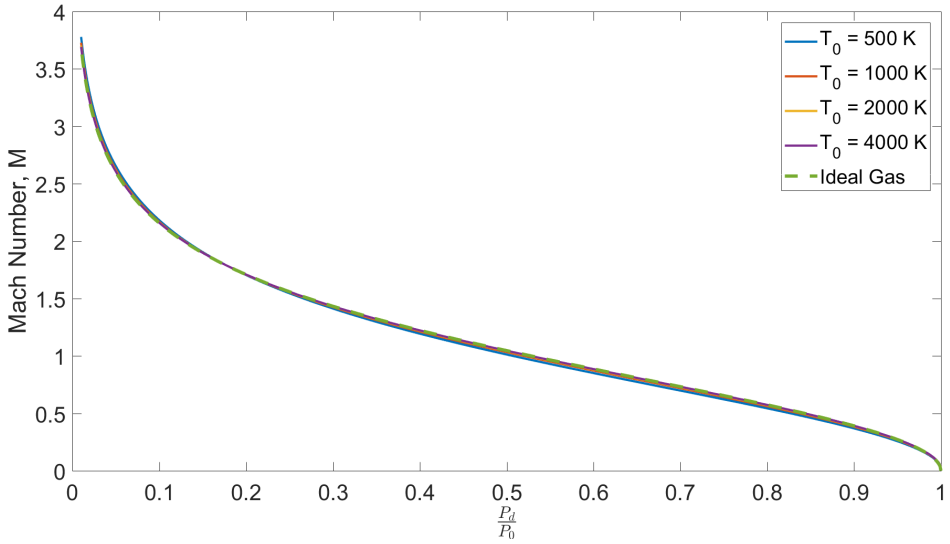

Figure 98: Comparison M versus $\frac{P_d}{P_0}$ for Air with fixed $P_0 = 200$ bar, while varying T_0, where $T_0 = 500$ K, 1000 K, 2000 K, 4000 K.

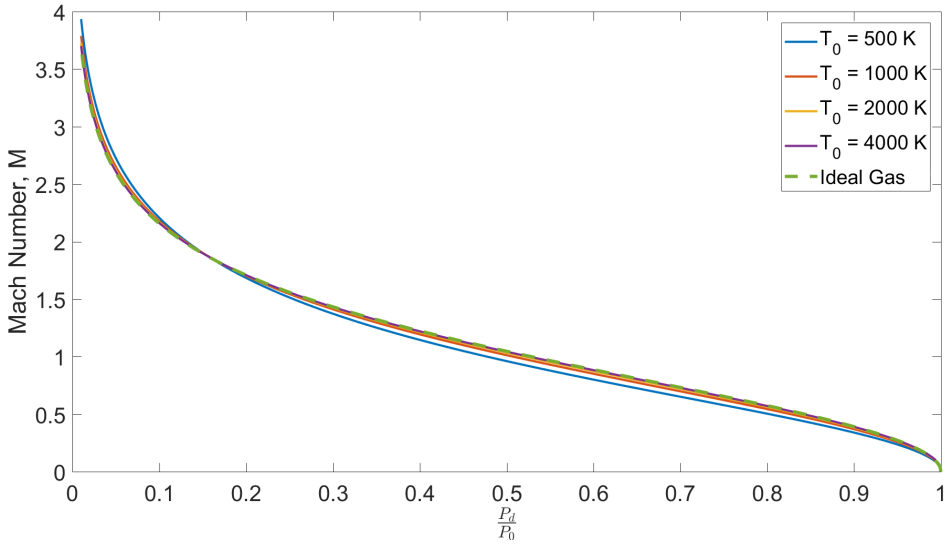

Figure 99: Comparison M versus $\frac{P_d}{P_0}$ for Air with fixed $P_0 = 500$ bar, while varying T_0, where $T_0 = 500$ K, 1000 K, 2000 K, 4000 K.

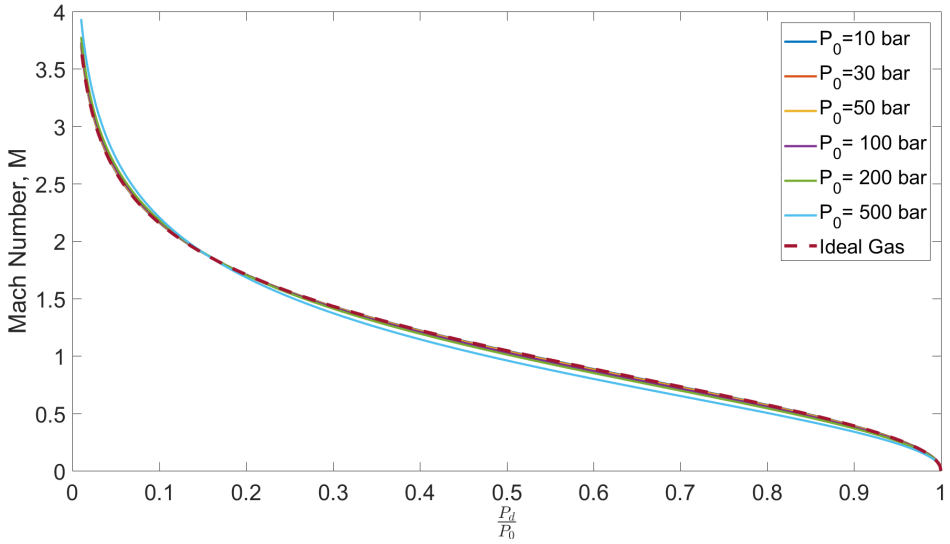

Figure 100: Comparison M versus $\frac{P_d}{P_0}$ for Air with fixed $T_0 = 500$ K, while varying P_0, where $P_0 = 10$ bar, 30 bar, 50 bar, 100 bar, 200 bar, 500 bar.

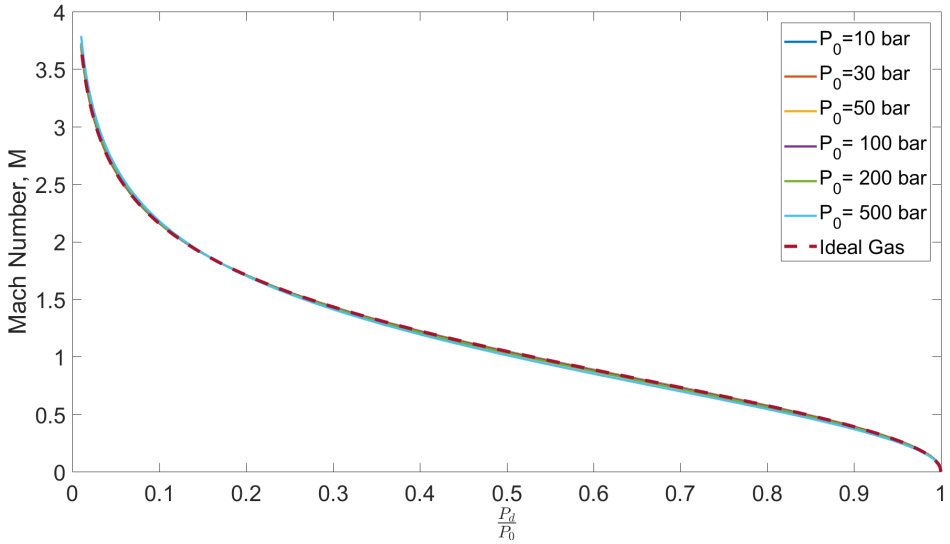

Figure 101: Comparison M versus $\frac{P_d}{P_0}$ for Air with fixed $T_0 = 1000$ K, while varying P_0, where $P_0 = 10$ bar, 30 bar, 50 bar, 100 bar, 200 bar, 500 bar.

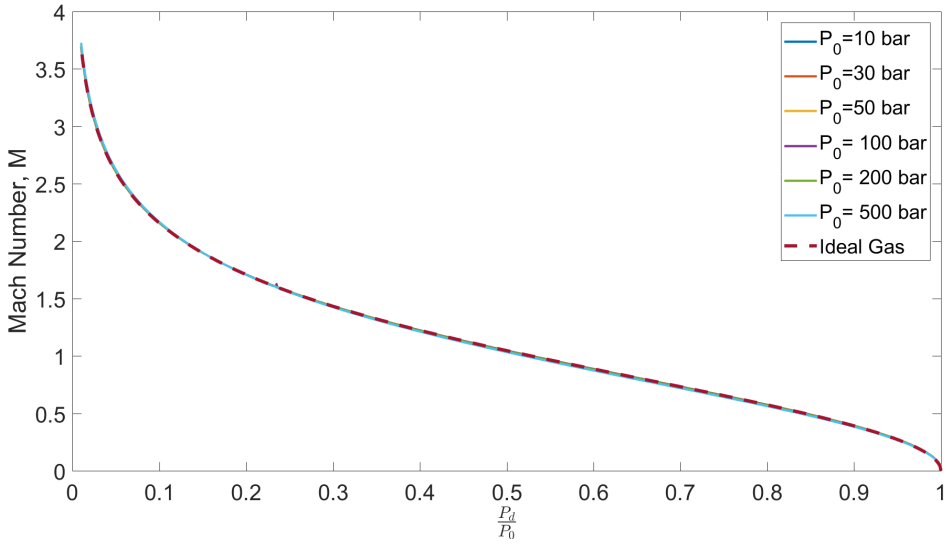

Figure 102: Comparison M versus $\frac{P_d}{P_0}$ for Air with fixed $T_0 = 2000$ K, while varying P_0, where $P_0 = 10$ bar, 30 bar, 50 bar, 100 bar, 200 bar, 500 bar.

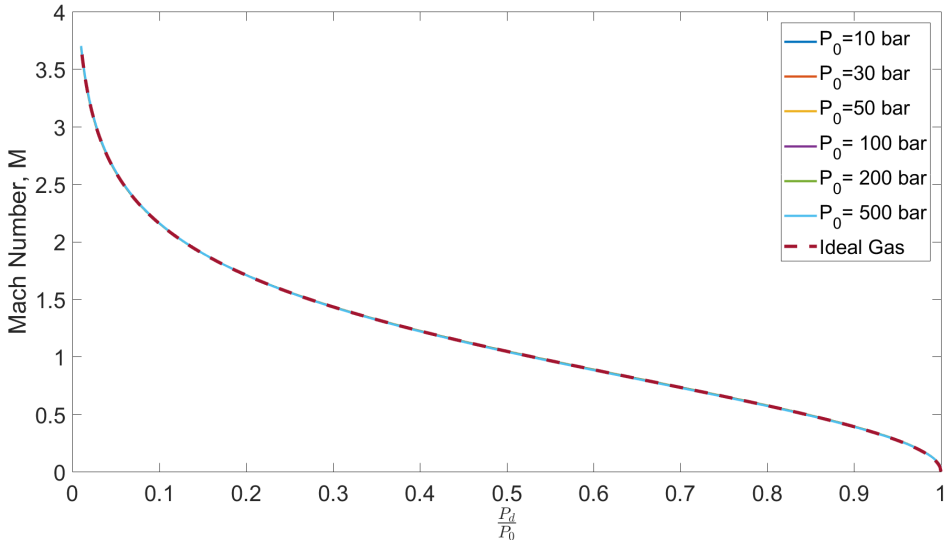

Figure 103: Comparison M versus $\frac{P_d}{P_0}$ for Air with fixed $T_0 = 4000$ K, while varying P_0, where $P_0 = 10$ bar, 30 bar, 50 bar, 100 bar, 200 bar, 500 bar.

4.2.10 Mass Ratio Results

Mass flow of ideal-gas and real-gas was compared by deriving equations to find the mass flow at a specific point in the nozzle. The throat was chosen for ease of calculation so that mach number is one and the area ratio, α, is also one. This will simplify some calculations. The general equation for mass flow is as follows:

$$\dot{m} = \rho u A \tag{77}$$

Ultimately, both the ideal-gas equations and real-gas calculations are dependent on the specific heat ratio, stagnation temperature, stagnation pressure, area at the throat, velocity at the throat and molecular weight. This is contrary to the usual case of where ideal-gas is only dependent on mach number and specific heat capacities. Recalling that flow at a chocked nozzle has a M of 1, the general equation becomes:

$$\dot{m} = \rho_{d,t} c_{d,t} A_t \tag{78}$$

To find the mass flow at the throat for an ideal-gas, one must recall Equations 65 and 67 as well as the ideal-gas equation for sound speed:

$$c_{ideal} = \sqrt{\gamma R T_d} \tag{79}$$

Setting M equal to 1 and substituting ideal-gas equations into the sound speed equation, Equation 77 becomes:

$$\dot{m}_{ideal} = \rho_0 \left(\frac{\gamma + 1}{2} \right)^{\frac{-1}{\gamma - 1}} \sqrt{\gamma R T_d} \tag{80}$$

Substituting ρ_0 for $\frac{P_0}{T_0 R}$ and simplifying leads to the following equation:

$$\dot{m}_{ideal} = \gamma^{\frac{1}{2}} \left(\frac{2}{\gamma + 1} \right)^{\frac{\gamma + 1}{2(\gamma - 1)}} \frac{P_0 A_t}{\sqrt{R T_0}} \tag{81}$$

Once the condition at the throat have been determined using the real-gas calculations, $\dot{m}_{real}$ can be determined easily by substituting Equations 51 and 42 into Equation 78:

$$\dot{m}_{real} = (\frac{\mathscr{R}P}{RT})(U\sqrt{\gamma T_0}) \tag{82}$$

Now, the mass ratio of the real mass flow is normalized by the ideal mass flow. Even though the area has not been determined, it is unnecessary because the A_t term will cancel out. The following table is a tabulation of $\frac{\dot{m}}{\dot{m}_{ideal}}$ for Air, Argon (Ar) and Nitrogen (N_2).

Air				Ar				N_2			
P_0 bar	T_0 K	$\frac{\dot{m}_{real}}{\dot{m}_{ideal}}$	Z_{throat}	P_0 bar	T_0 K	$\frac{\dot{m}_{real}}{\dot{m}_{ideal}}$	Z_{throat}	P_0 bar	T_0 K	$\frac{\dot{m}_{real}}{\dot{m}_{ideal}}$	Z_{throat}
10	500	1.0008	1.0019	1	500	1.0016	0.9999	1	500	1.0056	0.9937
10	1000	1.0003	1.0019	1	1000	1.0004	1.0015	1	1000	1.0007	1.0016
10	2000	1.0006	1.0009	1	2000	1.0005	1.0009	1	2000	1.0006	1.0011
10	4000	1.0009	1.0004	1	4000	1.0007	1.0004	1	4000	1.0009	1.0003
30	500	1.0004	1.0058	3	500	1.0030	0.9997	3	500	1.0149	0.9808
30	1000	0.9989	1.0058	3	1000	0.9993	1.0045	3	1000	1.0000	1.0047
30	2000	0.9999	1.0028	3	2000	0.9998	1.0027	3	2000	0.9997	1.0033
30	4000	1.0006	1.0011	3	4000	1.0004	1.0012	3	4000	1.0006	1.0010
50	500	0.9999	1.0097	5	500	1.0044	0.9996	5	500	1.0245	0.9675
50	1000	0.9975	1.0096	5	1000	0.9983	1.0075	5	1000	0.9992	1.0078
50	2000	0.9991	1.0046	5	2000	0.9991	1.0044	5	2000	0.9988	1.0055
50	4000	1.0002	1.0018	5	4000	1.0000	1.0020	5	4000	1.0002	1.0016
100	500	0.9983	1.0197	10	500	1.0074	0.9995	10	500	1.0502	0.9327
100	1000	0.9940	1.0192	10	1000	0.9957	1.0149	10	1000	0.9973	1.0157
100	2000	0.9971	1.0093	10	2000	0.9972	1.0089	10	2000	0.9964	1.0109
100	4000	0.9994	1.0036	10	4000	0.9992	1.0039	10	4000	0.9993	1.0033
200	500	0.9944	1.0404	20	500	1.0119	1.0002	20	500	1.1067	0.8610
200	1000	0.9872	1.0384	20	1000	0.9905	1.0298	20	1000	0.9933	1.0315
200	2000	0.9933	1.0186	20	2000	0.9935	1.0177	20	2000	0.9919	1.0219
200	4000	0.9978	1.0072	20	4000	0.9974	1.0079	20	4000	0.9975	1.0066
500	500	0.9799	1.1078	50	500	1.0025	1.0343	50	500	1.1640	0.8007
500	1000	0.9675	1.0954	50	1000	0.9750	1.0746	50	1000	0.9801	1.0797
500	2000	0.9822	1.0465	50	2000	0.9829	1.0442	50	2000	0.9788	1.0546
500	4000	0.9930	1.0181	50	4000	0.9923	1.0198	50	4000	0.9922	1.0167

Table 2: Mass ratio of real-gas calculations over ideal-gas calculations. $\frac{\dot{m}}{\dot{m}_{ideal}}$ was found using a wide range of T_0 and P_0 as well as different species of gas: Air, Ar and N_2

Reviewing Table 2 it is evident that the specific heat ratio does not have as large an effect on the deviation of ideal-gas between each species.

4.2.11 Momentum Flux Results

Momentum flux was calculated by multiplying the dimensional density ρ_d by the dimensional u_d^2. It is then normalized by the momentum flux of ideal-gas to compare. Note, the tremendous increase of the momentum flux between each P_0 at each graph. By first looking at y axis in Figure 104 (corresponding to 10 bar), the normalized momentum flux is on the range of 0.995 to 1.025. This is essentially a deviation from ideal-gas values of $-.5\%$ to 2.5%. Now looking forward to Figure 109 (corresponding to 500 bar), the range of value of real-gas value and ideal-gas range from 1 to 1.5. Reviewing the graphs shows reasonable results considering that the point with maximum density corresponds to $M = 1$. It is interesting to note how quickly the momentum flux drops with increasing M. Referring to the M graphs in Section 4.2.9, it is clear that as P diminishes, M increases.

In Section 4.2.8, U was demonstrated to increase as P increased, meaning as U increases in value, so does M. Now, looking at Section 4.2.2 it is evident that an increase in P correlates to an increase in $\mathscr{R}$. Thus, there is an inverse relationship between M and $\mathscr{R}$, as well as ρ_d. So, as M increases in value, U increases, but ρ decreases at such a rate that it counter acts the increase of U making $\rho_d u_d^2$ decrease at a quick rate.

In Figures 106 to Figure 109, it demonstrates that there is a higher momentum flux value for the real-gas case than there is for the ideal-gas case. In Figures 104 and Figure 105, the figures corresponding to lower pressures have some of the real-gas momentum flux values below that of the ideal-gas. Ultimately, most values are still above ideal-gas solutions. Similar to other properties, the difference in value of the real-gas calculation compared to the ideal-gas is seen more at higher pressure. However, increasing the temperature, especially for $T_0 = 4000$ K, the real-gas-solution is more in agreement with the ideal-gas solution. With that in mind, the two lines for low P and constant $T_0 = 4000$ K are indistinguishable, (Figures 104 and 105).

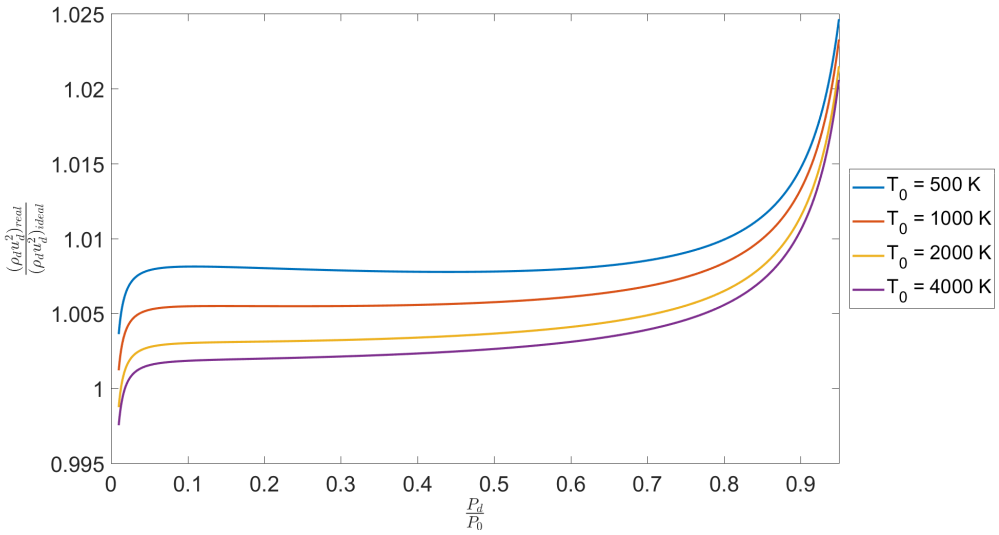

Figure 104: Comparison of normalized momentum flux, $\frac{(\rho_d u_d^2)_{real}}{(\rho_d u_d^2)_{ideal}}$, versus $\frac{P_d}{P_0}$ for Air with fixed $P_0 = 10$ bar, while varying T_0, where $T_0 = 500$ K, 1000 K, 2000 K, 4000 K.

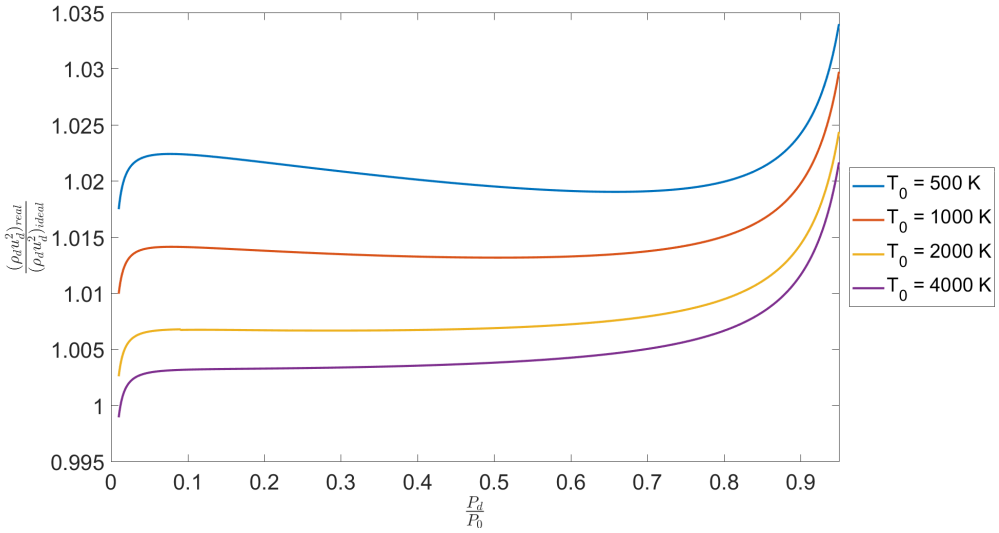

Figure 105: Comparison of normalized momentum flux, $\frac{(\rho_d u_d^2)_{real}}{(\rho_d u_d^2)_{ideal}}$, versus $\frac{P_d}{P_0}$ for Air with fixed $P_0 = 30$ bar, while varying T_0, where $T_0 = 500$ K, 1000 K, 2000 K, 4000 K.

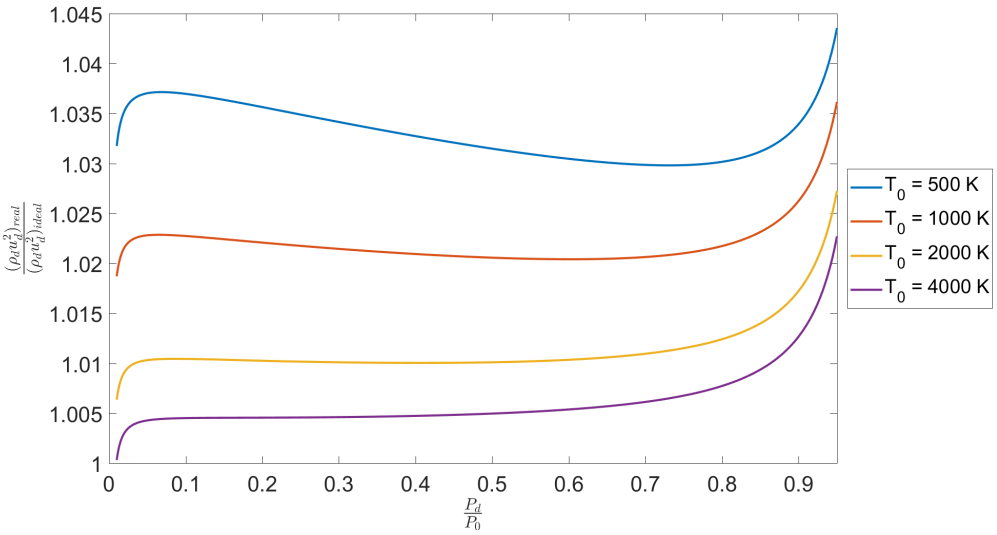

Figure 106: Comparison of normalized momentum flux, $\frac{(\rho_d u_d^2)_{real}}{(\rho_d u_d^2)_{ideal}}$, versus $\frac{P_d}{P_0}$ for Air with fixed $P_0 = 50$ bar, while varying T_0, where $T_0 = 500$ K, 1000 K, 2000 K, 4000 K.

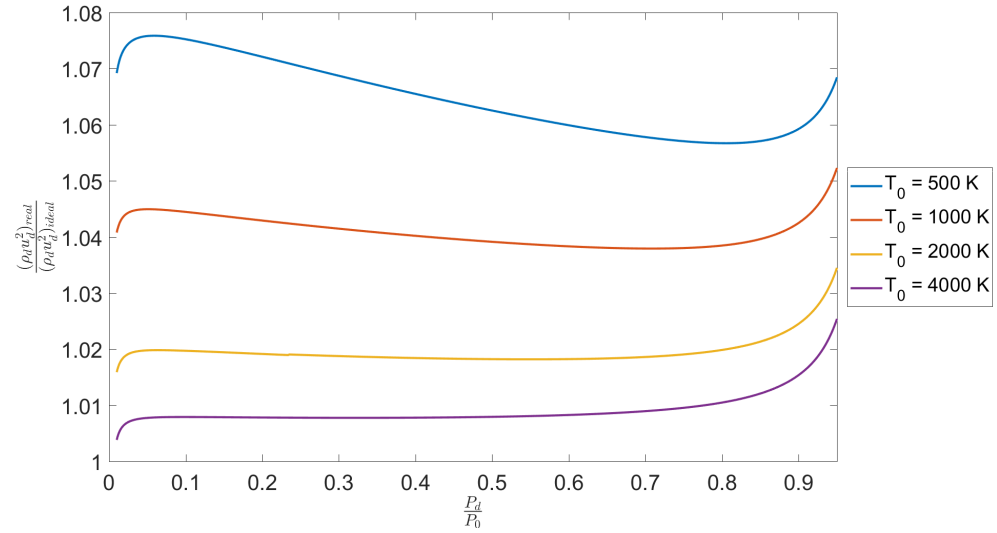

Figure 107: Comparison of normalized momentum flux, $\frac{(\rho_d u_d^2)_{real}}{(\rho_d u_d^2)_{ideal}}$, versus $\frac{P_d}{P_0}$ for Air with fixed $P_0 = 100$ bar, while varying T_0, where $T_0 = 500$ K, 1000 K, 2000 K, 4000 K.

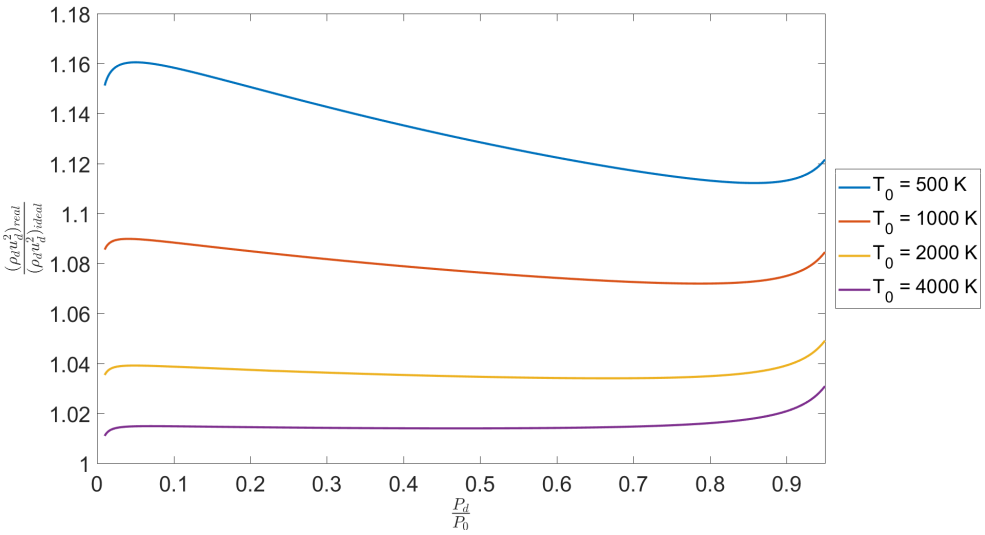

Figure 108: Comparison of normalized momentum flux, $\frac{(\rho_d u_d^2)_{real}}{(\rho_d u_d^2)_{ideal}}$, versus $\frac{P_d}{P_0}$ for Air with fixed $P_0 = 200$ bar, while varying T_0, where $T_0 = 500$ K, 1000 K, 2000 K, 4000 K.

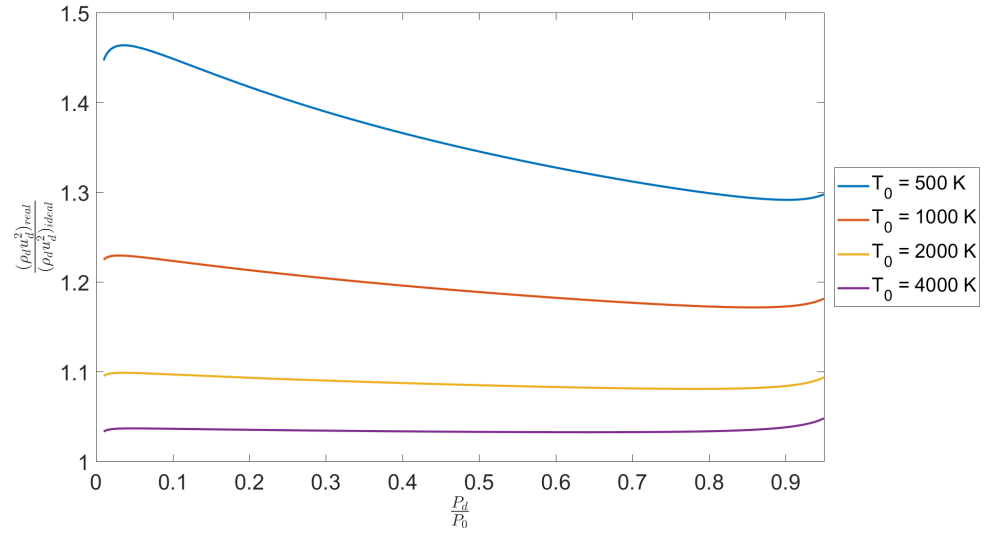

Figure 109: Comparison of normalized momentum flux, $\frac{(\rho_d u_d^2)_{real}}{(\rho_d u_d^2)_{ideal}}$, versus $\frac{P_d}{P_0}$ for Air with fixed $P_0 = 500$ bar, while varying T_0, where $T_0 = 500$ K, 1000 K, 2000 K, 4000 K.

4.3 Normal Shock

This section are the results of the normal shock solutions as described in Section 3. Sections 4.3.1 to 4.3.4 utilize method 1 of the normal shock solutions. Recall that this does not require the knowledge of upstream velocity and can only really be used to measure the behavior of real-gas undergoing normal shocks of varying strength. Section 4.3.5 utilizes method 2 by showing shocks at specific location in the divergent part of a nozzle.

4.3.1 Pressure Ratio, $\frac{P_2}{P_1}$ vs. Density Ratio, $\frac{\rho_2}{\rho_1}$

The following section graphs the pressure ratio versus the density ratio, demonstrating the effects of temperature and pressure on density. With respect to the density ratio, while increasing shock, at a certain point, increasing the shock strength will not change the density ratio. At a certain density ratio the curve becomes asymptotic and will not go past that value. In the case of air using ideal-gas, the density ratio will not go past a value of 6. However, this asymptotic value is dramatically changed with the influence of both pressure and density.

For the case of temperature, higher temperatures lead to a closer agreement with the ideal-gas solution. Contrarily, increasing the pressure will further increase the discrepancy of real-gas and ideal-gas. In the case of Figure 115, the density ratio does not even reach 2.5 for the 500 K curve. Comparing this to the ideal-gas value of 6, it is more than a 240% difference.

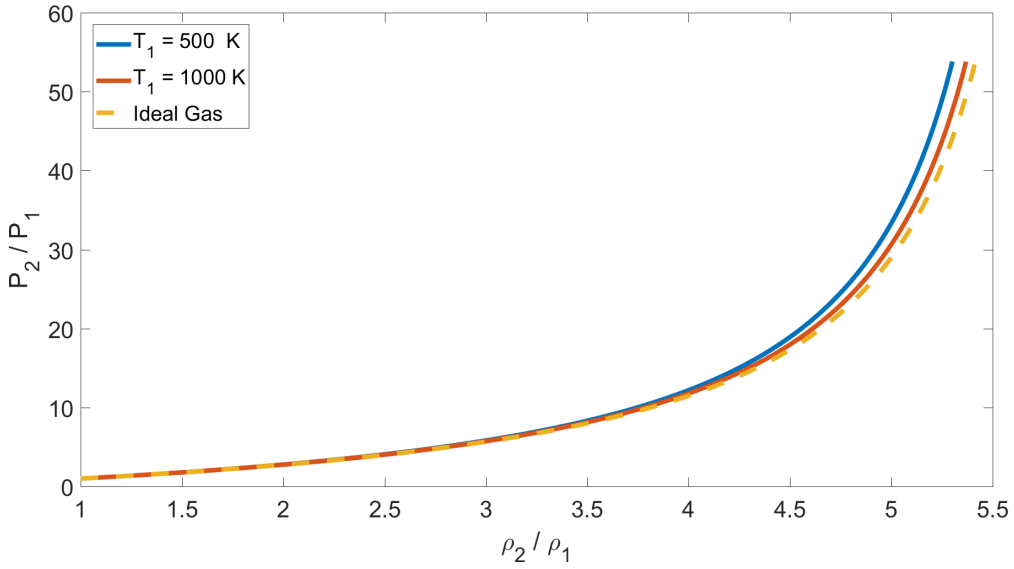

Figure 110: Comparison of properties across a normal shock, $\frac{P_2}{P_1}$ versus $\frac{\rho_2}{\rho_1}$ for Air with fixed $P_1 = 10$ bar, for $T_1 = 500$ K, 1000 K.

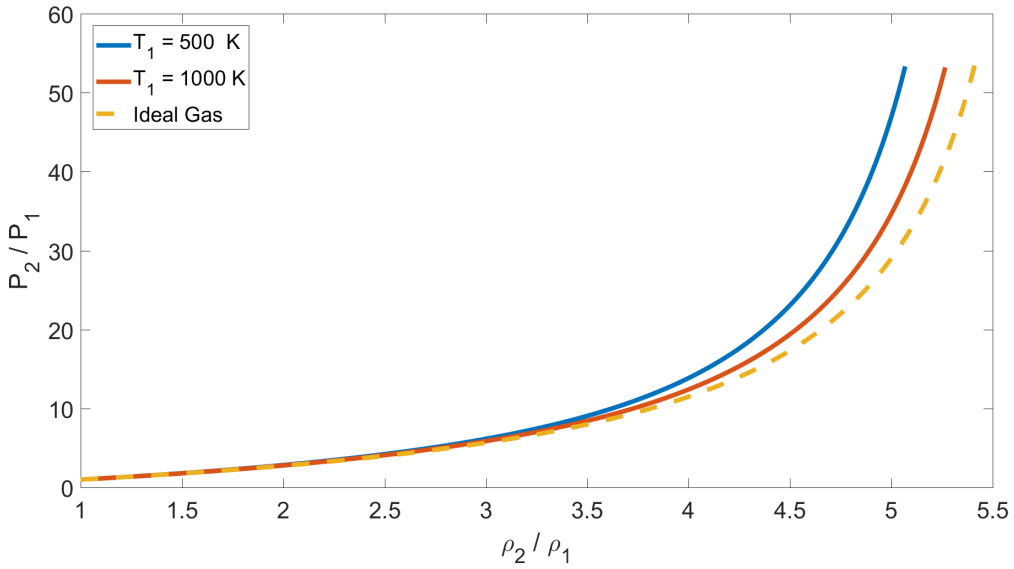

Figure 111: Comparison of properties across a normal shock, $\frac{P_2}{P_1}$ versus $\frac{\rho_2}{\rho_1}$ for Air with fixed $P_1 = 30$ bar, for $T_1 = 500$ K, 1000 K.

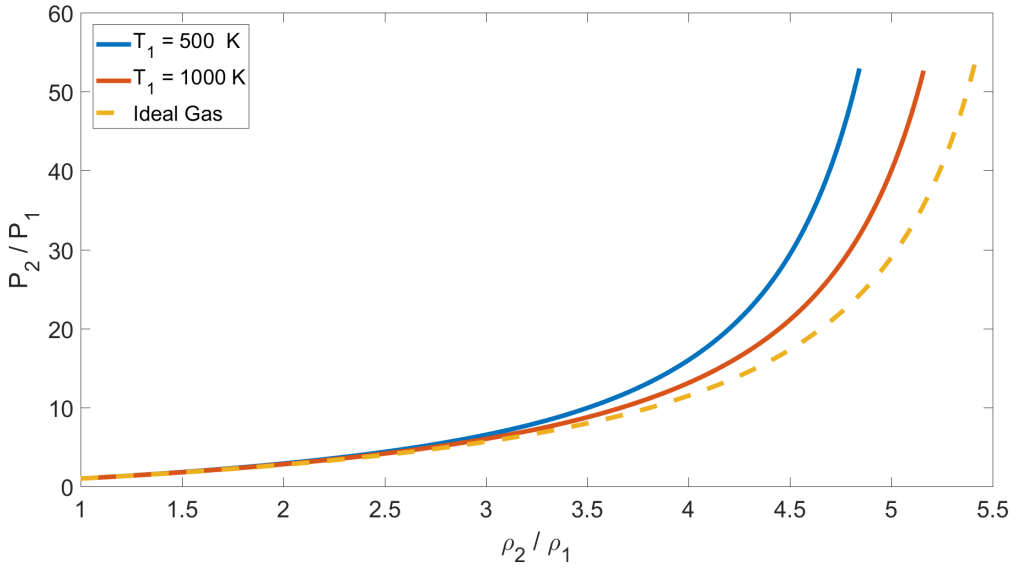

Figure 112: Comparison of properties across a normal shock, $\frac{P_2}{P_1}$ versus $\frac{\rho_2}{\rho_1}$ for Air with fixed $P_1 = 50$ bar, for $T_1 = 500$ K, 1000 K.

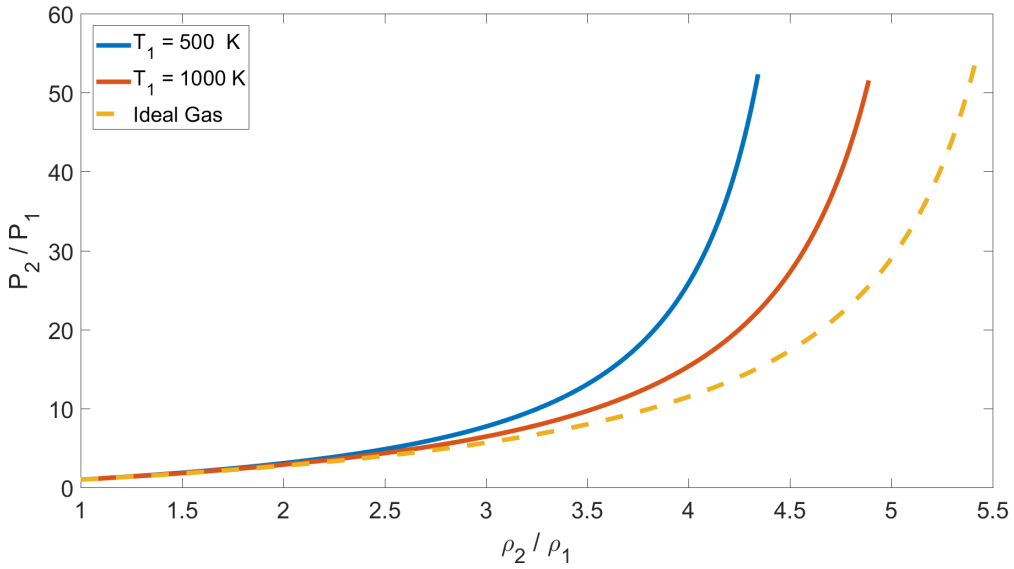

Figure 113: Comparison of properties across a normal shock, $\frac{P_2}{P_1}$ versus $\frac{\rho_2}{\rho_1}$ for Air with fixed $P_1 = 100$ bar, for $T_1 = 500$ K, 1000 K.

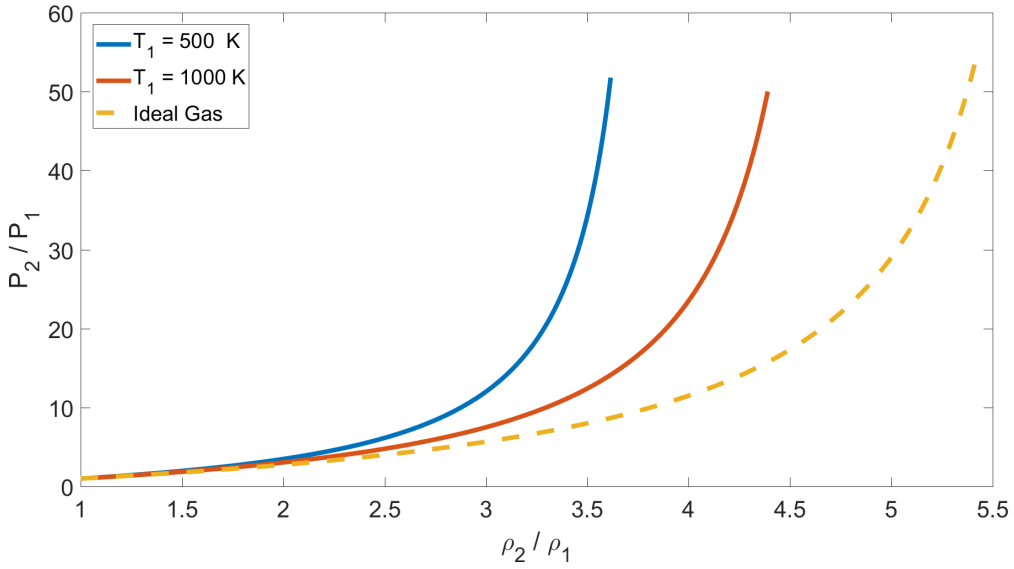

Figure 114: Comparison of properties across a normal shock, $\frac{P_2}{P_1}$ versus $\frac{\rho_2}{\rho_1}$ for Air with fixed $P_1 = 200$ bar, for $T_1 = 500$ K, 1000 K.

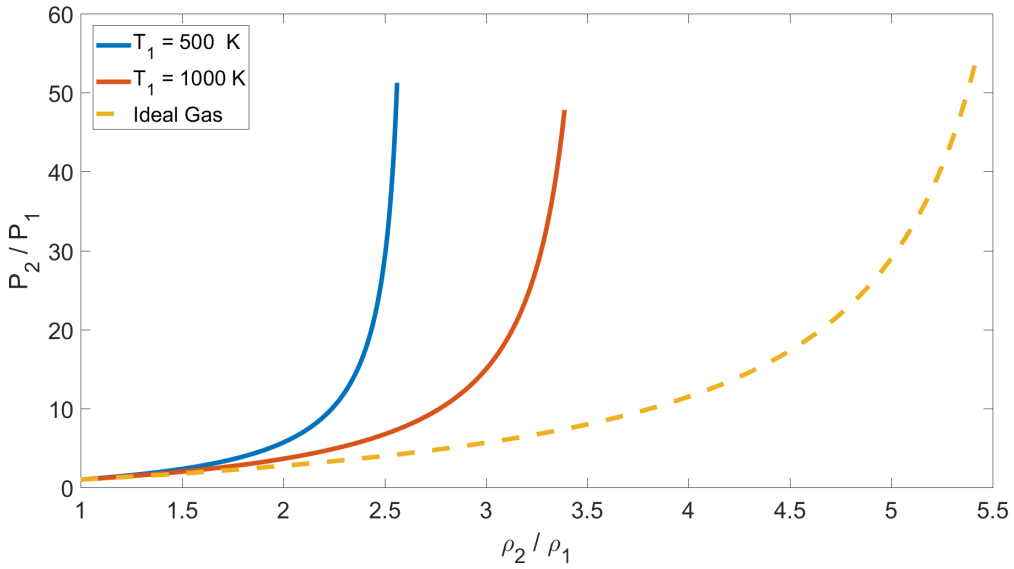

Figure 115: Comparison of properties across a normal shock, $\frac{P_2}{P_1}$ versus $\frac{\rho_2}{\rho_1}$ for Air with fixed $P_1 = 500$ bar, for $T_1 = 500$ K, 1000 K.

4.3.2 Temperature Ratio $\frac{T_2}{T_1}$ vs. Density Ratio, $\frac{\rho_2}{\rho_1}$

The temperature ratio versus density ratio curves are very similar to the curves shown in Section 4.3.1. Both the effects of temperature and pressure affect the real-gas solution in the same manner as the pressure ratio versus density ratio. Without the labels on the graphs, the only apparent difference between the sets of graphs is the axis values for the temperature ratio and pressure ratio. For the values of the temperature ratio are only about one sixth of the value for the pressure ratio.

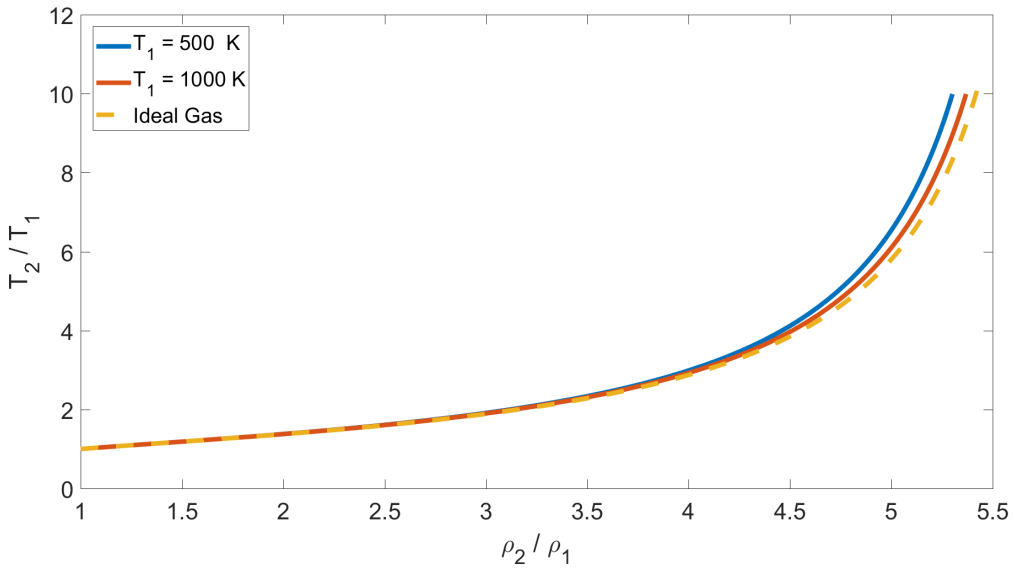

Figure 116: Comparison of properties across a normal shock, $\frac{T_2}{T_1}$ versus $\frac{\rho_2}{\rho_1}$ for Air with fixed $P_1 = 10$ bar, for $T_1 = 500$ K, 1000 K.

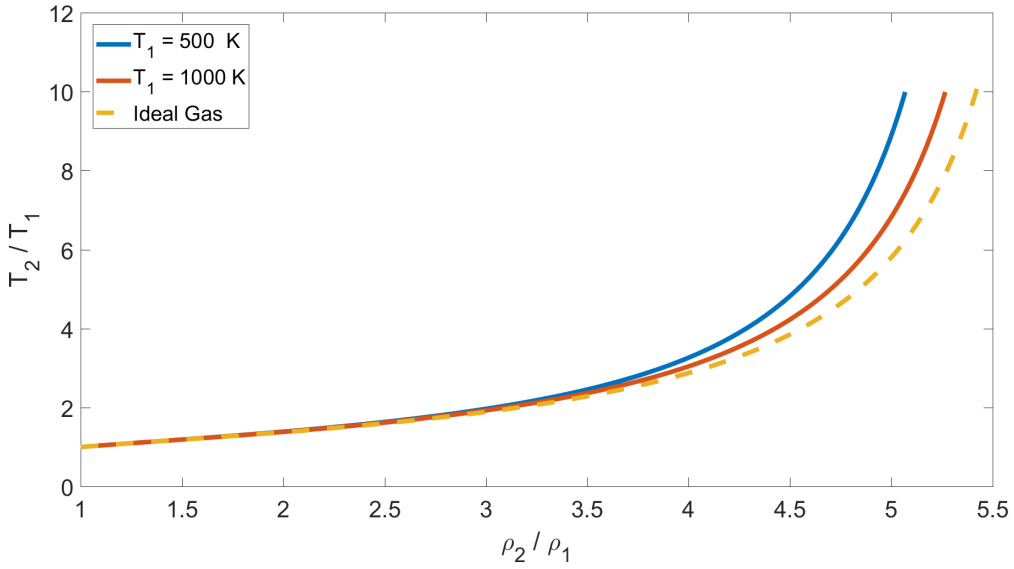

Figure 117: Comparison of properties across a normal shock, $\frac{T_2}{T_1}$ versus $\frac{\rho_2}{\rho_1}$ for Air with fixed $P_1 = 30$ bar, for $T_1 = 500$ K, 1000 K.

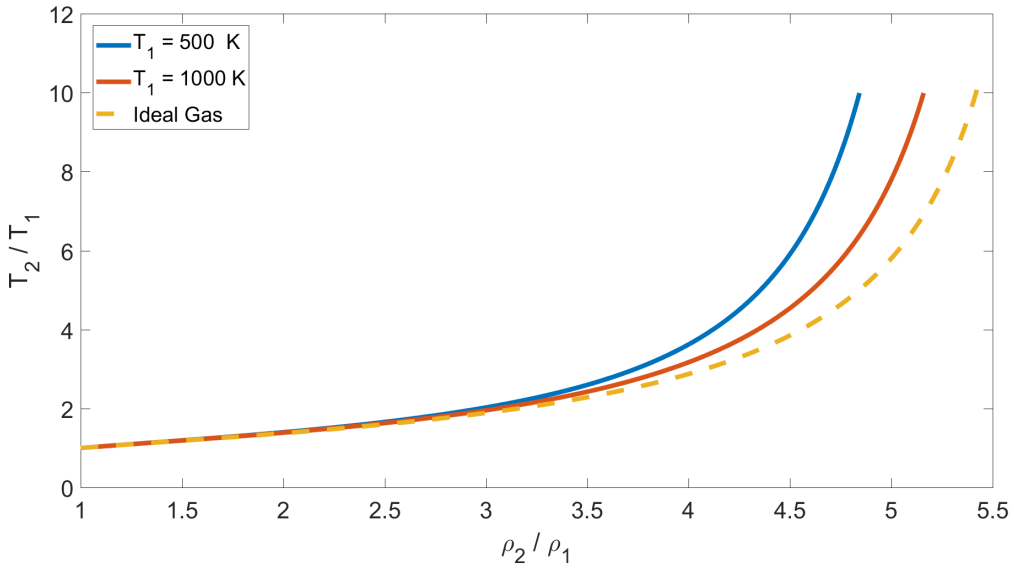

Figure 118: Comparison of properties across a normal shock, $\frac{T_2}{T_1}$ versus $\frac{\rho_2}{\rho_1}$ for Air with fixed $P_1 = 50$ bar, for $T_1 = 500$ K, 1000 K.

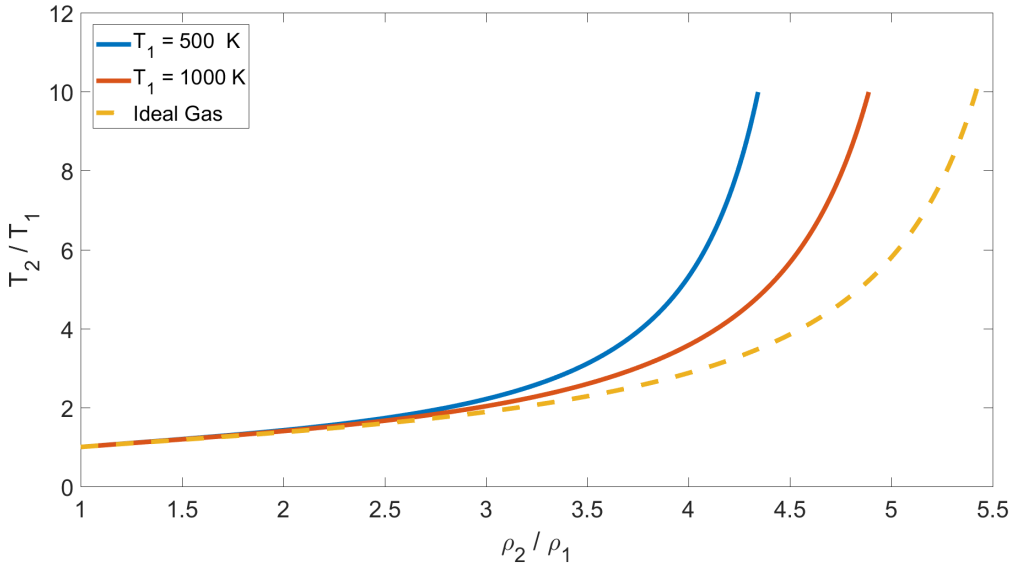

Figure 119: Comparison of properties across a normal shock, $\frac{T_2}{T_1}$ versus $\frac{\rho_2}{\rho_1}$ for Air with fixed $P_1 = 100$ bar, for $T_1 = 500$ K, 1000 K.

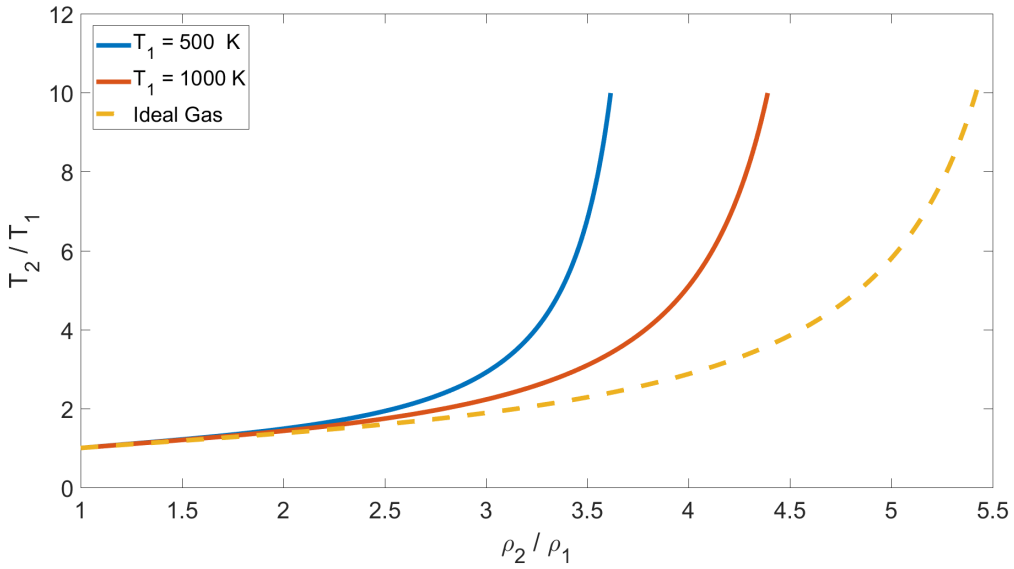

Figure 120: Comparison of properties across a normal shock, $\frac{T_2}{T_1}$ versus $\frac{\rho_2}{\rho_1}$ for Air with fixed $P_1 = 200$ bar, for $T_1 = 500$ K, 1000 K.

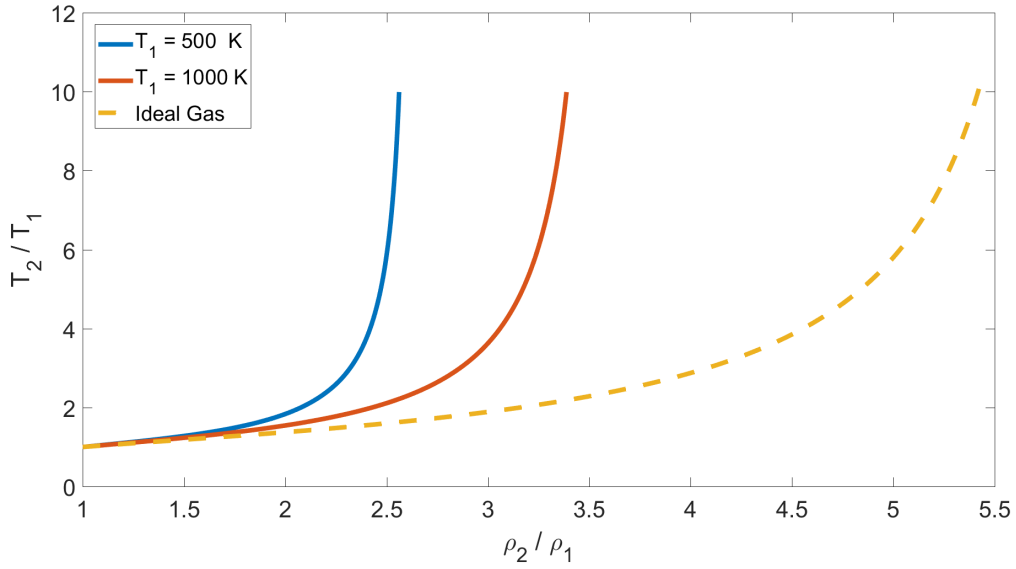

Figure 121: Comparison of properties across a normal shock, $\frac{T_2}{T_1}$ versus $\frac{\rho_2}{\rho_1}$ for Air with fixed $P_1 = 500$ bar, for $T_1 = 500$ K, 1000 K.

4.3.3 Temperature Ratio $\frac{T_2}{T_1}$ vs. Pressure Ratio, $\frac{P_2}{P_1}$

Initially the graphs in this section seem to be misleading. Thus far, in this thesis study, the higher the temperature, the closer to ideal-gas the real-gas properties become, (with only a few exceptions). However, this graph in this scale shows a different trend. by zooming into the lower pressure ratio region, (lower M_1 values) of Figure 126 shows that this trend holds. The higher temperature curve is closer to the ideal-gas solution than the lower temperature curve. However, Figure 127 has a limited pressure ratio range to show this trend.

When the range is expanded to see across a larger range of pressure ratios, not only do the 500 K curve and the 1000 K curve move to the other side of the ideal-gas curve, but the lower temperature is closer than the higher temperature. Thus, the effects of temperature and pressure have different affects on the curve depending on how strong the shock is. For stronger shocks, the discrepancy between ideal-gas and real-gas is increased by higher pressure and higher temperature. Meanwhile, for weaker strength shocks, higher pressure and lower temperatures show larger variations than ideal-gas.

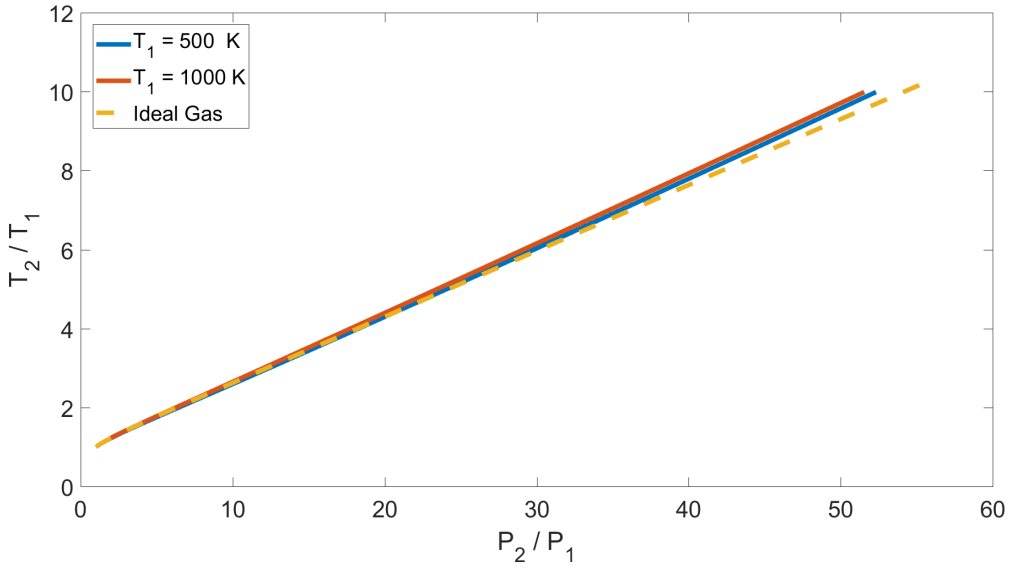

Figure 122: Comparison of properties across a normal shock, $\frac{T_2}{T_1}$ versus $\frac{P_2}{P_1}$ for Air with fixed $P_1 = 10$ bar, for $T_1 = 500$ K, 1000 K.

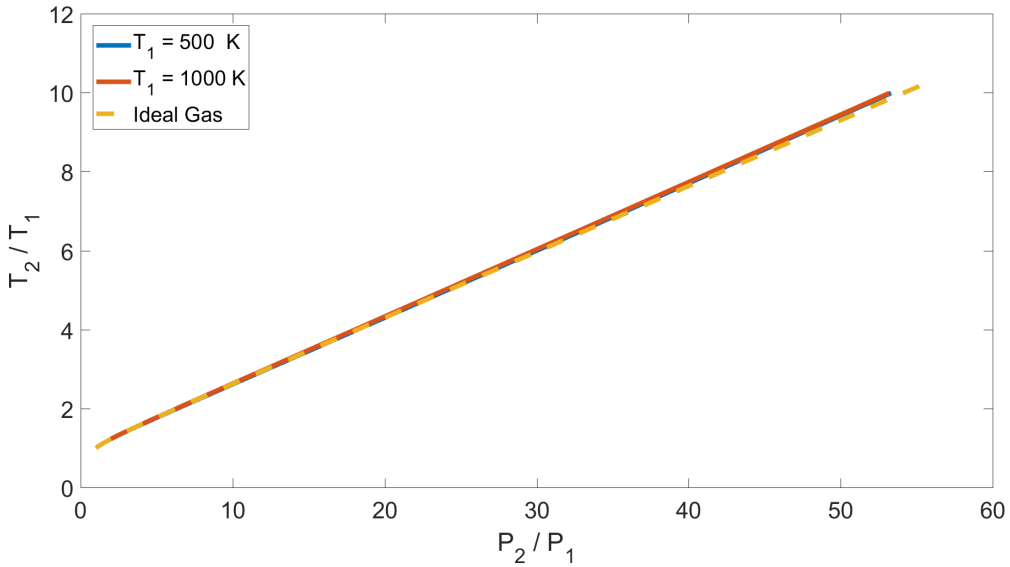

Figure 123: Comparison of properties across a normal shock, $\frac{T_2}{T_1}$ versus $\frac{P_2}{P_1}$ for Air with fixed $P_1 = 30$ bar, for $T_1 = 500$ K, 1000 K.

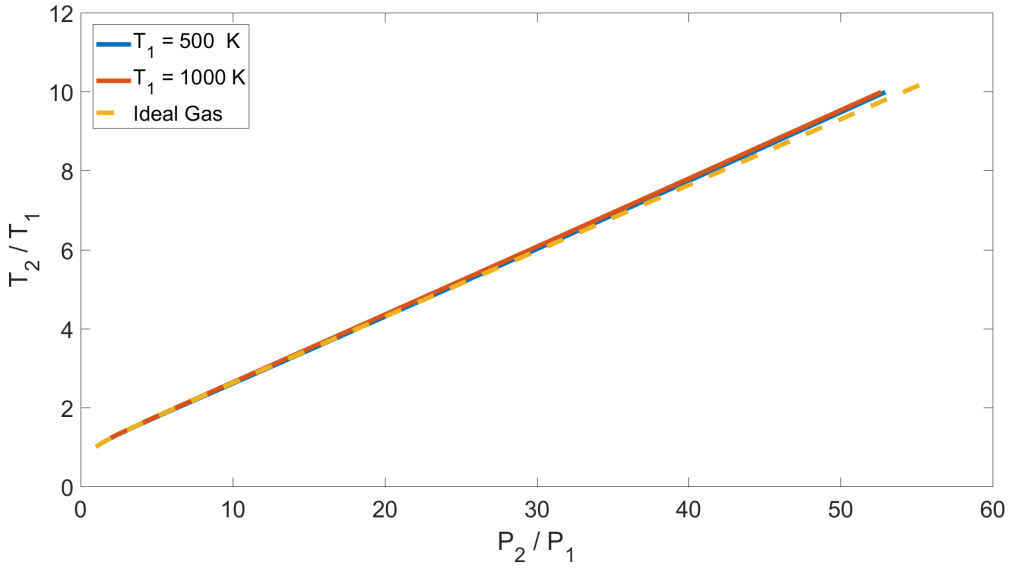

Figure 124: Comparison of properties across a normal shock, $\frac{T_2}{T_1}$ versus $\frac{P_2}{P_1}$ for Air with fixed $P_1 = 50$ bar, for $T_1 = 500$ K, 1000 K.

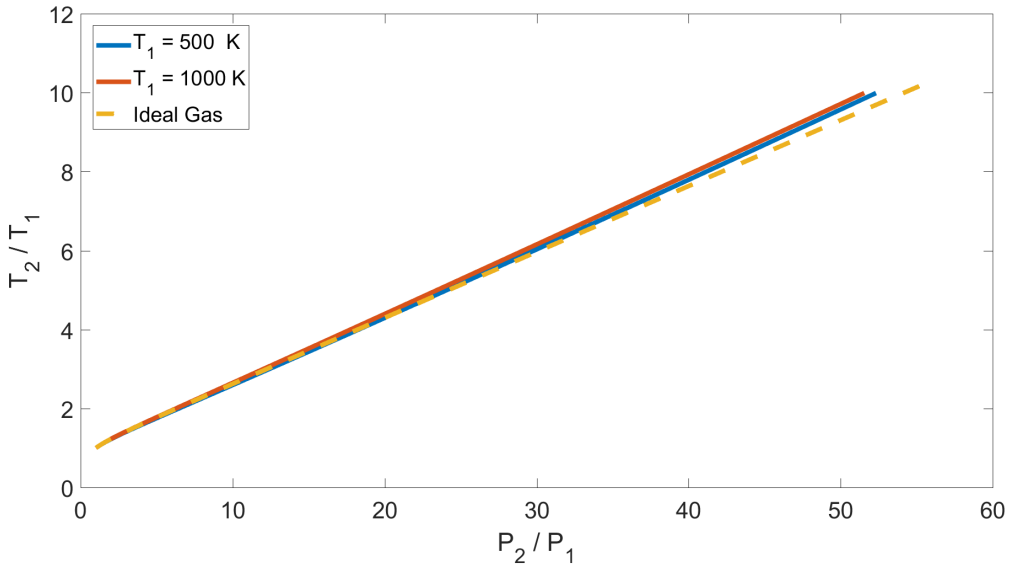

Figure 125: Comparison of properties across a normal shock, $\frac{T_2}{T_1}$ versus $\frac{P_2}{P_1}$ for Air with fixed $P_1 = 100$ bar, for $T_1 = 500$ K, 1000 K.

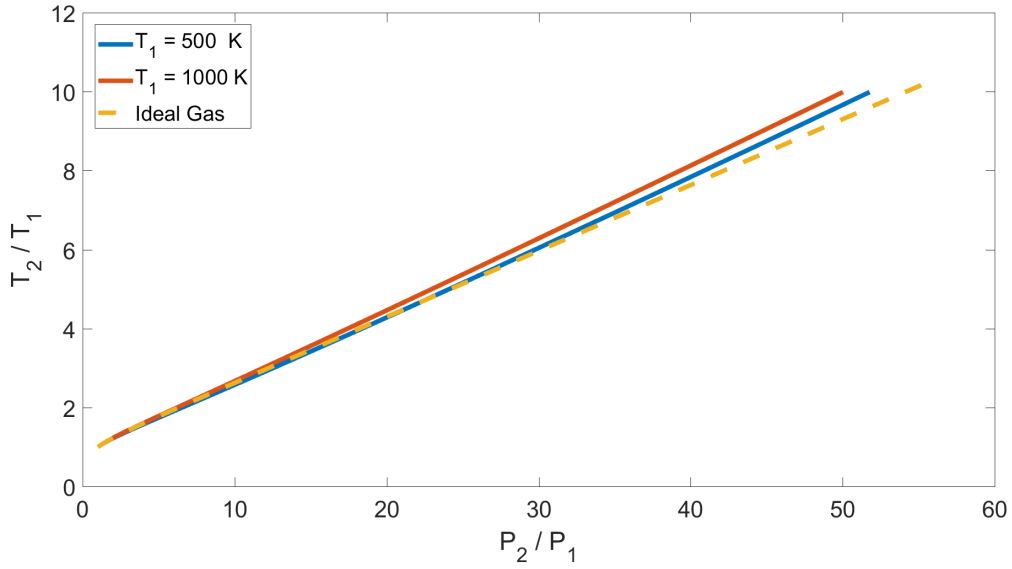

Figure 126: Comparison of properties across a normal shock, $\frac{T_2}{T_1}$ versus $\frac{P_2}{P_1}$ for Air with fixed $P_1 = 200$ bar, for $T_1 = 500$ K, 1000 K.

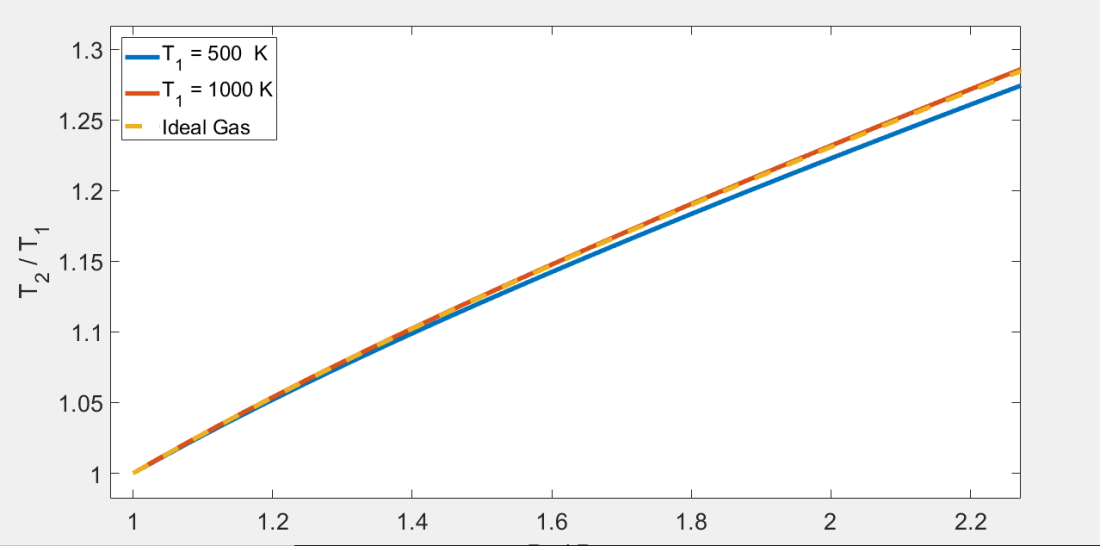

Figure 127: Comparison of properties across a normal shock, $\frac{T_2}{T_1}$ versus $\frac{P_2}{P_1}$ for Air with fixed $P_1 = 200$ bar, for $T_1 = 500$ K, 1000 K. This is the same graphs as Figure 126, but zoomed in to demonstrate the trends of real-gas on a smaller scale.

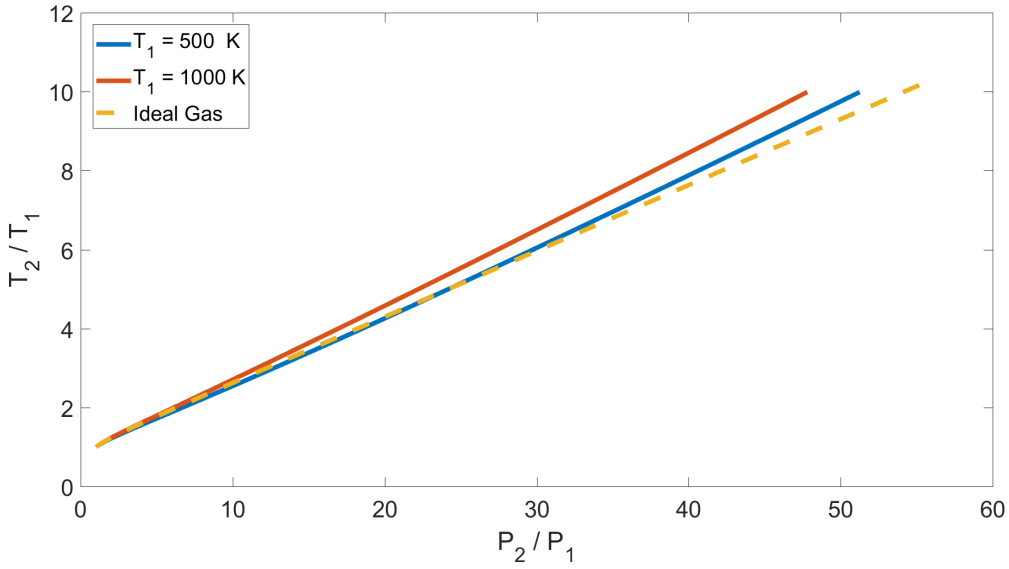

Figure 128: Comparison of properties across a normal shock, $\frac{T_2}{T_1}$ versus $\frac{P_2}{P_1}$ for Air with fixed $P_1 = 500$ bar, for $T_1 = 500$ K, 1000 K.

4.3.4 Comparison of Air, N_2, O_2

Air, N_2, and O_2 are all different species/ compounds but have the same specific heat ratio and thus give an interesting perspective on the effects of species on normal shock calculations. For normal shock calculations, the only term that distinguishes the make up of a gas in ideal-gas calculations is the specific heat ratio. Thus, according to these set of equations; Air, N_2, and O_2 should all have the same curve. In Figures 129 to 134, it compares the effect that different species have on real-gas solutions.

Air and N_2 are always the closest in solution than that of Air and O_2. This is most likely because N_2 makes up 80% of Air while the other 20% is O_2. For any given pressure and temperature, N_2 is the furthest from ideal-gas solution, followed by Air. Thus, O_2 is the closest to ideal-gas. Both O_2 and N_2 exhibit the same effects of varying temperature and pressure as Air does.

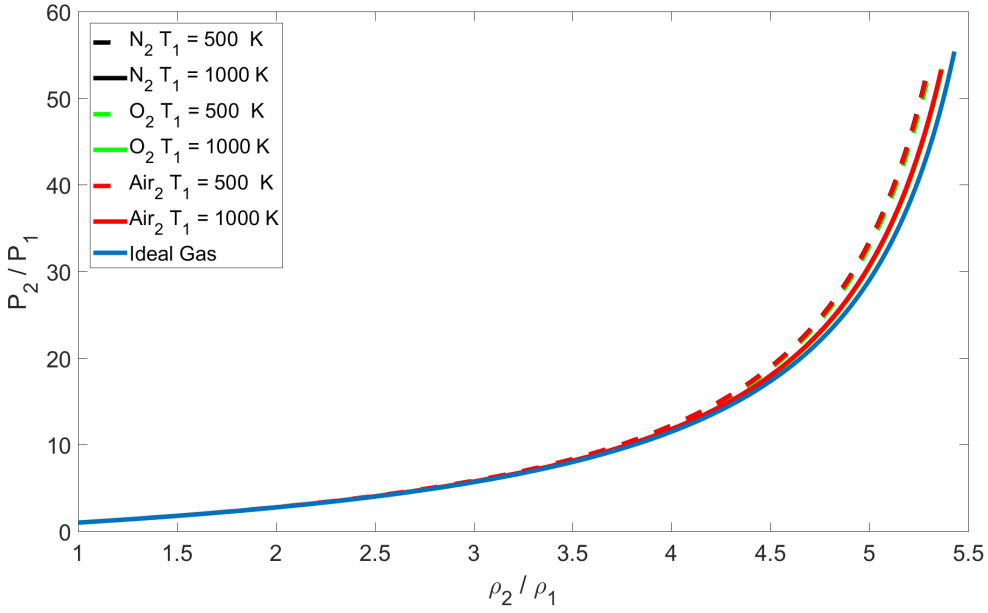

Figure 129: Comparison of properties across a normal shock, $\frac{P_2}{P_1}$ versus $\frac{\rho_2}{\rho_1}$ for Air with fixed $P_1 = 10$ bar, for $T_1 = 500$ K, 1000 K. This graph also compares the effects of the species on normal shock solutions, with N_2,O_2 and Air being compared.

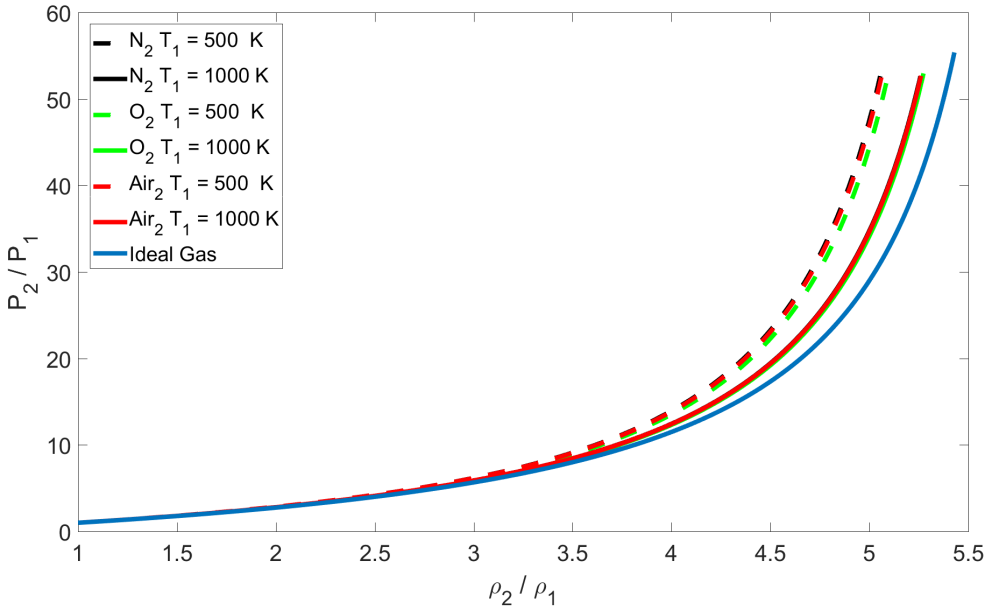

Figure 130: Comparison of properties across a normal shock, $\frac{P_2}{P_1}$ versus $\frac{\rho_2}{\rho_1}$ for Air with fixed $P_1 = 30$ bar, for $T_1 = 500$ K, 1000 K. This graph also compares the effects of the species on normal shock solutions, with N_2,O_2 and Air being compared.

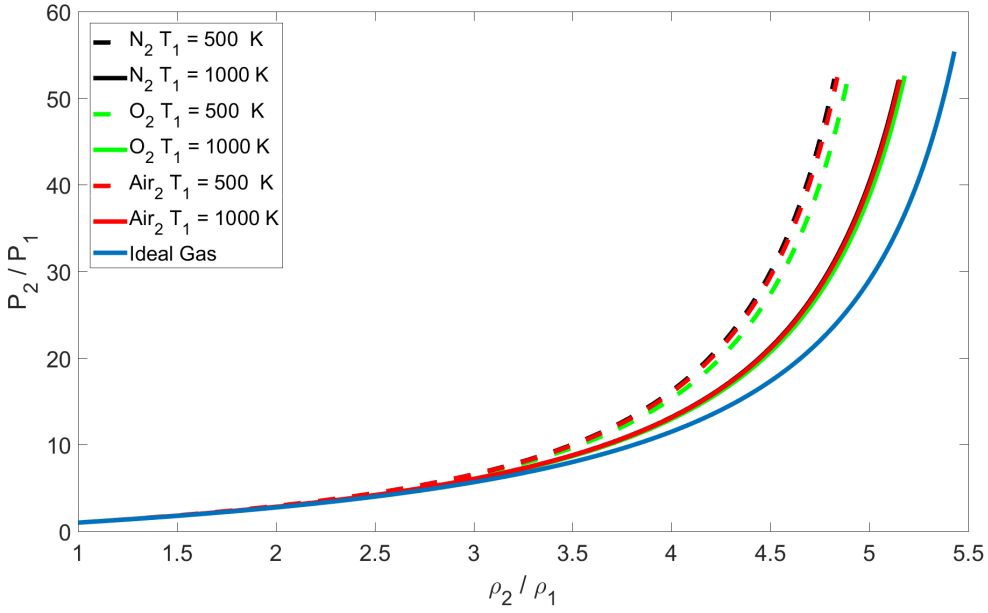

Figure 131: Comparison of properties across a normal shock, $\frac{P_2}{P_1}$ versus $\frac{\rho_2}{\rho_1}$ for Air with fixed $P_1 = 50$ bar, for $T_1 = 500$ K, 1000 K. This graph also compares the effects of the species on normal shock solutions, with N_2,O_2 and Air being compared.

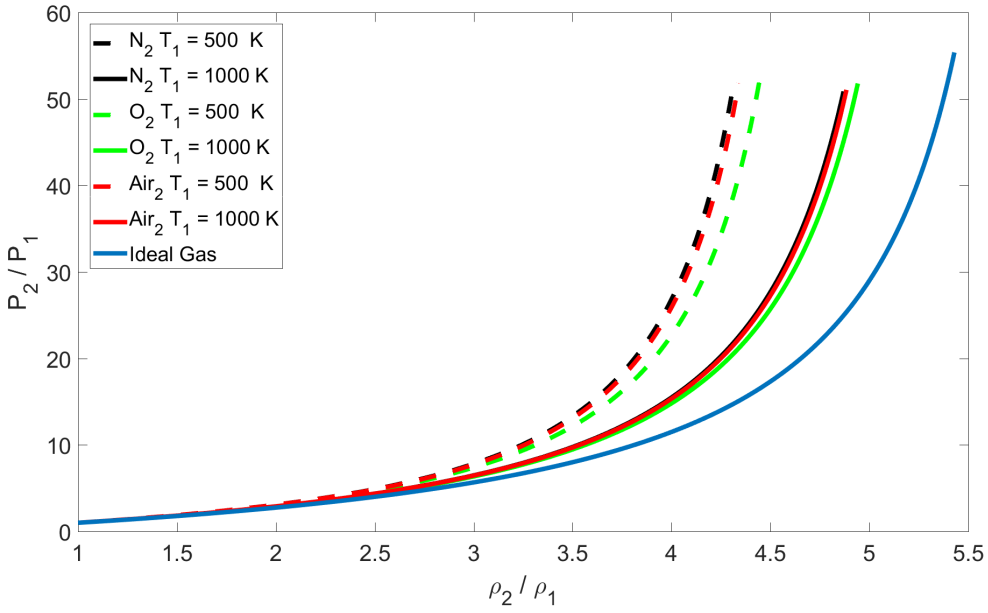

Figure 132: Comparison of properties across a normal shock, $\frac{P_2}{P_1}$ versus $\frac{\rho_2}{\rho_1}$ for Air with fixed $P_1 = 100$ bar, for $T_1 = 500$ K, 1000 K. This graph also compares the effects of the species on normal shock solutions, with N_2,O_2 and Air being compared.

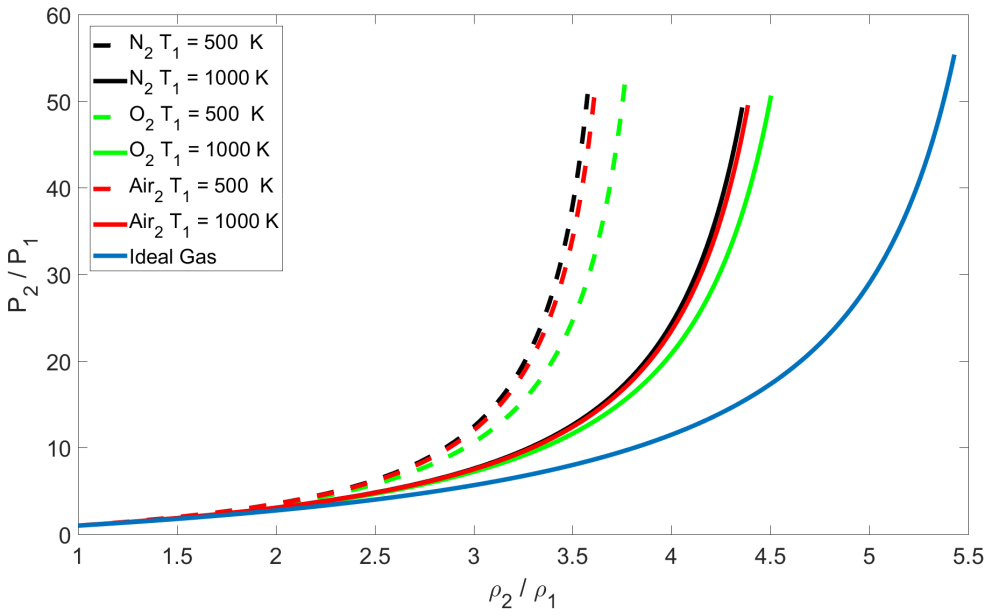

Figure 133: Comparison of properties across a normal shock, $\frac{P_2}{P_1}$ versus $\frac{\rho_2}{\rho_1}$ for Air with fixed $P_1 = 200$ bar, for $T_1 = 500$ K, 1000 K. This graph also compares the effects of the species on normal shock solutions, with N_2,O_2 and Air being compared.

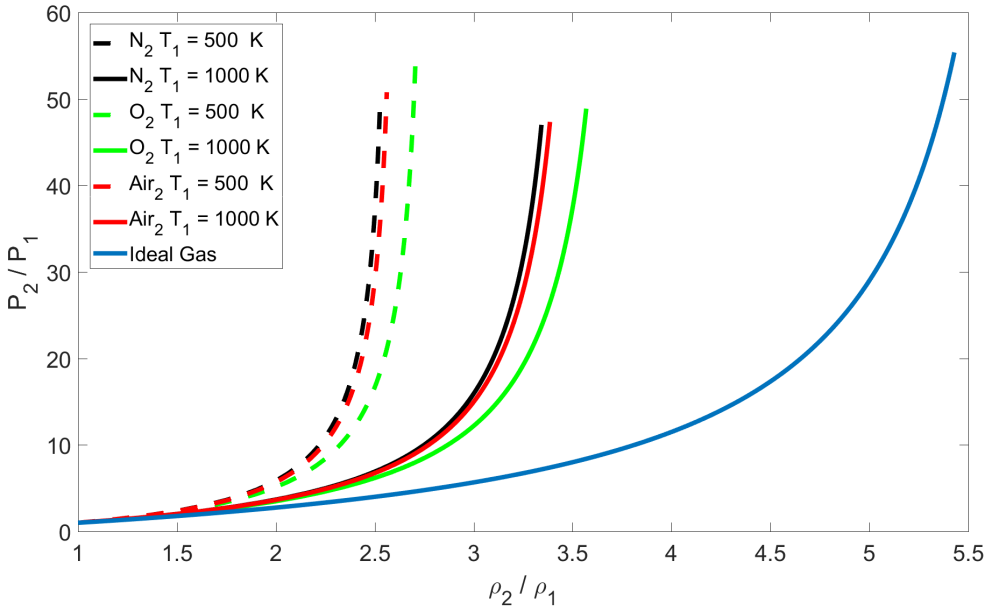

Figure 134: Comparison of properties across a normal shock, $\frac{P_2}{P_1}$ versus $\frac{\rho_2}{\rho_1}$ for Air with fixed $P_1 = 500$ bar, for $T_1 = 500$ K, 1000 K. This graph also compares the effects of the species on normal shock solutions, with N_2,O_2 and Air being compared.

4.3.5 Pressure and Area Ratio Results

In Figures 135 to 140, are graphs of the divergent portion of convergent/ divergent nozzle with normal shocks at specific points in the nozzle. Each graph has a specific stagnation pressure with varying stagnation temperatures. Each color refers to either 500 K, 1000 K or ideal-gas. The dashed lines mark the subsonic expansion of the flow, while the solid lines demonstrate the supersonic expansion, shock and then subsonic expansion. The curves plotted in comparison to ideal-gas seem very close to the solution of the real-gas for varying both stagnation pressure and temperature. There are two reason for this.

The first is that the upstream Mach numbers for the shock in the graphs are relatively low compared to those covered in earlier sections discussing the normal shock. Referring back to Section 4.2.3, discussing area ratio versus pressure, the area ratio does has a very small change with regards to a change in pressure throughout most of the nozzle. It is not until nominal pressure, P, moves from a lower number to 1 that area ratio makes a dramatic change. It is not until the area ratio starts to change a large amount, that the velocity of the flow increases and the sound speed decreases dramatically, to the point that larger variations in the value between ideal-gas and real-gas can be seen. Thus, at the expansion ratio limits, the speed and Mach number of the flow increase and thus the strength of the shock. The flow in Figure 141 is allowed to expand to a much larger area ratio to demonstrate the increased Mach number before the normal shock. However, the issue is seen as in the graphs with a smaller area ratio.

The second reason for their similarity is the view of the graph. The graph is plotted over a large range of pressures, so the scale of the graphs hides the discrepancies between real-gas and ideal-gas values. For these reasons, it is challenging to determine that for the case in Figure 140, the curve corresponding to 500 K at an area ratio, α, of 7.5, the error between real-gas and ideal-gas is 19.08%. For clarity on the supersonic and subsonic expansion of the real-gas through a nozzle, refer to Section 4.2.3.

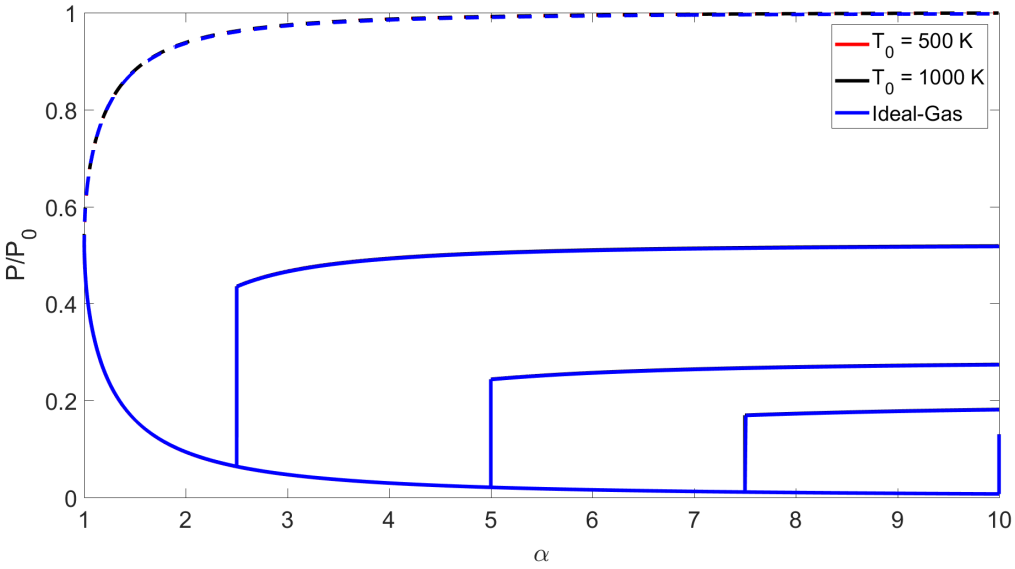

Figure 135: $\frac{P}{P_0}$ versus α at P_0= 10 bar

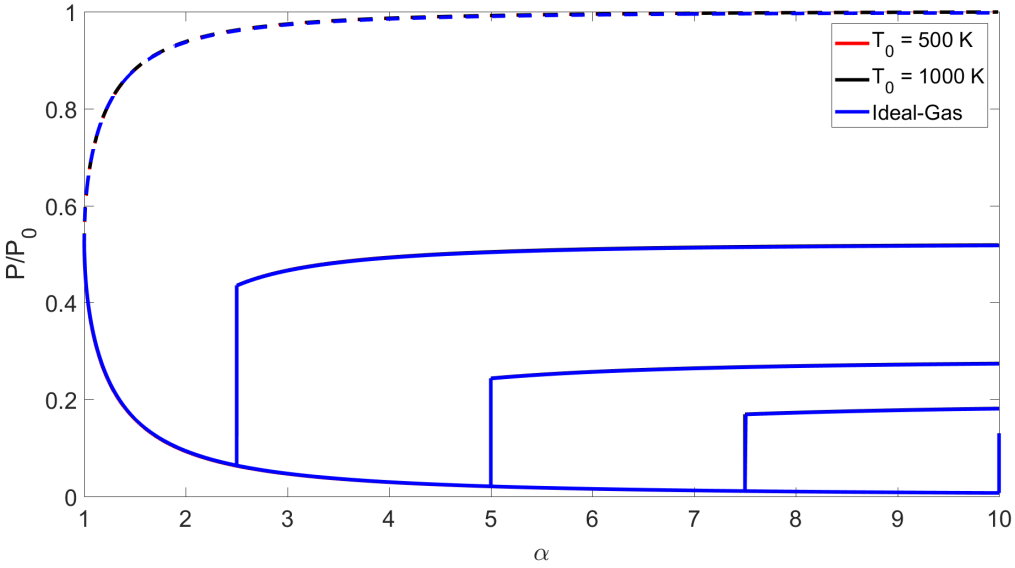

Figure 136: $\frac{P}{P_0}$ versus α at P_0= 30 bar

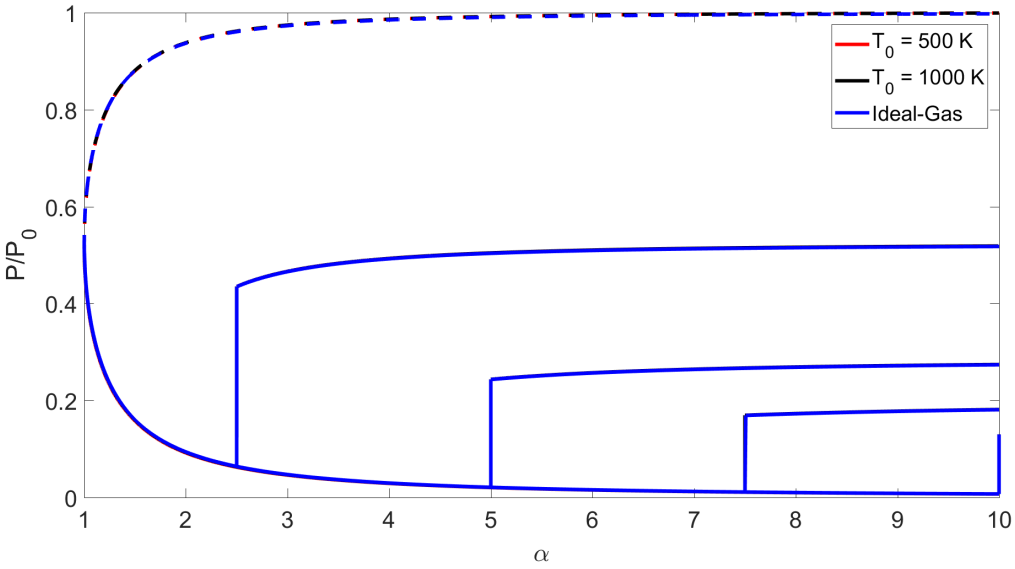

Figure 137: $\frac{P}{P_0}$ versus α at P_0= 50 bar

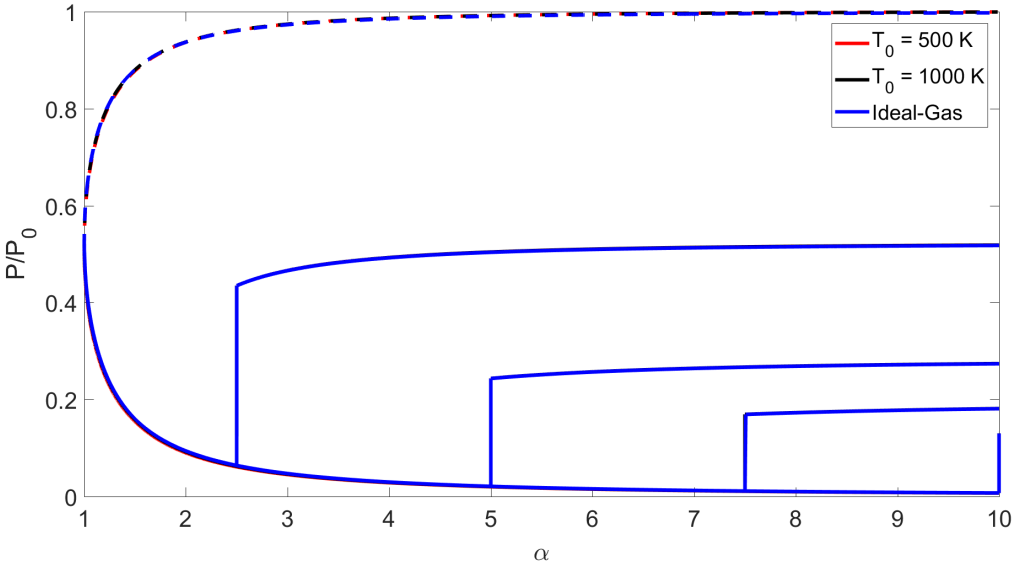

Figure 138: $\frac{P}{P_0}$ versus α at P_0= 100 bar

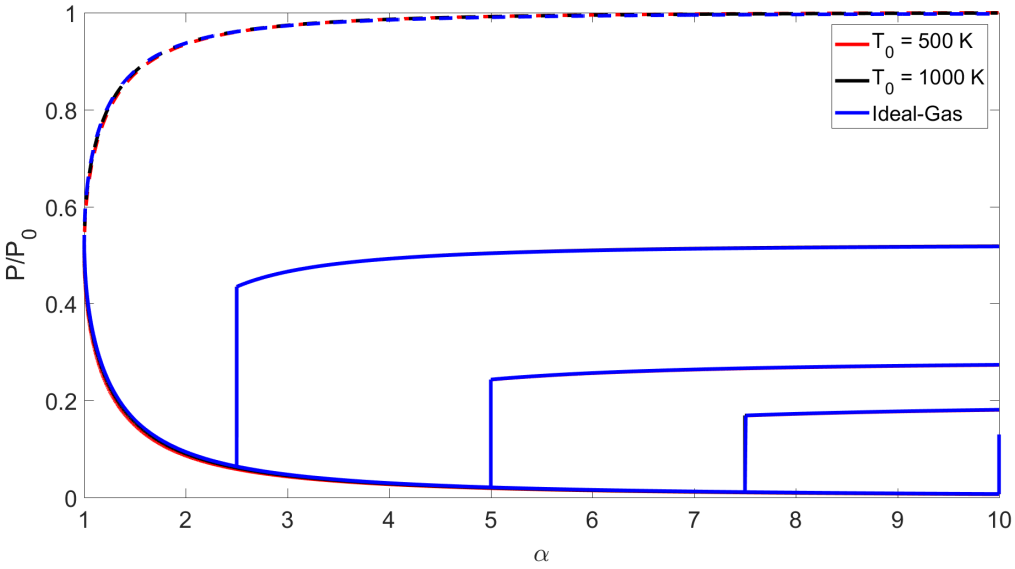

Figure 139: $\frac{P}{P_0}$ versus α at P_0= 200 bar

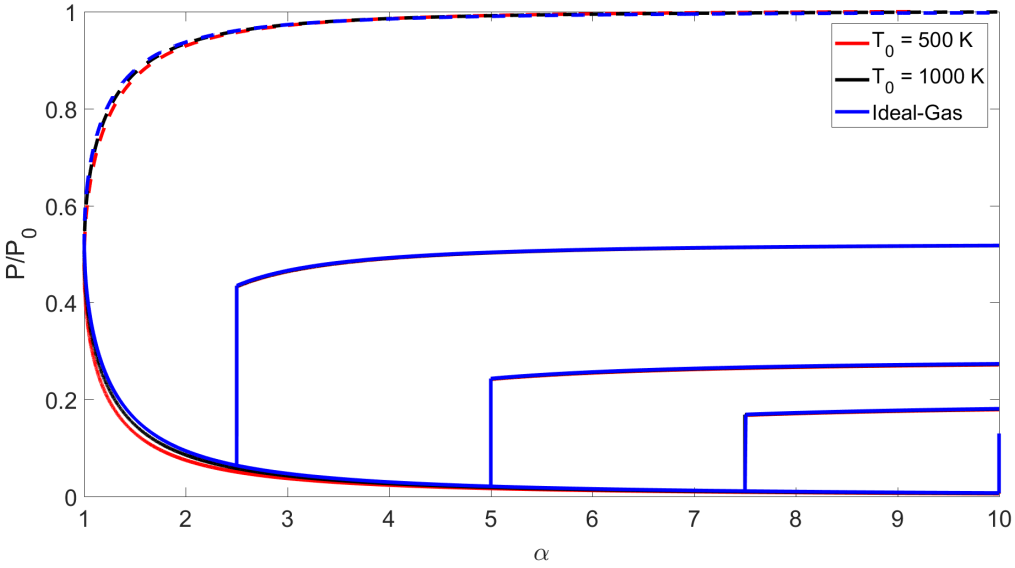

Figure 140: $\frac{P}{P_0}$ versus α at P_0= 500 bar

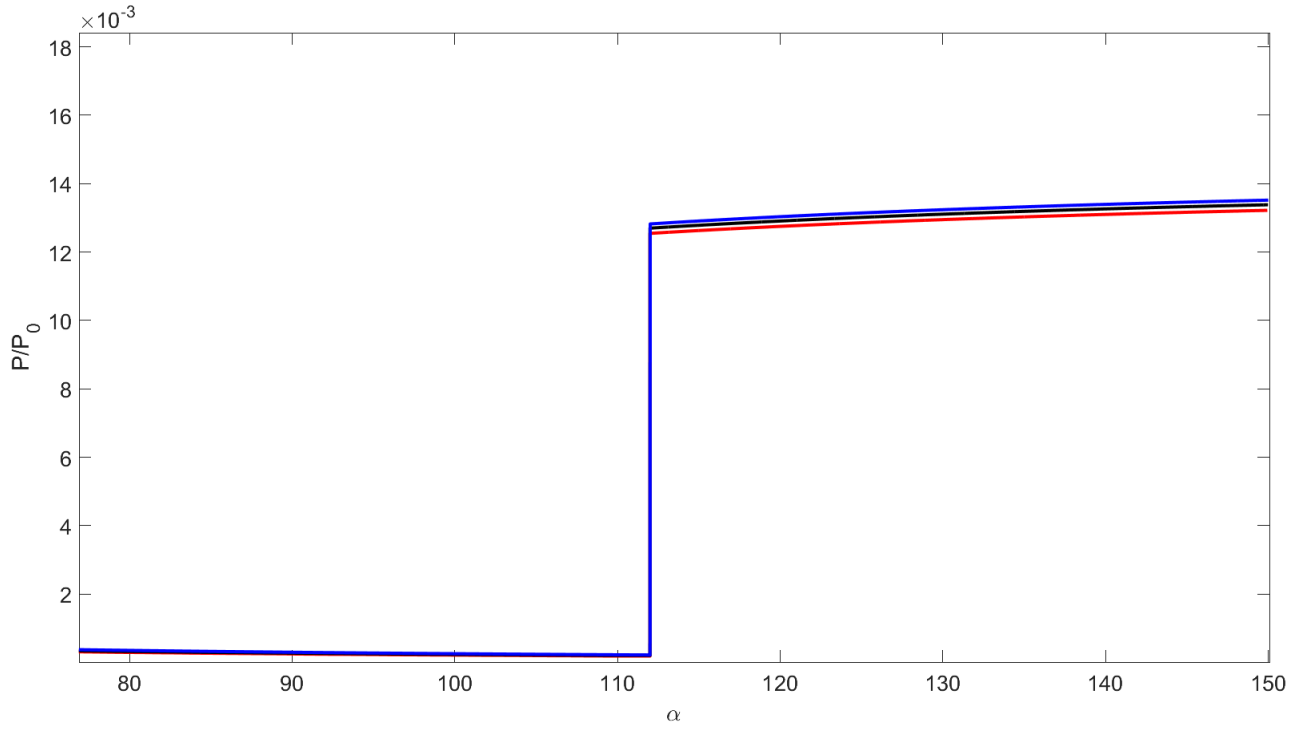

Figure 141: $\frac{P}{P_0}$ versus α at P_0= 500 bar. The flow for this graphs was allowed to expand to a much larger area ratio to show the effects of area ratio on the normal shocks in the nozzle.

4.3.6 Comparison To Previous Literature

There have only been a few relevant investigations that used real-gas calculations to solve for normal shock properties and then, even fewer that used the SKR EoS in order to do so. While there are a few that use the Redlich-Kwong EoS to approach normal shock solutions, such as Kouremenous they define specific heat capacity using the pressure, temperature and terms found in Redlich-Kwong equations [10]. Defining the specific heats in this way will have a large impact on the solution. Recall that this investigation uses a constant specific heat capacity and is defined by Equation 74.

Thus, the most reasonable work to compare the results of the normal shock calculations developed in this study are to that of Sirignano. Previously, Sirignano demonstrated two ways of calculating the normal shock; one using the conservation equations and a solver that

comes with MatLab. The second utilizes a completely different approach using a Taylor expansion [13]. The first method to be described by Sirignano was used to compare to this study's calculations, however, the algorithm and approach still differ from each other resulting in different values when the strength of the shock is increased. For lower strength shocks, this study and Sirignano's result in similar solutions, but at higher strengths shocks, the difference in value become more apparent. In Figure 142, note close agreement between each studies solutions, while Figure 144 shows there are differences in the stronger shocks.

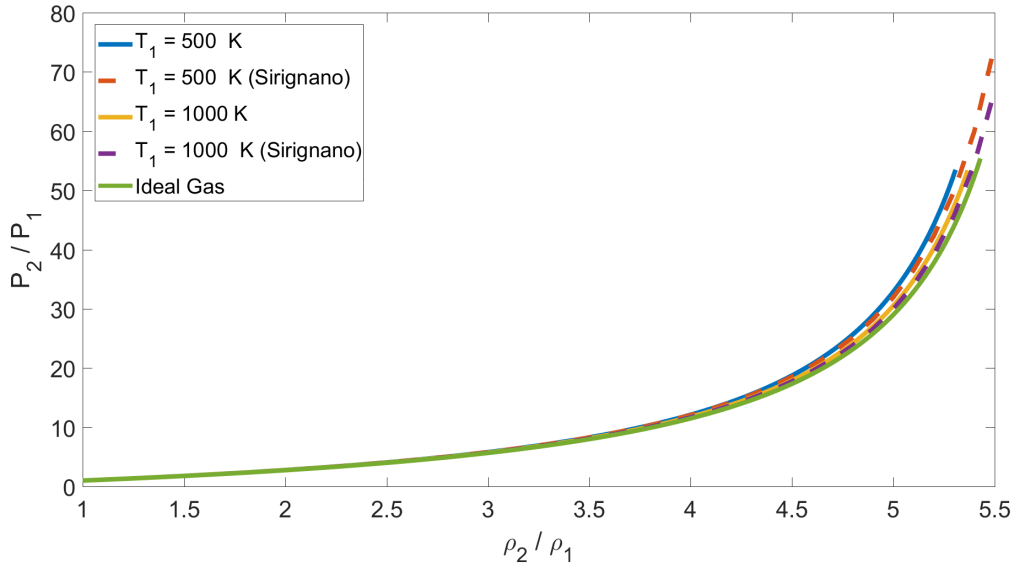

Figure 142: $\frac{P_2}{P_1}$ versus $\frac{\rho_2}{\rho_1}$, comparison to Sirignano [13]. $P_1 = 10$ bar and is held constant while the strength of the shock is varied. For this case $T_1 = 500$ K, and 1000 K.

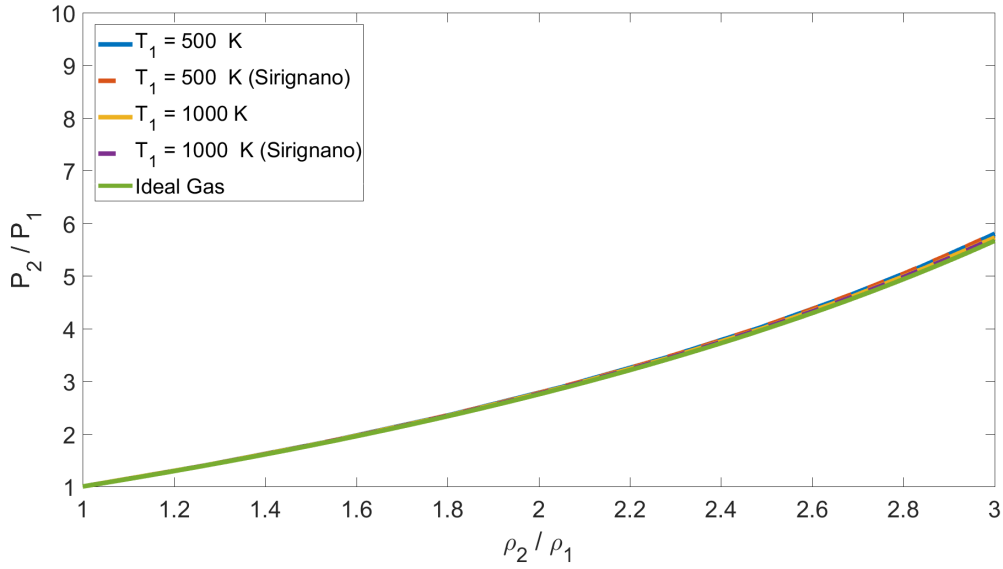

Figure 143: $\frac{P_2}{P_1}$ versus $\frac{\rho_2}{\rho_1}$, comparison to Sirignano [13]. $P_1 = 10$ bar and is held constant while the strength of the shock is varied. For this case $T_1 = 500$ K, and 1000 K. This graph in Figure 145, but zooms into the region of weaker strength shocks to show the comparison more clearly.

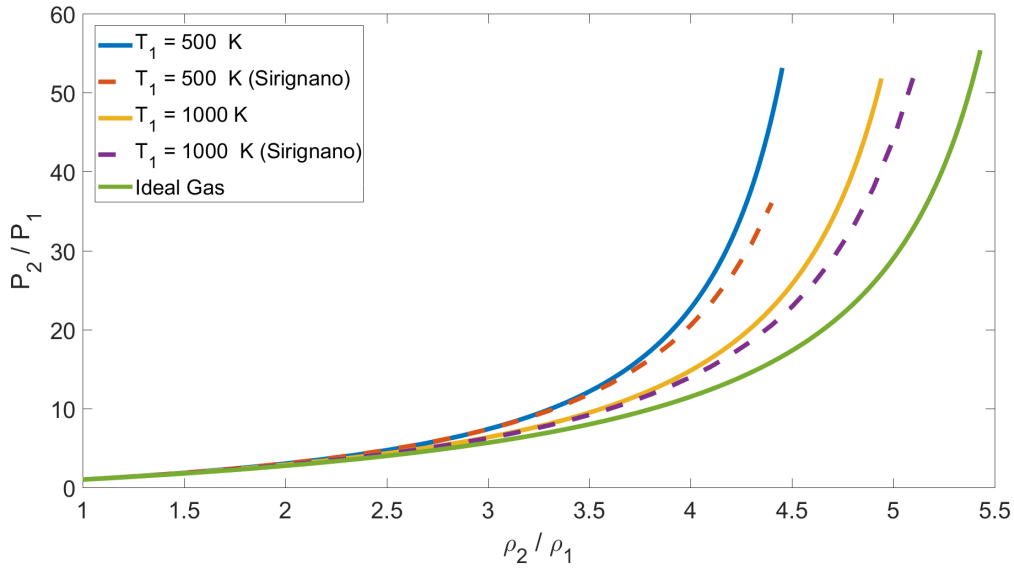

Figure 144: $\frac{P_2}{P_1}$ versus $\frac{\rho_2}{\rho_1}$, comparison to Sirignano [13]. $P_1 = 100$ bar and is held constant while the strength of the shock is varied. For this case $T_1 = 500$ K, and 1000 K.

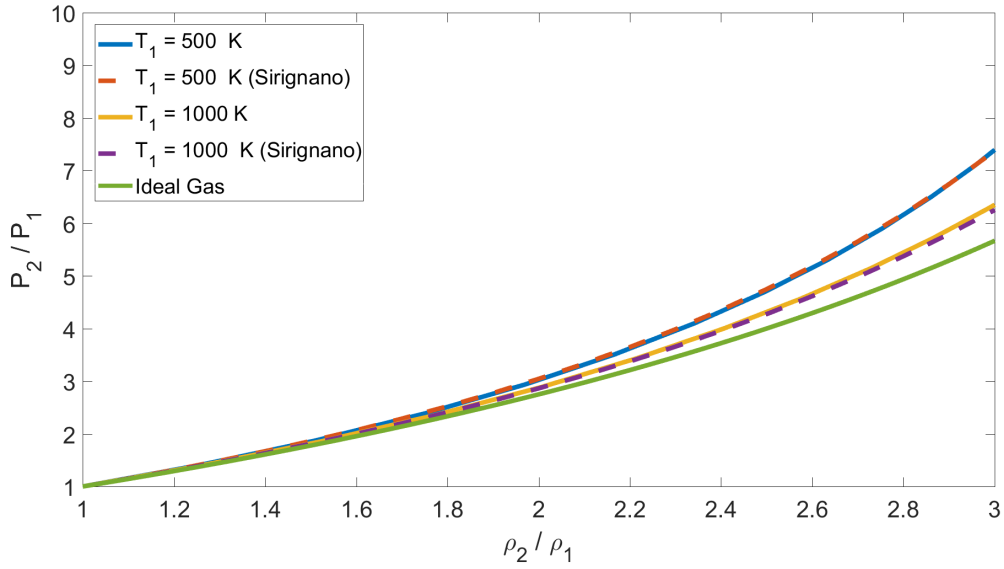

Figure 145: $\frac{P_2}{P_1}$ versus $\frac{\rho_2}{\rho_1}$, comparison to Sirignano [13]. $P_1 = 100$ bar and is held constant while the strength of the shock is varied. For this case $T_1 = 500$ K, and 1000 K. This is the same graph in Figure 145, but zooms into the region of weaker strength shocks to show the comparison more clearly.

5 Conclusion

The Soave-Redlich-Kwong EoS was used to compare real-gas calculations with predicted behavior for ideal-gas values. This thesis study demonstrates a novel application of the method for directly solving the cubic EoS associated with the SKR EoS. This increases the computational efficiency of the real-gas calculations. The flow is applied to convergent-divergent nozzle analysis as used in rocket and jet engines. Thus the investigated ranges of temperature and pressure are higher than most previous studies. Classical mixing rules were utilized to model the mixture of species. The primary focus for this investigation was air, along with limited investigation into some single-species gases.

Previous literature was discussed demonstrating the development of the SKR EoS and its initial applications in the energy industry. As more researchers studied the SKR EoS, more uses became apparent and eventually led to the SKR EoS being used to analyze isentropic flow and normal shocks for the real-gases. Methods for calculating isentropic flow were explained, as well as equations needed for modeling a mixtures of species.

This investigation examined stagnation temperatures, T_0 of: 500 K, 1000 K, 2000 K, and 4000 K. The values of stagnation pressure, P_0, investigated were at: 1 MPa, 3 MPa, 5 MPa, 10 MPa. 20 MPa, 50 MPa.

In regards to temperature, velocity, sound speed, A, B, compressibility factor, M, mass flux and momentum flux in an isentropic flow, it was found that generally a real-gas at higher pressures or at lower temperatures has a greater deviation from ideal-gas, than it has with higher temperature and lower pressure. However, for some values the difference between ideal-gas flow and real-gas flow was found to be very similar, even at low temperatures and low pressures. For example, the graphs displaying the P versus T curves appear to be closely harmonious with ideal-law, while on the other hand, $\mathscr{R}$ versus P varies significantly on wide ranges of P_0 and T_0. Overall, it was concluded that for a large range of pressures and temperatures, the difference between real-gas and ideal-gas was significant enough to

cause specifications when applying to practical applications.

Temperature of a real-gas compared to that of an ideal-gas was the mildest of the parameters investigated with regards to difference in ideal-gas and real-gas values. Across the entire range of the total pressures and temperatures investigated, the maximum difference was 4.25%. This means that for an ideal-gas, temperature should give a close estimate (but not accurate) answer for a *change* in pressure. Density the third of the state variables, had a maximum deviation of 28.19% from that of the ideal-gas calculations.

Pressure was the variable that was not investigated since all partial equations were dependent on a change in velocity. Consequently, the ideal-gas equations were also dependent on the change in pressure. The maximum deviation of velocity was not a decent metric to measure the difference of velocity. Instead, the average difference of values between ideal-gas and real-gas was found to be 8.41%. Sound speed had the largest deviation from ideal-gas at 24.05% at its maximum. The Mach numbers deviation had the same issues as velocity and was found to have an average difference of 8.64%.

In the literature an approximate solution for solving the compressibility factor Z was discussed and is demonstrated in Equation 7. While there is a significant amount of calculations for both Cardanos Method and a root finding function, it does show a maximum deviation of 3.89%. It should be noted that the previous stated discrepancies was for air, a mixture of species. For different species these deviations will change. For example, in the case of pure oxygen, all of the differences were higher in percentage, (except of Mach number).

There was not a constant trend based on either stagnation or static value for temperature or pressure that led to the most deviation from ideal-gas values with regards to mass flux. Changing the temperature or pressure did not lead to a monotonically increasing or decreasing difference in value unlike previous properties. Thus, the most that can be stated for this thesis study is that based on the points that were measured, (as seen in Table 2), the maximum difference between real-gas and ideal-gas mass flux was 3.25%.

This thesis study developed two different methods were developed for calculating normal

shocks. While there have been previous investigations into normal shock using some cubic EoS, there have been limited investigation using the SRK EoS. The few studies prior to this thesis study utilized different solvers to approach the calculations and confirmation of the normal shock properties differently. In this thesis study, however, the first method for analysis of shocks developed did not require the knowledge of upstream velocity / Mach number. This will result in an array of solutions for varying upstream velocity. The results demonstrated how dramatic the difference in value of downstream temperature and pressure are compared to ideal-gas results. The second method developed in this study is for use when all of the upstream conditions are known, primarily velocity. This method is used for specific upstream conditions and results in only one solution for downstream conditions.

In conclusion, the results of the normal shock solutions follow similar the same trends for isentropic real-gas solutions but differ in value. The higher the temperature is, the closer the solution is to ideal-gas. With higher pressure the opposite is true, where the difference in real-gas versus ideal-gas solutions becomes a larger variation. With this in mind, it was noted that the variation of pressure on a reasonable range has a higher effect on the real-gas than that of a practical range of temperature. Some of the parameters used are temperature dependent and vary such as the binary interaction coefficient (k_{ij}), constant pressure coefficient or specific heat ratio. Future studies should include the variation of these values for higher ranges of temperature. Some of the temperature dependent factors may need to be developed from experimental data. Previous studies focused on smaller temperature ranges where the changes in these values are relatively small, so the temperature dependency does not have as much of an effect as it would for the range investigated in this thesis study.

References

[1] O. Redlich and J. N. S. Kwong. On The Thermodynamics of Solutions V: An Equation of State. Fugacities of Gaseous Solutions. *Chemical Reviews*, 44:233, 1949.

[2] B. E. Poling, J. M. Prausnitz, and J. P. O'Connell. *The Properties of Gases and Liquids*. McGraw-Hill, 3 edition, 2001.

[3] G. Soave. Equilibrium Constants From A Modified Redlich-Kwong Equation of State. *Chemical Engineering Science*, 27:1197–1203, 1972.

[4] G. Soave, S. Gamba, and L. A. Pellegrini. SRK Equation of State: Predicting Binary Interaction Parameters of Hydrocarbons and Related Compounds. *Fluid Phase Equilibria*, 299:285–293, 2010.

[5] M. J. Huron and J. Vidal. New Mixing Rules in Simple Equations of State For Representing Vapour-Liquid Equilibria of Strongly Non-Ideal Mixtures. *Fluid Phase Equilibria*, 3:255–271, 1979.

[6] M. S. Graboski and T. E. Daubert. A Modified Soave Equation of State for Phase Equilibrium Calculations. 1. Hydrocarbon Systems. *Industrial and Engineering Chemistry Process Design and Deveolpment*, 17(4):443–448, 1978.

[7] M. S. Graboski and T. E. Daubert. A Modified Soave Equation of State for Phase Equilibrium Calculations. 2. Systems Containing CO2, H2S, N2, and CO. *Industrial and Engineering Chemistry Process Design and Development*, 17(4):448–454, 1978.

[8] M. S. Graboski and T. E. Daubert. A Modified Soave Equation of State for Phase Equilibrium Calculations. 3. Systems Containing Hydrogen. *Industrial and Engineering Chemistry Process Design and Development*, 18(3):300–306, 1979.

[9] J. L. Wilson and J. D. Regan. A simple method for real gas flow calculations. *Ministry of Aviation: Aeronautical Research Council Current Papers*, (772), 1965.

[10] D. A. Kouremenous. The normal shock waves of real gases and the generalized isentropic exponents. *Forschung im Ingenieurwesen*, 52(1):2187–2198, 1986.

[11] D. A. Kouremenos and K. A. Antonopoulos. Real Gas Normal Shock Wave With Redlich-Kwong Equation of State. *Acta Mechanica*, 76:223–233, 1989.

[12] M. Passmann, S. aus der Wiesche, and F. Joos. A One-Dimensional Analytical Calculation Method for Obtaining Normal Shock Losses in Supersonic Real Gas Flows. *Journal of Physics: Conference Series*, 821:012004, 2017.

[13] W. A. Sirignano. Normal Shocks with High Upstream Pressure. *Physical Review Fluids*, 3(9):093401, 2018.

[14] J. M. Lujan, J. R. Serrano, V. Dolz, and J. Sanchez. Model of the Expansion Process for R245fa in an Organic Rankine Cycle (ORC). *Applied Thermal Engineering*, 40:248–257, 2012.

[15] B. H. Sage, W. N. Lacey, and H. H. Reamer. *Thermodynamic Properties of the Lighter Paraffin Hydrocarbons and Nitrogen: Monograph on API Research Project 37*. American Petroleum Institute, 1950.

[16] G. G. Fuller. A Modified Redlich-Kwong-Soave Equation of State Capable of Representing the Liquid State. *Industrial and Engineering Chemistry Fundamentals*, 15(4):254–257, 1976.

[17] C. H. Twu, J. E. Coon, A. H. Harvey, and J. R. Cunningham. An Approach for the Application of a Cubic Equation of State to Hydrogen-Hydrocarbon Systems. *Industrial and Engineering Chemistry Research*, 35:905–910, 1995.

[18] W. A. Sirignano. Compressible Flow At High Pressure With Linear Equation of State. *Journal of Fluid Mechanics*, 843:244–292, 2018.

[19] J. van der Waals. Over de Continuiteit van den gas- en Vloeistoftoestand. *Universiteit Leiden.*, 1873.

[20] D. Peng and D. B. Robinson. A New Two-Constant Equation of State. *Industrial and Engineering Chemistry Research Fundamentals*, 15(1):59–64, 1975.

[21] M. A. Saad. *Compressible Fluid Flow*. Prentice-Hall, Inc., Englewood Cliffs, 2 edition, 1993.

[22] J. D. Anderson. *Modern Compressible Flow, With Historical Perspectives*. McGraw-Hill, New York, 2003.

[23] J. Stoll, J. Vrabec, and H. Hasse. Vapor-Liquid Equilibria of Mixtures Containing Nitrogen, Oxygen, Carbon Dioxide, and Ethane. *American Institute of Chemical Engineers Journal*, 49(8):2187–2198, 2003.

A List of Symbols

Term	Definition
A	Pressure / Temperature Dependent Term Used in Cubic EoS
a	Term Used in Calculating Cubic EoS and Other Terms
$\hat{a}$	Normalized Version of a, Account for Multiple a_i if Applicable
$\hat{a_i}$	Normalized Version of a for a Specific Species
B	Pressure / Temperature Dependent Term Used in Cubic EoS
b	Term Used in Calculating Cubic EoS and Other Terms
$\hat{b}$	Normalized Version of b, Account for Multiple b_i if Applicable
$\hat{b_i}$	Normalized Version of b for a Specific Species
C	Normalized Sound Speed
c	Dimensional Velocity
c_0	Initial Sound Speed
c_p	Specific Heat, Constant Pressure
f	Term Used in Calculations
g	Term Used in Calculations
H	Total Enthalpy
h	Specific Enthalpy
H_1	Normal Shock Upstream Total Enthalpy, Dimensionalized
h_1	Normal Shock Upstream Enthalpy, Dimensionalized
H_2	Normal Shock Downstream Total Enthalpy, Dimensionalized
h_2	Normal Shock Downstream Enthalpy, Dimensionalized
k_{ij}	Binary Interaction Coefficient
M	Mach Number
MW	Molecular Weight
P	Normalized Pressure by P_0
P_0	Total Pressure, Used as Initial Pressure
p_1	Normal Shock Upstream Pressure, Dimensionalized
p_2	Normal Shock Upstream Pressure, Dimensionalized
P_c	Normalized Critical Pressure
P_{cd}	Dimensional Critical Pressure
P_d	Dimensional Pressure (with units Pa)
q_1	Dummy Variable for Cardano Derivation
q_2	Dummy Variable for Cardano Derivation

List of Symbols Continued

Term	Definition
$\mathscr{R}$	Normalized Density (Section 2.3)
R	Specific Ideal Gas Constant
r	Dummy Variable for Cardano Derivation
R_u	Universal Ideal Gas Constant
S_i	Coefficient of a Specific Species of Gas Used In The Calculation of A
T	Normalized Temperature by T_0
T_0	Total Temperature, Used as Initial Temperature
T_1	Normal Shock Upstream Temeprature, Dimensionalized
T_2	Normal Shock Downstream Temeprature, Dimensionalized
T_c	Normalized Critical Temperature
T_{cd}	Dimensional Critical Temperature
T_d	Dimensional Temperature (With Units Kelvin)
U	Normalized Velocity
u	Dimensional Velocity
u_0	Initial Velocity
u_1	Normal Shock Upstream Velocity, Dimensionalized
u_2	Normal Shock Downstream Velocity, Dimensionalized
v	Specific Volume
X_i	Molar Fraction of i^{th} species
Z	Compressibility Factor
Z_i	i^{th}root of Cubic Equation of State
Z_1	Normal Shock Upstream Compressibility Factor
Z_2	Normal Shock Downstream Compressibility Factor
α	Area normalized by Area of the throat
β	Term used in Temperature Change Calculation
γ	Specific Heat Ratio
ρ	Static Density, Dimensionalized
ρ_0	Total Density, Dimensionalized
ρ_1	Normal Shock Upstream Density, Dimensionalized
ρ_2	Normal Shock Downstream Density, Dimensionalized
ω	Acentric Factor
ω_1	Cubic Root of 1

B Gas Properties

B.1 Property Tables

Species	Critical Temperture (K)	Critical Pressure (kPa)	ω	MW (g/mol)	γ
H_2O	647.1	22064	0.344	18.0	1.333
CO_2	304.25	7380	0.228	44.0	1.286
O_2	154.6	5050	0.228	32.0	1.400
N_2	126.2	3390	.040	28	1.400
Ar	150.8	4780	0	40	1.667

Table 3: Data taken from Sirignano [13]

B.2 Binary Reaction Coefficient

Table 4. Binary Equation of State Parameters k_{ij} for the Mixtures Modeled in this Work

Mixture	Peng-Robinson k_{ij}	PC-SAFT (cf. Appendix B) k_{ij}	BACKONE (cf. Appendix B) k_{ij}
$N_2 + O_2$	−0.00978	−0.00160	−0.003
$CO_2 + C_2H_6$	0.13008	0.10289	0.0914
$O_2 + CO_2$	−0.04838	0.05929	−0.01
$N_2 + CO_2$	−0.01493	−0.01793	−0.04
$N_2 + C_2H_6$	0.05233	0.04313	−0.025

Figure 146: Table taken from Stoll [23]

C Matrix Laboratory Code

Following is the Matrix Laboratory Code used for calculating the data shown in the graphs in Section 4. There are two main codes displayed here; one for isentropic flow and the second normal shock calculations using method 1. The codes use similar functions which are listed in Section C.3.

C.1 Isentropic Flow

The following code is used to calculate and graph isentropic flow through a convergent-divergent nozzle. This particular code holds P_0 constant while varying T_0 for each graph. The graphs are then plotted and stored as images. The original functions that are called upon are in Appendix C.3:

```
clc
clear
clear figure
close all
format long
%% Version 7
count=1;
Cp=1142; % J/kg/K
R=8134;

for P0=[1 3 5 10 20 50]*1e6 % Pascals
for  T0=[500 1000 2000 4000] %Kelvin
bar= P0*(1e-5);
T=1;
P=1;
dP=-0.001;
u0=0;
alpha=1;

Tci=[154.6 126.2]./T0;
Pci=[5050e3 3390e3]./P0;
MWi=[32 28];
gami=[1.4 1.4];
Xi=[0.2 .8];
MW=MWi(1)*Xi(1)+MWi(2)*Xi(2);

if sum(Xi)~=1
```

```
    disp('Mole Fraction Error')
    return
end

wi=[0.022 0.04];
Si=0.48508 + 1.5517.*wi-0.15613.*wi.^2;
kij=[0,-.00978; ...
    -.00978,0];

%%Cal ai, bi, etc
ai=[]; %initialize varibles
bi=[];
da_dTi=[];
d2a_dT2i=[];

for i=1:length(Xi)
     ai(i)=0.42748*Tci(i)^2/Pci(i)*(1+Si(i)*(1-sqrt(T/Tci(i))))^2;
     bi(i) = 0.08664*Tci(i)/Pci(i);
     da_dTi(i)= -0.42748*Tci(i)^1.5/Pci(i)*Si(i)*(1+ Si(i)...
        *(1-sqrt(T/Tci(i))))/sqrt(T);
     d2a_dT2i(i)=0.21374/Pci(i)*(Tci(i)/T)^1.5*Si(i)*(1+Si(i));
end

a=0;
b=0;
 for i=1:length(Xi)
     b=b+ Xi(i)*bi(i);
     for j=1:length(Xi)
         a=a+ sqrt(ai(i)*ai(j))*(1-kij(i,j))*Xi(i)*Xi(j);
     end
 end

 %% Calc A and B parts
 A=a*P/T^2;
 B=b*P/T;
 Apr=0;
 Aprpr=0;

 for i=1:length(Xi)
       for j=1:length(Xi)
         Apr=Apr + (1-kij(i,j))*0.5*Xi(i)*Xi(j)*P/T*(sqrt(ai(i))/sqrt(ai(j))...
             *da_dTi(j)+sqrt(ai(j))/sqrt(ai(i))*da_dTi(i));
         Aprpr=Aprpr+(1-kij(i,j))*0.5*P*Xi(i)*Xi(j)*P*(sqrt(ai(i))/sqrt(ai(j))*...
             d2a_dT2i(i)-0.5*sqrt(ai(i))/sqrt(ai(j))/ai(j)*(da_dTi(j)^2)+...
             sqrt(1/ai(i)/ai(j))*da_dTi(i)*da_dTi(j)+sqrt(ai(j))/sqrt(ai(i))*...
             d2a_dT2i(j)-0.5*sqrt(ai(j))/sqrt(ai(i))/ai(i)*(da_dTi(i)^2));
     end
 end

 %% Calc kij and specific Gas Constant for Mixture

m=0;
Rspec=0;
gamma=0;
```

```
for i=1:length(Xi)
    m=m+MWi(i)*Xi(i);
    Rspec=Rspec + R*Xi(i);
    gamma=gamma+gami(i)/MWi(i)*MWi(i)*Xi(i);
end

Rspec=Rspec/m;
%% Initial Speed of SOund Stuff

U=u0/sqrt(Rspec*T0);
U2=U^2;

%% Calculate Cubic Equation
N_1=-1;
N_2=A-B-B^2;
N_3=-A*B;

Z=cardano(N_1,N_2,N_3);
format short

Rscr=P/T/Z;   %non-dimensional Density
rho0=Rscr*P0/T0/Rspec;
%% Initialize matrix
U_m=[];
Rscr_m=[];
alpha_m=[];
Z_m=[];
A_m=[];
B_m=[];
T_m=[];
P_m=[];
C_m=[];
M_m=[];
TI_m=[];
err_m=[];
dT_m=[];
f_m=[];
g_m=[];
fgb_m=[];
beta_m=[];
Apr_m=[];
Aprpr_m=[];
mdot_m=[];
k_cv_m=[];
a1_m=[];
a2_m=[];
a_m=[];
b_m=[];
da_dTi1_m=[];
d2a_dT2i1_m=[];
da_dT_m=[];
da_dTi2_m=[];
d2a_dT2i2_m=[];
fgb_b_m=[];
```

```
Zapprox_m=[];

for n=P:dP:.01
%% Calculate f,g Rscript
f=(2*Z^3-Z^2+A*B)/(Z^3-B^2*Z);
g=1/(Z-B) - Apr/Z/(Z+B);
k_cv= (gamma-1)*Aprpr/B*log((Z+B)/Z);
beta=(gamma-1)*Z*g/(1+k_cv);

%% Calcualte Partial Gradients (equations 1-VII)
fgb=(f+g*beta); %I
fgb_m=[fgb_m fgb];
dalpha_dP=-alpha*(1/P/(fgb)-1/Rscr/U^2); %IV

dU2_dP=-2/Rscr;
dT_dP=beta*T/P/fgb; %VIII
C=sqrt(T*Z*fgb);
U2=U2+dU2_dP*dP;
U=sqrt(U2);
M=U/C; %Mach Number
mdot=Rscr*P0/T0/Rspec*U*sqrt(Rspec*T0)*1;

%% store variables
U_m=[U_m U] ;
f_m=[f_m f];
g_m=[g_m g];
mdot_m=[mdot_m mdot];
Apr_m=[Apr_m Apr];
Aprpr_m=[Aprpr_m Aprpr];
beta_m=[beta_m beta];
Rscr_m=[Rscr_m Rscr];
alpha_m=[alpha_m alpha];
Z_m=[Z_m Z];
k_cv_m=[k_cv_m k_cv];
A_m=[A_m A];
B_m=[B_m B];
T_m=[T_m T];
P_m=[P_m P];
C_m=[C_m C];
M_m=[M_m M];
TI_m=[TI_m P^((gamma-1)/gamma)];
Zapprox_m=[Zapprox_m 1+B-A];


dT_m=[dT_m dT_dP];
fgb_b_m=[fgb_b_m fgb/beta];
err_m=[err_m abs(U/C-1)*100];
a_m=[a_m a];
b_m=[b_m b];
a1_m=[a1_m ai(1)];
a2_m=[a2_m ai(2)];
da_dTi1_m=[da_dTi1_m da_dTi(2)];
d2a_dT2i1_m=[d2a_dT2i1_m d2a_dT2i(1)];
da_dT=0;
```

```
for j=length(Xi)
for i=length(Xi)
    da_dT=da_dT+Xi(i)*Xi(j)*(ai(i)/ai(j)*da_dTi(j)+ai(j)/ai(i)*da_dTi(i));

end
end
da_dT_m=[da_dT_m da_dT];
%% Calcualte Next Step's Variables

P=P+dP;
T=T+dT_dP*dP;


 for i=1:length(Xi)
     ai(i)=0.42748*Tci(i)^2/Pci(i)*(1+Si(i)*(1-sqrt(T/Tci(i))))^2;
     bi(i) = 0.08664*Tci(i)/Pci(i);
     da_dTi(i)= -0.42748*Tci(i)^1.5/Pci(i)*Si(i)*(1+ Si(i)...
        *(1-sqrt(T/Tci(i))))/sqrt(T);
     d2a_dT2i(i)=0.21374/Pci(i)*(Tci(i)/T)^1.5*Si(i)*(1+Si(i));
 end

a=0;
b=0;
 for i=1:length(Xi)
     b=b+ Xi(i)*bi(i);
     for j=1:length(Xi)
         a=a+ sqrt(ai(i)*ai(j))*(1-kij(i,j))*Xi(i)*Xi(j);
     end
 end

 %% Calc A and B parts
 A=a*P/T^2;
 B=b*P/T;
 Apr=0;
 Aprpr=0;

  for i=1:length(Xi)
       for j=1:length(Xi)
         Apr=Apr + (1-kij(i,j))*0.5*Xi(i)*Xi(j)*P/T*(sqrt(ai(i))/sqrt(ai(j)))...
             *da_dTi(j)+sqrt(ai(j))/sqrt(ai(i))*da_dTi(i));
         Aprpr=Aprpr+(1-kij(i,j))*0.5*P*Xi(i)*Xi(j)*P*(sqrt(ai(i))/sqrt(ai(j))*...
             d2a_dT2i(i)-0.5*sqrt(ai(i))/sqrt(ai(j))/ai(j)*(da_dTi(j)^2)+...
             sqrt(1/ai(i)/ai(j))*da_dTi(i)*da_dTi(j)+sqrt(ai(j))/sqrt(ai(i))*...
             d2a_dT2i(j)-0.5*sqrt(ai(j))/sqrt(ai(i))/ai(i)*(da_dTi(i)^2));
     end
 end

%% Calculate Cubic Equation
N_1=-1;
N_2=A-B-B^2;
N_3=-A*B;

Z=cardano(N_1, N_2, N_3);%input('Give Z input ')
format short
```

```
Rscr=P/T/Z;   %non-dimensional Density

end
C_m=real(C_m);
RIsen_m=P_m.^(1/gamma);
RscrIdeal_m=P_m./T_m;

%% Need points where M1 is exactly equal to 1
M1_err=sign(U_m-C_m);
for q=2:length(M1_err)
            if M1_err(q)~=M1_err(q-1)
                d=q;

            end
        end
%earlier we found where
M_m=U_m./C_m;
Pt=interpolate(M_m(d-1),M_m(d),P_m(d-1),P_m(d),1);
Ut=interpolate(M_m(d-1),M_m(d),U_m(d-1),U_m(d),1);
Ct=interpolate(M_m(d-1),M_m(d),C_m(d-1),C_m(d),1);
Tt=interpolate(M_m(d-1),M_m(d),T_m(d-1),T_m(d),1);
Rscrt=interpolate(M_m(d-1),M_m(d),Rscr_m(d-1),Rscr_m(d),1);
Zt=interpolate(M_m(d-1),M_m(d),Z_m(d-1),Z_m(d),1);
Bt=interpolate(M_m(d-1),M_m(d),B_m(d-1),B_m(d),1);
da_dTt=interpolate(M_m(d-1),M_m(d),da_dT_m(d-1),da_dT_m(d),1);
hhh=entropy(Z_m(d),da_dT_m(d),a_m(d),b_m(d),MW,B_m(d),Cp,T_m(d));

Pdt=Pt*P0;
udt=Ut*sqrt(Rspec*T0);
Tdt=Tt*T0;
rhodt=Pdt/Tdt/Rspec/Zt;

mdot_ae=udt*rhodt;
mdot_ae_i=sqrt(gamma)*(2/(gamma+1))^((gamma+1)/2/(gamma-1))*P0/sqrt(Rspec*T0);

mdot_r=mdot_ae/mdot_ae_i;
mom_real=(U_m.*sqrt(Rspec*T0)).^2.*P_m.*P0./T_m./T0./Rspec./Z_m;
TI=T0.*P_m.^((gamma-1)/gamma);
MII=sqrt(2/(gamma-1).*(P_m.^((gamma-1)/-gamma)-1));
mom_ideal=rho0.*(P_m).^(1/gamma).*(sqrt(gamma*Rspec*TI).*MII).^2;
mom_r=mom_real./mom_ideal;
% entropy=entropy(Z,da_dT,a,b,MW,B,Cp,T)

% plot(P_m,U_m, 'r-o',P_m,C_m,'b-x')
% legend('Velocity','Sound Speed')
% number=interpolate(X1,X2,Y1,Y2,Z)
%number=Y1+(Y2-Y1)*(Z-X1)/(X2-X1);
rhor_m=Rscr_m.*P0./T0./Rspec./rho0;


figure(1)
plot(P_m,T_m,'LineWidth',2)
hold on
```

```
figure(2)
plot(P_m,Rscr_m,'LineWidth',2)
hold on

figure(3)
plot(P_m,U_m,'LineWidth',2)
hold on

figure(4)
plot(P_m, Z_m,'LineWidth',2)
hold on

figure(5)
plot(P_m,C_m,'LineWidth',2)
hold on

figure(6)
plot(P_m,A_m,'LineWidth',2)
hold on

figure(7)
plot(P_m,B_m,'LineWidth',2)
hold on

figure(8)
plot(P_m,mom_r,'LineWidth',2)
hold on

figure(9)
plot(P_m,M_m,'LineWidth',2)
hold on

figure(10)
plot(P_m,rhor_m,'LineWidth',2)
hold on

fprintf('P= %2f, T= %4.0f, mdot_r= %6.4f, Zt= %5.4f \n',P0/(1e6),T0,mdot_r,Zt)

end
TI_m=(P_m).^(1-1/gamma);
rho_m=(P_m).^(1/gamma);
MI_m=sqrt(((P_m).^(1/gamma-1)-1)*2/(gamma-1));
CI_m=sqrt(gamma.*TI_m);
UI_m=MI_m.*CI_m;

temperature=join(['Temp_m' num2str(P0/(1e6))],0);
density=join(['Density_m' num2str(P0/(1e6))],0);
velocity=join(['U_m' num2str(P0/(1e6))],0);
compfactor=join(['Z_m' num2str(P0/(1e6))],0);
soundspeed=join(['C_m' num2str(P0/(1e6))],0);
Aname=join(['A_m' num2str(P0/(1e6))],0);
Bname=join(['B_m' num2str(P0/(1e6))],0);
mname=join(['mom_m' num2str(P0/(1e6))],0);
```

```
Machn=join(['M_m' num2str(P0/(1e6))],0);
rhoname=join(['rhor_m' num2str(T0)],0);


figure(1)
plot(P_m,TI_m,'--','LineWidth',3)
xlabel('Normalized Pressure, P')
ylabel('Normalized Temperature, T')
lgd=legend('T_0 = 500 K','T_0 = 1000 K','T_0 = 2000 K','T_0 = 4000 K','Ideal Gas');
lgd.Location='southeast';
lgd.FontSize=18;
set(gcf, 'Position', get(0, 'Screensize'))
 set(gca,'FontSize',20)
saveas(figure(1), temperature,'png');
hold on

figure(2)
plot(P_m,rho_m,'--','LineWidth',3)
xlabel('Normalized Pressure, P')
ylabel('Normalized Density, \Re ')
lgd=legend('T_0 = 500 K','T_0 = 1000 K','T_0 = 2000 K','T_0 = 4000 K','Ideal Gas');
lgd.Location='southeast';
lgd.FontSize=18;
set(gcf, 'Position', get(0, 'Screensize'))
 set(gca,'FontSize',20)
saveas(figure(2), density,'png');
hold on

figure(3)
xlabel('Normalized Pressure, P')
ylabel('Normalized Velocity, U')
lgd=legend('T_0 = 500 K','T_0 = 1000 K','T_0 = 2000 K','T_0 = 4000 K');
lgd.Location='northeast';
lgd.FontSize=18;
set(gcf, 'Position', get(0, 'Screensize'))
 set(gca,'FontSize',20)
saveas(figure(3), velocity,'png');
hold on

figure(4)
xlabel('Normalized Pressure, P')
ylabel('Z')
lgd=legend('T_0 = 500 K','T_0 = 1000 K','T_0 = 2000 K','T_0 = 4000 K');
lgd.Location='northwest';
lgd.FontSize=18;
set(gcf, 'Position', get(0, 'Screensize'))
 set(gca,'FontSize',20)
saveas(figure(4), compfactor,'png');
hold on

figure(5)
xlabel('Normalized Pressure, P')
ylabel('Normalized Sound Speed, C')
lgd=legend('T_0 = 500 K','T_0 = 1000 K','T_0 = 2000 K','T_0 = 4000 K');
```

```
lgd.Location='southeast';
lgd.FontSize=18;
set(gcf, 'Position', get(0, 'Screensize'))
 set(gca,'FontSize',20)
saveas(figure(5), soundspeed,'png');
hold on

figure(6)
xlabel('Normalized Pressure, P')
ylabel('A')
lgd=legend('T_0 = 500 K','T_0 = 1000 K','T_0 = 2000 K','T_0 = 4000 K');
lgd.Location='eastoutside';
lgd.FontSize=18;
set(gcf, 'Position', get(0, 'Screensize'))
 set(gca,'FontSize',20)
saveas(figure(6), Aname,'png');
hold on

figure(7)
xlabel('Normalized Pressure, P')
ylabel('B')
lgd=legend('T_0 = 500 K','T_0 = 1000 K','T_0 = 2000 K','T_0 = 4000 K');
lgd.Location='northwest';
lgd.FontSize=18;
set(gcf, 'Position', get(0, 'Screensize'))
 set(gca,'FontSize',20)
saveas(figure(7), Bname,'png');
hold on

figure(8)
xlabel('Normalized Pressure, P')
ylabel('(\rho u^2)_{real}/(\rho u^2 )_{ideal}')
lgd=legend('T_0 = 500 K','T_0 = 1000 K','T_0 = 2000 K','T_0 = 4000 K');
lgd.Location='eastoutside';
lgd.FontSize=18;
xlim([0 .95])
set(gcf, 'Position', get(0, 'Screensize'))
 set(gca,'FontSize',20)
saveas(figure(8), mname,'png');
hold on

figure(9)
plot(P_m,MI_m,'--','LineWidth',3)
xlabel('Normalized Pressure, P')
ylabel('Mach Number, M')
lgd=legend('T_0 = 500 K','T_0 = 1000 K','T_0 = 2000 K','T_0 = 4000 K','Ideal Gas');
lgd.Location='northeast';
lgd.FontSize=18;
set(gcf, 'Position', get(0, 'Screensize'))
 set(gca,'FontSize',20)
saveas(figure(9), Machn,'png');
hold on

figure(10)
```

```
plot(P_m,rhor_m,'--','LineWidth',3)
xlabel('Normalized Pressure, P')
ylabel('Normalized Density, $\frac{\rho}{\rho_0}$','interpreter','latex')
lgd=legend('P0=1 MPa','P0=3 MPa','P0=5 MPa','P0= 10 MPa','P0= 20 MPa','P0= 50 MPa','Ideal Gas');
lgd.Location='southeast';
lgd.FontSize=18;
set(gcf, 'Position', get(0, 'Screensize'))
 set(gca,'FontSize',20)
saveas(figure(10), rhoname,'png');
hold on


 close all
end
beep
```

C.2 Normal Shock using Method 1

This is the code used to calculate the normal shock given a value for upstream conditions T and P. Once the calculation is finished, both upstream and downstream conditions are stored in a text file to be plotted with a different script:

```
clc
clear
clear figure
close all
format long
%% Version 99 For use in the normal shock calc via ratio not a specific
% point in the nozzle
count=1;
Cp=1039.3; % J/kg/K
R=8134;
tic;
for P1=[1 3 5 10 20 50]*1e6; % Pascals
for T1=[500 1000]; %Kelvin

fprintf('Temperature = %4i \n',T1)
fprintf('Pressure    = %3.1e \n',P1)

bar= P1*(1e-5);

Tci=[154.6 126.2];
Pci=[5050e3 3390e3];
MWi=[32 28];
gami=[1.4 1.4];
Xi=[0.20 .8];
MW=MWi(1)*Xi(1)+MWi(2)*Xi(2);
```

```
if sum(Xi)~=1
    disp('Mole Fraction Error')
    return
end

wi=[0.022 0.04];
Si=0.48508 + 1.5517.*wi-0.15613.*wi.^2;
kij=[0,-.00978; ...
    -.00978,0];

m=0;
Rspec=0;
gamma=0;
for i=1:length(Xi)
    m=m+MWi(i)*Xi(i);
    Rspec=Rspec + R*Xi(i);
    gamma=gamma+gami(i)/MWi(i)*MWi(i)*Xi(i);
end

Rspec=Rspec/m;


%% Calculate Cubic Equation
[da_dT ahat A bhat B]=attraction(Si(1),Si(2),Xi(1),Xi(2),Tci(1),Tci(2),...
Pci(1),Pci(2),T1,P1,kij(2));
N_1=-1;
N_2=A-B-B^2;
N_3=-A*B;
Z1=cardano(N_1,N_2,N_3);

h1=entropy(Z1,da_dT,ahat,bhat,MW,B,Cp,T1);
rho1=P1/T1/Rspec/Z1;
%already have T1, and P1, so missing u1 and all other downstream conditions

%being loop with Tr Value
Pr=1.0001; %to initiliaze variable, educated guess
counterT=0;
err=0.5;
errnm1=1e20;
format short
for Tr=1:0.01:10
    counterT=counterT+1;
    T2=Tr*T1;
    disp(Tr)

%% Guess Pr
qP2=1;
while qP2==1
    P2=Pr*P1;
    [da_dT2 ahat2 A2 bhat2 B2]=attraction(Si(1),Si(2),Xi(1),Xi(2),Tci(1),Tci(2),...
Pci(1),Pci(2),T2,P2,kij(2));
    N_1=-1;
    N_2=A2-B2-B2^2;
    N_3=-A2*B2;
```

```
    Z2=cardano(N_1,N_2,N_3);
    rho2=P2/Rspec/Z2/T2;
    h2=entropy(Z2,da_dT2,ahat2,bhat2,MW,B2,Cp,T2);
    u1=sqrt((P2-P1)/rho1/(1-rho1/rho2));
    u2=rho1/rho2*u1;
    H1=h1+u1^2/2;
    H2=h2+u2^2/2;
    errcheck=abs(H2-H1);
    if (errcheck<=err) && (P2>P1);
        qP2=0;
    else
        % figure out if the error in increasing or decreasing and then
        %adjust accordingly
        %if total ENTHALPY_2 is greater than total ENTHALPY_1, then the Pr
        %assumed is too big.
        if H2>H1
            Pr=Pr+.000001;
        else
            Pr=Pr-.000001;
        end

        %reasign error of previous case


    end %end of error check


end %end of while loop for Pr

% disp(rho2/rho1)
% disp(P2/P1)
P2_m(counterT)=P2;
rho2_m(counterT)=rho2;
h2_m(counterT)=h2;
T2_m(counterT)=T2;
u1_m(counterT)=u1;
u2_m(counterT)=u2;


end %end of looper for Tr

rhor_m=rho2_m./rho1;
Pr_m=P2_m./P1;
Tr_m=T2_m./T1;

%% Plot Figures
filename=strcat(['data_information_m' num2str(P1/(1e6)) '_' num2str(T1)  '.txt'],0);

fileID = fopen(filename,'w');
for i=1:length(P2_m)
fprintf(fileID,'%9.7f %9.7f %9.7f %9.7f %9.7f %9.7f %9.7f %9.7f %9.7f %9.7f \n',P2_m(i),...
rho2_m(i), h2_m(i),T2_m(i),u2_m(i),P1, rho1, T1, h1, u1_m(i));
end
fclose(fileID);
```

```
end %% End Loop here for T1 values
end % End loop for pressure
toc
```

C.3 Functions

```
function [da_dT ahat A bhat B]=attraction(S1,S2,X1,X2,Tc1,Tc2,Pc1,Pc2,T,P,kij)
R=8134;
a1=0.42748*(Tc1^2)/Pc1*(1+S1*(1-sqrt(T/Tc1)))^2;
a2=0.42748*(Tc2^2)/Pc2*(1+S2*(1-sqrt(T/Tc2)))^2;
ahat=R^2*(a1*X1^2+a2*X2^2+2*sqrt(a1*a2)*(1-kij)*X1*X2);
da1_dT=-0.42748*(Tc1)^1.5/Pc1*S1*(1+S1*(1-sqrt(T/Tc1)))/sqrt(T)*R^2;
da2_dT=-0.42748*(Tc2)^1.5/Pc2*S2*(1+S2*(1-sqrt(T/Tc2)))/sqrt(T)*R^2;
da_dT=X1^2*da1_dT + X2^2*da2_dT+X1*X2*(a1/a2*da2_dT+a2/a1*da1_dT)  ;
b1=0.08664*R*Tc1/Pc1;
b2=0.08664*R*Tc2/Pc2;
bhat=X1*b1+X2*b2;

B=bhat*P/T/R;
A=ahat*P/(R*T)^2;
end
```

```
function cardan=cardano(N_1,N_2,N_3)
p=N_2 - (N_1^2)/3;
q=+N_3 + (2*N_1^3 - 9*N_1*N_2)/27;
if q^2/4 + p^3/27<=0
    u=nthroot((q/2)+sqrt(abs(q^2/4 + p^3/27)),3);
else
    u=nthroot(real(q/2+sqrt(q^2/4 + p^3/27)),3);
end

 omega= -1/2 + sqrt(3)/2 *i;
 sigma=u;
 epsilon=p/3/sigma;
 % format long
root_1=epsilon-sigma-N_1/3;
 root_2=epsilon*omega^2-sigma*omega-N_1/3;
root_3=epsilon*omega-sigma*omega^2-N_1/3;
cardan=root_1;
end
```

```
function entrop=entropy(Z,da_dT,a,b,MW,B,Cp,T)
R=8134;
entrop=Cp*T+1/MW*(R*T*(Z-1)+ (T*da_dT-a)/b*log(1+B/Z));
end
```

D Gas Results

This appendix displays the real-gas calculation that was demonstrated in the results section, but utilizing different species of gases.

D.1 Nitrogen, N_2

D.1.1 Temperature Results

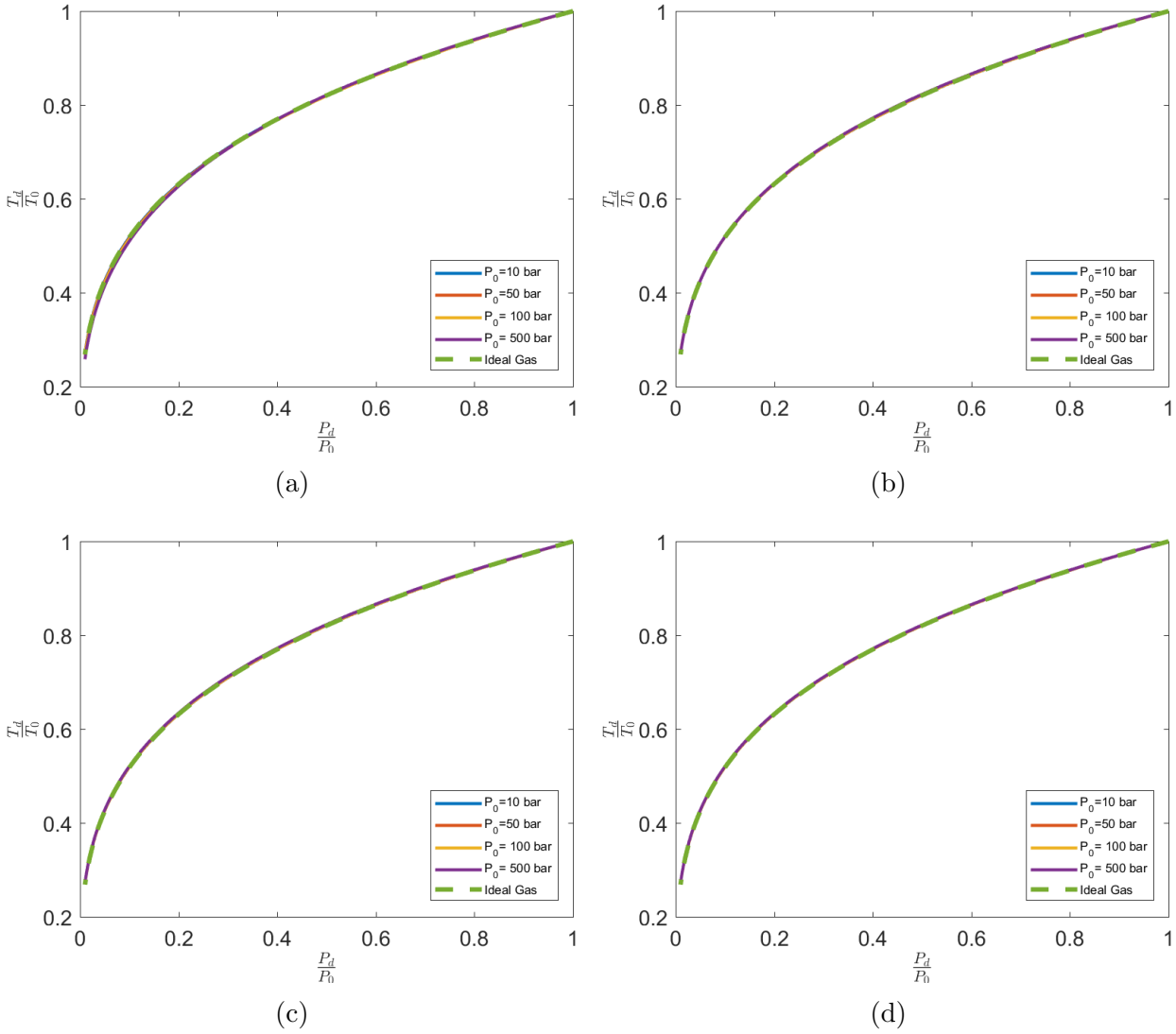

Figure 147: a) 500 K; b) 1000 K; c) 2000 K; d) 4000 K

D.1.2 Density Results

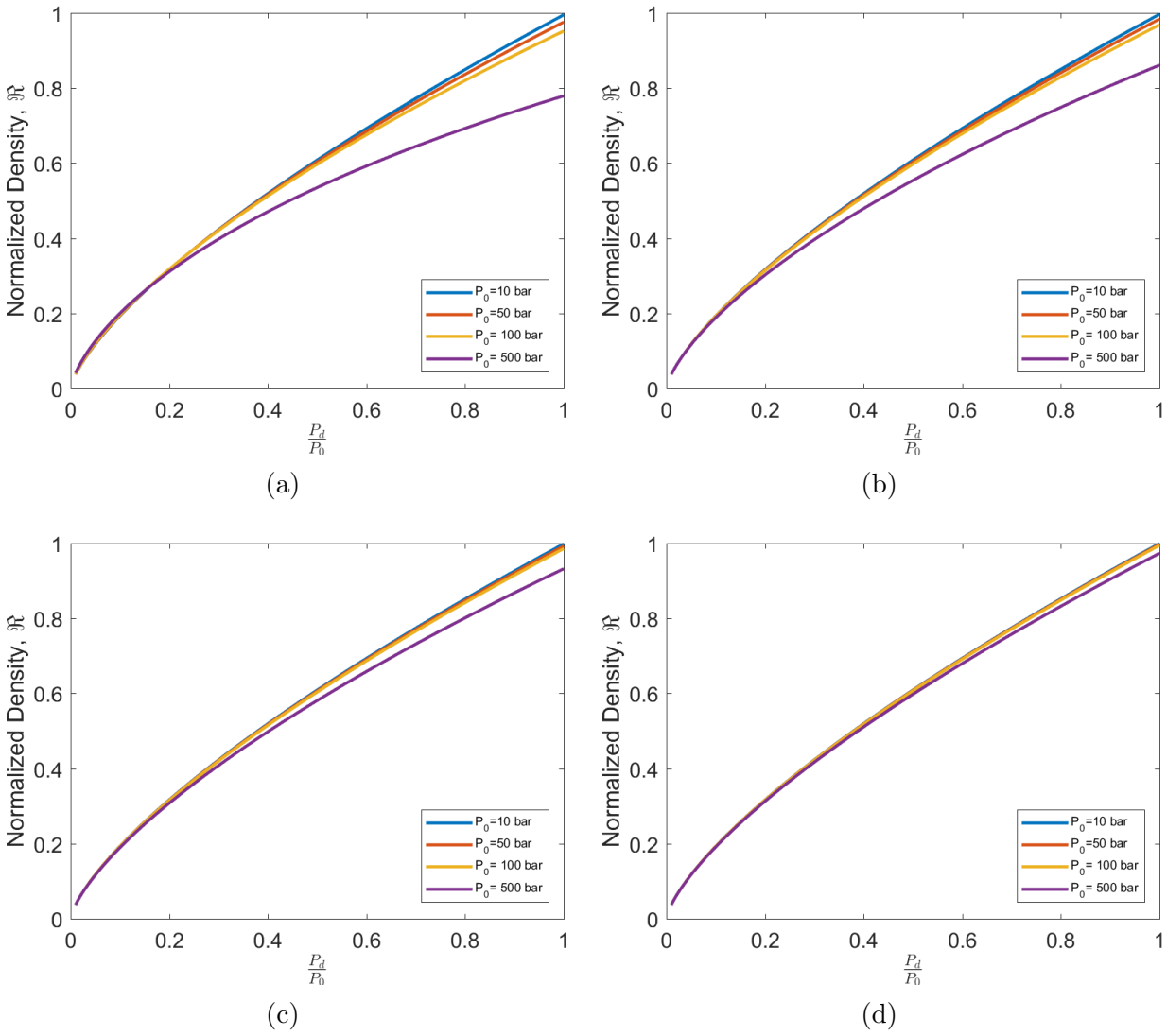

Figure 148: a) 500 K; b) 1000 K; c) 2000 K; d) 4000 K

D.1.3 Compressibility Factor Z Results

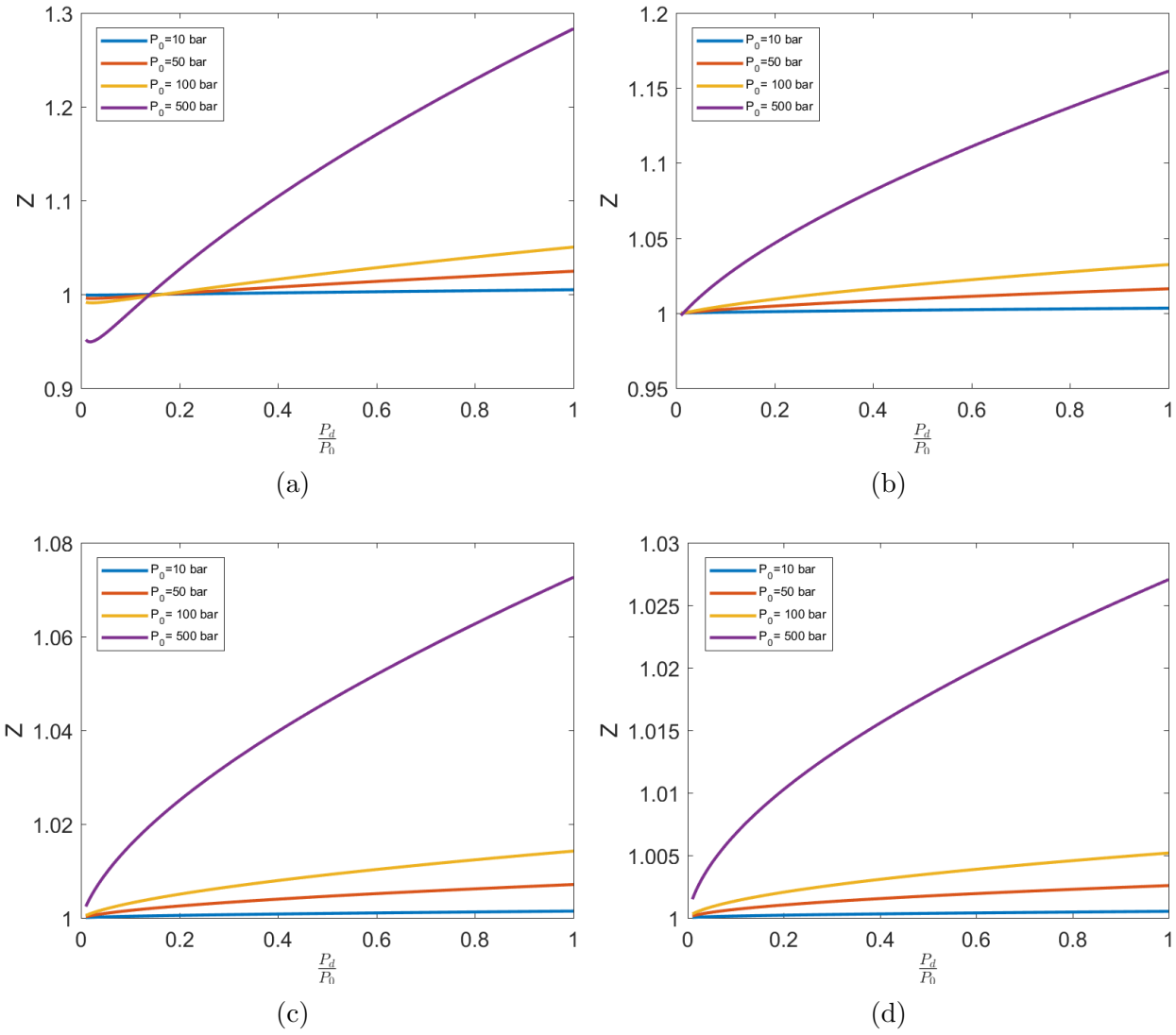

Figure 149: a) 500 K; b) 1000 K; c) 2000 K; d) 4000 K

D.1.4 A Results

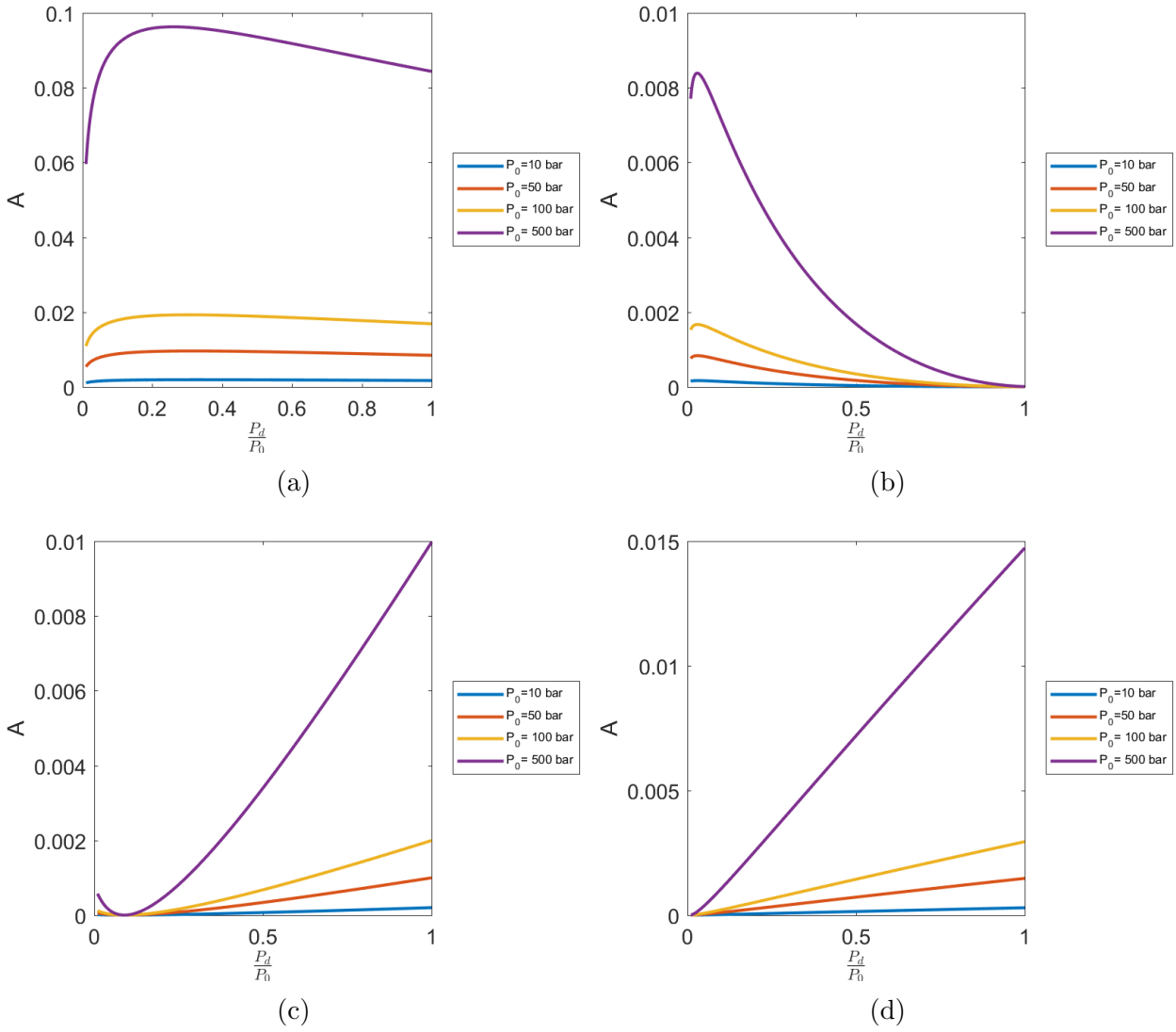

Figure 150: a) 500 K; b) 1000 K; c) 2000 K; d) 4000 K

D.1.5 B Results

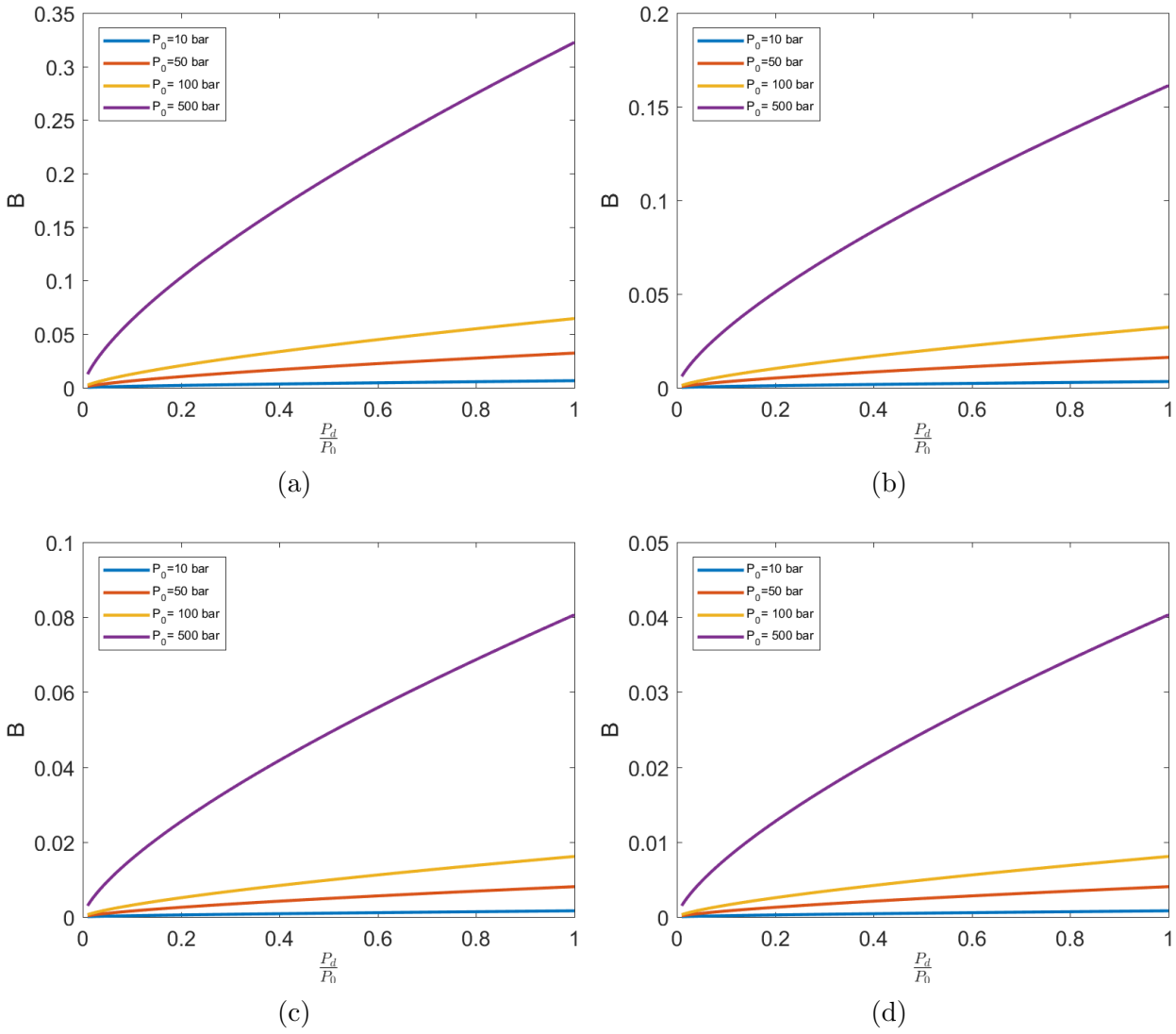

Figure 151: a) 500 K; b) 1000 K; c) 2000 K; d) 4000 K

D.1.6 Sound Speed Results

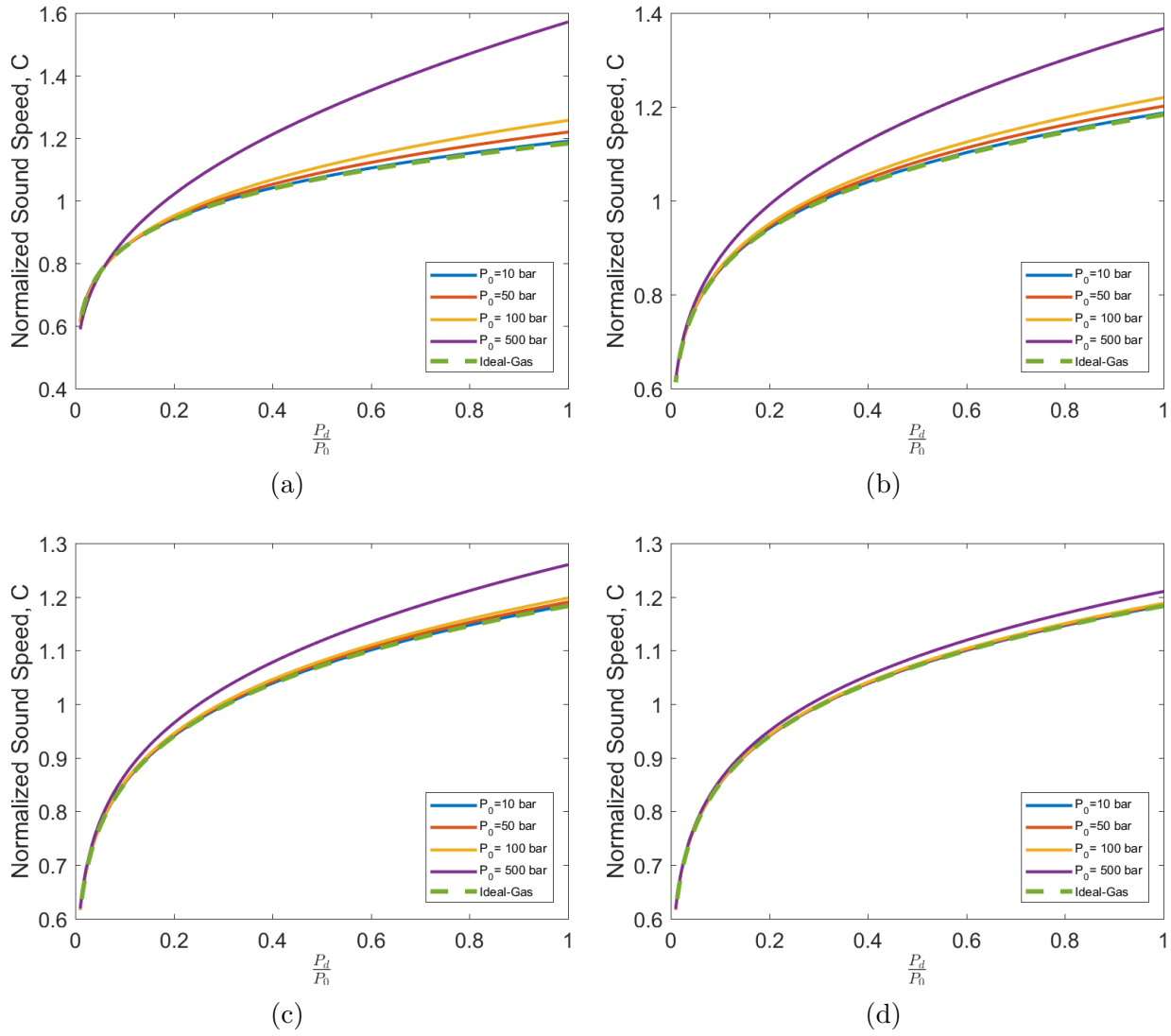

Figure 152: a) 500 K; b) 1000 K; c) 2000 K; d) 4000 K

D.1.7 Velocity Results

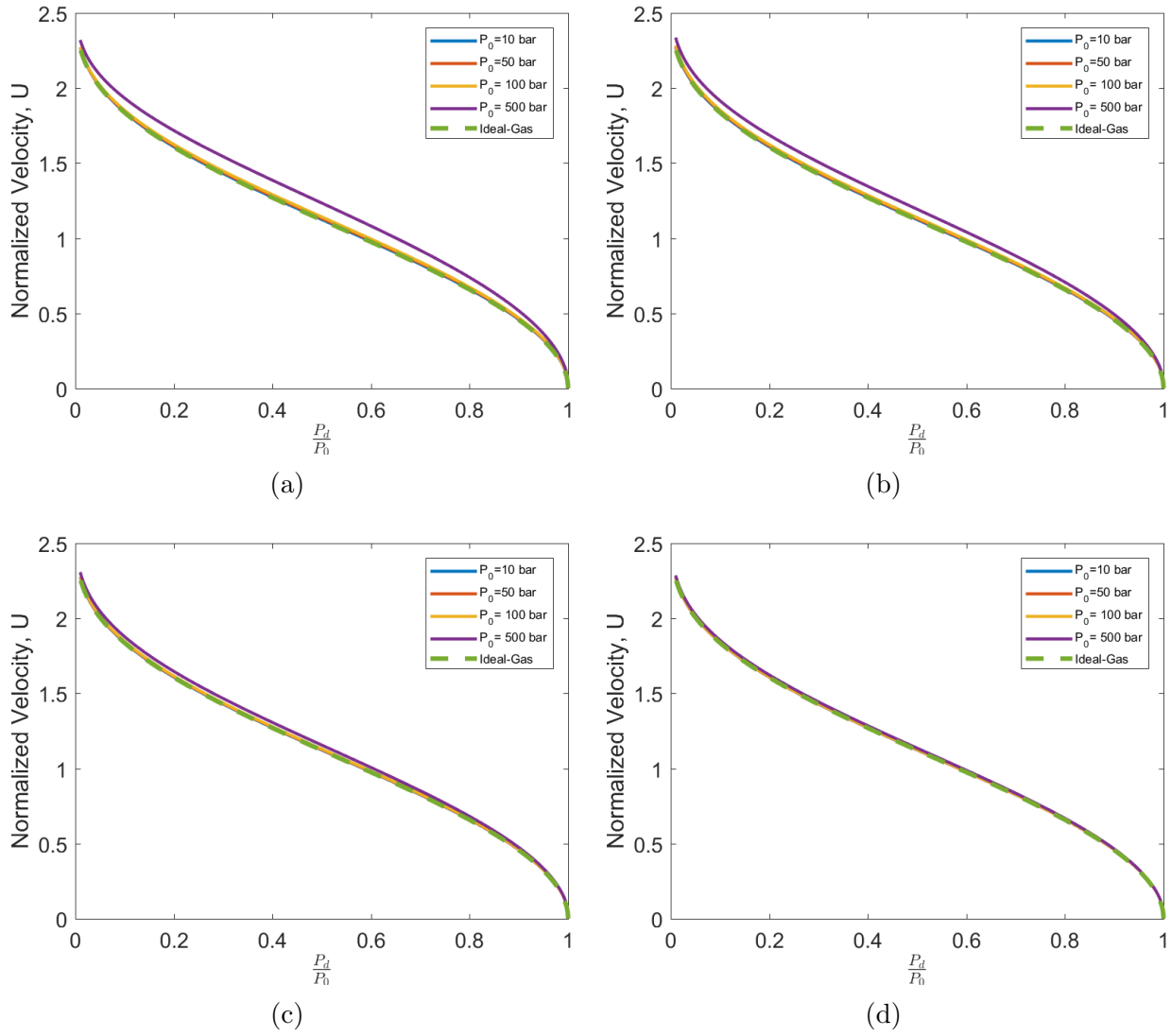

Figure 153: a) 500 K; b) 1000 K; c) 2000 K; d) 4000 K

D.1.8 Mach Number Results

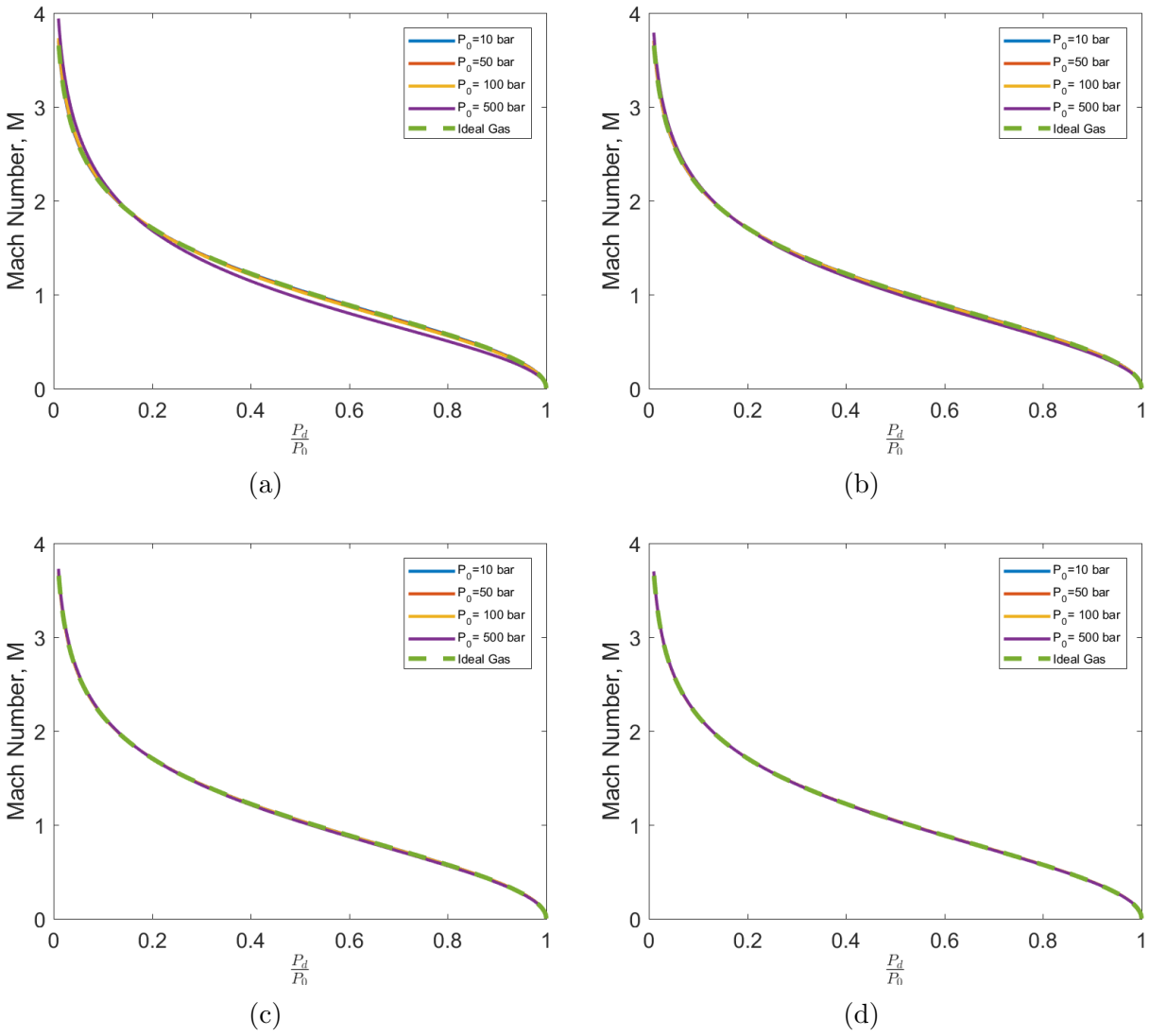

Figure 154: a) 500 K; b) 1000 K; c) 2000 K; d) 4000 K

D.2 Oxygen, O_2

D.2.1 Temperature Results

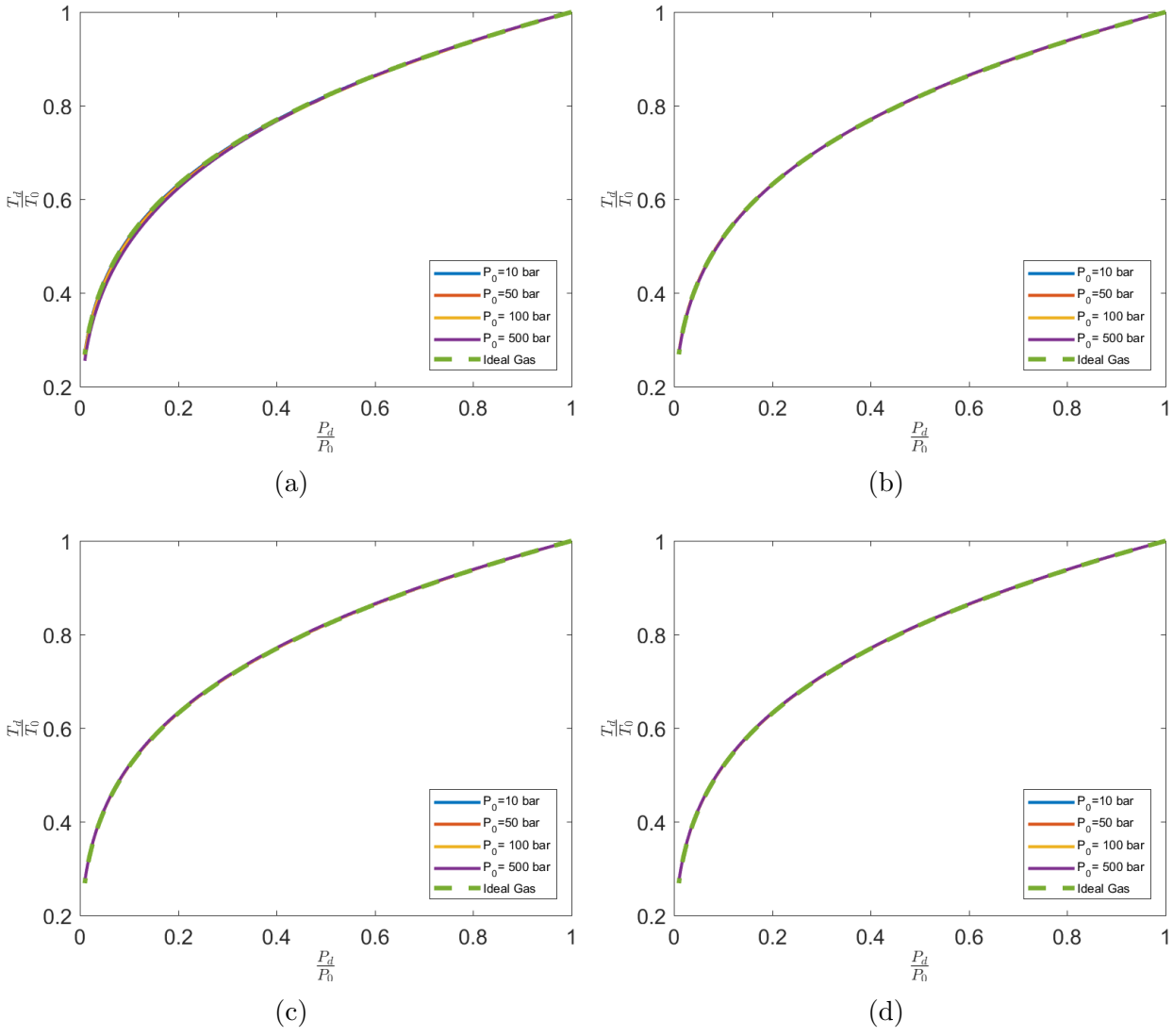

(a) (b)

(c) (d)

Figure 155: a) 500 K; b) 1000 K; c) 2000 K; d) 4000 K

D.2.2 Density Results

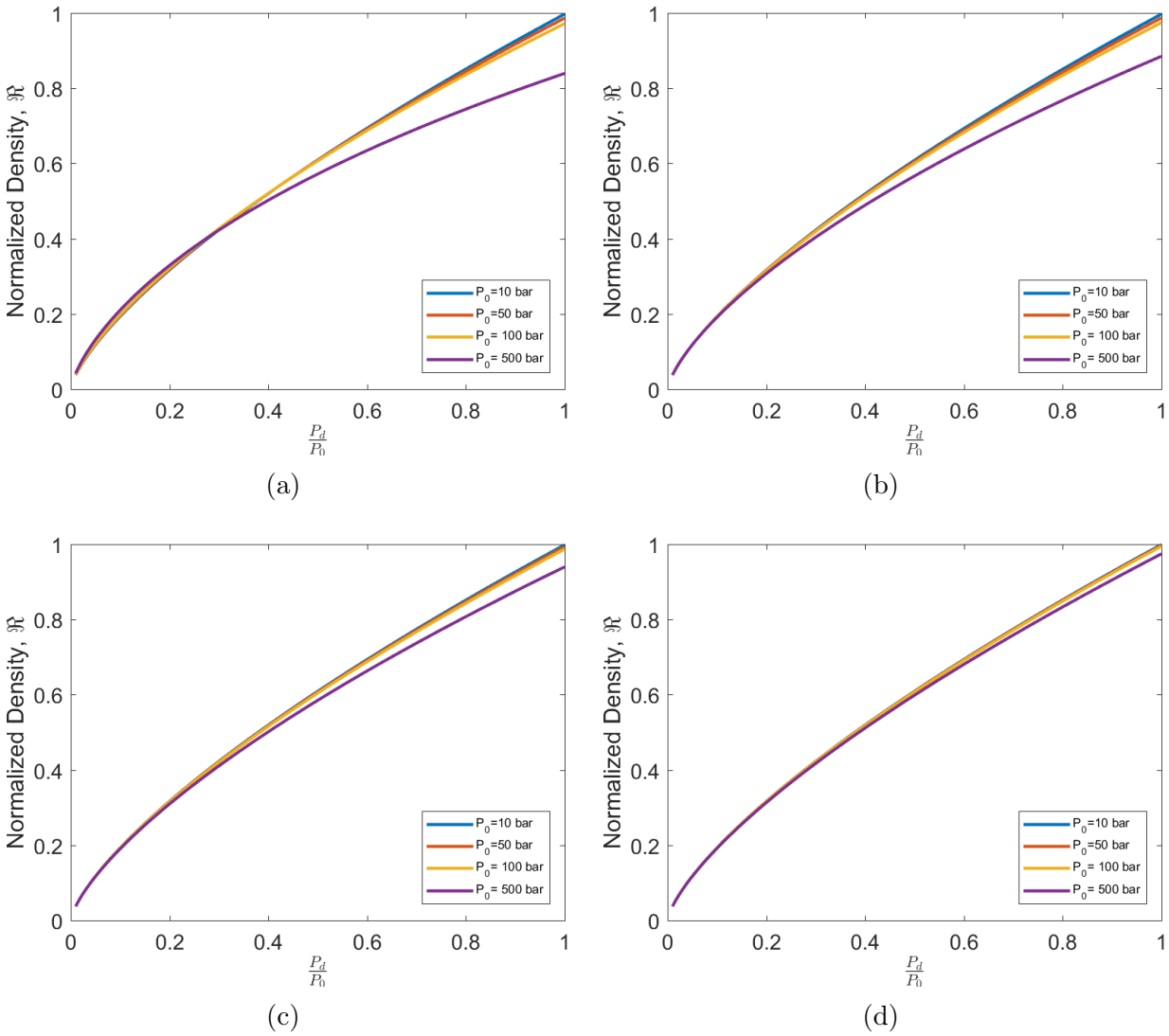

Figure 156: a) 500 K; b) 1000 K; c) 2000 K; d) 4000 K

D.2.3 Compressibility Factor Z Results

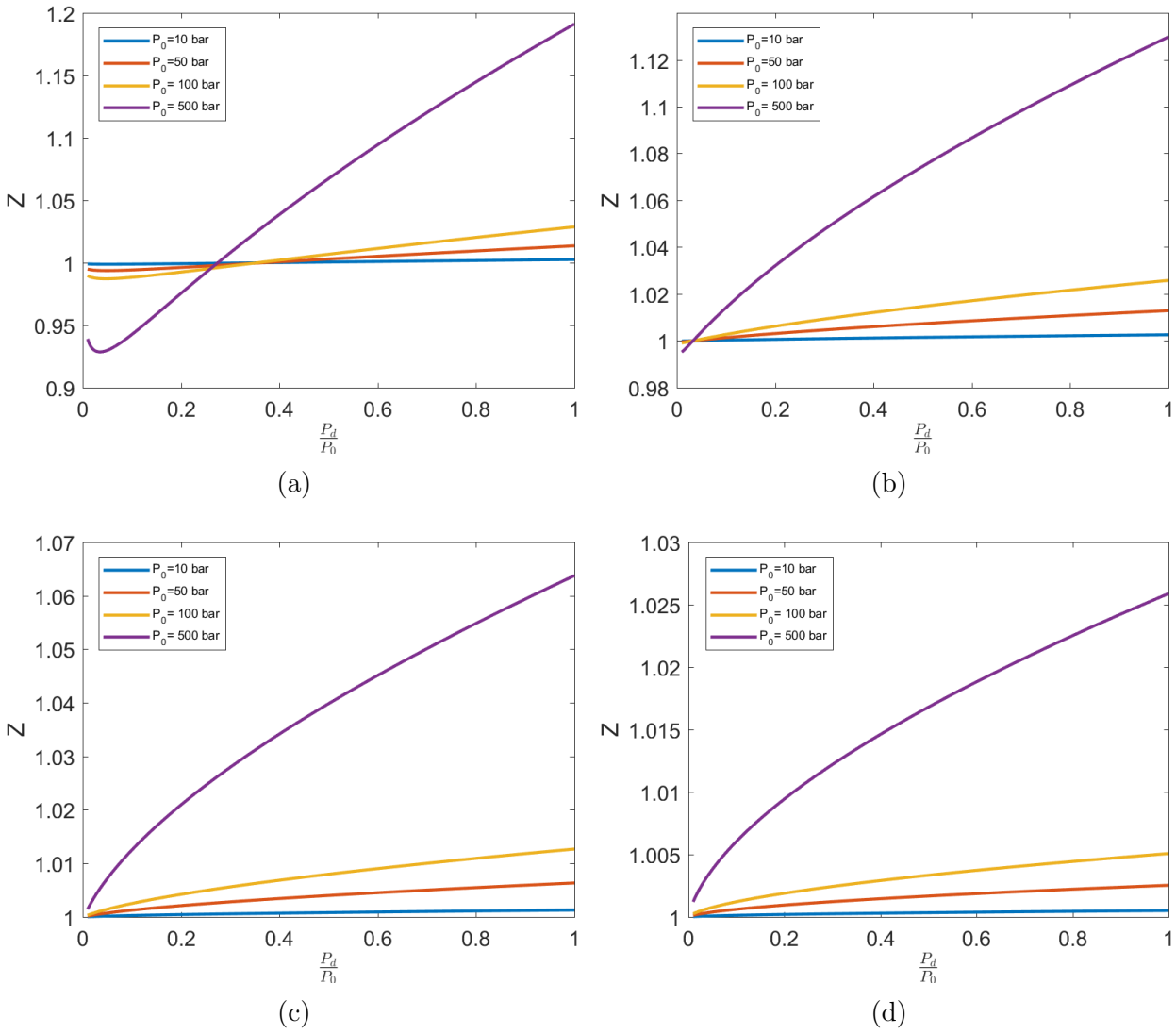

Figure 157: a) 500 K; b) 1000 K; c) 2000 K; d) 4000 K

D.2.4 A Results

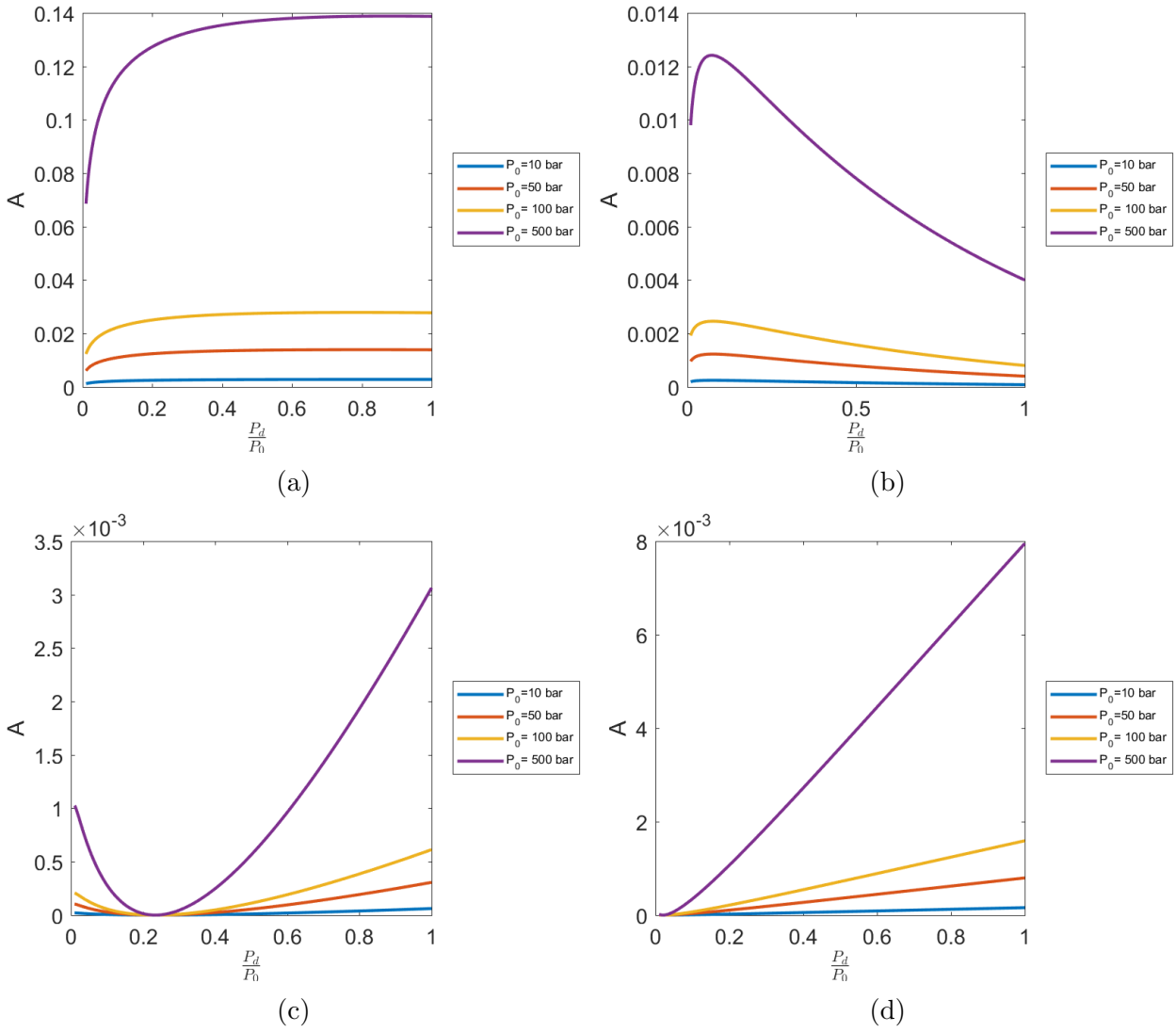

Figure 158: a) 500 K; b) 1000 K; c) 2000 K; d) 4000 K

D.2.5 B Results

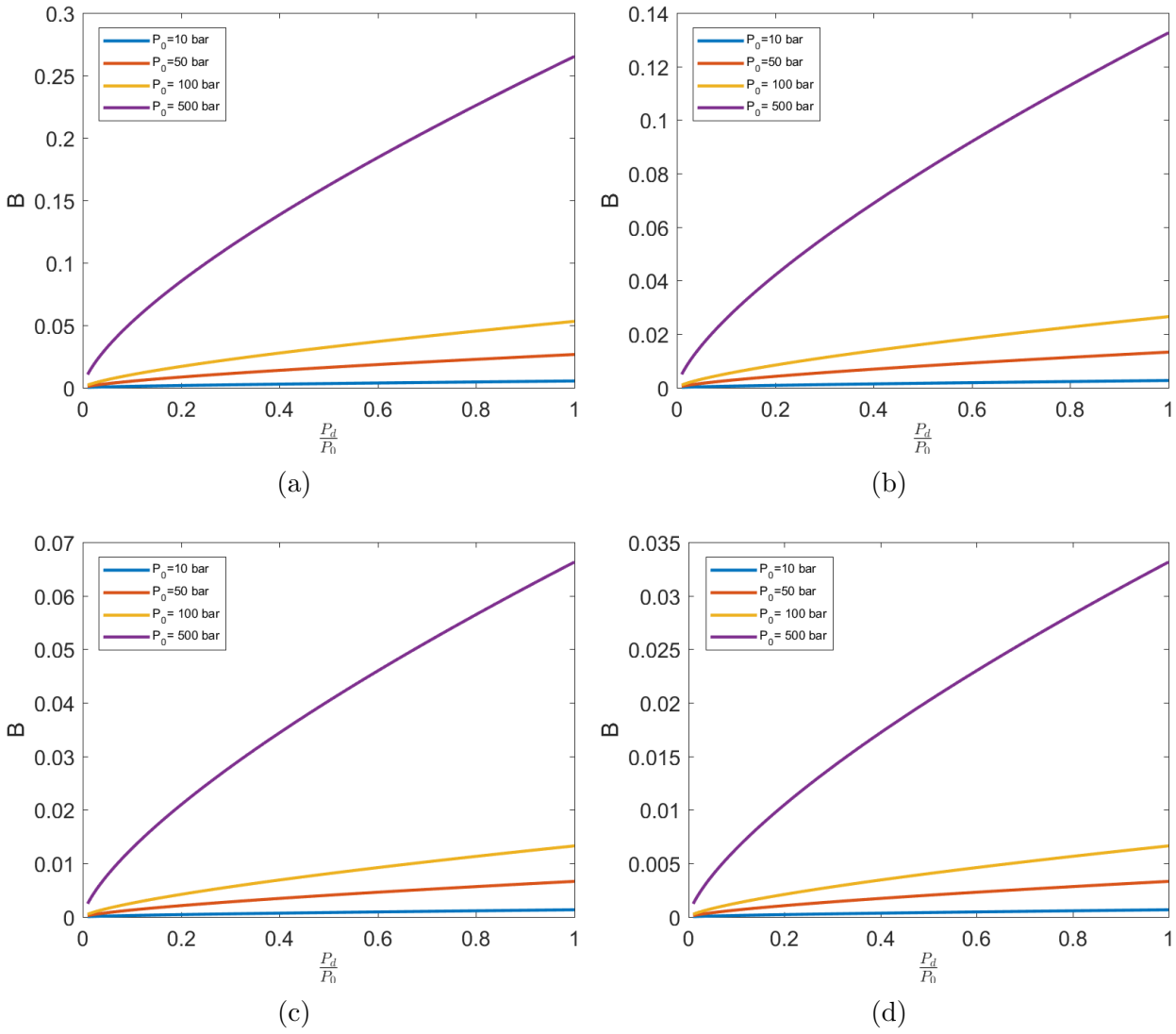

Figure 159: a) 500 K; b) 1000 K; c) 2000 K; d) 4000 K

D.2.6 Sound Speed Results

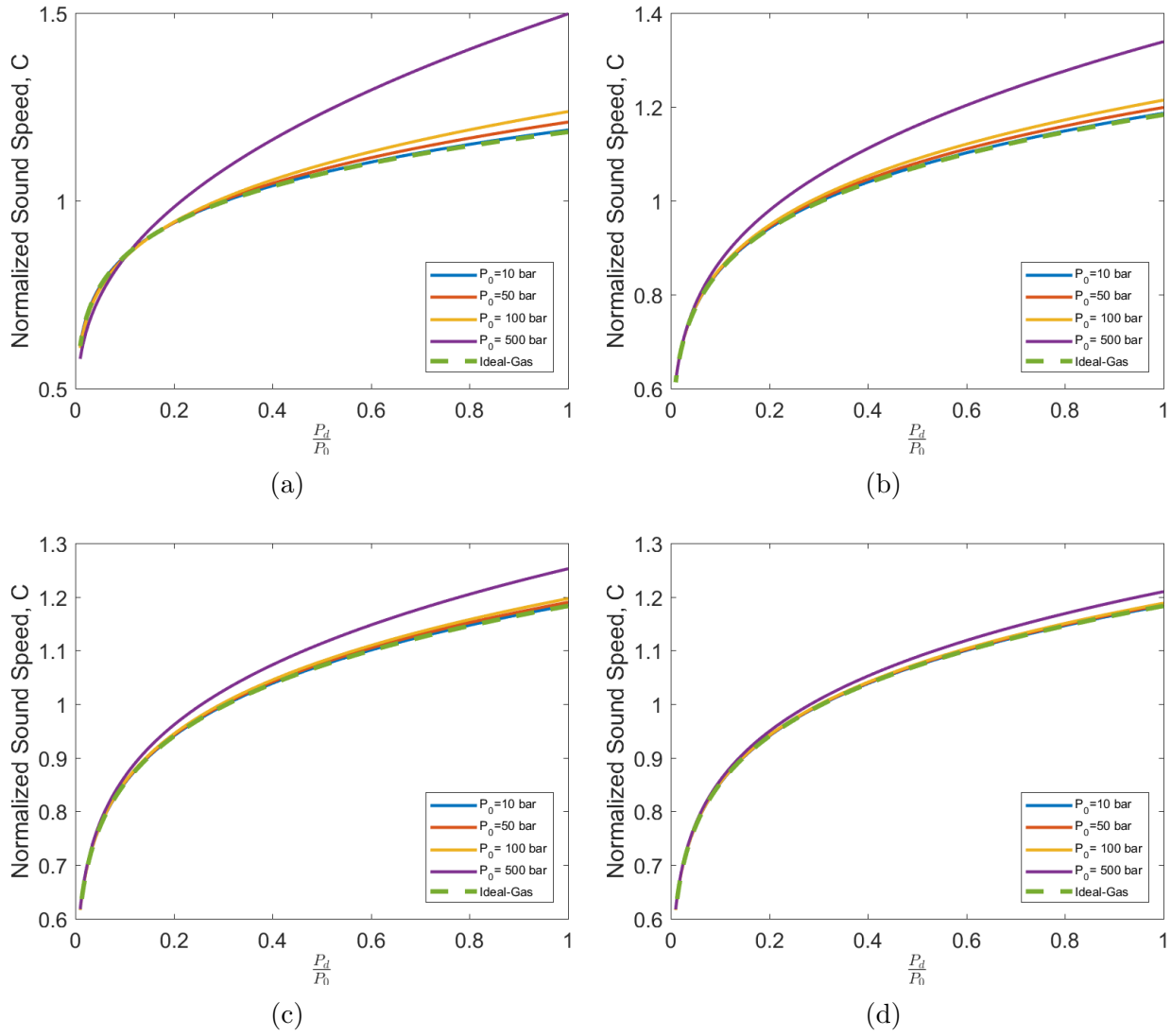

Figure 160: a) 500 K; b) 1000 K; c) 2000 K; d) 4000 K

D.2.7 Velocity Results

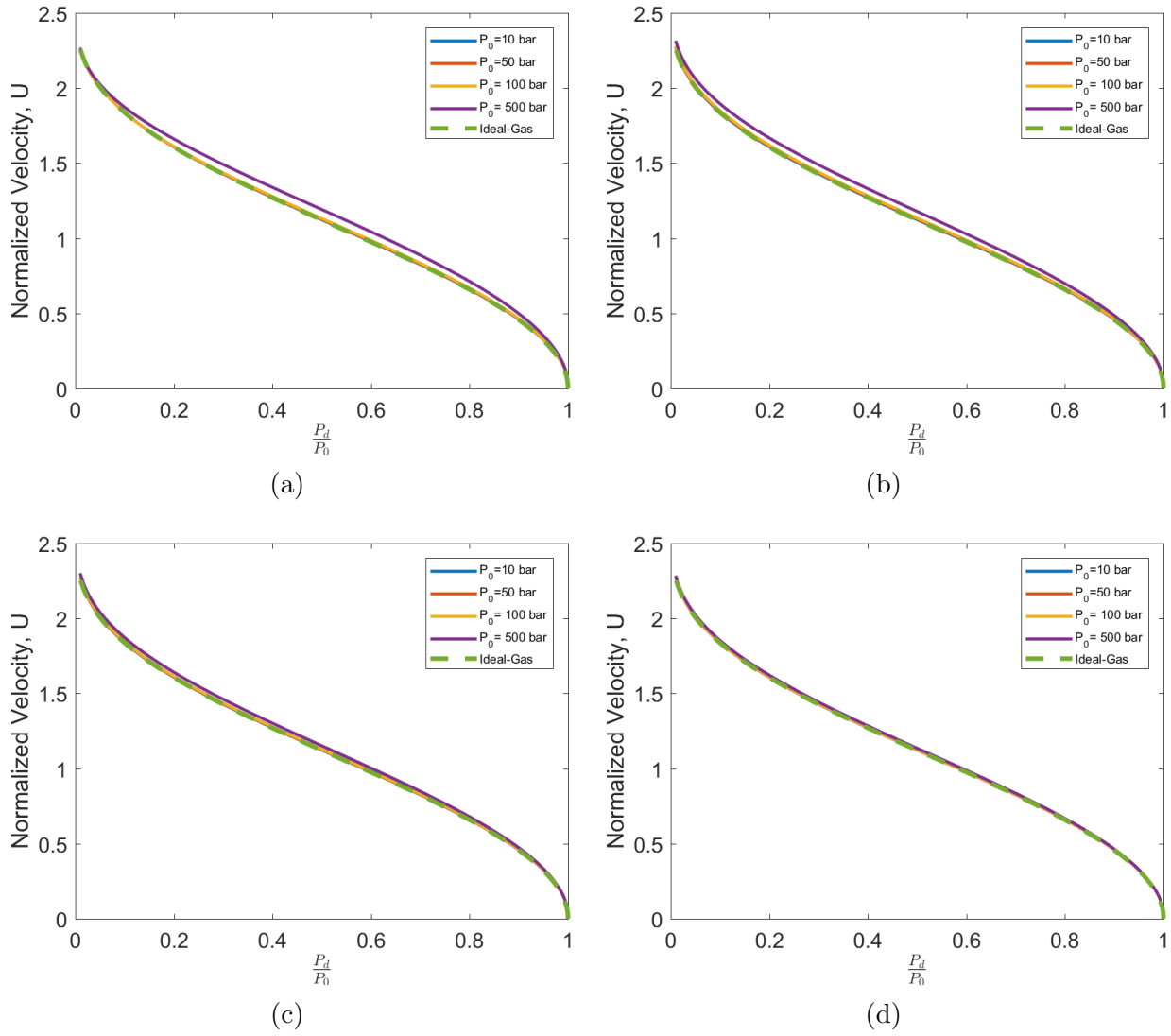

Figure 161: a) 500 K; b) 1000 K; c) 2000 K; d) 4000 K

D.2.8 Mach Number Results

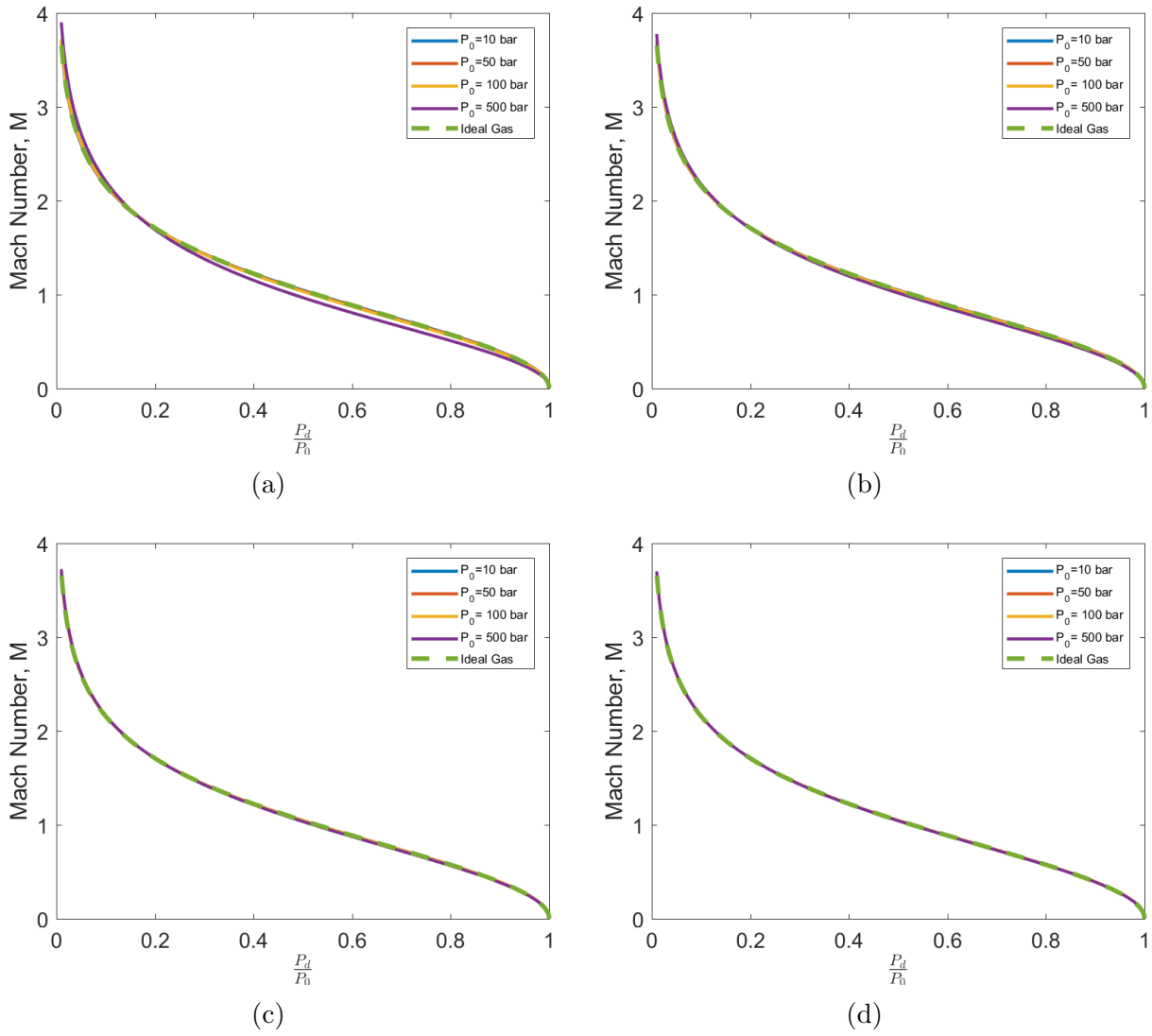

Figure 162: a) 500 K; b) 1000 K; c) 2000 K; d) 4000 K

D.3 Argon, *Ar*

D.3.1 Temperature Results

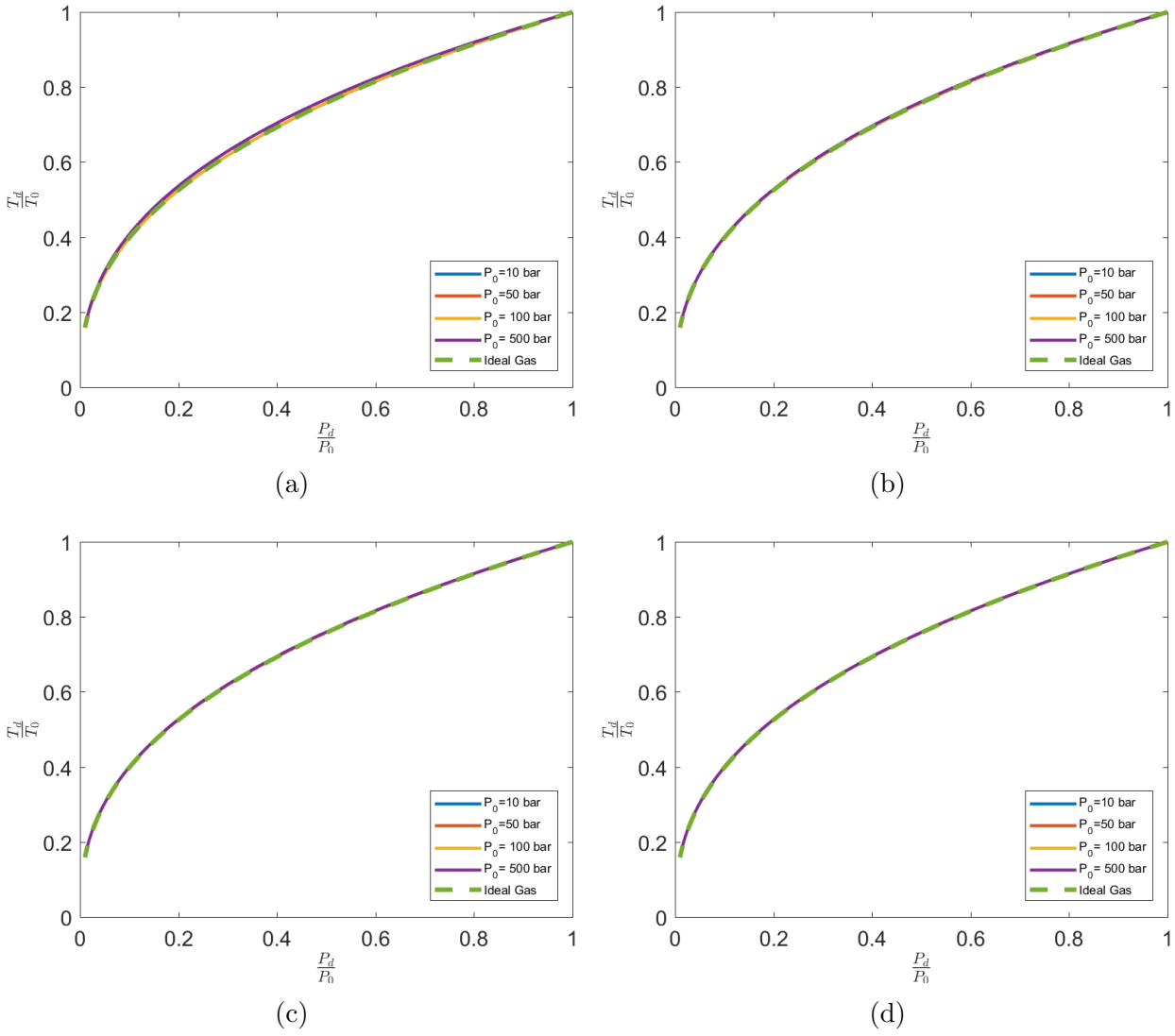

Figure 163: a) 500 K; b) 1000 K; c) 2000 K; d) 4000 K

D.3.2 Density Results

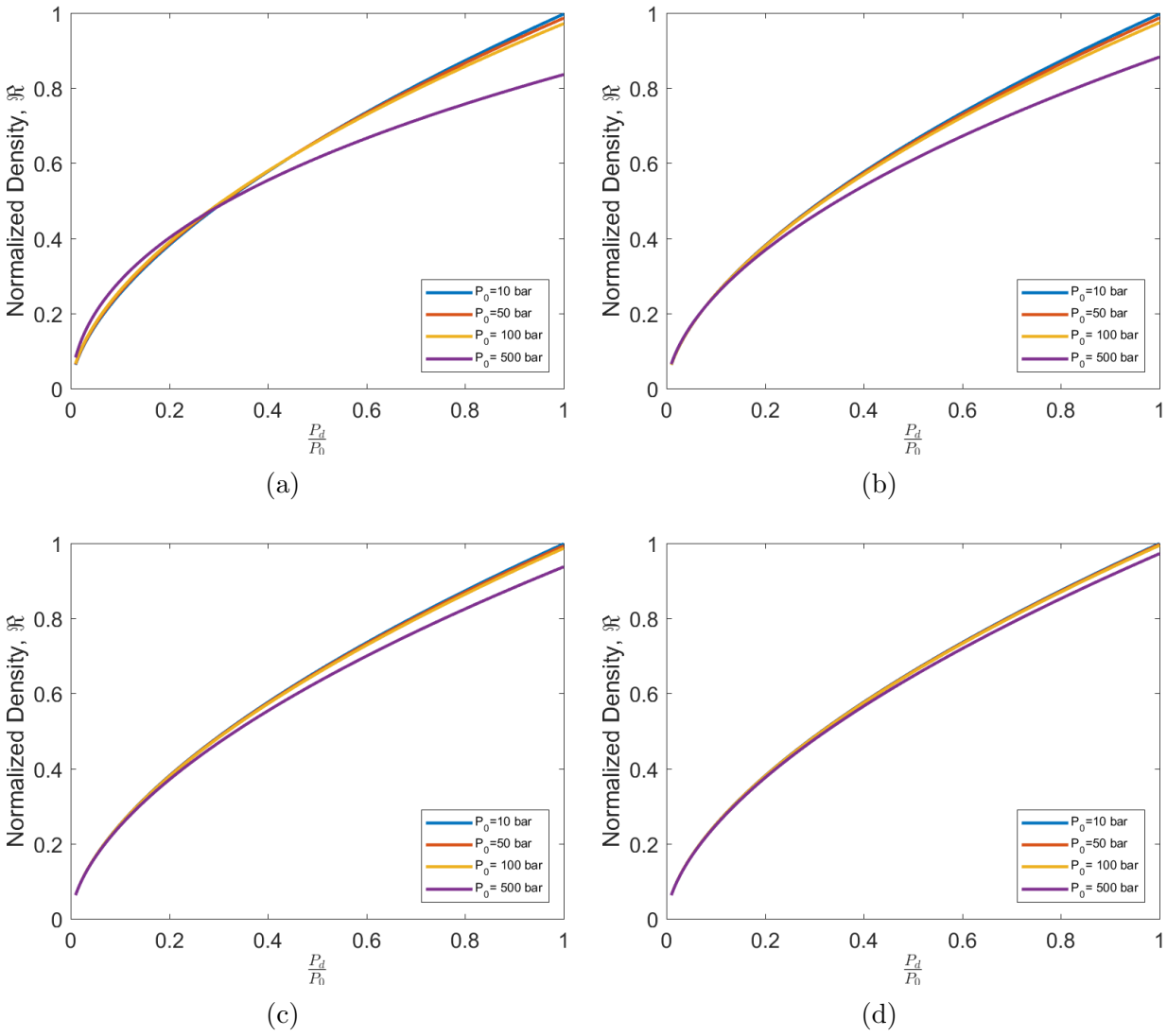

Figure 164: a) 500 K; b) 1000 K; c) 2000 K; d) 4000 K

D.3.3 Compressibility Factor Z Results

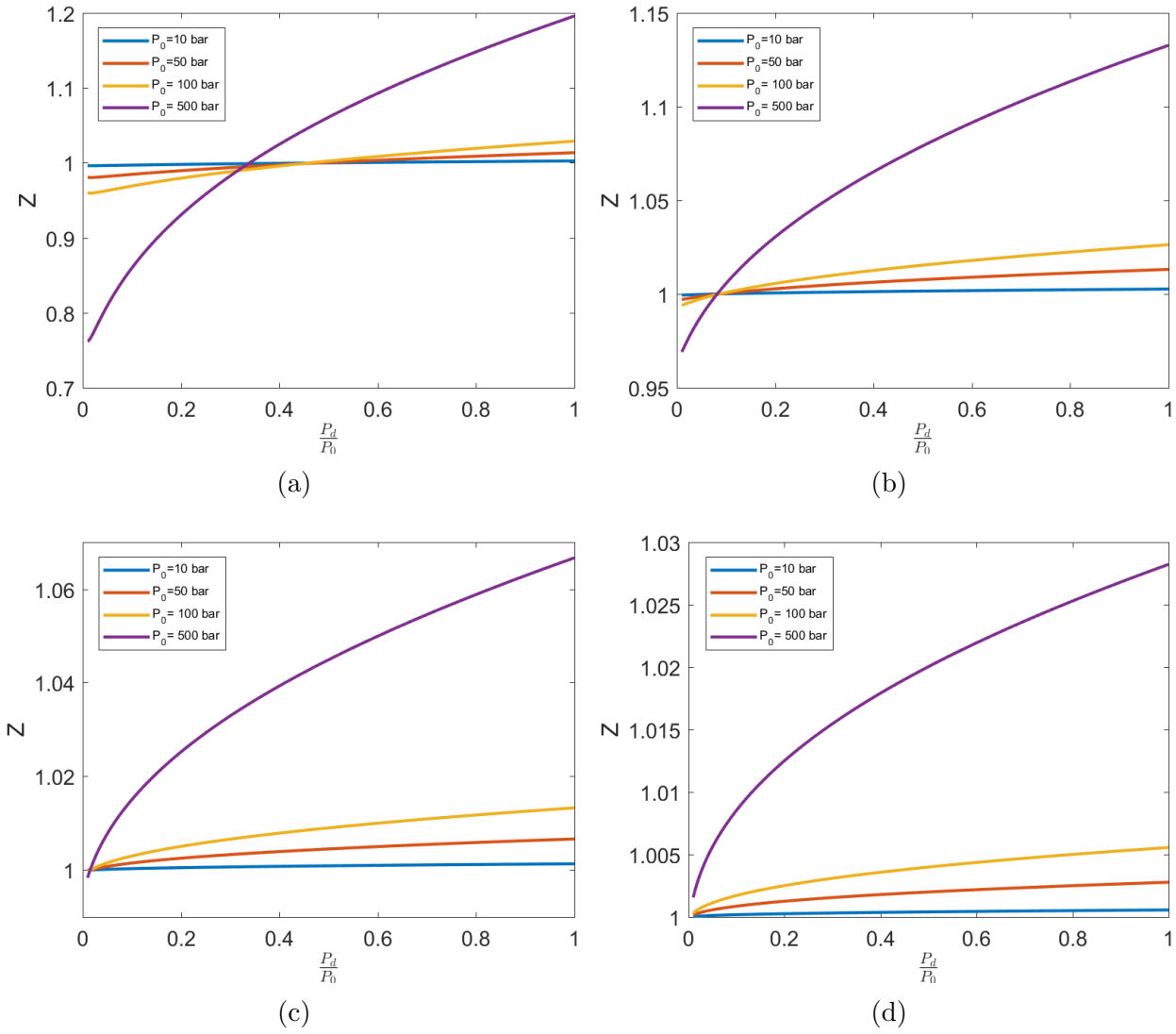

Figure 165: a) 500 K; b) 1000 K; c) 2000 K; d) 4000 K

D.3.4 A Results

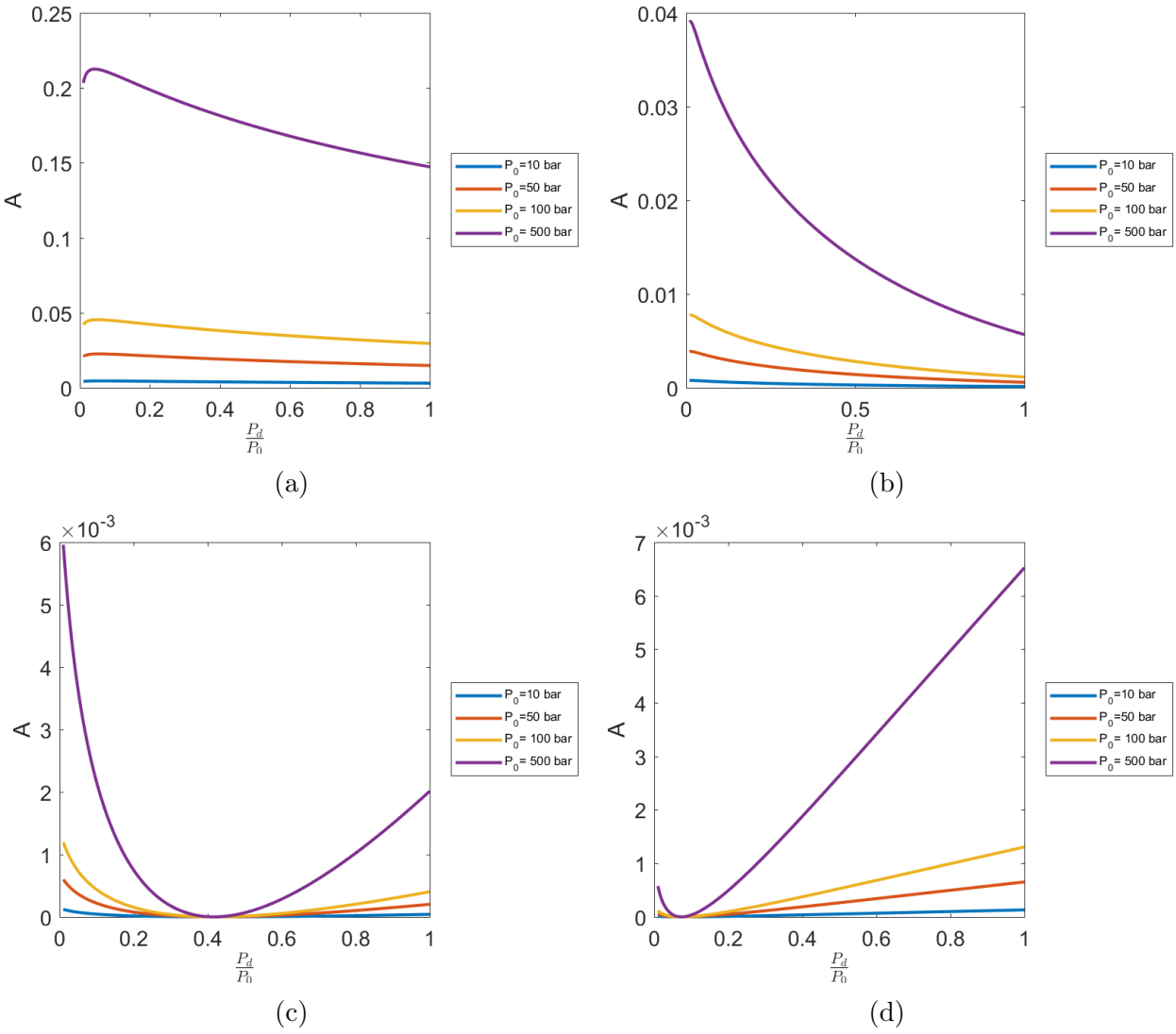

Figure 166: a) 500 K; b) 1000 K; c) 2000 K; d) 4000 K

D.3.5 B Results

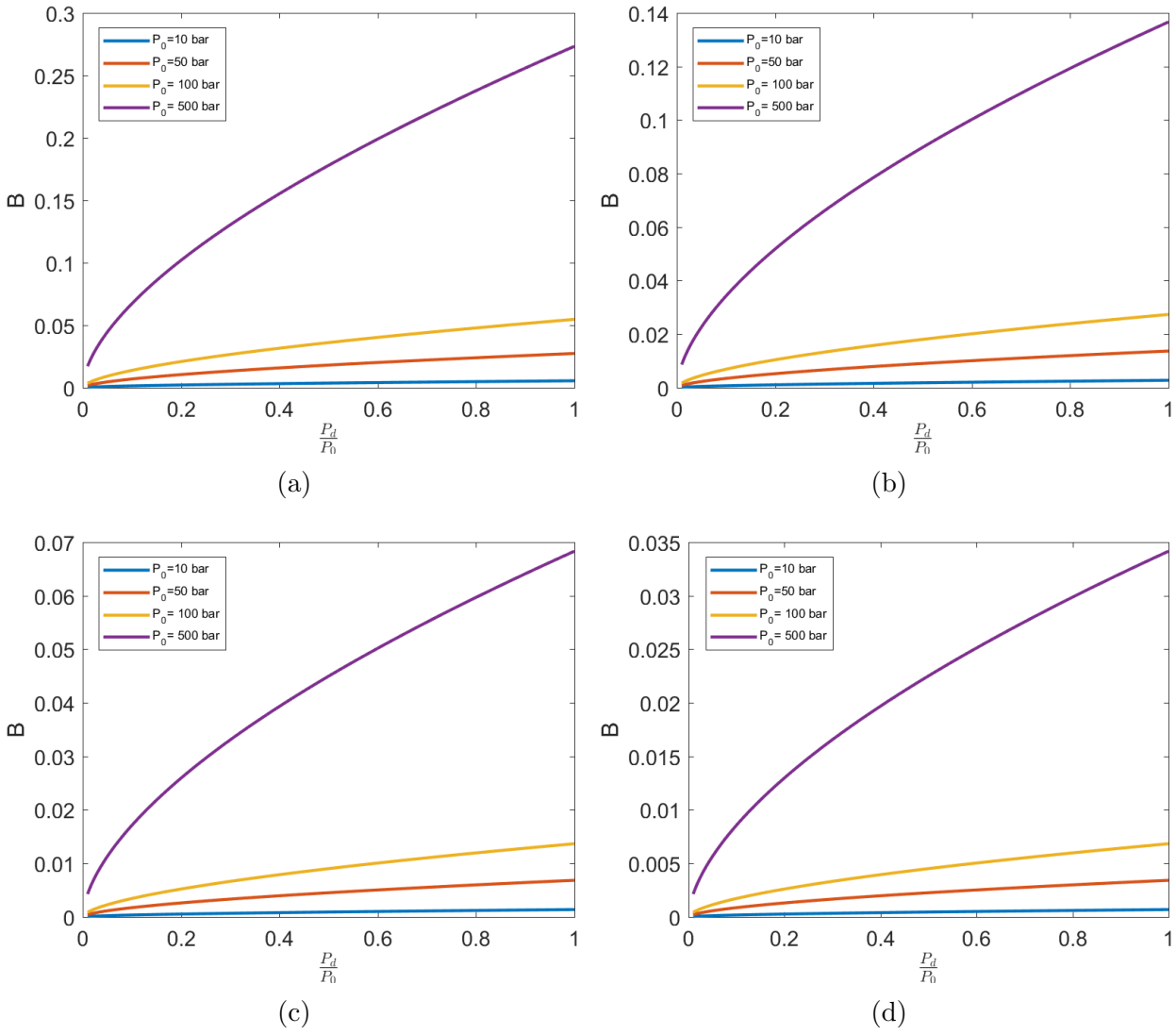

Figure 167: a) 500 K; b) 1000 K; c) 2000 K; d) 4000 K

D.3.6 Sound Speed Results

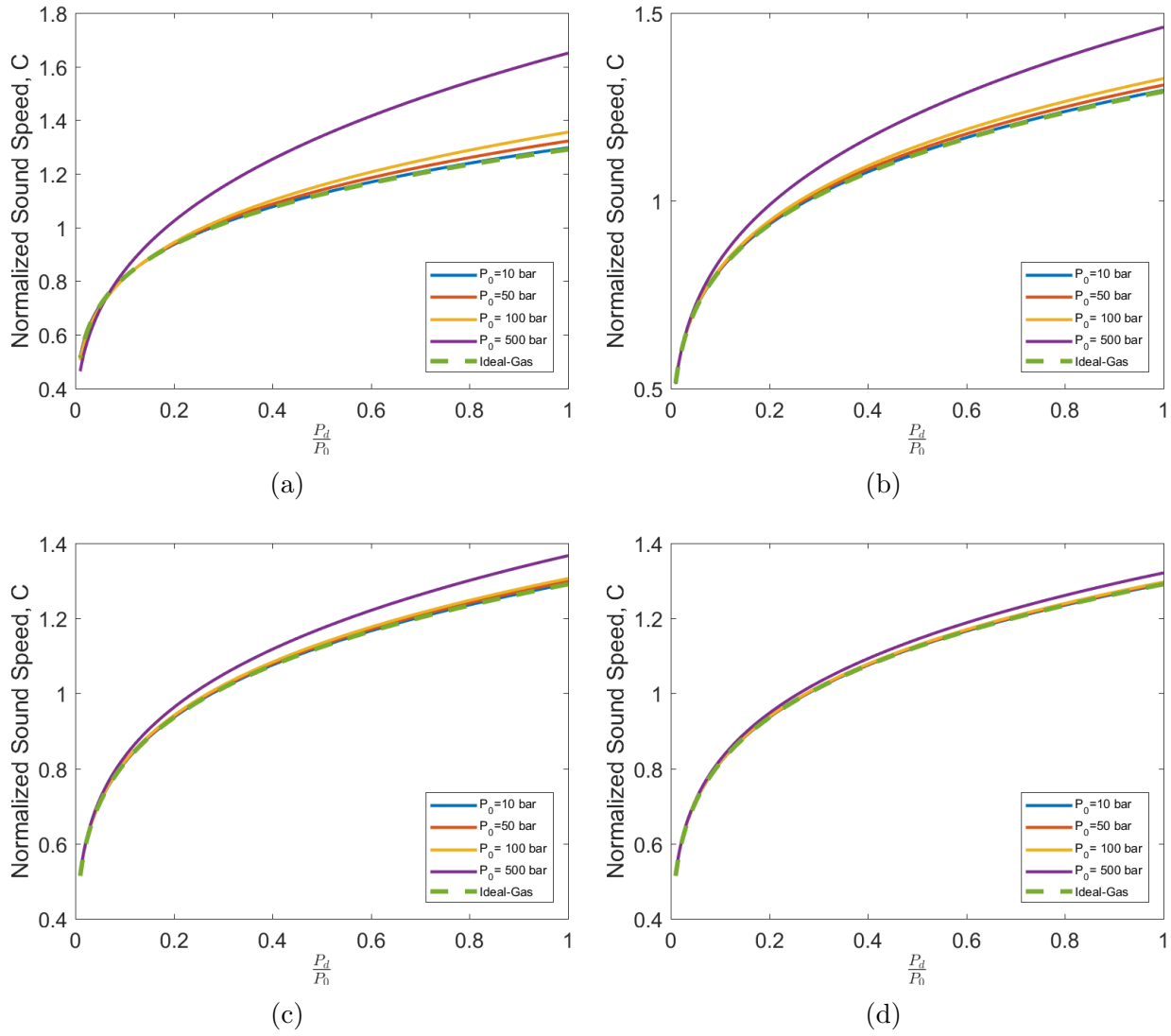

Figure 168: a) 500 K; b) 1000 K; c) 2000 K; d) 4000 K

D.3.7 Velocity Results

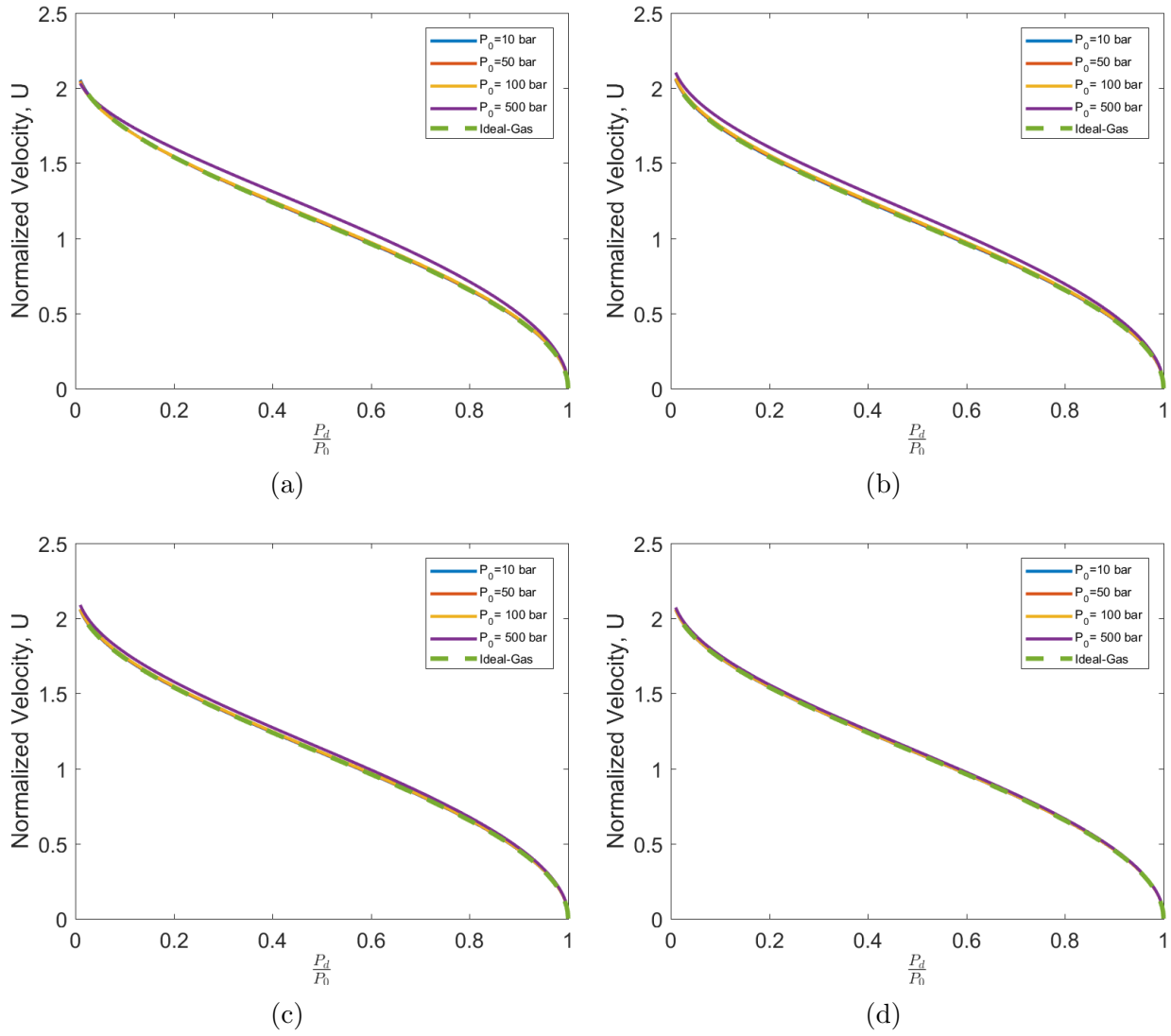

Figure 169: a) 500 K; b) 1000 K; c) 2000 K; d) 4000 K

D.3.8 Mach Number Results

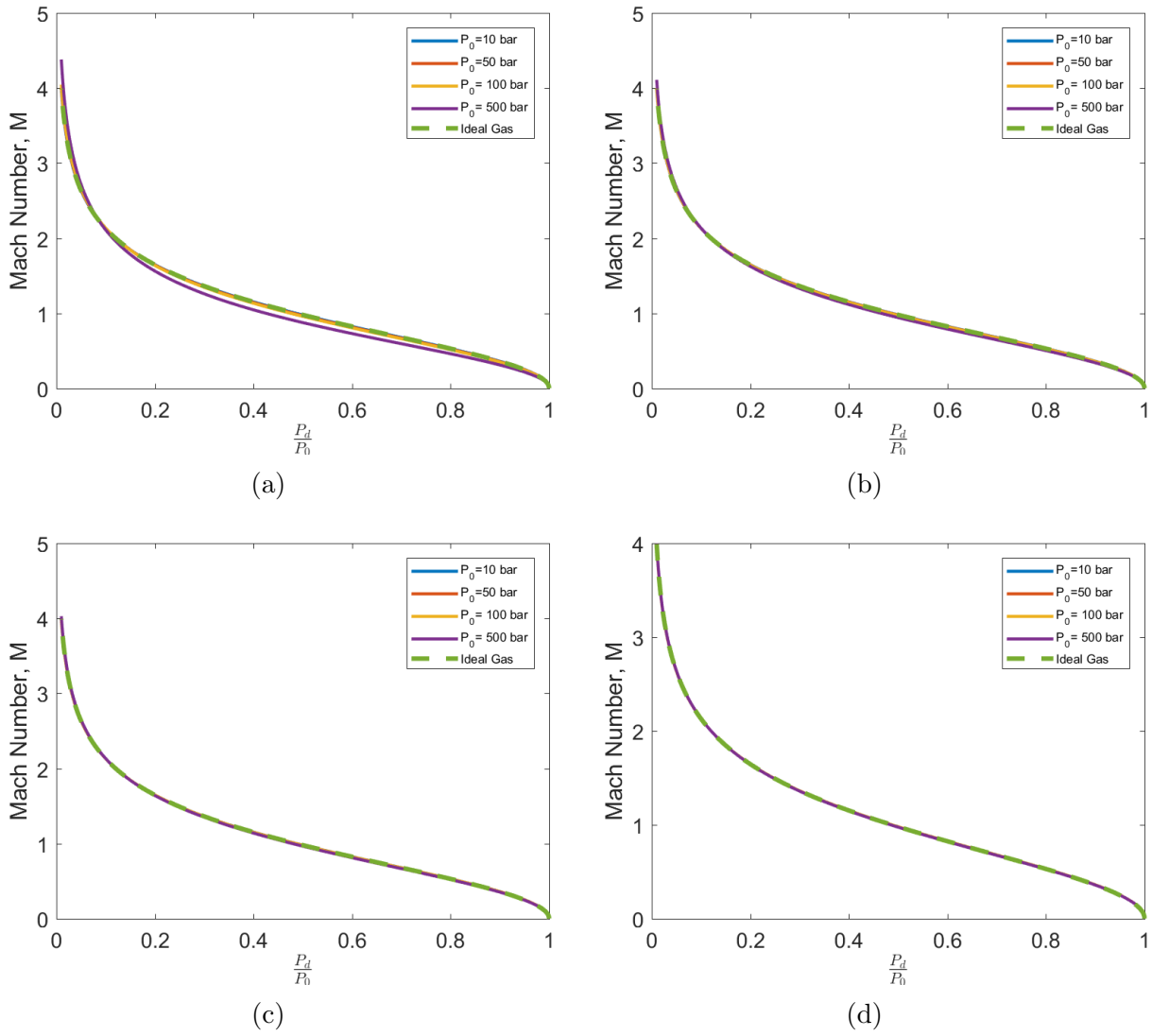

Figure 170: a) 500 K; b) 1000 K; c) 2000 K; d) 4000 K